Novel approaches for molecular tissue imaging of drugs and metabolites using high-resolution mass spectrometry

Dissertation

zur Erlangung des Grades

des Doktors der Naturwissenschaften

der Naturwissenschaftlich-Technischen Fakultät

Universität des Saarlandes

von

M.Sc. Ignacy Rzagalinski

Saarbrücken

2018

Tag des Kolloquiums: 03.04.2019

Dekan: Prof. Dr. Guido Kickelbick
Berichterstatter: Prof. Dr. Dietrich A. Volmer

                         Prof. Dr. Thomas Tschernig
Vorsitz: Prof. Dr. Gregor Jung
Akad. Mitarbeiter: Dr. Frank Hannemann

To my wife and best friend, Eliza, with love

"(…) because limits, like fears, are often just an illusion"

- Michael Jordan

Acknowledgements

First of all, I would like to express my sincere gratitude to Prof. Dietrich A. Volmer for giving me the opportunity to conduct PhD research in his laboratory, for his advice and stimulating discussions we had over these years, and particularly for his support in publishing the results of my research and his consistent enthusiasm about all my new research ideas.

Besides my advisor, I thank all fellow labmates from the Institute of Bioanalytical Chemistry at Saarland University for creating a very nice working environment and for all the funny, as well as scientific and stimulating discussions we had throughout the last four years.

This thesis would not have been possible without collaboration with members of the Institute of Anatomy and Cell Biology at Medical Department of Saarland University. In particular, I would like to thank Prof. Thomas Tschernig for setting up and maintaining this cooperation as well as Dr. Nadine Hainz for her expert knowledge in conducting all animal experiments. In addition, I thank Prof. Carola Meier for collaboration, as well as Alexander Grißmer and Alina Mattheis for histological staining and the light microscopy experiments.

I also would like to thank Pascal Schorr from the Department of Chemistry at Humboldt University Berlin for the rabbit brain preparations, as well as Sylvia Kuhn from the Physical Chemistry Group at Saarland University for the scanning electron microscopy experiments. Furthermore, I thank Dennis Becker from the Inorganic Solid State Chemistry Group at Saarland University for ball milling sample preparation, and Christina Muth from the Leibniz Institute of New Materials for solid-state UV-Vis spectroscopy measurements. Finally, I thank Prof. Uli Müller from the Neurobiology Group of Center of Human and Molecular Biology at Saarland University for helping me with cryosectioning of the animal tissues.

Last but not least, I want to thank my family and all friends for their consistent support. In particular, my deepest gratitude goes to my wife, Eliza, for her sacrifice, patience, understanding and above all, for her unfailing support and being my compass in tough times. Simple words cannot express my feelings, nor my thanks for all her help. Finally, I thank my little princess, Lila, who brings even more sunshine into my life.

Table of Contents

I. Zusammenfassung

Das Hauptziel der vorliegenden Arbeit war die Entwicklung neuartiger, analytischer Methoden zur molekularen Bildgebung niedermolekularer Verbindungen aus tierischen Gewebeabschnitten unter Verwendung der Matrix-unterstützten Laser-Desorption/Ionisation und der hochauflösenden Fourier-Transformations Ionenzyklotronresonanz Massenspektrometrie. Insgesamt wurden drei neue Ansätze entwickelt, bei denen die massenspektrometrische Bildgebung für die räumliche und molekulare Analyse von endogenen Metaboliten und Arzneimitteln aus Gewebeschnitten von Mäusen verwendet wurde. Zunächst wurde MALDI-FTICR-MSI erfolgreich für die molekulare Bildgebung von Gallensäuren mit hoher räumlicher Auflösung als der deprotonierten Spezies und Protonen-gebundenen Dimeren aus Mausleberabschnitten angewendet. Zweitens wurde die unpolare Matrix DCTB (2-[(2E)-3-(4-tert-Butylphenyl)-2-methylprop-2-enyliden]malononitril) erstmals für die hochempfindliche, quantitative MALDI-Bildgebung von im Zentralnervensystem wirkenden Medikamenten bei Hirnschnitten der Maus angewendet. Weiterhin konnten Beweise für Hirngewebsregion abhängige, sowie für die MALDI Matrix abhängige Ionensuppression vorgelegt werden. Schließlich wurde eine hochauflösende MALDI-FTICR-Bildgebung angewendet, um molekulare und räumliche Veränderungen im Gehirnstoffwechsel von Mäusen als Reaktion auf eine immunmodulatorische Behandlung mit Teriflunomid zu untersuchen, und zeigten sie offensichtliche Veränderungen.

II.   Abstract

The main goal of this work was to develop novel analytical methods for molecular imaging of low-molecular weight compounds from animal tissue sections using matrix-assisted laser desorption/ionization and high-resolution Fourier-transform ion cyclotron resonance mass spectrometry. In general, three novel approaches were proposed, in which mass spectrometry imaging was employed for spatial and molecular analysis of both endogenous metabolites and pharmaceutical drugs from mouse tissue sections. Firstly, MALDI-FTICR mass spectrometry was successfully employed for high-spatial resolution molecular imaging of bile acids observed as deprotonated molecules and proton-bound dimers from mouse liver sections. Secondly, the nonpolar matrix, DCTB (2-[(2E)-3-(4-tert-butylphenyl)-2-methylprop-2-enylidene]malononitrile), was applied for the first time for highly sensitive, quantitative MALDI imaging of central nervous system drugs from mouse brain sections. In addition, the evidence for brain tissue regions- as well as MALDI matrix-dependent ion suppression was presented. Finally, high-resolution/high-accuracy MALDI-MS imaging was applied for studying molecular and spatial changes in mouse brain metabolism in response to immunomodulatory treatment with teriflunomide, revealing evident alterations observed in particular for the certain metabolite classes.

III. Abbreviations

9-AA	9-aminoacridine
BBB	blood-brain barrier
CHCA	α-cyano-4-hydroxycinnamic acid
CID	collision-induced dissociation
CNS	central nervous system
DCTB	2-[(2E)-3-(4-tert-butylphenyl)-2-methylprop-2-enylidene]malononitrile
DESI	desorption electrospray ionization
DHB	2,5-dihydroxybenzoic acid
ESI	electrospray ionization
FTICR	Fourier-transform ion cyclotron resonance
GC-MS	gas chromatography-mass spectrometry
IE	ionization energy
IS	internal standard
LAESI	laser ablation electrospray ionization
LESA	liquid extraction surface analysis
MALDI	matrix-assisted laser desorption/ionization
MS	mass spectrometry
MS/MS	tandem mass spectrometry
MSI	mass spectrometry imaging
m/z	mass-to-charge ratio
LC-MS	liquid chromatography-mass spectrometry
PA	proton affinity
PBD	proton-bound dimer
PET	positron-emission tomography
qMSI	quantitative mass spectrometry imaging
QWBA	quantitative whole-body autoradiography
SALDI	surface-assisted laser desorption/ionization
SIMS	secondary ionization mass spectrometry

IV. Introduction

Mass spectrometry imaging – introduction, workflow and applications

Mass spectrometry imaging (MSI) enables label-free *in-situ* molecular imaging of chemical compounds directly from different two-dimensional surfaces [1]. Since its introduction in the '90s [2], MSI has proved to be a valuable tool for imaging of spatial distributions of different compounds from a wide variety of samples such as plants [3–5], different (bio)material surfaces [6, 7], bacterial cultures [8, 9] or even single cells [10–12]. The most predominant application of MSI, however, is determining the spatial distributions of different biologically relevant compounds directly from the animal tissue sections [13–16]. One of the strongest advantages of this method is that, in contrast to other imaging techniques such as QWBA or PET, MSI does not require any work- and time-consuming chemical labeling of the compounds of interest [17–19]. Furthermore, as MSI combines an unambiguous molecular identification of compounds with determination of their spatial distributions, it allows for simultaneous imaging of hundreds of both endogenous compounds and exogenous drugs from the same tissue section [20–22]. In turn, the method has a tremendous potential for different applications in biological, pharmaceutical or biomedical research [23–25].

While the complete and detailed MSI experimental procedure will strongly depend on many factors (such as the type of sample, analytes of interest, ion source used, etc.), an overview can be presented as the simplified workflow as shown in Figure 1.
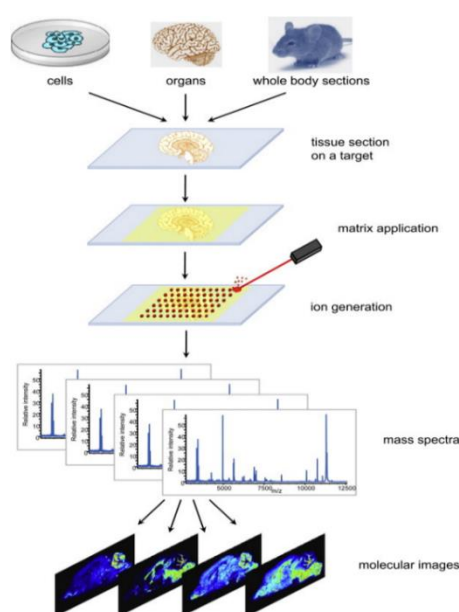

Figure 1. Schematic overview of MSI workflow. Reproduced with permission from reference [25].

The in-detail description of the particular steps of MSI experiment can be found in one of the numerous excellent review articles [16, 25–29]. In brief, MSI starts with sample preparation realized by tissue (or whole body) cryosectioning and mounting the 10-20-µm-thick sections onto the microscopic glass slides. Furthermore, different approaches to tissue pretreatment might be applied (depending on the compounds of interest to be analyzed), as well as MALDI matrix deposition in the case of MALDI imaging mass spectrometry [30, 31]. Finally, such prepared biological material is analyzed with mass spectrometry by sampling the tissue surface at each *x,y* coordinate in order to collect a single MSI pixel mass spectrum from each spot. Of note, the MSI pixel size is defined here as the distance between the centers of each sampled (ablated in the case of MALDI) spot. As a result, hundreds of single mass spectra are being collected and the following computerized data analysis lead to the visualization of spatial distributions either of a single compound detected at a certain *m/z* value (as a characteristic heat map) or of the several different compounds across the tissue section (as an RGB image) [32].

It is noteworthy that MSI can be performed by employing different ion sources. The only prerequisite is that the current technique has to enable systematic probing of the two-dimensional tissue surface at distinct locations that will further correspond to the single MSI pixels. Figure 2 summarizes currently the most common ionization methods used in MSI.
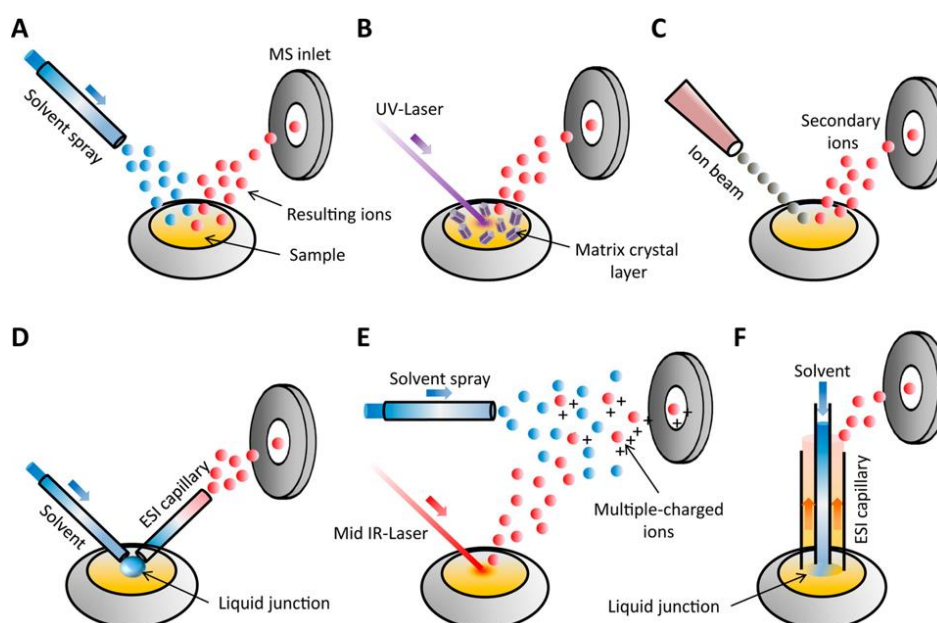

Figure 2. Different ionization methods used for MSI: desorption electrospray ionization, DESI (A), matrix-assisted laser desorption/ionization, MALDI (B), secondary ion mass spectrometry, SIMS (C), nano-DESI (D), laser ablation electrospray ionization mass spectrometry, LEASI (E), liquid extraction surface analysis, LESA (F). Reproduced with permission from [33].

Importantly, the most proper ion source for the certain MSI experimental setup is usually selected based on the ionization capabilities for a particular class of compounds of interest. It is crucial to remember, however, that this decision will also determine other experimental factors such as attainable spatial resolution (the minimum pixel size), signal response (sensitivity), speed of analysis, compound coverage and finally, sample pretreatment needed prior to MS analysis [15, 33, 34].

To date, MSI has proved to be a valuable tool for *in-situ* imaging of various classes of compounds directly from the surface of different organs or whole-body sections. These include endogenous metabolites [20, 35, 36], lipids [37–39], peptides [40–42], proteins [43–45] as well as different drugs [19, 24, 46, 47]. An interesting summary has been recently published by Palmer *et al.* [48], where the current status of mass spectrometry imaging field was presented as the results of survey addressed to the MSI practitioners. Three aspects are worth mentioning here. Firstly, as seen in Figure 3, the major MSI application area is the analysis of low-molecular weight compounds (metabolites, lipids, drugs), while few of the current MSI practitioners apply this technique to on-tissue detection of proteins and peptides. Furthermore, the results clearly show the dominant role of MALDI as the ionization method for most of the MSI users (95% of respondents). Finally, vast part of the small molecules MSI studies are performed using high-resolving power instruments (FTICR and Orbitrap mass analyzers), which are, as will be further explained in-detail, essential to provide sufficient mass resolution and mass accuracy in the low *m/z* range.
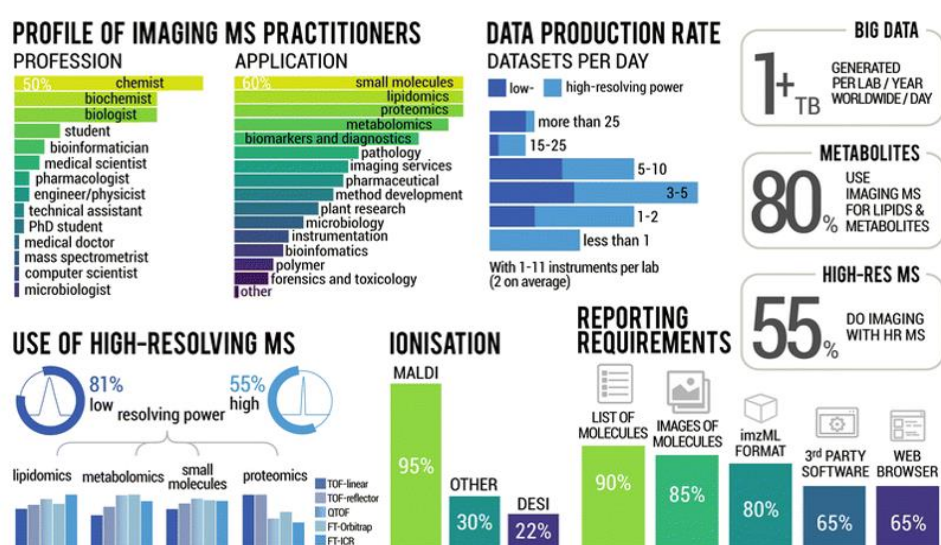

Figure 3. Summary findings of a survey conducted by Palmer *et al.*, showing the current status of the MSI field. Reproduced with permission from [48].

The central role of MALDI in MSI of low-molecular weight compounds

Within a group of different ionization methods that can be used for tissue mass spectral imaging (Figure 2), matrix-assisted laser desorption/ionization (MALDI) is the most predominant one [34, 49]. To date, MALDI has established its position as a key MSI technology for biological [36, 50], pharmaceutical [19, 51, 52], and even clinical [53, 54] applications. There are excellent (review) articles that cover the fundamental principles of MALDI (*i.e.* different ionization/protonation models including gas-phase theory and "lucky survivor" model) [55–57] as well as different experimental facets affecting desorption and ionization processes [58–60]. While all of these aspects should be carefully considered in order to successfully apply MALDI to MSI studies, it is essential to point out the key role of MALDI matrix in the whole experimental process. Briefly, as illustrated in Figure 4, the matrix absorbs the UV light at the laser operating wavelength and enables transfer of the analyte molecules into the gas phase. Therefore, both selecting of an appropriate matrix compound and assuring reproducible matrix deposition are essential for an efficient analytes extraction from the thin tissue slices and ultimately, the desorption/ionization of co-crystallized analyte molecules.
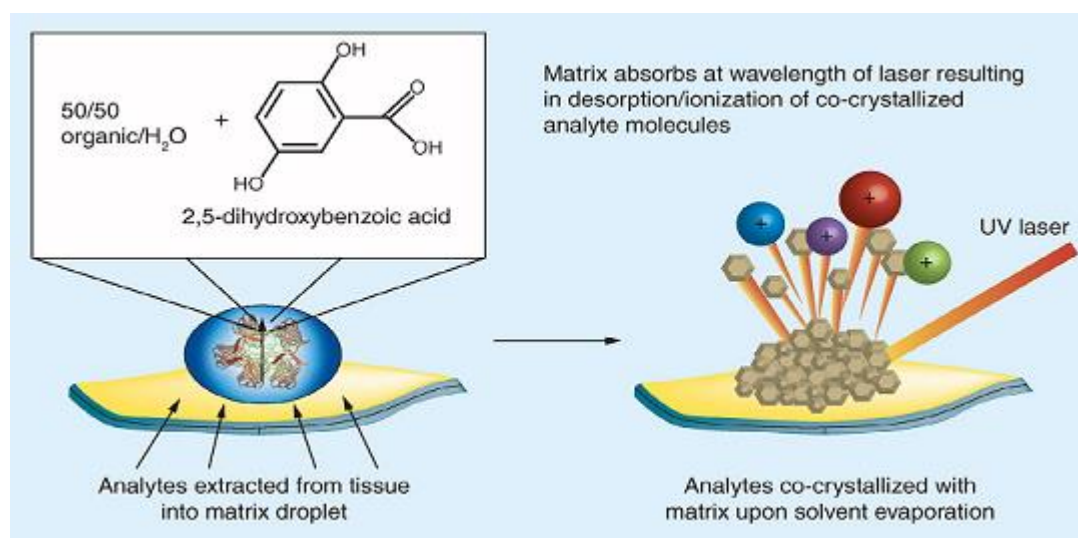

Figure 4. Function and importance of MALDI matrix in MALDI-MSI. Reproduced from reference [51] with permission of Future Science Group.

Selection of both the matrix compound and the solvent system (*e.g.* water/organic composition, pH, etc.) are crucial for the successful and sensitive analysis of the certain classes of compounds. In the recent years, a tremendous improvement has been made in order to better

understand the role of matrix in MALDI process [57]. This further led to the rational designing of some new MALDI matrices, with deliberately modified structures in order to obtain favorable gas-phase thermodynamic characteristic and thus, delivering higher sensitivity in both MALDI-MS and MALDI-MSI [59, 61, 62]. Moreover, numerous different new matrices were proposed, in particular for MALDI imaging of small molecules, including nanoparticle-based inorganic matrices (contributing to the whole concept of surface-assisted laser desorption/ionization (SALDI)) [63, 64] or more recently, conjugated polymers-based dual-mode matrices [65]. Surprisingly and despite the above, still the vast portion of MALDI-MSI studies of small molecules (drugs, metabolites, lipids) report about the usage of the most common, conventional MALDI matrices – CHCA and DHB in positive ion mode [66–69] and 9-AA in negative ion mode [70–72]. Therefore, an important part of this dissertation was the application of the nonpolar DCTB matrix for highly sensitive imaging of CNS drugs from mouse brain tissue sections. Of note, since DCTB was previously considered as an electron transfer matrix, the appropriate rationale (computational thermodynamic calculations of IE and PA) for an additional proton-transfer MALDI mechanism with this matrix was provided. The results of this study are included in the dissertation as the *Publication 3*.

In addition to the matrix selection, another crucial step in MSI is the process of matrix deposition on the top of tissue section. In contrast to the non-imaging MALDI-MS (where in dried-droplet method, matrix is pre-mixed with analyte before spotting and co-crystallizing on the MALDI target [73]), in MALDI-MSI matrix must be uniformly applied onto the tissue surface [31]. Therefore, the tissue during this process should be wet enough to achieve sufficient extraction of the tissue-embedded analyte molecules, but at the same time not over wetted to avoid delocalization of extracted compounds. Furthermore, the deposition process should lead to the formation of homogeneous and small crystals (ideally <1μm), what is particularly important for MALDI imaging at high lateral resolutions. To date, different devices were used for on-tissue matrix deposition, including manual airbrush and piezoelectric sprayers as well as sublimation apparatus. The most widespread and versatile technique, however, employed either one of the commercially available (from HTX or SunChrom) or home-built robotic sprayers such as the one constructed by the current author and used in all MALDI-MSI sample preparation processes described in this dissertation.

Importance of high-resolving power in MSI of small molecules

Due to the high molecular complexity of the analyzed tissue sections in MSI, the importance of high-resolving power mass analyzers is even more critical than in any other LC-MS or GC-MS analyses. Essentially, without any chromatographic separation, the whole analysis has to rely exclusively on the high-resolution and high-accuracy measurements in order to distinguish the analyte signal from different numerous interfering peaks. The latter ones are especially rich in the low *m/z* range and may origin from both endogenous compounds and the MALDI matrix-related species (different clusters and fragment ions) [74, 75]. For example, the detrimental role of high resolution capabilities in MSI research has been excellently visualized by Castellino *et al.* [51], where two different metabolites of the same parent drug (lapatinib) could be resolved during MALDI imaging experiment in dog liver sections (Figure 6). These two compounds showed different spatial distributions, which might be potentially significant for their mode of action or toxicity and is of the greatest importance in the drug development process. Of note, currently the mass analyzer with the highest resolving powers as well as the highest mass accuracy possibilities (used in all research included in this dissertation) is Fourier-transform ion cyclotron resonance (FTICR), where the gas-phase ions are trapped, excited and detected within the electric trapping plates (ion trap) placed in a high magnetic field [76]. The currently available resolving powers exceeds the values of $R > 10^6$ and mass accuracies <1 ppm [77, 78].
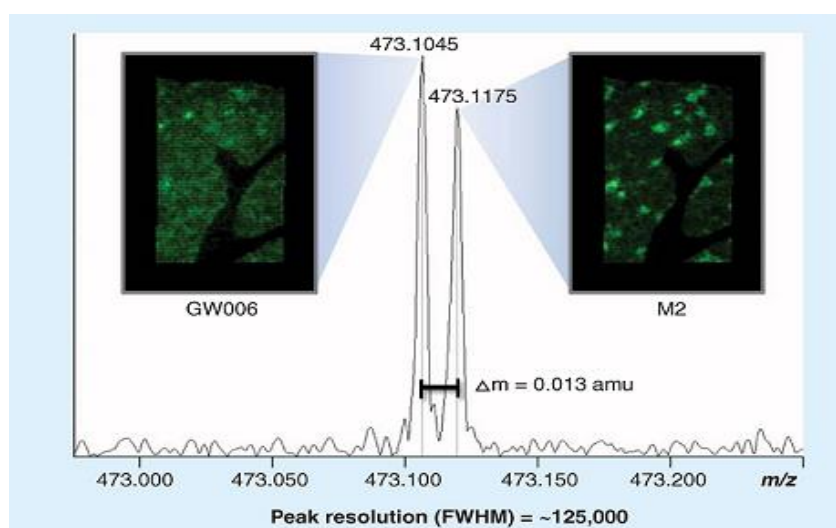

Figure 5. Example of the importance of high resolving power in MSI application to the pharmaceutical research (two different metabolites of lapatinib resolved by FTICR-MS showing different spatial distributions across the dog liver section). Reproduced from reference [51] with permission of Future Science Group.

While the (ultra-)high resolving power will always deliver the more detailed molecular information obtained from the MSI experiment (*e.g.* compared to much faster time-of-flight analyzers), one has to remember that the longer transient lengths during FTICR mass analysis will also result in much longer total experimental time. This might be even more critical when using high spatial resolution and thus, increasing the number of MSI pixels within the whole measurement. Furthermore, since MSI can be considered as a "sample volume limited" technique, the sensitivity will also deteriorate when employing the very small pixel sizes (=high spatial resolution). In all, the MSI methods need to compromise between the '4S-criteria' (speed, specificity, spatial resolution and sensitivity), which has been recently summarized and presented in a review by Schulz *et al.* (Figure 6) [79].
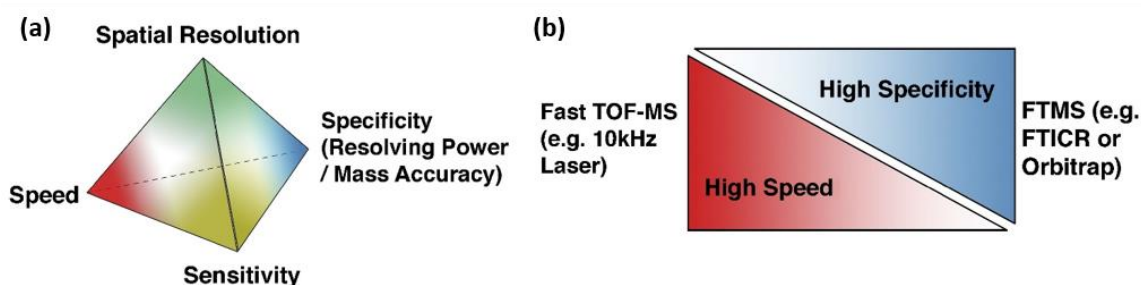

Figure 6. (a) 4-S criteria for MSI; (b) compromise between high speed by TOF-MS *versus* high specificity by FTMS in MSI. Reproduced with permission from [79].

Quantification, ion suppression and sensitivity challenges in MALDI-MSI

In MSI, similarly to other mass spectrometry-based analytical strategies, obtaining reliable information about the amount of compounds of interest is of great importance. Depending on the scientific question, either relative semi-quantitative differences between different compounds across the tissue or whole body section (*relative* quantification) or absolute concentrations of analyte in mole (or mass quantity) units per area (or mass) of tissue (*absolute* quantification) are required [80–83]. The relative quantitative mass spectrometry imaging (qMSI) approach is realized by applying different normalization routines (where each mass spectrum from every single MSI pixel is suspected to a correction with a certain factor), with the best results assured by normalization to the appropriately selected internal standard (IS), ideally isotope-labeled version of the target analyte [84–87]. On the other hand, obtaining the reliable absolute amounts of a compound of interest requires a special calibration/standardization strategy, with the matrix-matched calibration approach

guaranteeing the most precise and accurate results (Figure 7) [87–90]. Since this chapter provides only a brief introduction to the broad topic of quantification by MALDI imaging mass spectrometry, the further reading can be found in the tutorial review by the current author, included into this dissertation as the *Publication 1*.
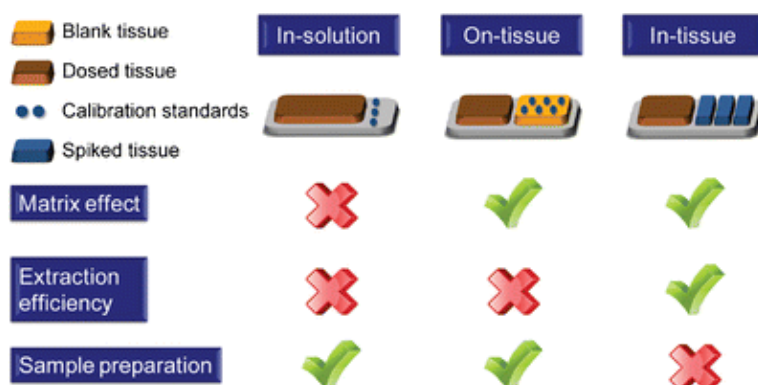

Figure 7. Comparison between various strategies in absolute qMSI. Reproduced with permission from [91].

Tissue-specific ion suppression is a form of matrix effect that cannot be entirely avoided in mass spectrometry imaging since no separation step can be implemented prior to the ionization process (in contrast to LC-MS or GC-MS approaches) [92–96]. The undesirable impact of ion suppression (as well as the other factors such as matrix crystallization and extraction inconsistencies) on the variability of signal intensities across the entire tissue section can be overcome by applying one of the above-mentioned normalization and calibration routines (ideally matrix-matched calibration combined with IS-normalization) [87]. The locally changing ion suppression, however, can also lead to the dramatic loss of signal response for the investigated analytes, resulting in some cases (*e.g.* in particular when employing small pixel sizes with highly limited effective amount of an analyte in the irradiated single spot area) in the entire analyte signal suppression. As a result, this phenomenon limits the broader application of qMSI to the certain sensitivity-challenging analytical fields such as the spatial analysis of some pharmaceuticals [52, 97–100]. While the different sophisticated strategies for overcoming ion suppression-caused poor sensitivity in MSI were reported to date [101–104], in MALDI imaging this can also be realized by simply utilizing different matrix compounds. Such an approach was employed in the current research by the application of the nonpolar DCTB matrix (which matches the polarity of the target analytes) for high sensitivity quantitative MALDI imaging of CNS drugs from mouse brain sections (results are included in the dissertation as the *Publication 2*).

Objectives

The aim of this work was to develop the novel analytical methods for molecular imaging of both drugs and endogenous metabolites from mouse tissue sections using matrix-assisted laser desorption/ionization (MALDI) and high-resolution Fourier-transform ion cyclotron resonance mass spectrometry (FTICR-MS). Firstly, MALDI-FTICR-MS was employed for on-tissue molecular identification, as well as high-spatial resolution imaging of bile acids directly from the mouse liver biliary networks. In order to achieve this goal, the home-built robotic sprayer was constructed and utilized for deposition of highly homogenous and reproducible MALDI matrix layers. In addition to the imaging experiments, the discovered phenomenon of the proton-bound dimer formation was utilized in order to improve the signal intensities from the deprotonated bile acids (using simple methods for broadband collision-induced dissociation of the dimers). Furthermore, the nonpolar MALDI matrix, DCTB (2-[(2E)-3-(4-tert-butylphenyl)-2-methylprop-2-enylidene]malononitrile) was applied for the first time for highly sensitive quantitative MALDI imaging of central nervous system (CNS) drugs from mouse brain sections. Moreover, the rationale (*i.e.* computational calculations of proton affinities (PA) and ionization energies (IE)) for proton-transfer MALDI mechanism with this matrix was provided; and the evidence for brain region- and MALDI matrix-dependent ion suppression of the CNS drugs was presented. Finally, high-resolution/high-accuracy MALDI-FTICR mass spectral imaging was applied for studying the molecular effects of the peripheral immunomodulatory agent teriflunomide on the mouse CNS compartment. Specifically, the potential penetration of the drug across the blood-brain barrier (BBB) was assessed, as well as the spatial and quantitative profiles of 24 endogenous metabolites after 4-day teriflunomide treatment were investigated.

V. Summary and Conclusions

The main goal of this dissertation was to develop the novel methods for label-free molecular imaging of different low-molecular weight compounds (including endogenous metabolites and pharmaceutical drugs) using matrix-assisted laser desorption/ionization (MALDI) and high-resolution Fourier-transform ion cyclotron resonance mass spectrometry (FTICR-MS). In general, several new approaches were successfully invented, developed and published in the international peer-reviewed journals (the list of publications as well as the articles are included in this thesis).

In the first part of the dissertation, MALDI-FTICR method was utilized for MS imaging of bile acids at high spatial resolutions. In this work, these essential metabolites (serving the key roles in secretion of cholesterol and lipid digestion processes) were for the first time molecularly identified and spatially imaged directly from the thin mouse liver sections. Different taurine-conjugated compounds were successfully identified. A comparison of the acquired MS ion images with histological staining showed a good correlation of the mass spectrometry data with the anatomical structures of the mouse liver biliary tree. Moreover, the imaging of the smaller sub-regions at the high-spatial resolution (MSI pixel size, 25 μm) allowed to distinguish between the tiny biliary ducts/capillaries and the large blood vessels and liver parenchyma. The developed method can be easily further applied for studying different pathological states that involve potential changes in the tissue bile acids content and spatial distribution (*e.g.* primary biliary cholangitis) [105].

Importantly, the new home-built robotic sprayer was constructed, based on the Probot micro fraction collector and nebulizing nozzle. The investigation of different configurations of spraying capillary diameter, nozzle height, distance between the lines and movement speed resulted in a excellent performance of the constructed device. The homogeneity of the matrix layers (observed for different MALDI matrices) as well as crystal sizes confirmed a superior performance of the constructed device in comparison to the commercially available piezoelectric sprayer (Bruker ImagePrep). Of note, this sprayer was later used in all research described in this dissertation.

In addition to the MS imaging assays, an extensive formation of proton-bound dimers (PBD) of bile acids and taurine was discovered. By using high-resolution/high-accuracy MS the strategy for unambiguous identification of these species corresponding signals was presented (even though they could be easily misinterpreted as the further BA conjugates). Since the ratio

of dimers to deprotonated bile acids was significant particularly for the certain tissue sub-regions, the new simple techniques for broadband dissociation of the proton-bound dimers were invented, which provided increased signal intensities from $[M - H]^-$ species. In summary, as PBD formation phenomenon is not limited to the taurinated bile acids (it was earlier observed also for amino acids [106] and peptides [107]), the newly developed technique (or even more the general concept of the non-selective broadband dissociation of different adducts and clusters) can be potentially applied for improving sensitivities during MALDI-MSI of different endogenous metabolites from both liver and other types of tissues.

In the second part of the dissertation, some novel approaches were developed and presented. In a nutshell, exploring the fundamental aspects of both MALDI mechanism and ion suppression phenomenon were utilized here in order to achieve better sensitivities for MALDI-MSI of CNS drugs. Specifically, the nonpolar and aprotic MALDI matrix, DCTB (2-[(2E)-3-(4-tert-butylphenyl)-2-methylprop-2-enylidene]malononitrile), previously well-known as an electron-transfer (ET) secondary reaction matrix, was investigated for an additional proton-transfer (PT) mechanism. The provided mechanistic rationale (*i.e.* computationally calculated gas-phase proton affinity almost equal to PA of the polar and acidic CHCA matrix) as well as the experiments with the two representative drugs (ketamine and xylazine) proved unequivocally the mixed (ET and PT) mechanism of DCTB-assisted laser desorption/ionization, with PT being evidently the main pathway.

Furthermore, the brain tissue-specific ion suppression phenomenon was thoroughly investigated for different MALDI matrices, DCTB *versus* CHCA and DHB. By using tissue-extinction coefficient (TEC) approach [108, 109], the MALDI matrix-dependent ionization suppression of the five different low-molecular weight lipophilic CNS drugs was clearly demonstrated. This is the first report showing an evident quantitative and spatial dependence of the ion suppression on the applied matrix in MALDI imaging studies. Furthermore, since the above-mentioned examination showed a superior performance of the nonpolar DCTB in comparison to the conventional polar and acidic matrices (DHB and CHCA), the developed method was applied to quantitative MALDI imaging of the common anesthetic drug, xylazine, directly from the mouse brain sections. Moreover, the novel approach for the tissue-matched standardization was also proposed. The newly developed strategy of spiking the calibration standards on the top of the "unified brain" sections, being in fact the combination of the "mimetic tissue" and "on-tissue" models, allowed for obtaining the linear calibration curves over the wide concentration range, assuring at the same time very good precision and limit of

detection. In summary, the proposed DCTB matrix is a superior alternative to the most commonly used polar and acidic matrices, and can be potentially applied not only to the CNS drugs but also to other pharmaceuticals studied by quantitative MALDI mass spectrometry imaging.

The aim of the third part of the dissertation was the application of high-resolution/high-accuracy MALDI-FTICR-MSI approach to pharmacometabolomics study of teriflunomide. Teriflunomide is a disease-modifying drug, approved for treatment of multiple sclerosis, but its mode of action has not been fully elucidated. Whereas the main mechanism of action is linked to the peripheral immune system, some in vitro studies showed that teriflunomide could also potentially acts directly in the CNS [110–112]. In this work, MALDI-MSI technique was utilized in order to investigate the drug's capacity to cross the blood-brain barrier (BBB), as well as to study the drug's effect on the metabolic compartment of the mouse brain. Even though the optimized method was capable for on-tissue drug detection at the low concentration level (confirmed in on-tissue spiked experiments), the drug was not detected in the brain samples from the animals after 4-day treatment. Interestingly, the further in-depth investigation of the spatial and quantitative profiles of 24 endogenous metabolites (amino acids, carbohydrates and nucleotides) revealed the evident alterations observed particularly for adenine and uracil nucleotides, glutathione and two carbohydrate intermediates. The applied strategy, when interpreted in a larger biochemical and pharmacological context, provided an additional understanding of the molecular effects of teriflunomide. Finally, these results proved also the high potential of the developed MALDI-MSI method for further pharmacometabolomics studies of teriflunomide applied to other than healthy animals samples (*e.g.* EAE mouse brain, post-mortem human brain or cerebrospinal fluid (CSF) from multiple sclerosis patients).

In all, the work included in this dissertation addressed several current limitations in MALDI-MSI field. First and foremost, the two completely new approaches for improving sensitivities were proposed (proton-bound dimers dissociation for endogenous metabolites and novel application of DCTB matrix for CNS drugs). Furthermore, the newly developed standardization/calibration strategy (by using "unified brain" tissue sections) is an attractive alternative to the time-consuming mimetic model Finally, the application of high-resolution/high-accuracy MALDI-MSI for pharmacometabolomics study of teriflunomide shed a new light on the potential impact of the drug on the mouse brain metabolism. Of note, all studies (in particular high-spatial resolution imaging as well as quantification of drugs) were

achievable thanks to the home-built robotic sprayer that assured far better MALDI matrix deposition results in comparison to the commercially available piezoelectric device. In summary, all developments presented in this dissertation bring the significant progress to the MSI field, and what is more, show the new potential path to be continued and further applied to other than studied here classes of compounds and types of animal and human tissues.

VI. References

1. Spengler, B.: Mass spectrometry imaging of biomolecular information. Anal. Chem. 87, 64–82 (2015).

2. Caprioli, R.M., Farmer, T.B., Gile, J.: Molecular Imaging of Biological Samples: Localization of Peptides and Proteins Using MALDI-TOF MS. Anal. Chem. 69, 4751–4760 (1997).

3. Sturtevant, D., Lee, Y.J., Chapman, K.D.: Matrix assisted laser desorption/ionization-mass spectrometry imaging (MALDI-MSI) for direct visualization of plant metabolites in situ. Curr. Opin. Biotechnol. 37, 53–60 (2016).

4. Lee, Y.J., Perdian, D.C., Song, Z., Yeung, E.S., Nikolau, B.J.: Use of mass spectrometry for imaging metabolites in plants. Plant J. 70, 81–95 (2012).

5. Kaspar, S., Peukert, M., Svatos, A., Matros, A., Mock, H.P.: MALDI-imaging mass spectrometry - An emerging technique in plant biology. Proteomics. 11, 1840–1850 (2011).

6. Paine, M.R.L., Kooijman, P.C., Fisher, G.L., Heeren, R.M.A., Fernández, F.M., Ellis, S.R.: Visualizing molecular distributions for biomaterials applications with mass spectrometry imaging: A review. J. Mater. Chem. B. 5, 7444–7460 (2017).

7. Goor, O.J.G.M., Keizer, H.M., Bruinen, A.L., Schmitz, M.G.J., Versteegen, R.M., Janssen, H.M., Heeren, R.M.A., Dankers, P.Y.W.: Efficient Functionalization of Additives at Supramolecular Material Surfaces. Adv. Mater. 29, (2017).

8. Watrous, J., Hendricks, N., Meehan, M., Dorrestein, P.C.: Capturing bacterial metabolic exchange using thin film desorption electrospray ionization-imaging mass spectrometry. Anal. Chem. 82, 1598–1600 (2010).

9. Yang, Y.L., Xu, Y., Straight, P., Dorrestein, P.C.: Translating metabolic exchange with imaging mass spectrometry. Nat. Chem. Biol. 5, 885–887 (2009).

10. Schober, Y., Guenther, S., Spengler, B., Römpp, A.: Single cell matrix-assisted laser desorption/ionization mass spectrometry imaging. Anal. Chem. 84, 6293–6297 (2012).

11. Zavalin, A., Todd, E.M., Rawhouser, P.D., Yang, J., Norris, J.L., Caprioli, R.M.: Direct imaging of single cells and tissue at sub-cellular spatial resolution using transmission geometry MALDI MS. J. Mass Spectrom. 47, 1473–1481 (2012).

12. Lanni, E.J., Rubakhin, S.S., Sweedler, J. V.: Mass spectrometry imaging and profiling of single cells. J. Proteomics. 75, 5036–5051 (2012).

13. Kiss, A., Hopfgartner, G.: Laser-based methods for the analysis of low molecular weight compounds in biological matrices. Methods. 104, 142–153 (2016).

14. Crecelius, A.C., Schubert, U.S., Von Eggeling, F.: MALDI mass spectrometric imaging meets "omics": recent advances in the fruitful marriage. Analyst. 140, 5806–5820 (2015).

15. Porta Siegel, T., Hamm, G., Bunch, J., Cappell, J., Fletcher, J.S., Schwamborn, K.: Mass Spectrometry Imaging and Integration with Other Imaging Modalities for Greater

Molecular Understanding of Biological Tissues. Mol. Imaging Biol. (2018).

16. Chughtai, K., Heeren, R.M.A.: Mass Spectrometric Imaging for Biomedical Tissue Analysis - Chemical Reviews (ACS Publications). Chem. Rev. 110, 3237–3277 (2011).

17. Rudin, M., Rausch, M., Stoeckli, M.: Molecular imaging in drug discovery and development: Potential and limitations of nonnuclear methods. Mol. Imaging Biol. 7, 5–13 (2005).

18. Solon, E.G., Schweitzer, A., Stoeckli, M., Prideaux, B.: Autoradiography, MALDI-MS, and SIMS-MS Imaging in Pharmaceutical Discovery and Development. AAPS J. 12, 11–26 (2010).

19. Prideaux, B., Stoeckli, M.: Mass spectrometry imaging for drug distribution studies. J. Proteomics. 75, 4999–5013 (2012).

20. Miura, D., Fujimura, Y., Wariishi, H.: In situ metabolomic mass spectrometry imaging: Recent advances and difficulties. J. Proteomics. 75, 5052–5060 (2012).

21. Caprioli, R.M.: Imaging mass spectrometry: Enabling a new age of discovery in biology and medicine through molecular microscopy. J. Am. Soc. Mass Spectrom. 26, 850–852 (2015).

22. Greer, T., Sturm, R., Li, L.: Mass spectrometry imaging for drugs and metabolites. J. Proteomics. 74, 2617–2631 (2011).

23. Trim, P.J., Francese, S., Clench, M.R.: Imaging mass spectrometry for the assessment of drugs and metabolites in tissue. Bioanalysis. 1, 309–319 (2009).

24. Sugiura, Y., Setou, M.: Imaging mass spectrometry for visualization of drug and endogenous metabolite distribution: Toward in situ pharmacometabolomes. J. Neuroimmune Pharmacol. 5, 31–43 (2010).

25. Schwamborn, K., Caprioli, R.M.: MALDI Imaging Mass Spectrometry - Painting Molecular Pictures. Mol. Oncol. 4, 529–538 (2010).

26. Caldwell, R.L., Caprioli, R.M.: Tissue profiling by mass spectrometry: a review of methodology and applications. Mol. Cell. Proteomics. 4, 394–401 (2005).

27. Amstalden van Hove, E.R., Smith, D.F., Heeren, R.M. a: A concise review of mass spectrometry imaging. J. Chromatogr. A. 1217, 3946–3954 (2010).

28. Schwamborn, K., Caprioli, R.M.: Molecular imaging by mass spectrometry-looking beyond classical histology. Nat. Rev. Cancer. 10, 639–646 (2010).

29. Chaurand, P.: Imaging mass spectrometry of thin tissue sections: A decade of collective efforts. J. Proteomics. 75, 4883–4892 (2012).

30. Shariatgorji, M., Källback, P., Gustavsson, L., Schintu, N., Svenningsson, P., Goodwin, R.J.A., Andren, P.E.: Controlled-pH tissue cleanup protocol for signal enhancement of small molecule drugs analyzed by MALDI-MS imaging. Anal. Chem. 84, 4603–4607 (2012).

31. Goodwin, R.J.A.: Sample preparation for mass spectrometry imaging: Small mistakes can lead to big consequences. J. Proteomics. 75, 4893–4911 (2012).

32. Race, A.M., Bunch, J.: Optimisation of colour schemes to accurately display mass spectrometry imaging data based on human colour perception. Anal. Bioanal. Chem. 407, 2047–2054 (2015).

33. Addie, R.D., Balluff, B., Bovée, J.V.M.G., Morreau, H., McDonnell, L.A.: Current State and Future Challenges of Mass Spectrometry Imaging for Clinical Research. Anal. Chem. 87, 6426–6433 (2015).

34. Bodzon-Kulakowska, A., Suder, P.: Imaging mass spectrometry: Instrumentation, applications, and combination with other visualization techniques. Mass Spectrom. Rev. 35, 147–169 (2016).

35. Irie, M., Fujimura, Y., Yamato, M., Miura, D., Wariishi, H.: Integrated MALDI-MS imaging and LC-MS techniques for visualizing spatiotemporal metabolomic dynamics in a rat stroke model. Metabolomics. 10, 473–483 (2014).

36. Dekker, T.J.A., Jones, E.A., Corver, W.E., van Zeijl, R.J.M., Deelder, A.M., Tollenaar, R.A.E.M., Mesker, W.E., Morreau, H., McDonnell, L.A.: Towards imaging metabolic pathways in tissues. Anal. Bioanal. Chem. 407, 2167–2176 (2015).

37. Marsching, C., Jennemann, R., Heilig, R., Gröne, H.-J., Hopf, C., Sandhoff, R.: Quantitative imaging mass spectrometry of renal sulfatides: validation by classical mass spectrometric methods. J. Lipid Res. 55, 2343–2353 (2014).

38. Cerruti, C.D., Benabdellah, F., Laprévote, O., Touboul, D., Brunelle, A.: MALDI imaging and structural analysis of rat brain lipid negative ions with 9-aminoacridine matrix. Anal. Chem. 84, 2164–2171 (2012).

39. Gode, D., Volmer, D. a: Lipid imaging by mass spectrometry - a review. Analyst. 138, 1289–315 (2013).

40. Altelaar, A.F.M., Taban, I.M., McDonnell, L.A., Verhaert, P.D.E.M., de Lange, R.P.J., Adan, R.A.H., Mooi, W.J., Heeren, R.M.A., Piersma, S.R.: High-resolution MALDI imaging mass spectrometry allows localization of peptide distributions at cellular length scales in pituitary tissue sections. Int. J. Mass Spectrom. 260, 203–211 (2007).

41. Chen, R., Hui, L., Sturm, R.M., Li, L.: Three Dimensional Mapping of Neuropeptides and Lipids in Crustacean Brain by Mass Spectral Imaging. J. Am. Soc. Mass Spectrom. 20, 1068–1077 (2009).

42. Guenther, S., Römpp, A., Kummer, W., Spengler, B.: AP-MALDI imaging of neuropeptides in mouse pituitary gland with 5 μm spatial resolution and high mass accuracy. Int. J. Mass Spectrom. 305, 228–237 (2011).

43. Seeley, E.H., Oppenheimer, S.R., Mi, D., Chaurand, P., Caprioli, R.M.: Enhancement of Protein Sensitivity for MALDI Imaging Mass Spectrometry After Chemical Treatment of Tissue Sections. J. Am. Soc. Mass Spectrom. 19, 1069–1077 (2008).

44. M. Reid Groseclose, Pierre P. Massion, P.C. and R.M.C.: High-throughput proteomic analysis of formalin-fixed paraffin- embedded tissue microarrays using MALDI imaging mass spectrometry. Proteomics. 8, 3715–3724 (2008).

45. Balluff, B., Rauser, S., Meding, S., Elsner, M., Schöne, C., Feuchtinger, A., Schuhmacher, C., Novotny, A., Jtting, U., MacCarrone, G., Sarioglu, H., Ueffing, M., Braselmann, H., Zitzelsberger, H., Schmid, R.M., Höfler, H., Ebert, M.P., Walch, A.:

MALDI imaging identifies prognostic seven-protein signature of novel tissue markers in intestinal-type gastric cancer. Am. J. Pathol. 179, 2720–2729 (2011).

46. Goodwin, R.J., Pitt, A.R.: Mass spectrometry imaging of pharmacological compounds in tissue sections. Bioanalysis. 2, 279–293 (2010).

47. Shariatgorji, M., Svenningsson, P., Andrén, P.E.: Mass spectrometry imaging, an emerging technology in neuropsychopharmacology. Neuropsychopharmacology. 39, 34–39 (2014).

48. Palmer, A., Trede, D., Alexandrov, T.: Where imaging mass spectrometry stands: here are the numbers. Metabolomics. 12, 107 (2016).

49. Norris, J.L., Caprioli, R.M.: Analysis of tissue specimens by matrix-assisted laser desorption/ionization imaging mass spectrometry in biological and clinical research. Chem. Rev. 113, 2309–2342 (2013).

50. Kleinridders, A., Ferris, H.A., Reyzer, M.L., Rath, M., Soto, M., Manier, M.L., Spraggins, J., Yang, Z., Stanton, R.C., Caprioli, R.M., Kahn, C.R.: Regional Differences in Brain Glucose Metabolism Determined by Imaging Mass Spectrometry. Mol. Metab. 1–9 (2018).

51. Castellino, S., Groseclose, M.R., Wagner, D.: MALDI imaging mass spectrometry: bridging biology and chemistry in drug development. Bioanalysis. 3, 2427–2441 (2011).

52. Cobice, D.F., Goodwin, R.J.A., Andren, P.E., Nilsson, A., Mackay, C.L., Andrew, R.: Future technology insight: mass spectrometry imaging as a tool in drug research and development. Br. J. Pharmacol. 172, 3266–3283 (2015).

53. Longuespée, R., Casadonte, R., Kriegsmann, M., Pottier, C., Picard de Muller, G., Delvenne, P., Kriegsmann, J., De Pauw, E.: MALDI mass spectrometry imaging: A cutting-edge tool for fundamental and clinical histopathology. Proteomics - Clin. Appl. 10, 701–719 (2016).

54. Ye, H., Gemperline, E., Li, L.: A vision for better health: Mass spectrometry imaging for clinical diagnostics. Clin. Chim. Acta. 420, 11–22 (2013).

55. Karas, M., Krüger, R.: Ion formation in MALDI: The cluster ionization mechanism. Chem. Rev. 103, 427–439 (2003).

56. Knochenmuss, R.: Ion formation mechanisms in UV-MALDI. Analyst. 131, 966 (2006).

57. Jaskolla, T.W., Karas, M.: Compelling evidence for lucky survivor and gas phase protonation: The unified MALDI analyte protonation mechanism. J. Am. Soc. Mass Spectrom. 22, 976–988 (2011).

58. Dreisewerd, K.: The desorption process in MALDI. (2003).

59. Niehaus, M., Schnapp, A., Koch, A., Soltwisch, J., Dreisewerd, K.: New Insights into the Wavelength Dependence of MALDI Mass Spectrometry. Anal. Chem. 89, 7734–7741 (2017).

60. Wiegelmann, M., Dreisewerd, K., Soltwisch, J.: Influence of the Laser Spot Size, Focal Beam Profile, and Tissue Type on the Lipid Signals Obtained by MALDI-MS Imaging in Oversampling Mode. J. Am. Soc. Mass Spectrom. 27, 1952–1964 (2016).

61. Soltwisch, J., Jaskolla, T.W., Hillenkamp, F., Karas, M., Dreisewerd, K.: Ion yields in UV-MALDI mass spectrometry as a function of excitation laser wavelength and optical and physico-chemical properties of classical and halogen-substituted MALDI matrixes. Anal. Chem. 84, 6567–6576 (2012).

62. Jaskolla, T.W., Lehmann, W.-D., Karas, M.: 4-Chloro-alpha-cyanocinnamic acid is an advanced, rationally designed MALDI matrix. Proc. Natl. Acad. Sci. U. S. A. 105, 12200–12205 (2008).

63. Taira, S., Sugiura, Y., Moritake, S., Shimma, S., Ichiyanagi, Y., Setou, M.: Nanoparticle-assisted laser desorption/ionization based mass imaging with cellular resolution. Anal. Chem. 80, 4761–4766 (2008).

64. Jackson, S.N., Baldwin, K., Muller, L., Womack, V.M., Schultz, J.A., Balaban, C., Woods, A.S.: Imaging of lipids in rat heart by MALDI-MS with silver nanoparticles. Anal. Bioanal. Chem. 406, 1377–1386 (2014).

65. Horatz, K., Giampà, M., Karpov, Y., Sahre, K., Bednarz, H., Kiriy, A., Voit, B., Niehaus, K., Hadjichristidis, N., Michels, D.L., Lissel, F.: Conjugated Polymers as a New Class of Dual-Mode Matrices for MALDI Mass Spectrometry and Imaging. J. Am. Chem. Soc. 140, 11416–11423 (2018).

66. Tanaka, Y., Hirata, M., Shinonome, S., Torii, M., Nezasa, K.I., Tanaka, H.: Distribution analysis of epertinib in brain metastasis of HER2-positive breast cancer by imaging mass spectrometry and prospect for antitumor activity. Sci. Rep. 8, 1–12 (2018).

67. Aikawa, H., Hayashi, M., Ryu, S., Yamashita, M., Ohtsuka, N., Nishidate, M., Fujiwara, Y., Hamada, A.: Visualizing spatial distribution of alectinib in murine brain using quantitative mass spectrometry imaging. Sci. Rep. 6, 23749 (2016).

68. Salphati, L., Shahidi-Latham, S., Quiason, C., Barck, K., Nishimura, M., Alicke, B., Pang, J., Carano, R.A., Olivero, A.G., Phillips, H.S.: Distribution of the phosphatidylinositol 3-kinase inhibitors pictilisib (GDC-0941) and GNE-317 in U87 and GS2 intracranial glioblastoma models - Assessment by matrix-assisted laser desorption ionization imaging. Drug Metab. Dispos. 42, 1110–1116 (2014).

69. Swales, J.G., Tucker, J.W., Strittmatter, N., Nilsson, A., Cobice, D., Clench, M.R., Mackay, C.L., Andren, P.E., Takáts, Z., Webborn, P.J.H., Goodwin, R.J.A.: Mass spectrometry imaging of cassette-dosed drugs for higher throughput pharmacokinetic and biodistribution analysis. Anal. Chem. 86, 8473–8480 (2014).

70. Benabdellah, F., Touboul, D., Brunelle, A., Laprévote, O.: In situ primary metabolites localization on a rat brain section by chemical mass spectrometry imaging. Anal. Chem. 81, 5557–5560 (2009).

71. Miura, D., Fujimura, Y., Yamato, M., Hyodo, F., Utsumi, H., Tachibana, H., Wariishi, H.: Ultrahighly sensitive in situ metabolomic imaging for visualizing spatiotemporal metabolic behaviors. Anal. Chem. 82, 9789–9796 (2010).

72. Yukihira, D., Miura, D., Saito, K., Takahashi, K., Wariishi, H.: MALDI-MS-based high-throughput metabolite analysis for intracellular metabolic dynamics. Anal. Chem. 82, 4278–4282 (2010).

73. Gabriel, S.J., Schwarzinger, C., Schwarzinger, B., Panne, U., Weidner, S.M.: Matrix segregation as the major cause for sample inhomogeneity in MALDI dried droplet spots.

J. Am. Soc. Mass Spectrom. 25, 1356–1363 (2014).

74. Svatoš, A.: Mass spectrometric imaging of small molecules. Trends Biotechnol. 28, 425–434 (2010).

75. Trim, P.J., Snel, M.F.: Small molecule MALDI MS imaging: Current technologies and future challenges. Methods. 104, 127–141 (2016).

76. Marshall, A.G., Hendrickson, C.L.: Fourier transform ion cyclotron resonance detection: Principles and experimental configurations. Int. J. Mass Spectrom. 215, 59–75 (2002).

77. Marshall, A.G., Hendrickson, C.L.: High-Resolution Mass Spectrometers. Annu. Rev. Anal. Chem. 1, 579–599 (2008).

78. Xian, F., Hendrickson, C.L., Marshall, A.G.: High resolution mass spectrometry. Anal. Chem. 84, 708–719 (2012).

79. Schulz, S., Becker, M., Groseclose, M.R., Schadt, S., Hopf, C.: Advanced MALDI mass spectrometry imaging in pharmaceutical research and drug development. Curr. Opin. Biotechnol. 55, 51–59 (2019).

80. Pirman, D.: Quantitative profiling of tissue drug distribution by MS imaging. Bioanalysis. 7, 2649–2656 (2015).

81. Ellis, S.R., Bruinen, A.L., Heeren, R.M.A.: A critical evaluation of the current state-of-the-art in quantitative imaging mass spectrometry. Anal. Bioanal. Chem. 406, 1275–1289 (2014).

82. Sun, N., Walch, A.: Qualitative and quantitative mass spectrometry imaging of drugs and metabolites in tissue at therapeutic levels. Histochem. Cell Biol. 140, 93–104 (2013).

83. Stauber, J.: Quantitation by MS imaging: needs and challenges in pharmaceuticals. Bioanalysis. 4, 2095–2098 (2012).

84. Fonville, J.M., Carter, C., Cloarec, O., Nicholson, J.K., Lindon, J.C., Bunch, J., Holmes, E.: Robust data processing and normalization strategy for MALDI mass spectrometric imaging. Anal. Chem. 84, 1310–1319 (2012).

85. Alexandrov, T.: MALDI imaging mass spectrometry: statistical data analysis and current computational challenges. BMC Bioinformatics. 13 Suppl 1, S11 (2012).

86. Deininger, S.O., Cornett, D.S., Paape, R., Becker, M., Pineau, C., Rauser, S., Walch, A., Wolski, E.: Normalization in MALDI-TOF imaging datasets of proteins: Practical considerations. Anal. Bioanal. Chem. 401, 167–181 (2011).

87. Rzagalinski, I., Volmer, D.A.: Quantification of low molecular weight compounds by MALDI imaging mass spectrometry − A tutorial review. Biochim. Biophys. Acta - Proteins Proteomics. 1865, 726–739 (2017).

88. Groseclose, M.R., Castellino, S.: A Mimetic Tissue Model for the Quanti fi cation of Drug Distributions by MALDI Imaging Mass Spectrometry. Anal. Chem. 85, 10099–10106 (2013).

89. Takai, N., Tanaka, Y., Saji, H.: Quantification of small molecule drugs in biological tissue sections by imaging mass spectrometry using surrogate tissue-based calibration standards. Mass Spectrom. (Tokyo, Japan). 3, A0025 (2014).

90. Reich, R.F., Cudzilo, K., Levisky, J.A., Yost, R.A.: Quantitative MALDI-MSn Analysis of Cocaine in the Autopsied Brain of a Human Cocaine User Employing a Wide Isolation Window and Internal Standards. J. Am. Soc. Mass Spectrom. 21, 564–571 (2010).

91. Porta, T., Lesur, A., Varesio, E., Hopfgartner, G.: Quantification in MALDI-MS imaging: what can we learn from MALDI-selected reaction monitoring and what can we expect for imaging? Anal. Bioanal. Chem. 407, 2177–2187 (2015).

92. Furey, A., Moriarty, M., Bane, V., Kinsella, B., Lehane, M.: Ion suppression; A critical review on causes, evaluation, prevention and applications. Talanta. 115, 104–122 (2013).

93. Annesley, T.M.: Ion suppression in mass spectrometry. Clin. Chem. 49, 1041–1044 (2003).

94. Antignac, J.P., De Wasch, K., Monteau, F., De Brabander, H., Andre, F., Le Bizec, B.: The ion suppression phenomenon in liquid chromatography-mass spectrometry and its consequences in the field of residue analysis. Anal. Chim. Acta. 529, 129–136 (2005).

95. Jessome, L.L., Volmer, D.A.: Ion Suppression: A Major Concern in Mass Spectrometry. LCGC North Am. 24, 498–510 (2006).

96. Gosetti, F., Mazzucco, E., Zampieri, D., Gennaro, M.C.: Signal suppression/enhancement in high-performance liquid chromatography tandem mass spectrometry. J. Chromatogr. A. 1217, 3929–3937 (2010).

97. Swales, J.G., Hamm, G., Clench, M.R., Goodwin, R.J.A.: Mass spectrometry imaging and its application in pharmaceutical research and development: A concise review. Int. J. Mass Spectrom. (2018).

98. Karlsson, O., Hanrieder, J.: Imaging mass spectrometry in drug development and toxicology. Arch. Toxicol. 91, 2283–2294 (2017).

99. Nilsson, A., Goodwin, R.J.A., Shariatgorji, M., Vallianatou, T., Webborn, P.J.H., Andren, P.E.: Mass spectrometry imaging in drug development. Anal. Chem. 87, 1437–1455 (2015).

100. Lodén, H., Shariatgorji, M., Nilsson, A., Andrén, P.E.: An introduction to MS imaging in drug discovery and development. Bioanalysis. 7, 2621–2627 (2015).

101. Seeley, E.H., Oppenheimer, S.R., Mi, D., Chaurand, P., Caprioli, R.M.: Enhancement of Protein Sensitivity for MALDI Imaging Mass Spectrometry After Chemical Treatment of Tissue Sections. J. Am. Soc. Mass Spectrom. 19, 1069–1077 (2008).

102. Andersson, M., Groseclose, M.R., Deutch, A.Y., Caprioli, R.M.: Imaging mass spectrometry of proteins and peptides: 3D volume reconstruction. Nat. Methods. 5, 101–108 (2008).

103. Wang, X., Han, J., Yang, J., Pan, J., Borchers, C.H.: Matrix coating assisted by an electric field (MCAEF) for enhanced tissue imaging by MALDI-MS. Chem. Sci. 6, 729–738 (2015).

104. Sugiyama, E., Masaki, N., Matsushita, S., Setou, M.: Ammonium Sulfate Improves Detection of Hydrophilic Quaternary Ammonium Compounds through Decreased Ion Suppression in Matrix-Assisted Laser Desorption/Ionization Imaging Mass Spectrometry. Anal. Chem. 87, 11176–11181 (2015).

105. Li, T., Chiang, J.Y.L.: Bile Acid Signaling in Metabolic Disease and Drug Therapy. 948–983 (2014).

106. Wu, Z., Fenselau, C.: Proton affinity of arginine measured by the kinetic approach. Rapid Commun. Mass Spectrom. 6, 403–405 (1992).

107. Cheng, X.H., Wu, Z.C., Fenselau, C.: Collision Energy Dependence of Proton-Bound Dimer Dissociation - Entropy Effects, Proton Affinities, and Intramolecular Hydrogen-Bonding in Protonated Peptides. J. Am. Chem. Soc. 115, 4844–4848 (1993).

108. Stoeckli, M., Staab, D., Schweitzer, A.: Compound and metabolite distribution measured by MALDI mass spectrometric imaging in whole-body tissue sections. Int. J. Mass Spectrom. 260, 195–202 (2007).

109. Hamm, G., Bonnel, D., Legouffe, R., Pamelard, F., Delbos, J.M., Bouzom, F., Stauber, J.: Quantitative mass spectrometry imaging of propranolol and olanzapine using tissue extinction calculation as normalization factor. J. Proteomics. 75, 4952–4961 (2012).

110. Hamilton, L.C., Vojnovic, I., Warner, T.D.: A771726, the active metabolite of leflunomide, directly inhibits the activity of cyclo-oxygenase-2 in vitro and in vivo in a substrate-sensitive manner. Br. J. Pharmacol. 127, 1589–1596 (1999).

111. Manna, S.K., Aggarwal, B.B.: Immunosuppressive leflunomide metabolite (A77 1726) blocks TNF-dependent nuclear factor-kappa B activation and gene expression. J. Immunol. 162, 2095–2102 (1999).

112. González-Alvaro, I., Ortiz, A.M., Domínguez-Jiménez, C., Aragón-Bodi, A., Díaz Sánchez, B., Sánchez-Madrid, F.: Inhibition of tumour necrosis factor and IL-17 production by leflunomide involves the JAK/STAT pathway. Ann. Rheum. Dis. 68, 1644–1650 (2009).

VII. List of Publications

The following review article was included in the dissertation as an introduction to the research field but does not contain any relevant research results:

1. Rzagalinski I., Volmer D.A. Quantification of low molecular weight compounds by MALDI imaging mass spectrometry – a tutorial review. *Biochimica et Biophysica Acta – Proteins and Proteomics* (**2017**), 1865(7): 726-739. DOI: 10.1016/j.bbapap.2016.12.011.

The results of the dissertation have been published in the following peer-reviewed journals:

2. Rzagalinski I, Hainz N, Meier C, Tschernig T, Volmer DA. MALDI mass spectral imaging of bile acids observed as deprotonated molecules and proton-bound dimers from mouse liver sections. *Journal of the American Society for Mass Spectrometry* (**2018**), 29:711-722, DOI: 10.1007/s13361-017-1886-6

3. Rzagalinski I, Kovacevic B, Hainz N, Meier C, Tschernig T, Volmer DA. Toward higher sensitivity in quantitative MALDI imaging mass spectrometry of CNS drugs using a nonpolar matrix. *Analytical Chemistry* (**2018**), 90, 12592−12600, DOI: 10.1021/acs.analchem.8b02740

4. Rzagalinski I, Hainz N, Meier C, Tschernig T, Volmer DA. Spatial and molecular changes of mouse brain metabolism in response to immunomodulatory treatment with teriflunomide as visualized by MALDI-MSI. *Analytical and Bioanalytical Chemistry* (**2018**), 411:353–365, DOI: 10.1007/s00216-018-1444-5

Publication 1

26

Quantification of low molecular weight compounds by MALDI imaging mass spectrometry – A tutorial review

Ignacy Rzagalinski and Dietrich A. Volmer

Review

Quantification of low molecular weight compounds by MALDI imaging mass spectrometry – A tutorial review☆

Ignacy Rzagalinski, Dietrich A. Volmer *

Institute of Bioanalytical Chemistry, Saarland University, 66123 Saarbrücken, Germany

ABSTRACT

Matrix-assisted laser desorption/ionization (MALDI)-mass spectrometry imaging (MSI) permits label-free *in situ* analysis of chemical compounds directly from the surface of two-dimensional biological tissue slices. It links qualitative molecular information of compounds to their spatial coordinates and distribution within the investigated tissue. MALDI-MSI can also provide the quantitative amounts of target compounds in the tissue, if proper calibration techniques are performed. Obviously, as the target molecules are embedded within the biological tissue environment and analysis must be performed at their precise locations, there is no possibility for extensive sample clean-up routines or chromatographic separations as usually performed with homogenized biological materials; ion suppression phenomena therefore become a critical side effect of MALDI-MSI. Absolute quantification by MALDI-MSI should provide an accurate value of the concentration/amount of the compound of interest in relatively small, well-defined region of interest of the examined tissue, ideally in a single pixel. This goal is extremely challenging and will not only depend on the technical possibilities and limitations of the MSI instrument hardware, but equally on the chosen calibration/standardization strategy. These strategies are the main focus of this article and are discussed and contrasted in detail in this tutorial review. This article is part of a Special Issue entitled: MALDI Imaging, edited by Dr. Corinna Henkel and Prof. Peter Hoffmann.

© 2016 Elsevier B.V. All rights reserved.

1. Introduction

Matrix-assisted laser desorption/ionization (MALDI) mass spectrometry (MS) has revolutionized the analysis of large biopolymers such as peptides, proteins and nucleic acids [1]. For small molecules, the application of MALDI-MS has often been described as difficult or impossible because of the intense, strongly fluctuating matrix background signals, which appear at virtually every mass in the low *m/z* region, thus creating serious isobaric interferences when using low resolving power instruments [2]. Moreover, because of the strong signal variations – which result mostly from the non-uniform crystal dispersity as well as co-crystallization issues of matrix and analyte across the substrate – MALDI-MS is still seen as a non-quantitative technique by many researchers today. This is clearly not the case, however, as demonstrated by many research groups specialized in quantitative MALDI-MS, who have illustrated the benefits of the technique, including the high throughput capability, ease of use and limited contamination between samples [3–13]. To take advantage of these benefits, researchers have

developed several technical solutions to remove or circumvent many of the above mentioned limitations; these innovations include novel matrices and matrix deposition techniques for generating mono-disperse layers of matrix/analyte crystals [14–18], hydrophobic substrate surface coatings that optimize crystal growth behavior [19–22], internal standards that exactly mirror the behavior of the analytes during MALDI [23–29], matrix-free laser desorption/ionization techniques to avoid low *m/z* interferences [30], high frequency lasers that enable massive data averaging and improve precision [3–11,31,32], selective tandem mass spectrometry (MS/MS) data acquisition routines that circumvent isobaric signals in the MS/MS domain [3–5,7,10,11,13,26,31], high resolution mass spectral measurements to resolve analytes from matrix [33], and software or hardware routines for sweet-spot detection, automatic laser power adjustments and signal filtering [34,35]. Another inherent, chemistry-related problem of MALDI-MS is ion suppression of analyte molecules by components of complex sample matrices such as serum or plasma [36,37]. Applying proper sample preparation protocols, similar to those used in liquid chromatography-(tandem) mass spectrometry (LC-MS(/MS)) assays, however, has been shown to effectively remove components that cause co-crystallization issues and induce ion suppression [38].

Sample clean-up protocols cannot be applied in situations, however, where the integrity of the sample matrix has to be entirely preserved, as is the case in MALDI-imaging mass spectrometry (MSI), where the

---

☆ This article is part of a Special Issue entitled: MALDI Imaging, edited by Dr. Corinna Henkel and Prof. Peter Hoffmann.
 * Corresponding author at: Institute of Bioanalytical Chemistry, Saarland University, Campus B2.2, 66123 Saarbrücken, Germany.
  E-mail address: dietrich.volmer@mx.uni-saarland.de (D.A. Volmer).

signal intensities are recorded for analytes at specific *x,y* coordinates of the tissue section. At these coordinates, the analytes are embedded within the biological material of the tissue in their native states and often bound to other components of the tissue. They have to be extracted, ionized and analyzed without changing their geometrical location. This also means that ion suppression cannot usually be avoided, as no mass or shape-specific separation can be implemented before the ionization process. The extent of ion suppression for a given analyte will therefore differ at different spatial locations within the tissue. Furthermore, internal standards cannot readily be applied in MSI by simply mixing them with the analytes, and neither can the MALDI matrix easily be co-crystallized with the analytes within the tissue. Furthermore, the range of useful chemical matrices for MALDI-MSI has been shown to be much wider than in conventional quantitative MALDI-MS, where most applications use α-cyano-hydroxycinnamic acid (CHCA), dihydroxybenzoic acid (DHB) or sinapinic acid (SA). These and other issues seriously complicate quantitative applications of MALDI-MSI. Nevertheless, for quantitative MALDI-MSI of low molecular weight compounds, it is important to make use of the achievements and knowledge gained from conventional quantitative MALDI-MS, as much of it can also be applied to improve quantitative MALDI imaging mass spectrometry. In fact, the present authors suggest that several previous technical solutions for quantitative MALDI-MS should be considered for quantitative MSI. For example, the optimum analyte-to-matrix ratio [39,40], the possibilities from reactive matrices [41–45], as well as the role of matching physicochemical properties of the system analyte/internal standard/matrix [26] have been extensively investigated in quantitative MALDI-MS, but their importance in MALDI-MSI is still not fully considered. Porta et al. have recently provided an excellent treatment of theoretical and practical aspects of quantitative MALDI-MS of low molecular weight molecules based on experiments on a MALDI-triple quadrupole instrument, and, importantly, discuss how their findings will impact quantification in MALDI-MSI [46]. The authors conclude that "the main challenge for absolute quantification remains the quest for the perfect dilution series to better mimic the behavior of an analyte in its biological environment" [46]. Technical solutions and strategies for addressing this very challenge are the topic of the present article.

Designed as a short tutorial review, the article focuses on the different data pre-processing and calibration procedures for quantitative MALDI-MSI and how they impact the analytical figures of merit. Other technical aspects such as the deposition procedure of the MALDI matrix or influence of different mass analyzers on spectral quality are outside the scope of this paper, even though they may also control quantitative performance. The interested reader is referred to several recent reviews of MALDI-MSI techniques, including instrumentation overviews, role of MALDI matrix and deposition techniques, and MSI applications [47–55].

2. Strategies for quantitative MALDI-MSI

In addition to the many challenges encountered during the quantitative MALDI analysis of low molecular weight compounds described in the previous section, determining the concentration levels of molecules from within thin slices of tissue by MALDI mass spectrometry adds several more complications and requires very different data processing and calibration routines. Several promising general strategies have been established for this purpose, which can be grouped into *absolute* and *relative* quantification approaches. Absolute quantitative MSI experiments deliver concentration levels of analytes, which are expressed in units of moles or mass quantity of compound per mass/volume or area of tissue. Successful absolute quantification by MALDI-MSI should provide an accurate value of the compound not only in the entire section of the examined tissue, but also in relatively small, well-defined regions of interest, ideally in a single pixel or the area corresponding to a single data point acquisition. The latter goal is extremely challenging, as recently demonstrated by Porta et al. [46], who presented quantitative data for different compounds including synthetic drugs and endogenous peptides after

protein digestion. Obtaining meaningful quantitative results from MALDI-MSI experiments also depends strongly on the chosen calibration/standardization approach, which will be discussed in detail below.

In contrast to absolute quantification, relative quantification is achieved by visualizing and estimating relative concentration values of the analyte across the tissue or whole body section *in comparison* to other compounds. Achieving reliable relative quantification by MALDI-MSI requires the application of a signal intensity normalization method as pre-processing tool, along with baseline correction (subtraction) and mass spectral realignment (recalibration) [56,57]. In fact, the same careful normalization and calibration is also required for absolute quantification, to obtain results comparable to reference methods such as LC-MS/MS or autoradiography [58].

Today, a broad range of different chemical compound classes have been investigated by MALDI-MSI in biological tissues in quantitative or semi-quantitative fashion, with most studies dedicated to small (<1000 Da) or medium-sized molecules (<2000 Da), as recently summarized by Palmer et al. [59], who pointed out that most MSI practitioners study small molecules such as drugs, metabolites or lipids. In recent years, different normalization strategies and different calibration approaches have been developed for quantitative MALDI-MSI of exogenous compounds, in particular drugs and other xenobiotics, as well as endogenous metabolites such as lipids and peptides [60,61].

Application of appropriate signal intensity normalization is very important for the correct interpretation of the MS imaging data [62]. Semi-quantitative methods are often sufficient for the investigation of endogenous compounds, where frequently the differences of relative concentrations of compounds within a single tissue section are visualized [63]. This approach also allows the evaluation of relative changes of the level of one compound (or a set of compounds) in different regions of the same tissue (*e.g.*, normal *versus* tumor), or in different tissues (*e.g.*, vehicle *versus* drug-treated or control *versus* animal disease model). This strategy, in combination with appropriate data mining and statistical tools, was shown to enable implementation of MALDI-MS imaging for discovery of potential cancer biomarkers. For example, Thomas et al. compared lipid signatures of normal tissue to tumor regions [64]. In addition, a similar methodology was used to evaluate potential metabolic markers of clinical response to drug therapy [65] and to visualize spatiotemporal metabolic dynamics of different pathological states [63,66,67].

In contrast to the imaging of endogenous compounds, accessing the absolute levels of synthetic drugs is vital during drug discovery and development [68,69]. As a result, the majority of published absolute quantitative MSI studies report methods for administered drugs and their metabolites, mostly low molecular weight pharmaceuticals [70–75] and therapeutic peptides [76]. In addition, other xenobiotics such as environmental toxins [77] and biocides [78] have been quantified in tissues, as well as neurotransmitters [79], metabolites [80], lipids [81,82] and peptides [83–85]. These examples for absolute quantification utilized various normalization strategies and calibration (standardization) techniques, which will be further discussed in detail below.

2.1. Data pre-processing and normalization routines

Efficient signal intensity correction is a vital component of any quantitative measurement by mass spectrometry, most importantly in MALDI-MSI. In conventional quantitative LC-MS/MS, normalization is usually achieved by employing an internal standard (IS), as early as possible, during the sample preparation process. The ratio of the signal of analyte and internal standard provides an adequate correction of matrix effects such as inconsistent extraction and ionization efficiencies, as well as instrumentation-related variables such as injection instability. In MALDI-MSI, normalization of the signal intensity needs to compensate for additional effects. A frequent problem is variability of the signal resulting from irregularities of MALDI matrix deposition and crystallization processes (see Section 1). This can be the result of inhomogeneous MALDI matrix deposition or, additionally, different chemical

compositions within particular regions of tissue (*e.g.*, different lipid and salts contents) or variations of morphology of the physical structures. Moreover, the signal intensities for a given analyte are influenced by different extraction and ionization efficiencies at a specific region, which is the result of the changing chemical environments on the tissue surface, with different chemical interferences and ionization suppression phenomena [55]. Finally, varying signal intensity can result from instability of the chemical matrix under high vacuum conditions, notably sublimation during long imaging experiments [86]. To circumvent these problems, several normalization approaches have been developed and successfully implemented to enable both relative and absolute quantification by MALDI-MSI.

2.1.1. Normalization to TIC, RMS or median intensity of the peaks

Briefly, normalization of MSI data entails correcting each mass spectrum (from each single pixel on the tissue!) by applying a certain correction factor. The three most common strategies to correct signal intensities are normalization to the total ion current (TIC), the root mean square (RMS) or the median intensity of the peaks [62,87]. All three approaches – combined with other data processing tools (baseline subtraction, spectral realignment) – generally allow correcting for experimental bias such as variations resulting from irregularities of the matrix coating procedure. TIC, RMS and median normalizations have been widely applied to semi-quantitative MALDI imaging study of endogenous molecules, because for most of these compounds no commercial stable isotope standards exist. Moreover, for the hundreds of different endogenous compounds often used in biomarker research, it is impracticable to use well-matched internal standards for every analyte. Therefore, in untargeted analyses, normalization to the total ion current (TIC) is the most widely applied technique, as demonstrated by different groups for MALDI imaging of lipids [64], neurotransmitters [79] and metabolites [63,66,67]. Normalization to RMS was implemented for relative quantification of metabolites in response to drug therapy

[65] as well as for monitoring relative changes of drug concentrations [88]. Finally, the TIC approach was also shown for imaging of drugs and compared to another instrumental techniques such as liquid extraction surface analysis (LESA)-MSI and LC-MS/MS [89].

TIC and RMS strategies were also successfully employed to quantify absolute amounts of compounds in entire tissue sections or smaller regions of interest. TIC correction was used for the absolute quantification of endogenous metabolites and neurotransmitters [79] as well as several drugs [72,75], whereas RMS was shown for imaging of drugs [90] and several endogenous phosphatidylcholines [82]. In the latter study, RMS normalization along with a mimetic tissue-based calibration curve (see below) significantly improved both the linearity of the calibration curves (expressed as changes of the coefficient of determination (R^2) from 0.9500 up to 0.9991 for the $[M + H]^+$ ionic species) (Fig. 1) and the precision of analysis (expressed as SD and RSD) [82].

Different normalization techniques were also evaluated for MALDI-TOF analyses of proteins; normalization to TIC or noise levels were demonstrated to be the most efficient and accurate procedures [56]. It is important to point out that the TIC and RMS approaches can also lead to false interpretation of MSI data, in particular for highly heterogeneous tissues such as kidney (cortex and medulla regions) or brain (several different sub-regions) [62]. As shown for proteins in different tissues, these normalization routines can create artifacts, in particular when peaks with very high intensities are present in certain regions of the tissue [62]. Furthermore, these artifacts very often comply with the histological structures of the tissue and can lead to wrong conclusions. One solution to avoid this problem is the normalization to TIC or RMS after manual exclusion of the irregular peaks (or *m/z* ranges). Another possibility is the normalization to the noise or to the median intensity. The latter was successfully implemented as normalization tool for MALDI imaging of small molecules in the range *m/z* range of 50–1000 [87]. The authors illustrated a powerful comparison of different approaches, including normalization to TIC and median intensity with different
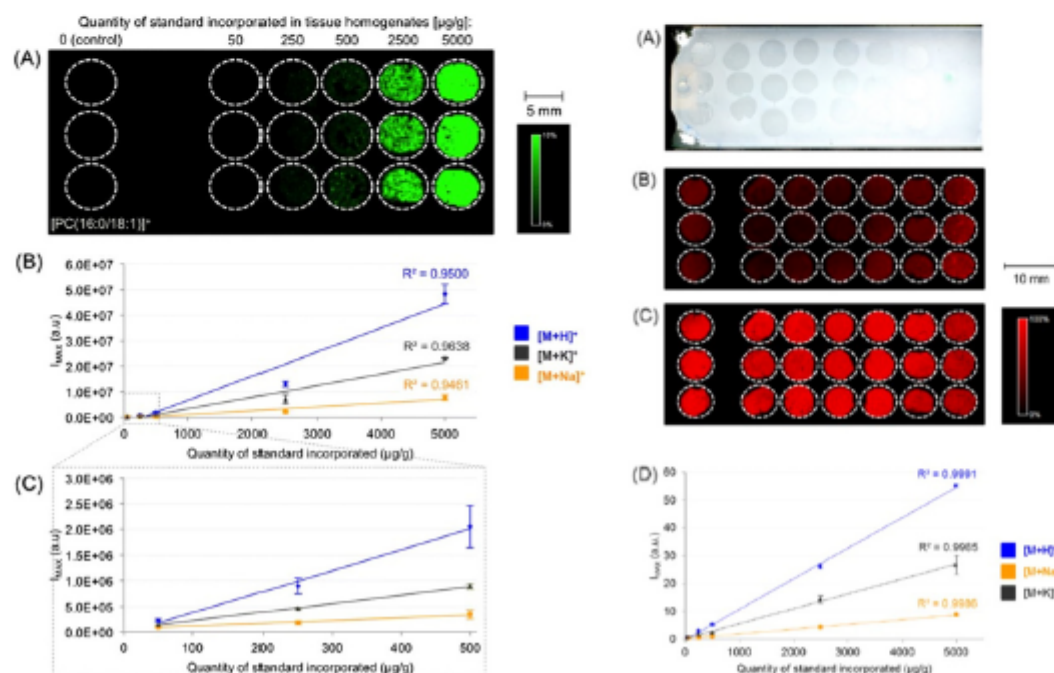

Fig. 1. Calibration curves obtained by using a mimetic tissue approach for different PC(16:0 d31/18:1) ionic species ($[M + H]^+$, $[M + K]^+$, $[M + Na]^+$) without any normalization (left) and after normalization to the root mean square (RMS, right). Reproduced with permission from reference [82].

strategies of selecting peaks to include or exclude for the particular normalization methods.

In conclusion, even though TIC, RMS and median intensity normalization can result in wrong interpretations, they generally are efficient and reliable pre-processing tools for MALDI imaging data sets if applied properly.

2.1.2. Normalization to MALDI matrix-related peak or endogenous species signal

In cases where appropriate internal standards (stable isotope compounds, structural analogs) are not available, it is possible to use other signals from the mass spectrum for an "internal standard-like" normalization process. Using matrix-related signals is one of these methods, which enables scan-by-scan normalization, and as a result, efficiently overcomes variations of the signal intensity resulting from irregularities in matrix deposition and crystallization processes. This strategy has been frequently applied to semi-quantitative MALDI imaging of small molecules. Goodwin et al. [91] mapped the distribution of a pharmaceutical compound in rat brain using normalization against the CHCA matrix dimer at m/z 379. The authors achieved very good correlation between relative quantification by MALDI-MSI and absolute quantification by LC-MS/MS after laser-capture micro-dissection [91]. Bunch et al. [92] spatially determined ketoconazole in skin samples using normalization to the CHCA sodium adduct, which was the highest abundant matrix-derived peak in the spectrum. Furthermore, Takai et al. presented an efficient normalization routine against a DHB matrix signal for relative and absolute quantification of the low molecular weight drug raclopride [93] and the therapeutic peptide octreotide [76]. For the latter compound, a combination of DHB normalization and matrix-matched standard calibration allowed the authors to achieve quantitative performance comparable to LC-MS/MS (accuracy, 76–127%). Finally, Park et al. [94] investigated the potential of relative quantification after spraying a peptide standard across the mouse brain tissue. By maintaining a constant TIC and controlling the MALDI matrix suppression effect at the same time, the authors successfully employed normalization against a MALDI matrix-derived signal.

In addition to matrix-derived peaks, signals from some endogenous species can also be employed for "internal standard-like" normalization. This strategy requires careful selection of an appropriate endogenous compound, which should ideally be of the same or a similar class of molecule as the target analyte, which would then allow the (partial) correction of signal variations from chemical interferences and ionization suppression. Importantly, the selected compound should be highly abundant and evenly distributed across the entire tissue section to avoid creating artifacts. Although it is difficult to match all these requirements, the technique has been successfully applied several times for MALDI imaging. Hankin et al. determined several phosphocholines using normalization against the averaged signals from different ionic species ($[M + H]^+$, $[M + Na]^+$ and $[M + K]^+$) of the endogenous lipid (16:0/18:1 PC) [95]. Wang et al. employed normalization to the base peak (m/z 266.2) of the entire mass spectrum to map the relative abundance of the drug chlorisondamine; the authors also normalized to cholesterol after water loss (m/z 369.6) to detect cocaine directly on rat brain tissue sections [96].

Although normalization against matrix peaks and against endogenous components are both efficient procedures, they exhibit drawbacks. The MALDI matrix signal approach does not provide correction for signal variations resulting from the different extraction and ionization efficiencies in different regions of the tissue; the endogenous compound strategy only works when the selected compound has similar physicochemical properties as compared to target analyte and is evenly distributed across the entire section, which is extremely rare for heterogeneous tissues such as brain or kidney. For these reasons, both strategies should be used with caution and the application decided on a case-by-case basis, when isotope standards or structural analogs are not available or their application is too difficult. In such cases,

normalization to the homogenously applied matrix appears to be the better choice for both relative and absolute quantification by MALDI-MSI.

2.1.3. Normalization to structural analogs or stable isotope internal standards

The importance of an internal standard for quantification by MALDI mass spectrometry has been demonstrated multiple times, in particular for low molecular weight xenobiotics [4,26,33,97,98], but also for small endogenous compounds [23]. Sleno and Volmer investigated the potential of MALDI-triple quadrupole mass spectrometry for quantification of small molecules employing different MALDI matrices and different chemical compounds as internal standards. They also investigated the role of laser power and frequency on quantitative analytical figures of merit such as sensitivity and dynamic range [26]. Moreover, essential physicochemical properties were investigated that provide a possible match of analyte and internal standard for a range of low molecular weight compounds [4]. It was shown that the closeness of the analyte's and internal standard's solution-phase ionization properties (exemplified by log D and pK_a), as well as the molecular weight and solubility properties, were crucial in achieving satisfactory analytical figures of merit. A stable isotope-labeled version of the analyte ensured optimum results, but if not available, a carefully matched compound can also provide good signal intensity correction.

In the recent years, normalization to the internal standard has been applied many times, either for relative or for absolute quantification. For example, there are a number of studies showing imaging of exogenous compounds, in particular xenobiotics, with structural analogs employed as internal standards [73,99–102], or standards based on isotopically-labeled derivatives of the analyte [70,73,74,78,103–109]. Additionally, normalization against the IS signal was described for certain classes of endogenous compounds, including lipids [81,110,111], peptides [83, 85,112,113] and metabolites [80]. Kälback et al. presented an excellent comparison of different calibration curves for imipramine from different normalization methods, showing the impact on the linearity and the dramatic improvements of the coefficient of determination (R^2) (Fig. 2) [83].

Normalization of the MSI data against the internal standard is simply achieved by dividing the signal intensity of the target compound by the signal intensity of the IS. To ensure reliable signal intensity correction, MSI images should ideally be normalized within the same imaging pixel and within the same MS scan (one scan per pixel!). While this requirement is easily realized for MSI acquisition in MS mode (e.g., full scan using high resolution mass spectrometry), it is more difficult to employ in MS/MS mode, in particular for certain mass analyzers. For instance, the MRM data acquisition on a MALDI-triple quadrupole instrument requires a dwell time component between two MS/MS transitions (analyte and IS), so both signals are not acquired from exactly the same positions [114]. To overcome this problem, Reich et al. proposed a wide isolation window (IW) surrounding two precursor ions (compound and IS) in combination with a linear ion trap mass analyzer and data acquisition in product ion scan mode. Employment of a single wide IW (single MS/MS experiment) instead of two separate IWs for each ion (two independent MS/MS experiments) resulted in significantly improved precision (RSD improvement from 12 to 30% to 0.50–5.1%) [115]. This approach was used by the same group, in combination with an appropriate calibration curve and isotope-labeled internal standard, as a reliable strategy for absolute quantitative MALDI-MSI of both exogenous [108] and endogenous compounds [80,81].

The matching conditions described above for quantitative MALDI-MS equally apply to quantitative MALDI-MSI on two-dimensional tissue surfaces. However, determination of the compound directly from the tissue section requires more elaborate procedures as compared to homogenized samples. Firstly, internal standard cannot simply be added to the sample but needs to be evenly and homogenously incorporated into the tissue or whole body section. In general, internal standard
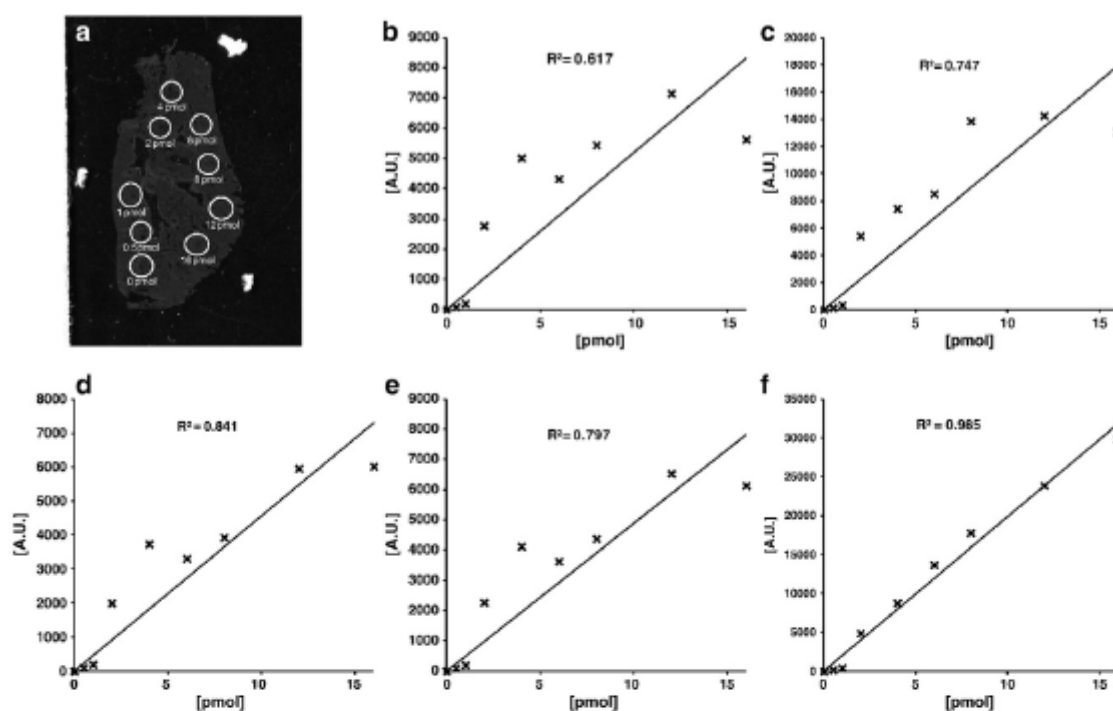
Fig. 2. Comparison of linearity of calibration curves of imipramine standards obtained with different normalization methods; a optical image of a lung section with circles indicating places where the drug standard solutions were applied; b non-normalization; c median normalization; d TIC normalization; e RMS normalization; f isotope-labelled normalization. R^2, coefficient of determination. Reproduced with permission from reference [83].

solution can either be sprayed or spotted (printed) by different deposition instruments, as long as chosen method ensures highly homogeneous and reproducible deposition. Of note, while spotting the internal standard provides better tissue penetration as compared to spraying, the potential delocalization of the target molecules within a large single spot has the potential to defocus the image. Several methods for IS application have been reported over the past years. In most cases, internal standard was added to the MALDI matrix solution and sprayed over the entire tissue section [78,99–107,111,112]. Alternatively, internal standard solution was deposited separately from the MALDI matrix, either beneath the tissue section [81,108] or on the top, followed by matrix deposition [65,73,74,85]. Additionally, Yost and coworkers presented different IS application strategies and demonstrated that deposition of IS under wet tissue provides extraction and ionization efficiencies most similar to the endogenous compounds [110]. Moreover, the same group showed that the deposition below the tissue only lead to improvements in analytical performance (better precision) compared to non-normalized data if it was applied separately from the MALDI matrix [80]. Recently, Caprioli and coworkers compared different internal standard deposition techniques and its influence on the quality of absolute quantification results. The authors developed a reference tissue model with an *in vitro* administered drug, rifampicin, to evaluate accuracy and precision of quantitative MALDI-MSI using on-tissue calibration curve and different IS deposition methods (Fig. 3). Importantly, only application of IS on top of the tissue section – prior to MALDI matrix application – gave a quantitative performance that was comparable to LC-MS/MS analysis of the tissue extract [116].

2.1.4. Normalization to the tissue-specific ionization efficiency coefficient

Two of the main challenges in quantification by MALDI-MSI are compound-specific ionization efficiencies and tissue-specific ion suppression effects. Both effects result in widely varying response factors and signal suppression for the analytes, which vary significantly between different regions of the tissue or even between two neighboring single pixels during a MSI acquisition. To overcome these difficulties, Stoeckli et al. [117] and Hamm et al. [118] proposed similar approaches, which consider the different biochemical micro-environments of tissues or tissue regions for calculation of a tissue-specific ionization efficiency normalization factor.

Stoeckli et al. demonstrated their strategy by semi-quantitatively mapping the distribution of pharmaceutical compounds in whole-body rodent sections and compared the results with whole-body autoradioluminography (WBAL) method. The authors illustrated the characteristic ionization suppression effects for some regions of the WB section by homogenously spraying the analyte solution over the entire sample and carrying out the typical MALDI imaging measurement. The obtained histograms demonstrated a significant reduction of the signal intensity in some regions. Furthermore, to calculate tissue-specific ionization efficiency factors for different tissue types, the target compound solution was spiked onto the specific regions of the control body section (stomach, lung and trachea) and signal intensities from particular regions of interest were averaged to acquire numerical values for the coefficients. MSI signals from these particular tissue regions were then divided by the corresponding coefficients. Subsequently, MSI-based relative quantification showed good correlation with WBAL results, as well as ensured good precision (RSD < 10%, $n = 3$) [117].

Hamm et al. employed a similar approach and demonstrated its usefulness for absolute MALDI-MSI quantification of two low molecular weight drugs, propranolol and olanzapine, in mice and rat whole-body sections. To calculate tissue extinction coefficient (TEC), the authors sprayed the control section with a "pseudo internal standard" solution (a solution of the target analyte) and divided the average intensity of the drug signal from the specific tissue area by the averaged intensity from the glass slide (selected reference region). In addition, varying
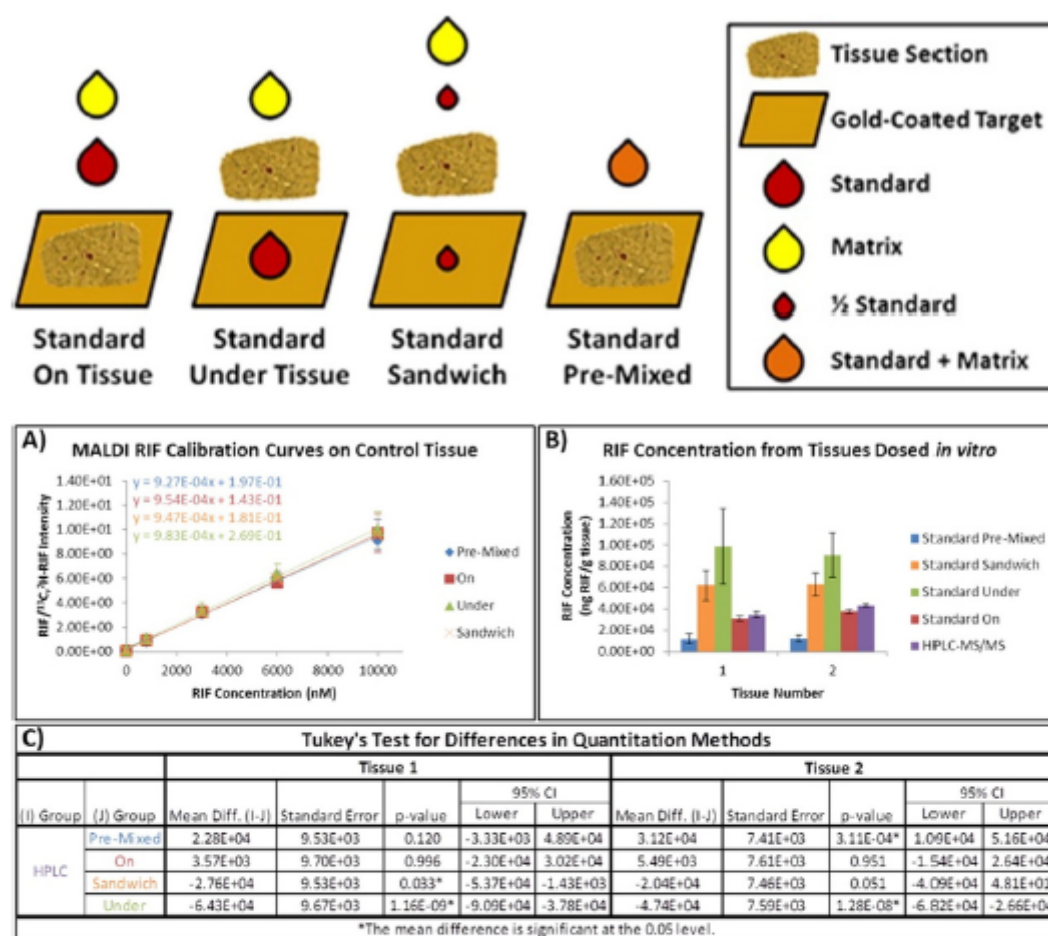
Fig. 3. (Top) Schematic illustration of the four application methods of internal standard. (Bottom) Calibration curves generated for different methods of application of IS (A); diagram illustrating results obtained by quantitative MALDI-MSI and LC-MS/MS (error bars represent standard deviation of multiple experiments) (B); results of the statistical analysis (ANOVA, Tukey test) showing significant differences of LC-MS/MS and quantitative MALDI-MSI employing IS premixed with matrix, sandwich method and IS under the tissue, but no significant difference for IS applied onto the tissue prior to MALDI matrix (C). Reproduced with permission from reference.

concentrations of the sprayed analyte were investigated to demonstrate the non-dependence of this parameter on TEC. Three different concentrations were used for five different tissue types: liver, lung, kidney, stomach and brain. The observed variation of TEC depending on the concentration was different for different organs. The most consistent results were obtained for stomach, the least consistent for brain and kidney, which was probably a result of the large heterogeneity of these two tissues. Finally, the new method was used for absolute quantification by MALDI-MSI and compared with two other techniques, QWBA and LC-MS/MS, revealing strong correlation [118]. Of note, for the calculation of TEC, the analyte was pre-mixed with the MALDI matrix compound, which could favor co-crystallization of the investigated analyte with the matrix, thus decreasing the impact of endogenous tissue compounds on the ionization and extraction suppression of the target drug. The present authors therefore suggest that it is of potential interest to evaluate the same TEC calculation approach, but with the pseudo-IS sprayed separately prior to the MALDI matrix.

There are some doubts whether the TEC approach is equally useful for endogenous molecules. It is still necessary to initially spray the control tissue section with the target analyte, thus there is the potential for bias because of inherent endogenous quantities of the target molecules. It is therefore required to use a stable isotope-labeled version of the endogenous molecule as a pseudo-internal standard, which limits this method as compared to conventional normalization against isotope internal standard. Nevertheless, normalization to the calculated tissue-specific ionization suppression coefficients still has an important advantage over the conventional IS approach; viz., it permits the use of the same calibration curve (based on glass-spotted standard solutions) for the quantification by MALDI-MSI in different specific regions or tissue types across the whole-body section.

2.2. Absolute quantification - different calibration routines

The absolute quantification abilities of MALDI-MSI have been readily demonstrated in recent years [109]. To obtain absolute concentration values of a particular analyte directly from the tissue section, an appropriate calibration model based on a series of standard solutions of different concentration levels is required, similar to procedures used in conventional analytical method development. MALDI-MSI, however, has inherent limitations that introduce additional challenges and difficulties. In particular, the calibration standards have to be incorporated into the tissue material, to ensure that the quantitative instrumental response is as similar as possible to an in vivo dosed drug molecule, a protein-bound endogenous molecule, etc. The most suitable method for

implementing standard calibration solutions involves one of the normalization strategies discussed above, combined with an internal standard. The calibration strategy requires a careful decision on the number of calibration standards, which is sometimes restricted because of material or size limitations (e.g., for hair or spinal cord samples) and the linear dynamic range of the analyte (which could potentially vary over several orders of magnitude). There are also the extremely challenging practical aspects of properly preparing the calibration standards, which result from the fact that tissue-bound compounds (endogenous or administered in vivo) experience different chemical (covalent or non-covalent) or physical environments across the tissue section. Therefore, mass spectrometry imaging analysis is characterized by different recoveries of analyte from different regions (or even adjacent pixels) of the sample. As a result, selection of the exact matrix for the calibration solutions, which should be as closely matched to that of the sample, in each acquired pixels, is virtually impossible. Even though this severely complicates quantitative MALDI-MSI methods, different calibration strategies have been developed as illustrated in Fig. 4 [46] and are discussed in the following text.

2.2.1. Calibration curves from glass slides – with/without TEC correction ('in-solution' strategy)

The most straightforward approach to prepare a calibration curve in MALDI-MSI is achieved by deposition of standard solutions onto sample targets or glass slides; e.g., next to the investigated tissue section. This strategy has been frequently described in the literature. For example, Signor et al. performed sample deposition of calibration samples on a metal target using the dried-droplet method (analyte pre-mixed with MALDI matrix and internal standard) to quantify erlotinib and its metabolites in rat tissue sections [9]. Clemis et al. developed a quantification routine for peptides based on spraying glass slides with the internal standard and then spotting the calibration standard solutions, which were pre-mixed with matrix, onto the IS-covered slides [85]. Although this in-solution strategy was very simple to apply, even in a combination with internal standard normalization, it was shown to be inaccurate in quantitative MALDI-MSI applications, because it did not account for ionization suppression or varying extraction efficiency. It is possible to make this approach more reliable by implementation of an appropriate correction for tissue-based matrix effects, however, i.e., by employing tissue extinction coefficients (TEC) as described in the previous section. Hamm et al. quantified two drugs in different rodent tissues (see calibration curves in Fig. 5), showing good linearity (with coefficient of determination, R^2, amounted to 0.98 and 0.96 for propranolol and olanzapine, respectively). The authors achieved very good quantitative performance in kidney for propranolol (5.6 μg/g tissue)

and olanzapine (41.6 μg/g tissue) in comparison to the reference methods QWBA (propranolol, 5.5 μg/g tissue) and LC-MS/MS (olanzapine, 41.1 μg/g tissue) [118].

2.2.2. Calibration curves from the top or beneath the tissue ('on/under-tissue' strategy)

In contrast to the in-solution method employed without TEC correction, the on-tissue strategy, as an example of matrix-matched approach, allows for compensation of variations resulting from different ionization efficiencies across the tissue sections. Briefly, this technique is performed by spotting the calibration solutions onto the control tissue followed by all steps of the subsequent imaging sample preparation process [65,72,74,75,79,90]. Another variant of this strategy comprises spotting the calibration solutions onto the glass slide before tissue mounting, which results in the calibration samples deposited beneath the control tissue [80,81,108,115]. It is important that the control section with calibration spots (on-top or below the tissue) is ideally placed on the same glass slide or sample target as the tissue section of interest. This procedure reduces additional variations from irregularities during sample preparation and it eliminates the risk of instrumental changes between measurement cycles. Since the on/under-tissue strategy is convenient to use and takes into account matrix effects, it has been frequently reported for quantification of exogenous compounds. Lagarrigue and colleagues demonstrated absolute quantification of the pesticide chlordecone in mouse liver sections, showing good linearity of calibration (R^2 ranging from 0.9807 to 0.99814 for six replicates) and good repeatability (coefficient of variation 10.2% for six replicates) [78]. Sun et al. employed calibration curves based on standards spotted onto control lung tissue sections for quantification of pirfenidone in different tissues including lung, kidney and liver. The authors utilized the same calibration curve for the parent drug and its two structurally similar metabolites [65]. Other studies describe absolute quantitative applications of MALDI-MSI employing on-tissue calibration curves for dopamine antagonists in rat brain tissue sections [72], for the chemotherapeutic agent irinotecan and its active metabolite in different tissues from a colon cancer murine model [74], for the MRI contrast agent gadofluorine M in tissues from a mouse model of myocardial infarction [119], and for the exogenous neurotoxin β-N-methylamino-L-alanine in different regions of rat brain tissue [77]. In another study, Shariatgorji and colleagues employed on-tissue calibration for endogenous compounds, namely three neurotransmitters, acetylcholine, dopamine and γ-amino butyric acid. As those compounds are naturally present in control brain tissue, calibration curves were prepared based on deuterated analogues of the analytes spotted onto the sections [79].
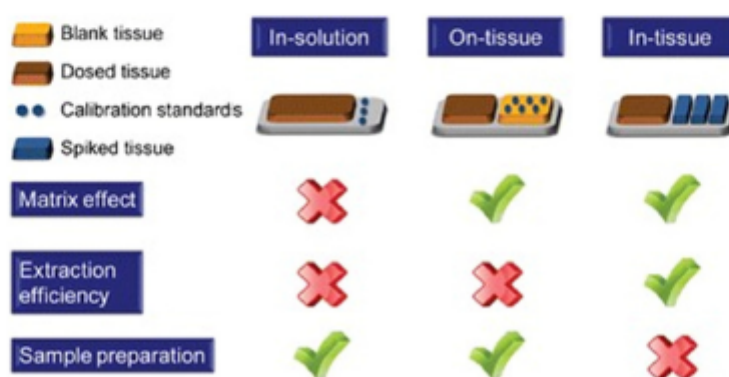

Fig. 4. Comparison of different routines for absolute quantification via MALDI-MSI. The in-solution method is based on calibration standard solutions spotted onto the target plate (glass slide). The on-tissue strategy relies on a calibration range deposited onto the control tissue. The in-tissue approach makes use of a mimetic (surrogate) tissue closely matching the properties of analyte present in the real sample. Only the mimetic tissue approach enables for correction of both ionization and extraction efficiencies. However, the two other techniques have the advantage of a much simpler and faster preparation procedure. Reproduced with permission from reference [46].
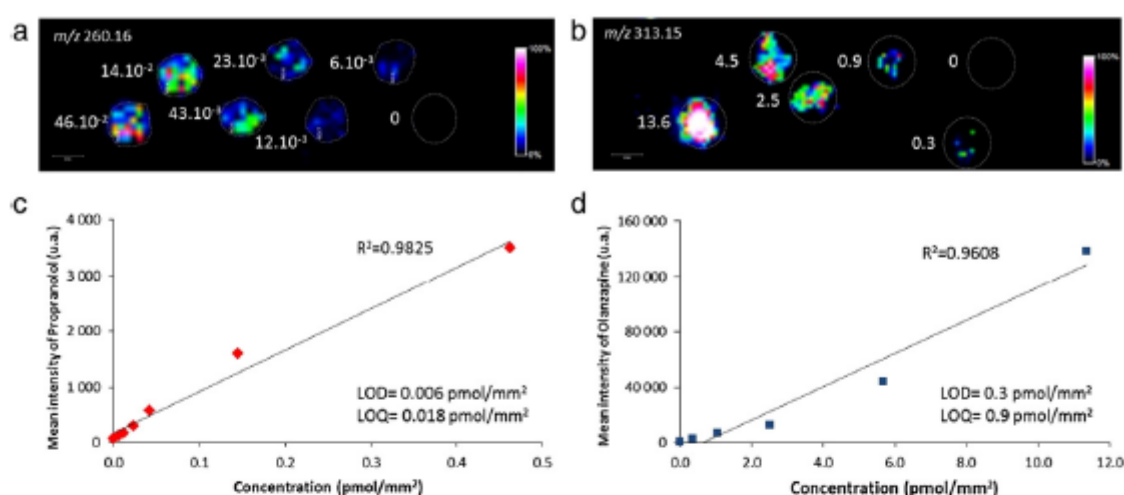
Fig. 5. MSI analysis of calibration spots deposited on glass slides, acquired for propranolol ([M + H]⁺, m/z 260.16) (a) and olanzapine (M + H]⁺, m/z 313.15) (b). Calibration curves obtained using an in-solution strategy combined with TIC normalization for propranolol (c) and olanzapine (d); R^2, coefficient of determination; LOD, limit of detection; LOQ, limit of quantification. Reproduced with permission from reference [118].

During calibration, special care has to be taken with respect to on-tissue spotting. Goodwin et al. noticed that when MALDI matrix was applied immediately after the calibration solutions, preferential matrix adhesion occurred at those places where the standards where spotted, causing higher ion abundances in these regions. To avoid this, calibration spots should be left to dry under vacuum conditions and placed at −80 °C. Then, calibration sections should be processed in identical manner to the in vivo dosed tissues [72].

In addition to the on-tissue strategy, calibration samples can be also deposited under the control tissue section, which has proven to be a reliable method for quantitative MALDI-MSI. Several papers suggested that this strategy more accurately reflects the extraction efficiency typical for in vivo dosed samples as compared to the on-tissue method [80, 81,108,115]. Reich et al. used under-tissue calibration to quantify cocaine in post-mortem human brain sections [115]. Pirman and colleagues described this approach for absolute quantification of the endogenous compounds acetylcholine [80] and acetyl-L-carnitine [81] in piglet brain tissue. In both studies, standard solutions at different concentration levels of the analyte were spotted onto the glass slide before or after homogenous deposition of isotopically-labeled internal standard, followed by tissue mounting. As both analytes were naturally present in the control sections, the authors employed calibration by standard addition instead of more commonly used external calibration, showing good linearity for acetylcholine ($R^2 = 0.9912$) as well as acetyl-L-carnitine ($R^2 = 0.998$) In another study, Pirman et al. compared the quantification of cocaine in post-mortem human brain tissues by quantitative MALDI-MSI – using two different calibration techniques (external calibration versus standard additions) – with LC-MS/MS [108]. For both calibration models, the authors observed very good linearity by MALDI-MSI in MS/MS mode on a QTOF instrument with normalization to deuterated internal standard (Fig. 6). Moreover, the quantitative MALDI-MSI results were within 25% of the values determined by LC-MS/MS.

In conclusion, if the matrix-matched standardization method (either on/under-tissue or mimetic tissue) is employed for MALDI-MSI quantification of endogenous compounds, the standard addition technique presently appears to be the method of choice. An alternative approach is the preparation of a calibration range of isotopically-labeled standards of the analyte, which then requires normalization to another isotopically-labeled internal standard signal.

2.2.3. Calibration curves from mimetic tissue models ('in-tissue' strategy)

Recently, a mimetic tissue approach was proposed to correct for both ionization and extraction efficiency variations, which was previously reported for quantitative imaging of elements in tissue by laser ablation (LA)-inductively-coupled (ICP)-MS [120]. Its implementation for quantitative MALDI-MSI was first described by Groseclose et al. for quantification of the low molecular weight drugs nevirapine in rat liver sections and lapatinib in dog liver as well as for xenograft mouse tumor model [70]. The preparation technique was based on a series of control tissue homogenates with added standard solutions of the analyte at increasing concentrations. Spiked homogenates were deposited into separate channels drilled into an OCT block, which was placed at −80 °C. This mimetic tissue was then processed on exactly the same manner as in vivo-dosed tissues (Fig. 7). The authors obtained a wide linear dynamic range ($R^2 = 0.9995$) and very good correlation with LC-MS/MS, even though the spiked homogenates were prepared from rat liver and used for quantification from dog liver and xenograft tumor sections. In another study, the same group employed a similar strategy for imaging of carboxy metabolite of dabrafenib in rat kidney, showing comparable amounts of target analyte by MALDI-MSI and LC-MS/MS [71].

Although the mimetic tissue approach appears to be the most reliable calibration strategy for quantitative MALDI-MSI, it presents several challenges. Firstly, the entire procedure is much more time consuming than on/under-tissue approaches, which becomes even more disadvantageous, when quantitative MALDI imaging of whole body sections is performed. Whole body sections would ideally require a different calibration block for each single tissue type. Moreover, for structurally diverse organs such as brain or kidney, with varying levels of endogenous compounds, a perfect calibration model would use separate calibration curves for each sub-region or subtype with specific chemical and morphological characteristics (e.g., white matter versus grey matter in brain, medulla versus cortex in kidney). The same problem occurs for size or amount-limited tissues (e.g., spinal cord, optic nerve.), which do not allow the preparation of range of tissue
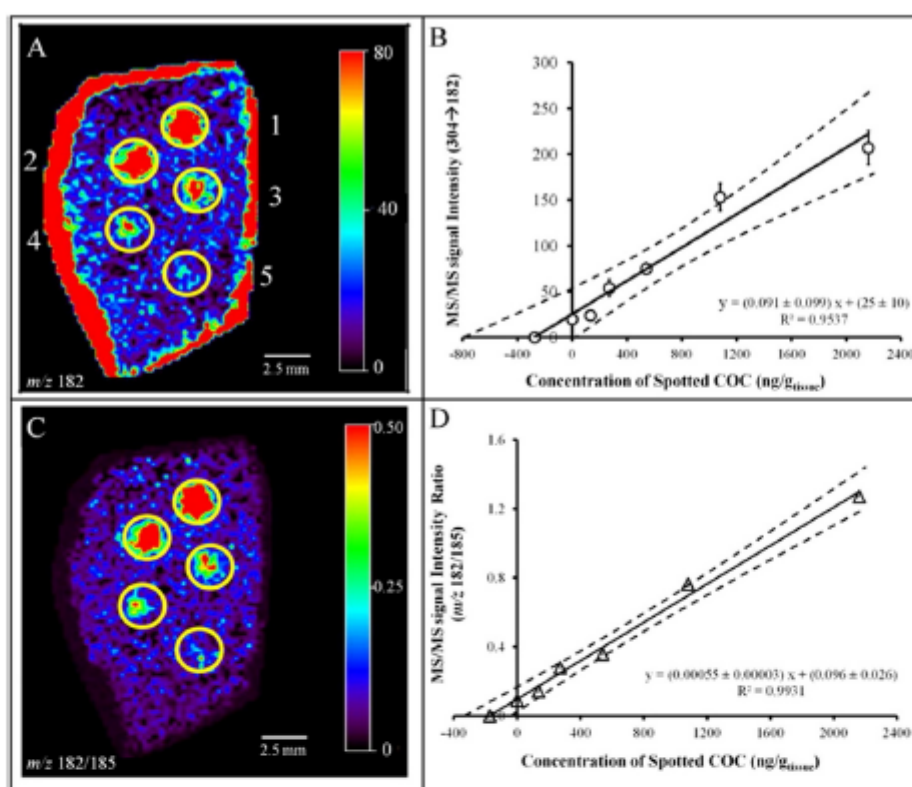
734   *I. Rzagalinski, D.A. Volmer / Biochimica et Biophysica Acta 1865 (2017) 726–739*

Fig. 6. Calibration solution spots and corresponding calibration curves employing the standard addition technique for non-normalized (A, B) and IS-normalized (C, D) imaging data. Experiments were carried out using wide isolation MS/MS scans on a QTOF instrument. Normalization of the cocaine signal (m/z 182) to cocaine-d_3 (m/z 185) improved linearity (R^2 from 0.9537 to 0.9931) and precision (expressed as standard deviation of slope and intercept). Reproduced with permission from reference [108].

homogenates. To overcome some of these difficulties, Takai et al. employed liver-based surrogate tissue quantification for liver samples and other tissues such as kidney, brain and lung. Although the measured concentration values were more accurate when the liver surrogate was implemented for liver samples (80–120% as compared to LC-MS/MS), the data for the other tissues were acceptable (104–160%) [73]. In another example, the same group proposed gelatin as surrogate material (pseudo-tissue) instead of tissue homogenate, to quantify therapeutic peptides in mice liver and kidney sections. The paper demonstrated good correlation between results from MALDI-MSI and LC-MS/MS (accuracy, 76–127%) [76].

An important parameter that needs to be considered in mimetic tissues is the quality of the morphological structures of the tissue homogenate cores. This is typically accomplished by histological evaluation of mimetic tissue sections with respect to tissue density and number and distribution of cell nuclei (Fig. 7). Jadoul et al. compared four different homogenization techniques to achieve optimum reconstruction of the morphology of the intact tissue [82]. The most satisfying results were seen with a simple tissue grinder (Potter-Elvehjem homogenization) or an automated bead mill homogenizer. The authors also assessed the role of the freezing speed on mimetic tissue section morphology. Best results were obtained by immersing the material in pre-cooled isopentane at −50 °C, instead of placing it in the freezer at −80 °C, which allowed for faster freezing and prevented formation of large ice crystals and additional tissue damages [82]. Finally, for quantification of drugs, Groseclose et al. noted that it is necessary to confirm that the drug is incorporated properly into tissue homogenates, in particular for liver, and that it does not undergo metabolism, to maintain the appropriate concentration of parent drug in the calibration spots [70].

3. Conclusions

Different normalization and calibration routines for MALDI-MSI quantification of low-molecular weight compounds were discussed and compared in this article. The most important conclusion from the presented experimental strategies is that reliable absolute quantitative results from MALDI-MSI can only be obtained if a carefully designed workflow is implemented that combines appropriate calibration curves with proper data normalization of signals intensities. Currently, the most reliable approach for absolute quantification appears to be based on mimetic tissue-based calibration curves along with normalization to well-matched internal standards (stable isotope compounds or structural analogs). This strategy has yielded accurate, spatially resolved quantitative data in research fields such as drug distribution studies, which have been comparable to the established standard techniques autoradiography or LC-MS/MS. The method is time-consuming, however, and therefore calibration curves based on standard solutions spiked onto the tissue are reasonable alternatives, as well as the combination of tissue extinction coefficient normalization with *on-glass* calibration curves.

Although different quantitative strategies have been successfully implemented for MALDI-MSI, the technique is still in constant flux with innovations. Recently, new developments significantly improved detection sensitivity (*e.g.*, post-ionization using the MALDI-2 concept [121] or on-tissue derivatization [77]), precision (*e.g.*, automated devices for reproducible homogenous matrix deposition [86]) and selectivity (*e.g.*, reactive matrices for on-tissue derivatization [122]). In addition, new software readily supports different MSI normalization procedures and absolute quantification [83,118,123,124]. In the end,
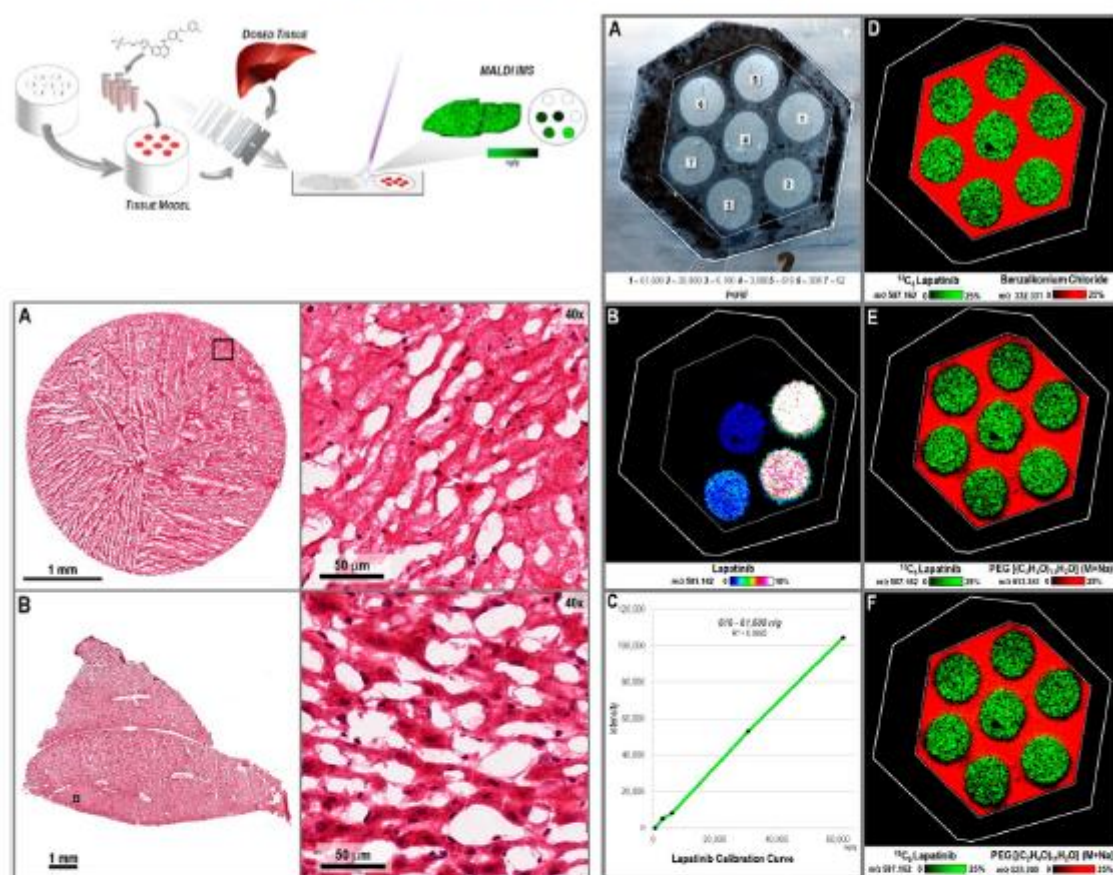
Fig. 7. (Top left) - A schematic workflow representing the preparation of a mimetic tissue model for absolute quantification by MALDI-MSI. (Bottom left) Histological (H&E staining) evaluation of the level of similarity in the morphological structures of the mimetic tissue model single core section (A) and intact rat liver tissue section (B) to ensure possibly close emulation of the real non-homogenized tissue in its influence on the extraction and ionization efficiencies. The 40× enlarged images prove that the overall location of cell nuclei as well as tissue structure remained similar after homogenization. (Right) Optical image of MALDI matrix-coated mimetic tissue section with seven channels containing different lapatinib concentrations (A); lapatinib MS image (m/z 581.142) (B); lapatinib external calibration curve created using average intensity from each single channel (normalized to $^{13}C_6$-labeled drug, which was spiked into every tissue homogenate) (C); MS images of $^{13}C_6$-lapatinib (m/z 587.162) and different OCT components: benzalkonium chloride (m/z 332.331) (D), PEG(C_2H_4O)$_{13}H_2O$ (m/z 613.341) (E) and PEG(C_2H_4O)$_{11}H_2O$ (F) overlaid for assessing potential contamination of tissue regions by OCT. Reproduced with permission from reference [70].

the final goal of these developments will hopefully provide a technology that permits accurate, absolute quantification of each single pixel within the acquired MSI data set.

Some existing guidelines on the validation of (bio)analytical methods such as those provided by the International Conference on Harmonization (ICH Q2(R1)) [125], the European Medicines Agency (EMA) [126] or the U.S. Food and Drug Administration (FDA) [127], which are routinely used in the validation of LC-MS/MS assays, have also been implemented in quantitative (non-imaging!) MALDI-MS studies, including several systematic comparisons and cross-validations between these two techniques [6,10,38]. It is necessary, however, to recognize the challenges and limitations of these guidelines for application to quantitative MSI. First of all, analyzing tissue samples as tissue homogenates is already significantly more challenging in comparison to analysis of body fluids (plasma, serum, urine) [128]. Moreover, the particular feature of imaging analysis, that is, the preservation of the integrity of the intact tissue section (in comparison to bulk analysis by LC-based techniques), determines that some of regulatory guidance for LC-MS/MS assays cannot be directly transferred and applied to quantitative MALDI-MSI.

One of the major current obstacles in determining trueness of the method (usually expressed in terms of bias) is the lack of appropriate reference materials (tissue sections) with known (certified) values for the embedded analytes – for specific x,y coordinates at appropriate lateral resolution – which would permit single pixel accuracy for quantitative MALDI-MSI. In theory, a gold standard technique such as LC-MS/MS could be used as reference tool for this purpose after laser-capture micro-dissecting the areas of interest at sufficient lateral resolution. Such an approach would not compare exactly the same tissue sections, however, but only adjacent slices; it would also require careful spatial alignment of two highly resolved quantitative molecular images. Therefore, most of the reported cross-validation examples (quantitative MSI versus LC-MS/MS) are based on the comparison of the quantitative results obtained for the whole tissue sections.

In contrast to trueness, determining the precision does not require the measurement of the exact concentration of the analyte (= true value) in the samples, as it is simply realized by repeating individual measurements of identical samples, usually at several different concentrations. Therefore, the proposed mimetic tissue model [70], which is in fact an adaptation of spiked matrix-matched standards used in LC-MS/MS,

can be successfully employed to determine repeatability as well as intermediate precision of the method. Determining selectivity, defined as an ability of the method to ensure that the quantified compound is indeed the target analyte, can, in theory, be realized along the lines of chromatographic approaches, through analyses of blank matrix samples obtained from several different sources (at least six according to the FDA). However, since obtaining tissue samples may require the sacrifice of additional animals (in contrast to sampling body fluids), the present authors suggest to follow the recommendations developed during the conference on "Analytical Methods Validation - Bioavailability, Bioequivalence and Pharmacokinetic Studies"; that is, accepting the analysis of a blank sample from one source for mass spectrometry-based methods [129]. The decision on an appropriate calibration model, which is essential for reliable quantification, as well as determination of linearity, working range and limits of quantification, does not differ substantially for MALDI-MSI as compared to well-established LC-MS/MS guidelines.

In contrast to the aforementioned validation parameters, assessing the recovery and stability of the quantitative MSI method is even more challenging and cannot simply rely on applying existing bioanalytical guidelines. In imaging experiments, the preparation of reference samples for studying the recovery by spiking analytes to tissue homogenates does not provide a realistic representation of the drug distribution in the intact tissues. Thus, determination of recovery based on the mimetic tissue model is only possible to certain degree, limited by the degree of closeness of this model to the real tissue environment, as well as by the intra- and extra-cellular content of the analyte in its biological surroundings [128]. Reliable assessment of stability for mass spectrometry imaging methods appears to be even more challenging. According to the regulatory guidelines for bioanalytical methods, testing the stability of the analyte should be provided for the entire analytical procedure, including sample collection and handling, storage of frozen samples (long-term stability), sample preparation and analytical measurement processes (short-term stability), as well as after freeze-and-thaw cycles. Unfortunately, many of these suggested procedures cannot be tested and documented in MSI analysis of intact tissue sections and organs in a straightforward manner, as reference materials for certified tissue (and whole organs) are not available.

Finally, determination of any of the mentioned method validation parameters requires repeated independent measurements of identical samples at different concentration levels. Therefore, the single acquired pixel in MSI analysis essentially corresponds to the single sample analysis by LC-MS/MS (using a single chromatographic injection of a liquid sample). However, we cannot replicate measurements of the same pixel, as we simply do by replicate injections of the same sample onto the chromatography column. Thus, the complete validation of "pixel-to-pixel" quantitative MALDI-MSI method (in contrast to the quantification of whole tissue sections) without using a series of (certified) reference tissue sections, with known true value of the analyte for every single pixel, remains extremely challenging or even impossible, likely requiring alternative models in the future.

Transparency document

The Transparency document associated with this article can be found, in online version.

References

[1] F. Hillenkamp, J. Peter-Katalinic, A Practical Guide to MALDI-MS. Instrumentation, Methods and Applications, Wiley-VCH, 2006.
[2] M.W. Duncan, H. Roder, S.W. Hunsucker, Quantitative matrix-assisted laser desorption/ionization mass spectrometry, Brief. Funct. Genomic. Proteomic. 7 (2008) 355–370, http://dx.doi.org/10.1093/bfgp/eln041.
[3] P. Hatsis, S. Brombacher, J. Corr, P. Kovarik, D.A. Volmer, Quantitative analysis of small pharmaceutical drugs using a high repetition rate laser matrix-assisted laser/desorption ionization source, Rapid Commun. Mass Spectrom. 17 (2003) 2303–2309, http://dx.doi.org/10.1002/rcm.1192.

[4] L. Sleno, D.A. Volmer, Some fundamental and technical aspects of the quantitative analysis of pharmaceutical drugs by matrix-assisted laser desorption/ionization mass spectrometry, Rapid Commun. Mass Spectrom. 19 (2005) 1928–1936, http://dx.doi.org/10.1002/rcm.2006.
[5] L. Sleno, D.A. Volmer, Toxin screening in phytoplankton: detection and quantitation using MALDI triple quadrupole mass spectrometry, Anal. Chem. 77 (2005) 1509–1517, http://dx.doi.org/10.1021/ac0486600.
[6] J.J.A. Van Kampen, P.C. Burgers, R.A. Gruters, A.D.M.E. Osterhaus, R. De Groot, T.M. Luider, D.A. Volmer, Quantitative analysis of antiretroviral drugs in lysates of peripheral blood mononuclear cells using MALDI-triple quadrupole mass spectrometry, Anal. Chem. 80 (2008) 4969–4975, http://dx.doi.org/10.1021/ac800218a.
[7] P. Kovarik, C. Grivet, E. Bourgogne, G. Hopfgartner, Method development aspects for the quantitation of pharmaceutical compounds in human plasma with a matrix-assisted laser desorption/ionization source in the multiple reaction monitoring mode, Rapid Commun. Mass Spectrom. 21 (2007) 911–919, http://dx.doi.org/10.1002/rcm.2912.
[8] T. Porta, C. Grivet, R. Knochenmuss, E. Varesio, G. Hopfgartner, Alternative CHCA-based matrices for the analysis of low molecular weight compounds by UV-MALDI-tandem mass spectrometry, J. Mass Spectrom. 46 (2011) 144–152, http://dx.doi.org/10.1002/jms.1875.
[9] L. Signor, E. Varesio, R.F. Staack, V. Starke, W.F. Richter, G. Hopfgartner, Analysis of erlotinib and its metabolites in rat tissue sections by MALDI quadrupole time-of-flight mass spectrometry, J. Mass Spectrom. 42 (2007) 900–909, http://dx.doi.org/10.1002/jms.1225.
[10] M. Wagner, E. Varesio, G. Hopfgartner, Ultra-fast quantitation of saquinavir in human plasma by matrix-assisted laser desorption/ionization and selected reaction monitoring mode detection, J. Chromatogr. B Anal. Technol. Biomed. Life Sci. 872 (2008) 68–76, http://dx.doi.org/10.1016/j.jchromb.2008.07.009.
[11] J.J. Corr, P. Kovarik, B.B. Schneider, J. Hendrikse, A. Loboda, T.R. Covey, Design considerations for high speed quantitative mass spectrometry with MALDI ionization, J. Am. Soc. Mass Spectrom. 17 (2006) 1129–1141, http://dx.doi.org/10.1016/j.jasms.2006.04.026.
[12] P.J. Lee, W. Chen, J.C. Gebler, Qualitative and quantitative analysis of small amine molecules by MALDI-TOF mass spectrometry through charge derivatization, Anal. Chem. 76 (2004) 4888–4893, http://dx.doi.org/10.1021/ac035537k.
[13] A. Koulman, D. Petras, V.K. Narayana, L. Wang, D.A. Volmer, Comparative high-speed profiling of carboxylic acid metabolite levels by differential isotope-coded MALDI mass spectrometry, Anal. Chem. 81 (2009) 7544–7551, http://dx.doi.org/10.1021/ac900562j.
[14] A.J. Nicola, A.J. Gusev, A. Proctor, E.K. Jackson, D.M. Hercules, Application of the fast-evaporation sample preparation method for improving quantification of angiotensin II by matrix-assisted laser desorption/ionization, Rapid Commun. Mass Spectrom. 9 (1995) 1164–1171, http://dx.doi.org/10.1002/rcm.1290091216.
[15] R.R. Hensel, R.C. King, K.G. Owens, Electrospray sample preparation for improved quantitation in matrix-assisted laser desorption/ionization time-of-flight mass spectrometry, Rapid Commun. Mass Spectrom. 11 (1997) 1785–1793.
[16] M.R. O'Rourke, S.P. Djordjevic, M.P. Padula, The Quest for Improved Reproducibility in MALDI Mass Spectrometry, Mass Spectrom. Rev. 2016http://dx.doi.org/10.1002/mas.21515.
[17] M. Palmblad, R. Cramer, Liquid matrix deposition on conductive hydrophobic surfaces for tuning and quantitation in UV-MALDI mass spectrometry, J. Am. Soc. Mass Spectrom. 18 (2007) 693–697, http://dx.doi.org/10.1016/j.jasms.2006.11.013.
[18] L. Molin, S. Cristoni, R. Seraglia, P. Traldi, Sieve-based device for MALDI sample preparation. III. Its power for quantitative measurements, J. Mass Spectrom. 46 (2011) 230–236, http://dx.doi.org/10.1002/jms.1885.
[19] S. König, J. Grote, Hydrophobic targets for MALDI mass spectrometry, BioTechniques 32 (2002) 912–915.
[20] S.J. Owen, F.S. Meier, S. Brombacher, D.A. Volmer, Increasing sensitivity and decreasing spot size using an inexpensive, removable hydrophobic coating for matrix-assisted laser desorption/ionisation plates, Rapid Commun. Mass Spectrom. 17 (2003) 2439–2449, http://dx.doi.org/10.1002/rcm.1210.
[21] R.L. Gundry, R. Edward, T.P. Kole, C. Sutton, R.J. Cotter, Disposable hydrophobic surface on MALDI targets for enhancing MS and MS/MS data of peptides, Anal. Chem. 77 (2005) 6609–6617, http://dx.doi.org/10.1021/ac050500g.
[22] M. Pabst, S.R. Fagerer, R. Köhling, S.K. Küster, R. Steinhoff, M. Badertscher, F. Wahl, P.S. Dittrich, K. Jefimovs, R. Zenobi, Self-aliquoting microarray plates for accurate quantitative matrix-assisted laser desorption/ionization mass spectrometry, Anal. Chem. 85 (2013) 9771–9776, http://dx.doi.org/10.1021/ac4021775.
[23] M.W. Duncan, G. Matanovic, A. Cerpa-Poljak, Quantitative analysis of low molecular weight compounds of biological interest by matrix-assisted laser desorption ionization, Rapid Commun. Mass Spectrom. 7 (1993) 1090–1094, http://dx.doi.org/10.1002/rcm.1290071207.
[24] D. Bungert, E. Heinzle, A. Tholey, Quantitative matrix-assisted laser desorption/ionization mass spectrometry for the determination of enzyme activities, Anal. Biochem. 326 (2004) 167–175, http://dx.doi.org/10.1016/j.ab.2003.11.013.
[25] N. Kaneko, R. Yamamoto, T.-A. Sato, K. Tanaka, Identification and quantification of amyloid beta-related peptides in human plasma using matrix-assisted laser desorption/ionization time-of-flight mass spectrometry, Proc. Jpn. Acad. Ser. B Phys. Biol. Sci. 90 (2014) 104–117, http://dx.doi.org/10.2183/pjab.90.104.
[26] L. Sleno, D.A. Volmer, Assessing the properties of internal standards for quantitative matrix-assisted laser desorption/ionization mass spectrometry of small molecules, Rapid Commun. Mass Spectrom. 20 (2006) 1517–1524, http://dx.doi.org/10.1002/rcm.2498.
[27] K.L. Howard, G.L. Boyer, Quantitative analysis of cyanobacterial toxins by matrix-assisted laser desorption ionization mass spectrometry, Anal. Chem. 79 (2007) 5980–5986, http://dx.doi.org/10.1021/ac0705723.

[28] E. Szájli, T. Fehér, K.F. Medzihradszky, Investigating the quantitative nature of MALDI-TOF MS, Mol. Cell. Proteomics 7 (2008) 2410–2418, http://dx.doi.org/10.1074/mcp.M800108-MCP200.

[29] A.F. Roegner, M.P. Schirmer, B. Puschner, B. Brena, G. Gonzalez-Sapienza, Rapid quantitative analysis of microcystins in raw surface waters with MALDI MS utilizing easily synthesized internal standards, Toxicon 78 (2014) 94–102, http://dx.doi.org/10.1016/j.toxicon.2013.12.007.

[30] J.J. Thomas, Z. Shen, J.E. Crowell, M.G. Finn, G. Siuzdak, Desorption/ionization on silicon (DIOS): a diverse mass spectrometry platform for protein characterization, Proc. Natl. Acad. Sci. U. S. A. 98 (2001) 4932–4937, http://dx.doi.org/10.1073/pnas.081069298.

[31] A. Lesur, E. Varesio, B. Domon, G. Hopfgartner, Peptides quantification by liquid chromatography with matrix-assisted laser desorption/ionization and selected reaction monitoring detection, J. Proteome Res. 11 (2012) 4972–4982, http://dx.doi.org/10.1021/pr300514u.

[32] J.E. Elsila, N.P. De Leon, R.N. Zare, Factors affecting quantitative analysis in laser desorption/laser ionization mass spectrometry, Anal. Chem. 76 (2004) 2430–2437, http://dx.doi.org/10.1021/ac0354140.

[33] M. Persike, M. Karas, Rapid simultaneous quantitative determination of different small pharmaceutical drugs using a conventional matrix-assisted laser desorption/ionization time-of-flight mass spectrometry system, Rapid Commun. Mass Spectrom. 23 (2009) 3555–3562, http://dx.doi.org/10.1002/rcm.4283.

[34] H. Thomas, J. Havlis, J. Peychl, A. Shevchenko, Dried-droplet probe preparation on AnchorChip targets for navigating the acquisition of matrix-assisted laser desorption/ionization time-of-flight spectra by fluorescence of matrix/analyte crystals, Rapid Commun. Mass Spectrom. 18 (2004) 923–930, http://dx.doi.org/10.1002/rcm.1427.

[35] J. Horak, W. Werther, E.R. Schmid, Optimisation of the quantitative determination of chlormequat by matrix-assisted laser desorption/ionisation mass spectrometry, Rapid Commun. Mass Spectrom. 15 (2001) 241–248, http://dx.doi.org/10.1002/rcm.217.

[36] S. Vaidyanathan, R. Goodacre, Quantitative detection of metabolites using matrix-assisted laser desorption/ionization mass spectrometry with 9-aminoacridine as the matrix, Rapid Commun. Mass Spectrom. 21 (2007) 2072–2078, http://dx.doi.org/10.1002/rcm.3063.

[37] D. Gode, C. Schmitt, M. Engel, D.A. Volmer, Screening Dyrk1A inhibitors by MALDI-QqQ mass spectrometry: Systematic comparison to established radiometric, luminescence, and LC-UV-MS assays, Anal. Bioanal. Chem. 406 (2014) 2841–2852, http://dx.doi.org/10.1007/s00216-014-7703-1.

[38] D.A. Volmer, L. Sleno, K. Bateman, C. Sturino, R. Oballa, T. Mauriala, J. Corr, Comparison of MALDI to ESI on a triple quadrupole platform for pharmacokinetic analyses, Anal. Chem. 79 (2007) 9000–9006, http://dx.doi.org/10.1021/ac7016234.

[39] A.I. Gusev, W.R. Wilkinson, A. Proctor, D.M. Hercules, Direct quantitative analysis of peptides using matrix assisted laser desorption ionization, Anal. Bioanal. Chem. 354 (1996) 455–463, http://dx.doi.org/10.1007/s0021663540455.

[40] L.H. Cohen, A.I. Gusev, Small molecule analysis by MALDI mass spectrometry, Anal. Bioanal. Chem. 373 (2002) 571–586, http://dx.doi.org/10.1007/s00216-002-1321-z.

[41] S. Brombacher, S.J. Owen, D.A. Volmer, Automated coupling of capillary-HPLC to matrix-assisted laser desorption/ionization mass spectrometry for the analysis of small molecules utilizing a reactive matrix, Anal. Bioanal. Chem. 376 (2003) 773–779, http://dx.doi.org/10.1007/s00216-003-2024-9.

[42] A. Monopoli, C.D. Calvano, A. Nacci, F. Palmisano, Boronic acid chemistry in MALDI MS: a step forward in designing a reactive matrix with molecular recognition capabilities, Chem. Commun. (Camb.) 50 (2014) 4322–4324, http://dx.doi.org/10.1039/c4cc01185f.

[43] Y. Shigeri, A. Yasuda, M. Sakai, S. Ikeda, R. Arakawa, H. Sato, T. Kinumi, Hydrazide and hydrazine reagents as reactive matrices for matrix-assisted laser desorption/ionization mass spectrometry to detect steroids with carbonyl groups, Eur. J. Mass Spectrom. 21 (2015) 79–90, http://dx.doi.org/10.1255/ejms.1336.

[44] V. Zaikin, R. Borisov, N. Polovkov, M. Slyundina, Reactive matrices for matrix-assisted laser desorption/ionization mass spectrometry of primary amines, Eur. J. Mass Spectrom. 21 (2015) 403–411, http://dx.doi.org/10.1255/ejms.1353.

[45] B. Flinders, J. Morrell, P.S. Marshall, L.E. Ranshaw, M.R. Clench, The use of hydrazine-based derivatization reagents for improved sensitivity and detection of carbonyl containing compounds using MALDI-MSI, Anal. Bioanal. Chem. 407 (2015) 2085–2094, http://dx.doi.org/10.1007/s00216-014-8223-8.

[46] T. Porta, A. Lesur, E. Varesio, G. Hopfgartner, Quantification in MALDI-MS imaging: what can we learn from MALDI-selected reaction monitoring and what can we expect for imaging? Anal. Bioanal. Chem. 407 (2015) 2177–2187, http://dx.doi.org/10.1007/s00216-014-8315-5.

[47] J.H. Jungmann, R.M.A. Heeren, Emerging technologies in mass spectrometry imaging, J. Proteome 75 (2012) 5077–5092, http://dx.doi.org/10.1016/j.jprot.2012.03.022.

[48] B. Spengler, Mass spectrometry imaging of biomolecular information, Anal. Chem. 87 (2015) 64–82, http://dx.doi.org/10.1021/ac504543v.

[49] D. Gode, D.A. Volmer, Lipid imaging by mass spectrometry - a review, Analyst 138 (2013) 1289–1315, http://dx.doi.org/10.1039/c2an36337b.

[50] P.J. Trim, M.F. Snel, Small molecule MALDI MS imaging: current technologies and future challenges, Methods 104 (2015) 127–141, http://dx.doi.org/10.1016/j.ymeth.2016.01.011.

[51] A. Bodzon-Kulakowska, P. Suder, Imaging mass spectrometry: instrumentation, applications, and combination with other visualization techniques, Mass Spectrom. Rev. 35 (2016) 147–169, http://dx.doi.org/10.1002/mas.21468.

[52] K. Dreisewerd, Recent methodological advances in MALDI mass spectrometry, Anal. Bioanal. Chem. 406 (2014) 2261–2278, http://dx.doi.org/10.1007/s00216-014-7646-6.

[53] B.A. Boughton, D. Thinagaran, D. Sarabia, A. Bacic, U. Roessner, Mass spectrometry imaging for plant biology: a review, Phytochem. Rev. 15 (2015) 445–488, http://dx.doi.org/10.1007/s11101-015-9440-2.

[54] M.M. Gessel, J.L. Norris, R.M. Caprioli, MALDI imaging mass spectrometry: spatial molecular analysis to enable a new age of discovery, J. Proteome 107 (2014) 71–82, http://dx.doi.org/10.1016/j.jprot.2014.03.021.

[55] J.L. Norris, R.M. Caprioli, Analysis of tissue specimens by matrix-assisted laser desorption/ionization imaging mass spectrometry in biological and clinical research, Chem. Rev. 113 (2013) 2309–2342, http://dx.doi.org/10.1021/cr3004295.

[56] J.L. Norris, D.S. Cornett, J.A. Mobley, M. Andersson, E.H. Seeley, P. Chaurand, R.M. Caprioli, Processing MALDI mass spectra to improve mass spectral direct tissue analysis, Int. J. Mass Spectrom. 260 (2007) 212–221, http://dx.doi.org/10.1016/j.ijms.2006.10.005.

[57] T. Alexandrov, MALDI imaging mass spectrometry: statistical data analysis and current computational challenges, BMC Bioinf.s 13 (Suppl. 1) (2012) S11, http://dx.doi.org/10.1186/1471-2105-13-S16-S11.

[58] D. Pirman, Quantitative profiling of tissue drug distribution by MS imaging, Bioanalysis 7 (2015) 2649–2656, http://dx.doi.org/10.4155/bio.15.179.

[59] A. Palmer, D. Trede, T. Alexandrov, Where imaging mass spectrometry stands: here are the numbers, Metabolomics 12 (2016) 107, http://dx.doi.org/10.1007/s11306-016-1047-0.

[60] S.R. Ellis, A.L. Bruinen, R.M.A. Heeren, A critical evaluation of the current state-of-the-art in quantitative imaging mass spectrometry, Anal. Bioanal. Chem. 406 (2014) 1275–1289, http://dx.doi.org/10.1007/s00216-013-7478-9.

[61] A. Kubo, M. Kajimura, M. Suematsu, Matrix-assisted laser desorption/ionization (MALDI) imaging mass spectrometry (IMS): a challenge for reliable quantitative analyses, Mass Spectrom. (Tokyo, Jpn.) 1 (2012) A0004, http://dx.doi.org/10.5702/massspectrometry.A0004.

[62] S.O. Deininger, D.S. Cornett, R. Paape, M. Becker, C. Pineau, S. Rauser, A. Walch, E. Wolski, Normalization in MALDI-TOF imaging datasets of proteins: practical considerations, Anal. Bioanal. Chem. 401 (2011) 167–181, http://dx.doi.org/10.1007/s00216-011-4929-z.

[63] D. Miura, Y. Fujimura, M. Yamato, F. Hyodo, H. Utsumi, H. Tachibana, H. Wariishi, Ultrahighly sensitive in situ metabolomic imaging for visualizing spatiotemporal metabolic behaviors, Anal. Chem. 82 (2010) 9789–9796, http://dx.doi.org/10.1021/ac101998z.

[64] A. Thomas, N.H. Patterson, M.M. Marcinkiewicz, A. Lazaris, P. Metrakos, P. Chaurand, Histology-driven data mining of lipid signatures from multiple imaging mass spectrometry analyses: application to human colorectal cancer liver metastasis biopsies, Anal. Chem. 85 (2013) 2860–2866, http://dx.doi.org/10.1021/ac30B4294.

[65] N. Sun, I.E. Fernandez, M. Wei, Y. Wu, M. Aichler, O. Eickelberg, A. Walch, Pharmacokinetic and pharmacometabolomic study of pirfenidone in normal mouse tissues using high mass resolution MALDI-FTICR-mass spectrometry imaging, Histochem. Cell Biol. 145 (2016) 201–211, http://dx.doi.org/10.1007/s00418-015-1382-7.

[66] K. Hattori, M. Kajimura, T. Hishiki, T. Nakanishi, A. Kubo, Y. Nagahata, M. Ohmura, A. Yachie-Kinoshita, T. Matsuura, T. Morikawa, T. Nakamura, M. Setou, M. Suematsu, Paradoxical ATP elevation in ischemic penumbra revealed by quantitative imaging mass spectrometry, Antioxid. Redox Signal. 13 (2010) 1157–1167, http://dx.doi.org/10.1089/ars.2010.3290.

[67] M. Irie, Y. Fujimura, M. Yamato, D. Miura, H. Wariishi, Integrated MALDI-MS imaging and LC-MS techniques for visualizing spatiotemporal metabolomic dynamics in a rat stroke model, Metabolomics 10 (2014) 473–483, http://dx.doi.org/10.1007/s11306-013-0588-8.

[68] B. Prideaux, M. Stoeckli, Mass spectrometry imaging for drug distribution studies, J. Proteome 75 (2012) 4999–5013, http://dx.doi.org/10.1016/j.jprot.2012.07.028.

[69] A. Nilsson, R.J.A. Goodwin, M. Shariatgorji, T. Vallianatou, P.J.H. Webborn, P.E. Andrén, Mass spectrometry imaging in drug development, Anal. Chem. 87 (2015) 1437–1455, http://dx.doi.org/10.1021/ac5047 34s.

[70] M.R. Groseclose, S. Castellino, A mimetic tissue model for the quantification of drug distributions by MALDI imaging mass spectrometry, Anal. Chem. 85 (2013) 10099–10106, http://dx.doi.org/10.1021/ac400892z.

[71] M.R. Groseclose, S.B. Laffan, K.S. Frazier, A. Hughes-Earle, S. Castellino, Imaging MS in toxicology: an investigation of juvenile rat nephrotoxicity associated with dabrafenib administration, J. Am. Soc. Mass Spectrom. 26 (2015) 887–898, http://dx.doi.org/10.1007/s13361-015-1103-4.

[72] R.J.A. Goodwin, C.L. MacKay, A. Nilsson, D.J. Harrison, L. Farde, P.E. Andrén, S.L. Iverson, Qualitative and quantitative MALDI imaging of the positron emission tomography ligands raclopride (a D2 dopamine antagonist) and SCH 23390 (a D1 dopamine antagonist) in rat brain tissue sections using a solvent-free dry matrix application method, Anal. Chem. 83 (2011) 9694–9701, http://dx.doi.org/10.1021/ac202630t.

[73] N. Takai, Y. Tanaka, H. Saji, Quantification of small molecule drugs in biological tissue sections by imaging mass spectrometry using surrogate tissue-based calibration standards, Mass Spectrom. (Tokyo, Japan) 3 (2014) A0025, http://dx.doi.org/10.5702/massspectrometry.A0025.

[74] A. Buck, S. Halbritter, C. Späth, A. Feuchtinger, M. Aichler, H. Zitzelsberger, K.P. Janssen, A. Walch, Distribution and quantification of irinotecan and its active metabolite SN-38 in colon cancer murine model systems using MALDI MSI, Anal. Bioanal. Chem. 407 (2015) 2107–2116, http://dx.doi.org/10.1007/s00216-014-8237-2.

[75] A. Nilsson, T.E. Fehniger, L. Gustavsson, M. Andersson, K. Kenne, G. Marko-Varga, P.E. Andrén, Fine mapping the spatial distribution and concentration of unlabeled drugs within tissue micro-compartments using imaging mass spectrometry, PLoS One 5 (2010) http://dx.doi.org/10.1371/journal.pone.0011411.

[76] N. Takai, Y. Tanaka, A. Watanabe, H. Saji, Quantitative imaging of a therapeutic peptide in biological tissue sections by MALDI MS, Bioanalysis 5 (2013) 603–612, http://dx.doi.org/10.4155/bio.13.13.

I. Rzagalinski, D.A. Volmer / Biochimica et Biophysica Acta 1865 (2017) 726–739

[77] M. Shariatgorji, A. Nilsson, P. Källback, O. Karlsson, X. Zhang, P. Svenningsson, P.E. Andrén, Pyrylium salts as reactive matrices for MALDI-MS imaging of biologically active primary amines, J. Am. Soc. Mass Spectrom. 26 (2015) 934–939, http://dx.doi.org/10.1007/s13361-015-1119-9.

[78] M. Lagarrigue, R. Lavigne, E. Tabet, V. Genet, J.P. Thomé, K. Rondel, B. Guével, L. Multigner, M. Samson, C. Pineau, Localization and in situ absolute quantification of chlordecone in the mouse liver by MALDI imaging, Anal. Chem. 86 (2014) 5775–5783, http://dx.doi.org/10.1021/ac500313s.

[79] M. Shariatgorji, A. Nilsson, R.J.A. Goodwin, P. Källback, N. Schintu, X. Zhang, A.R. Crossman, E. Bezard, P. Svenningsson, P.E. Andrén, Direct targeted quantitative molecular imaging of neurotransmitters in brain tissue sections, Neuron 84 (2014) 697–707, http://dx.doi.org/10.1016/j.neuron.2014.10.011.

[80] D.A. Pirman, A. Kiss, R.M.A. Heeren, R.A. Yost, Identifying tissue-specific signal variation in MALDI mass spectrometric imaging by use of an internal standard, Anal. Chem. 85 (2013) 1090–1096, http://dx.doi.org/10.1021/ac3029618.

[81] D.A. Pirman, R.A. Yost, Quantitative tandem mass spectrometric imaging of endogenous acetyl-L-carnitine from piglet brain tissue using an internal standard, Anal. Chem. (2011) 8575–8581, http://dx.doi.org/10.1021/ac201949b.

[82] L. Jadoul, R. Longuespée, A. Noël, E. De Pauw, A spiked tissue-based approach for quantification of phosphatidylcholines in brain section by MALDI mass spectrometry imaging, Anal. Bioanal. Chem. 407 (2015) 2095–2106, http://dx.doi.org/10.1007/s00216-014-8232-7.

[83] P. Källback, M. Shariatgorji, A. Nilsson, P.E. Andrén, Novel mass spectrometry imaging software assisting labeled normalization and quantitation of drugs and neuropeptides directly in tissue sections, J. Proteome 75 (2012) 4941–4951, http://dx.doi.org/10.1016/j.jprot.2012.07.034.

[84] Z. Zhang, J. Kuang, L. Li, Liquid chromatography-matrix-assisted laser desorption/ionization mass spectrometry imaging with sprayed matrix for improved sensitivity, reproducibility and quantitation, Analyst 138 (2013) 6600–6606, http://dx.doi.org/10.1039/c3an01225e.

[85] E.J. Clemis, D.S. Smith, A.G. Camenzind, R.M. Danell, C.E. Parker, C.H. Borchers, Quantitation of spatially-localized proteins in tissue samples using MALDI-MRM imaging, Anal. Chem. 84 (2012) 3514–3522, http://dx.doi.org/10.1021/ac202875d.

[86] A. Thomas, P. Chaurand, Advances in tissue section preparation for MALDI imaging MS, Bioanalysis 6 (2014) 967–982, http://dx.doi.org/10.4155/bio.14.63.

[87] J.M. Fonville, C. Carter, O. Cloarec, J.K. Nicholson, J.C. Lindon, J. Bunch, E. Holmes, Robust data processing and normalization strategy for MALDI mass spectrometric imaging, Anal. Chem. 84 (2012) 1310–1319, http://dx.doi.org/10.1021/ac201767g.

[88] L. Tomlinson, J. Fuchser, A. Fütterer, M. Baumert, D.G. Hassall, A. West, P.S. Marshall, Using a single, high mass resolution mass spectrometry platform to investigate ion suppression effects observed during tissue imaging, Rapid Commun. Mass Spectrom. 28 (2014) 995–1003, http://dx.doi.org/10.1002/rcm.6869.

[89] J.G. Swales, J.W. Tucker, M.J. Spreadborough, S.L. Iverson, M.R. Clench, P.J.H. Webborn, R.J.A. Goodwin, Mapping drug distribution in brain tissue using liquid extraction surface analysis mass spectrometry imaging, Anal. Chem. 87 (2015) 10146–10152, http://dx.doi.org/10.1021/acs.analchem.5b02998.

[90] R.J.A. Goodwin, A. Nilsson, D. Borg, P.R.R. Langridge-Smith, D.J. Harrison, C.L. Mackay, S.L. Iverson, P.E. Andrén, Conductive carbon tape used for support and mounting of both whole animal and fragile heat-treated tissue sections for MALDI MS imaging and quantitation, J. Proteome 75 (2012) 4912–4920, http://dx.doi.org/10.1016/j.jprot.2012.07.006.

[91] R.J.A. Goodwin, P. Scullion, L. MacIntyre, D.G. Watson, A.R. Pitt, Use of a solvent-free dry matrix coating for quantitative matrix-assisted laser desorption ionization imaging of 4-bromophenyl-1,4-diazabicyclo(3.2.2)nonane-4-carboxylate in rat brain and quantitative analysis of the drug from laser microdissected tissue, Anal. Chem. 82 (2010) 3868–3873, http://dx.doi.org/10.1021/ac100398y.

[92] J. Bunch, M.R. Clench, D.S. Richards, Determination of pharmaceutical compounds in skin by imaging matrix-assisted laser desorption/ionisation mass spectrometry, Rapid Commun. Mass Spectrom. 18 (2004) 3051–3060, http://dx.doi.org/10.1002/rcm.1725.

[93] N. Takai, Y. Tanaka, K. Inazawa, H. Saji, Quantitative analysis of pharmaceutical drug distribution in multiple organs by imaging mass spectrometry, Rapid Commun. Mass Spectrom. 26 (2012) 1549–1556, http://dx.doi.org/10.1002/rcm.6256.

[94] K.M. Park, J.H. Moon, K.P. Kim, S.H. Lee, M.S. Kim, Relative quantification in imaging of a peptide on a mouse brain tissue by matrix-assisted laser desorption ionization, Anal. Chem. 86 (2014) 5131–5135, http://dx.doi.org/10.1021/ac500911x.

[95] J.A. Hankin, R.C. Murphy, Relationship between MALDI IMS intensity and measured quantity of selected phospholipids in rat brain sections, Anal. Chem. 82 (2010) 8476–8484, http://dx.doi.org/10.1021/ac101079v.

[96] H.Y.J. Wang, S.N. Jackson, J. McEuen, A.S. Woods, Localization and analyses of small drug molecules in rat brain tissue sections, Anal. Chem. 77 (2005) 6682–6686, http://dx.doi.org/10.1021/ac050868d.

[97] M.-J. Kang, A. Tholey, E. Heinzle, Quantitation of low molecular mass substrates and products of enzyme catalyzed reactions using matrix-assisted laser desorption/ionization time-of-flight mass spectrometry, Rapid Commun. Mass Spectrom. 14 (2000) 1972–1978, http://dx.doi.org/10.1002/1097-0231(20001115)14:21<1972::AID-RCM119>3.0.CO;2-5.

[98] A. Singh, V. Panchagnula, High throughput quantitative analysis of melamine and triazines by MALDI-TOF MS, Anal. Methods 3 (2011) 2360, http://dx.doi.org/10.1039/c1ay05262d.

[99] B. Prideaux, V. Dartois, D. Staab, D.M. Weiner, A. Goh, L.E. Via, C.E. Barry, M. Stoeckli, High-sensitivity MALDI-MRM-MS imaging of moxifloxacin distribution in tuberculosis-infected rabbit lungs and granulomatous lesions, Anal. Chem. 83 (2011) 2112–2118, http://dx.doi.org/10.1021/ac1029049.

[100] M.L. Reyzer, Y. Hsieh, K. Ng, W.A. Korfmacher, R.M. Caprioli, Direct analysis of drug candidates in tissue by matrix-assisted laser desorption/ionization mass spectrometry, J. Mass Spectrom. 38 (2003) 1081–1092, http://dx.doi.org/10.1002/jms.525.

[101] S.M. Boudon, G. Morandi, B. Prideaux, D. Staab, U. Junker, A. Odermatt, M. Stoeckli, D. Bauer, Evaluation of sparfloxacin distribution by mass spectrometry imaging in a phototoxicity model, J. Am. Soc. Mass Spectrom. 25 (2014) 1803–1809, http://dx.doi.org/10.1007/s13361-014-0947-3.

[102] H. Aikawa, M. Hayashi, S. Ryu, M. Yamashita, N. Ohtsuka, M. Nishidate, Y. Fujiwara, A. Hamada, Visualizing spatial distribution of alectinib in murine brain using quantitative mass spectrometry imaging, Sci. Rep. 6 (2016) 23749, http://dx.doi.org/10.1038/srep23749.

[103] C.M. Quiason, S.K. Shahidi-Latham, Imaging MALDI MS of dosed brain tissues utilizing an alternative analyte pre-extraction approach, J. Am. Soc. Mass Spectrom. 26 (2015) 967–973, http://dx.doi.org/10.1007/s13361-015-1132-z.

[104] M. Poetzsch, A.E. Steuer, A.T. Roemmelt, M.R. Baumgartner, T. Kraemer, Single hair analysis of small molecules using MALDI-triple quadrupole MS imaging and LC-MS/MS: Investigations on opportunities and pitfalls, Anal. Chem. 86 (2014) 11758–11765, http://dx.doi.org/10.1021/ac503193w.

[105] S. Schulz, D. Gerhardt, B. Meyer, M. Seegel, B. Schubach, C. Hopf, K. Matheis, DMSO-enhanced MALDI MS imaging with normalization against a deuterated standard for relative quantification of dasatinib in serial mouse pharmacology studies, Anal. Bioanal. Chem. 405 (2013) 9467–9476, http://dx.doi.org/10.1007/s00216-013-7393-0.

[106] T. Porta, C. Grivet, T. Kraemer, E. Varesio, G. Hopfgartner, Single hair cocaine consumption monitoring by mass spectrometric imaging, Anal. Chem. 83 (2011) 4266–4272, http://dx.doi.org/10.1021/ac200610c.

[107] T. Nakanishi, S. Takai, D. Jin, T. Takubo, Quantification of candesartan in mouse plasma by MALDI-TOFMS and in tissue sections by maldi-imaging using the stable-isotope dilution technique, Mass Spectrom. 2 (2013) A0021, http://dx.doi.org/10.5702/massspectrometry.A0021.

[108] D.A. Pirman, R.F. Reich, A. Kiss, R.M.A. Heeren, R.A. Yost, Quantitative MALDI tandem mass spectrometric imaging of cocaine from brain tissue with a deuterated internal standard, Anal. Chem. 85 (2013) 1081–1089, http://dx.doi.org/10.1021/ac302960j.

[109] N. Sun, A. Walch, Qualitative and quantitative mass spectrometry imaging of drugs and metabolites in tissue at therapeutic levels, Histochem. Cell Biol. 140 (2013) 93–104, http://dx.doi.org/10.1007/s00418-013-1127-4.

[110] R.R. Landgraf, T.J. Garrett, M.C.P. Conaway, N.A. Calcutt, P.W. Stacpoole, R.A. Yost, M.C. Prieto Conaway, Considerations for quantification of lipids in nerve tissue using matrix-assisted laser desorption/ionization mass spectrometric imaging, Rapid Commun. Mass Spectrom. 25 (2011) 3178–3184, http://dx.doi.org/10.1002/rcm.5189.

[111] N. Hosokawa, Y. Sugiura, M. Setou, Spectrum normalization method using an external standard in mass spectrometric imaging, J. Mass Spectrom. Soc. Jpn. 56 (2008) 77–81, http://dx.doi.org/10.5702/massspec56.77.

[112] T.C. Rohner, D. Staab, M. Stoeckli, MALDI mass spectrometric imaging of biological tissue sections, Mech. Ageing Dev. 126 (2005) 177–185, http://dx.doi.org/10.1016/j.mad.2004.09.032.

[113] M. Stoeckli, D. Staab, M. Staufenbiel, K.-H. Wiederhold, L. Signor, Molecular imaging of amyloid beta peptides in mouse brain sections using mass spectrometry, Anal. Biochem. 311 (2002) 33–39 (doi:S0003269702003886X).

[114] L.A. McDonnell, A. Römpp, B. Balluff, R.M.A. Heeren, J.P. Albar, P.E. Andrén, G.L. Corthals, A. Walch, M. Stoeckli, Discussion point: reporting guidelines for mass spectrometry imaging, Anal. Bioanal. Chem. 407 (2015) 2035–2045, http://dx.doi.org/10.1007/s00216-014-8322-6.

[115] R.F. Reich, K. Cudzilo, J.A. Levisky, R.A. Yost, Quantitative MALDI-MSn analysis of cocaine in the autopsied brain of a human cocaine user employing a wide isolation window and internal standards, J. Am. Soc. Mass Spectrom. 21 (2010) 564–571, http://dx.doi.org/10.1016/j.jasms.2009.12.014.

[116] C.W. Chumbley, M.L. Reyzer, J.L. Allen, G.A. Marriner, L.E. Via, C.E. Barry, R.M. Caprioli, Absolute quantitative MALDI imaging mass spectrometry: a case of rifampicin in liver tissues, Anal. Chem. 88 (2016) 2392–2398, http://dx.doi.org/10.1021/acs.analchem.5b04409.

[117] M. Stoeckli, D. Staab, A. Schweitzer, Compound and metabolite distribution measured by MALDI mass spectrometric imaging in whole-body tissue sections, Int. J. Mass Spectrom. 260 (2007) 195–202, http://dx.doi.org/10.1016/j.ijms.2006.10.007.

[118] G. Hamm, D. Bonnel, R. Legouffe, F. Pamelard, J.M. Delbos, F. Bouzom, J. Stauber, Quantitative mass spectrometry imaging of propranolol and olanzapine using tissue extinction calculation as normalization factor, J. Proteome 75 (2012) 4952–4961, http://dx.doi.org/10.1016/j.jprot.2012.07.035.

[119] M. Aichler, K. Huber, F. Schilling, F. Lohöfer, K. Kosanke, R. Meier, E.J. Rummeny, A. Walch, M. Wildgruber, Spatially resolved quantification of gadolinium(III)-based magnetic resonance agents in tissue by MALDI imaging mass spectrometry after in vivo MRI, Angew. Chem. Int. Ed. 54 (2015) 4279–4283, http://dx.doi.org/10.1002/anie.201410555.

[120] D.J. Hare, J. Lear, D. Bishop, A. Beavis, P.A. Doble, Protocol for production of matrix-matched brain tissue standards for imaging by laser ablation-inductively coupled plasma-mass spectrometry, Anal. Methods 5 (2013) 1915–1921, http://dx.doi.org/10.1039/c3ay26248k.

[121] J. Soltwisch, H. Kettling, S. Vens-Cappell, M. Wiegelmann, J. Muthing, K. Dreisewerd, Mass spectrometry imaging with laser-induced postionization, Science 348 (2015) 211–215, http://dx.doi.org/10.1126/science.aaa1051.

[122] P. Chaurand, Introducing specificity and sensitivity in imaging MS, Bioanalysis 7 (2015) 2279–2281, http://dx.doi.org/10.4155/bio.15.160.

[123] P. Källback, A. Nilsson, M. Shariatgorji, P.E. Andrén, msIQuant – quantitation software for mass spectrometry imaging enabling fast access, visualization and

analysis of large data sets, Anal. Chem. 88 (2016) http://dx.doi.org/10.1021/acs.analchem.5b04603.

[124] G. Robichaud, K.P. Garrard, J.A. Barry, D.C. Muddiman, MSiReader: an open-source interface to view and analyze high resolving power MS imaging files on matlab platform, J. Am. Soc. Mass Spectrom. 24 (2013) 718–721, http://dx.doi.org/10.1007/s13361-013-0607-z.

[125] ICH, ICH topics Q2 (R1) validation of analytical procedures: text and methodology, http://www.ich.org/fileadmin/Public_Web_Site/ICH_Products/Guidelines/Quality/Q2_R1/Step4/Q2_R1__Guideline.pdf2006.

[126] EMA, Guideline on bioanalytical method validation, http://www.ema.europa.eu/docs/en_GB/document_library/Scientific_guideline/2011/08/WC500109686.pdf2011.

[127] Food and Drug Administration, Guidance for industry: bioanalytical method validation, http://www.fda.gov/downloads/drugs/guidancecomplianceregulatory-information/guidances/ucm368107.pdf2001.

[128] P. Timmerman, N. Mokrzycki, P. Delrat, M. De Meulder, E. Erbach, I. Lentheric, M. McIntosh, P. Dzygiel, Recommendations from the European Bioanalysis Forum on method establishment for tissue homogenates, Bioanalysis 6 (2014) 1647–1656, http://dx.doi.org/10.4155/bio.14.34.

[129] V.P. Shah, K.K. Midha, J.W.A. Findlay, H.M. Hill, J.D. Hulse, I.J. Mcgilveray, G. Mckay, K.J. Miller, R.N. Patnaik, M.L. Powell, A. Tonelli, C.T. Viswanathan, Bioanalytical Method Validation - A Revisit With a Decade of Progress, 17, 2000.

Publication 2

MALDI mass spectral imaging of bile acids observed as deprotonated molecules and proton-bound dimers from mouse liver sections

Ignacy Rzagalinski, Nadine Hainz, Carola Meier, Thomas Tschernig and Dietrich A. Volmer

Publication 2
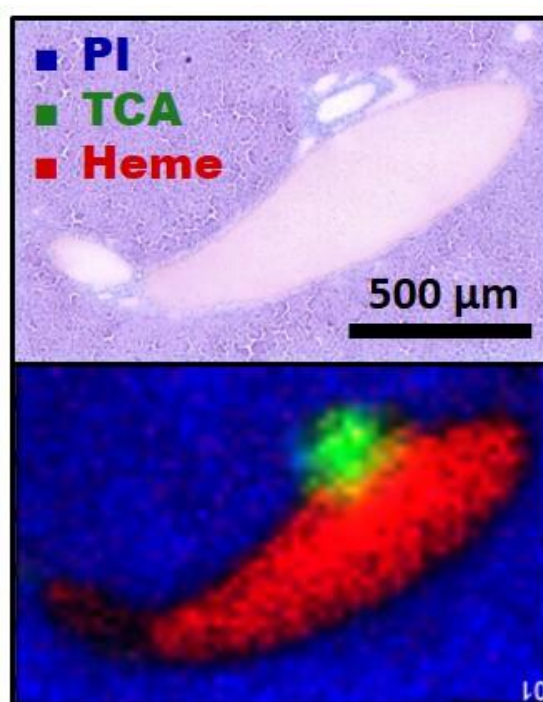
RESEARCH ARTICLE

MALDI Mass Spectral Imaging of Bile Acids Observed as Deprotonated Molecules and Proton-Bound Dimers from Mouse Liver Sections

Ignacy Rzagalinski,[1] Nadine Hainz,[2] Carola Meier,[2] Thomas Tschernig,[2] Dietrich A. Volmer[1,3]

[1]Institute of Bioanalytical Chemistry, Saarland University, 66123, Saarbrücken, Germany
[2]Institute of Anatomy and Cell Biology, Saarland University, 66421, Homburg, Germany
[3]Department of Chemistry, Humboldt University of Berlin, 12489, Berlin, Germany
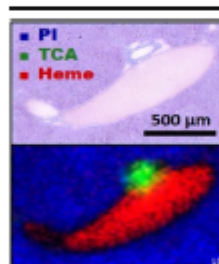
Abstract. Bile acids (BAs) play two vital roles in living organisms, as they are involved in (1) the secretion of cholesterol from liver, and (2) the lipid digestion/absorption in the intestine. Abnormal bile acid synthesis or secretion can lead to severe liver disorders. Even though there is extensive literature on the mass spectrometric determination of BAs in biofluids and tissue homogenates, there are no reports on the spatial distribution in the biliary network of the liver. Here, we demonstrate the application of high mass resolution/mass accuracy matrix-assisted laser desorption/ ionization (MALDI)-Fourier-transform ion cyclotron resonance (FTICR) to MS imaging (MSI) of BAs at high spatial resolutions (pixel size, 25 µm). The results show chemical heterogeneity of the mouse liver sections with a number of branching biliary and blood ducts. In addition to ion signals from deprotonation of the BA molecules, MALDI-MSI generated several further intense signals at larger m/z for the BAs. These signals were spatially co-localized with the deprotonated molecules and easily misinterpreted as additional products of BA biotransformations. In-depth analysis of accurate mass shifts and additional electrospray ionization and MALDI-FTICR experiments, however, confirmed them as proton-bound dimers. Interestingly, dimers of bile acids, but also unusual mixed dimers of different taurine-conjugated bile acids and free taurine, were identified. Since formation of these complexes will negatively influence signal intensities of the desired [M − H] ions and significantly complicate mass spectral interpretations, two simple broadband techniques were proposed for non-selective dissociation of dimers that lead to increased signals for the deprotonated BAs.

Keywords: Mass spectrometry imaging, MALDI, FTICR, Bile acids, Taurocholic acid, Taurine, Proton-bound dimers, Adducts

Introduction

Bile acids (BAs) are an integral part of the digestive system of living organisms, where they play two essential roles: firstly, they are synthesized from cholesterol in the liver hepatocytes and this process maintains cholesterol homeostasis. Secondly, bile acids in their conjugated forms ("bile salts")

participate in digestion and absorption of lipids and lipid soluble compounds (e.g., vitamins) in the intestine [1]. Interestingly, difference of bile acids composition exist between vertebrates, which makes this an interesting biochemical trait not only from an evolutionary biology point of view, but also from a biomedical perspective [2]. For example, recent reports have shown a link between characteristic BA composition in mice and their resistance to high fat diet-induced obesity and diabetes [3–5]. In contrast to these beneficial effects, some bile acids (e.g., litocholic acid) are considered toxic endobiotics [6]. Moreover, abnormalities in BA synthesis (which is tightly controlled by 17 different enzymes) as well as secretion processes can lead to development of serious

Correspondence to: Dietrich Volmer; *e-mail:* dietrich.volmer@hu-berlin.de

diseases, including bile acid (inborn) synthesis disorder and primary biliary cholangitis [7–9]. Furthermore, accumulation of BAs in undesirable organs/tissues causes oxidative/nitrosative stress, damages of DNA and cell apoptosis [10–12].

The complex biosyntheses of primary bile acids in liver hepatocytes results in large structural diversity of endogenous metabolites. In addition, secondary bile acids are formed in the colon as a result of bacterial action, and some of them re-enter hepatic circulation (enterohepatic recirculation) [13]. In mammals, bile composition is almost exclusively limited to compounds consisting of 24 carbon atoms; that is, acidic steroids with typical four-ring steroid core and C-5 side chain (Figure 1a). They differ in the number and position of hydroxyl groups attached to the rings and also include epimers, for example, muricholic acid (characteristic for mice) with four

a

b

Bile Acid	Abbreviation	R_1	R_2	R_3	R_4	
Unconjugated bile acids						
Cholic	CA	H	α-OH	α-OH	OH	
Chenodeoxycholic	CDCA	H	α-OH	H	OH	
α-Muricholic	αMCA	β-OH	α-OH	H	OH	Primary BAs
β-Muricholic	βMCA	β-OH	β-OH	H	OH	
γ-Muricholic	γMCA	α-OH	α-OH	H	OH	
ω-Muricholic	ωMCA	α-OH	β-OH	H	OH	
Tetrahydroxy-BA	THBA	α-OH	α-OH	α-OH	OH	
Deoxycholic	DCA	H	H	α-OH	OH	
Litocholic	LCA	H	H	H	OH	
Murideoxycholic	MDCA	β-OH	H	H	OH	Secondary BAs
Hyodeoxycholic	HDCA	α-OH	H	H	OH	
Ursodeoxycholic	UDCA	H	β-OH	H	OH	
Conjugated bile acids						
Taurinated-BAs	T...	"	"	"	NH-(CH$_2$)$_2$-SO$_3$H	
Glycinated-BAs	G...	"	"	"	NH-CH$_2$-COOH	

Figure 1. (a) Typical four-ring steroid structures of 24-carbon bile acids, including differences in number and positions of hydroxyl groups (R_1-R_3) as well as N-amide conjugation (R_4). (b) Most common non-conjugated bile acids present in humans and rodents, with the different positions of hydroxyl groups as well as two major conjugation types

different combinations of two hydroxyl groups attached to C-6 and C-7 positions. In addition, unconjugated BAs undergo further biotransformation routes, from which the most important is N-acyl amidation with taurine or glycine at C-24. Moreover, conjugations at C-3, C-6, or C-7 include sulfation, glucuronidation, glucosidation, and N-acetylglucosaminidation [14, 15]. The nomenclature of bile acids was developed by Hoffman et al. [16] (Figure 1 summarizes structures and abbreviations of the most common human and mouse bile acids). There is a large group of intermediate products of 24 carbon bile acids containing a keto group at C-3 (oxo-BAs) and/or unsaturated double bonds at C-4 or C-6. The latter were used as potential biomarkers of pathological change in severe liver diseases [7, 10].

All these processes combined with recent findings presenting bile acids as pleiotropic signaling molecules [17, 18] require powerful analytical assays to fully decipher the complete molecular signatures of BAs in different biological matrices and link them to the pathology of the corresponding disease. As a result, MS-based techniques have been the primary analytical tools for bile acid characterization over the last few decades. Initially, fast-atom bombardment (FAB) was often implemented, delivering mostly deprotonated molecules for BAs in negative ion mode. FAB was frequently used with double focusing magnetic sector instruments, which allowed high-energy collisions (>1 keV) and subsequent dissociation of the steroid backbone via charge-remote fragmentation (CRF) [19, 20]. Of note, conjugation through N-acyl amidation of the side chain has two practical implications for BAs. Firstly, it increases acidity (e.g., pK_a of TCA ~1.5 versus CA ~4.5) and thus improves ionization efficiency. Secondly, it enlarges cross-sections for CRF, resulting in intense and informative MS/MS spectra. This phenomenon was used to improve FAB-MS of bile acids after derivatization with taurine or other aminosulphonates [21, 22]. Other ionization techniques were also used, including thermospray [23, 24], atmospheric pressure chemical ionization [25–28] – both coupled to liquid chromatography – and electron ionization after derivatization/separation by gas chromatography [29, 30]. Today, matrix-assisted laser desorption/ionization (MALDI) and electrospray ionization (ESI) dominate analysis of BAs [31]. Particularly LC-ESI-MS/MS is the method of choice for analysis from different biological samples such as biofluids (urine, bile, plasma/serum) [32–34] and liver tissue homogenates [35, 36]. Efficient LC separation is vital, as LC-MS/MS instruments usually only provide low energy collision induced dissociation (CID) (0–100 eV), with less structure-informative spectra as high-energy CID [19]. In contrast to ESI, MALDI has not been extensively applied to analysis of BAs, except for the quantification of bile acids in urine and plasma [37, 38] and for MALDI imaging of taurocholic acid in a murine model of polycystic kidney disease [39]. Mass spectrometry imaging (MSI), however, which combines detailed molecular characterization with spatial distribution measurements, has not yet been applied for determining spatial distribution of BAs in mouse liver biliary networks, which is the main purpose of

the present work. In addition, we were concerned with unusual adducts observed during MALDI-MSI analysis of bile acids.

Adduct formation is common in mass spectrometry and adducts often seriously complicate mass spectral interpretation [40]; sometimes they enhance detection when deliberately formed (e.g., lithium adducts of phospholipids [41] or silver adducts of cholesterol [42]). Interestingly, gas-phase ESI or MALDI adducts are often stable in positive ion mode. Anion adducts, however, often do not survive the MALDI process, which is attributed to the larger amount of energy transferred to the desorbed molecules upon ionization [43, 44]. A particular type of ionic cluster is the proton-bound dimer (PBD), which consists of the same (=homodimer) or different (=heterodimer) species (ions or neutrals). Their weak hydrogen bonding was used as principle of the *kinetic method*, which was developed by Cook and coworkers [45–47] and later refined, e.g., by the Fenselau group [48, 49]. In this method, ESI combined with CID of m/z-selected PBD is used to determine relative proton affinities (PA) of ions contributing to the isolated cluster. Bile acids were investigated by this method and exhibited different MS/MS spectra, depending on the PA of the contributing ions [50, 51].

The present work reports on proton-bound dimers formed during MALDI and the extensive presence of these clusters from endogenous tissue metabolites in MSI. Specifically, we describe application of high resolution FTICR-MS at high MALDI-MSI spatial resolving powers (25 μm) for bile acids in the biliary network of mouse liver sections and demonstrate identification of taurine-conjugated bile acids directly from tissue sections and formation of proton-bound dimers of different bile acids and taurine.

Experimental

Materials and Reagents

Taurine (99%), 9-aminoacridine (9-AA, 99.5%), ethanol (HPLC grade) and standard microscopic glass slides were purchased from Sigma-Aldrich (Steinheim, Germany). Taurocholic acid (sodium salt, 95%) was from Biomol GmbH (Hamburg, Germany), and potassium chloride (99.5%) from Gruessing GmbH (Filsum, Germany). Purified water was generated by a Millipore (Bedford, MA, USA) purification system.

Animals and Tissue Preparation

All animal experiments were performed in accordance with international regulations and permission from the local research ethics committee (Saarland Government TVV 27/2014). Female C57BL/6 mice (12-wk) were purchased (Charles River, Sulzbach, Germany). The animals were anesthetized with xylazine/ketamine and organs were dissected immediately after sacrifice, snap-frozen in liquid N_2, and stored at –80 °C until the sample preparation process. The longitudinal mouse liver sections were prepared at 12 μm thicknesses using a

Reichert Jung 2800 Frigocut cryostat microtome (Leica Microsystems, Wetzlar, Germany), thaw-mounted onto the plain microscope glass slides, and dried for 30 min in a vacuum desiccator. The tissues were then stored at –80 °C prior to mass spectrometry imaging experiment.

MALDI Matrix Deposition and Evaluation of its Quality

The MALDI matrix 9-aminoacridine was chosen in this study because of its ability to efficiently ionize acidic compounds in negative ion mode, including bile acids [37–39]. A solution of 9-AA (5 mg/mL) was freshly prepared in ethanol/water (70/30 [v/v]) prior to deposition. Matrix was applied on top of the tissue sections using a home-built automatic sprayer, based on the Probot micro fraction collector (Thermo Scientific, Germering, Germany) and MicroIonSpray nebulizing nozzle (Sciex, Concord, ON, Canada). Fused silica spray capillaries (Molex Polymicro Technologies, USA) of several different internal diameters were tested with respect to homogeneity of matrix layers, crystal sizes, and resistance to clogging during the longer spraying process. Eventually, the capillaries of 200 μm internal diameter were chosen as they provided optimum performance. The nozzle height was 44 mm, distance between the lines was 3 mm, and the movement speed was 199.25 mm/min along the y-axis in a meandering pattern. For final imaging experiments, seven layers of 9-AA were sprayed with increasing flow rate in the following pattern: two layers at 20 μL/min and five layers at 40 μL/min. From these experiments, the estimated amount of matrix added to the tissue (=matrix density) was calculated at 0.0201 mg/mm². Eventually, in-depth visual inspection of the obtained 9-AA layers was carried out using optical and scanning electron (SEM) microscope images, which revealed high homogeneity and reproducibility as well as crystal sizes down to 1 μm (Figure S1, Supplementary Material).

Mass Spectrometry and Data Analysis

MALDI imaging, MALDI and ESI experiments were performed in negative ion mode on a Bruker (Bremen, Germany) 7 Tesla Solarix FTICR mass spectrometer, equipped with a dual ESI/MALDI ion source and Smartbeam II Nd:YAG (355 nm) laser. MALDI imaging data were collected from m/z 50 to 2000 with a transient length of ~0.5 s and resolving power (FWHM) of ~90,000 at m/z 400. Internal mass calibration was performed using a series of peaks originating from MALDI matrix and endogenous compounds. Two different MSI pixel size settings were used: 70 μm for low spatial resolution imaging of the whole liver section and 25 μm for the high spatial resolution imaging of selected sub-regions of the adjacent tissue section. This particular approach was chosen because of analysis time considerations. The run time for the whole liver section at the larger raster step size of 70 μm was ca. 8 h (approximately 22,000 single points). The same whole section imaged at 25 μm would have required ~189,000 points, with an estimated total run time exceeding 63 h. Selecting the

smaller regions of interest for imaging at high spatial resolution, however, allowed us to keep the single experiment analysis within a few hours. For low resolution experiments, the laser was set to the "small" spot size, laser power to 20%, number of laser shots/pixel to 100, and frequency to 1 kHz. For high spatial resolution experiments, different laser settings were tested with respect to signal intensities as well as to ablated area, assuring dense pixel deposition and avoiding overlap between neighboring laser spots (Figure S2, Supplementary Material). As a result of these optimization experiments, the optimal laser settings were set to "minimum" spot size, laser power to 10%, number of laser shots/pixel to 200, and frequency to 1 kHz. MALDI experiments with standards were carried out by using dried-droplet sample preparation and spotting onto steel MALDI target plates (Bruker). ESI was performed using direct infusion using the instrument's syringe pump at 2 μL/min. All MS/MS experiments were performed by isolation of precursor ions in the external quadrupole (isolation window: 3–5 u) and accumulation in the hexapole for collision-induced dissociation (CID) at varying collision energies (5–55 V). Data were processed and analyzed using the Bruker Data Analysis and FlexImaging software for single mass spectra and imaging data sets, respectively. Mass spectral interpretations were conducted using the METLIN and LIPID MAPS databases to match the accurate masses of the precursor ions, and by manually interpreting MS/MS fragmentation patterns and comparing with standards. MS images were normalized to the deprotonated 9-AA signal, which was previously described as an efficient normalization routine when isotope labeled internal standards are not available [52–55]. This approach was chosen here over the more common TIC and RMS routines because both TIC and RMS caused unrealistic enhancements of ion yields in our MSI data sets (data not shown). Such artifacts, in particular for signals of high intensity in certain regions, which comply well with the histological structures of heterogeneous tissues, have previously been described by Deininger et al. [56].

Histological Staining and Optical Microscopy

After MALDI-MSI measurements, the glass slides were gently washed with 70% ethanol to remove the matrix. The tissue sections were stained with hematoxylin and eosin (H&E) as follows: glass slides were dipped in 100% ethanol at –20 °C for 5 min, followed by distilled water for 2 min. The slides were then immersed in Ehrlich's hematoxylin (Carl Roth, Karlsruhe, Germany) for 5 min, washed with deionized water, followed by bluing in running tap water for 10 min. Staining by eosin (Carl Roth) for 10 s was followed by a wash with deionized water. Slides were then dipped in 80% ethanol for 3 min, 90% ethanol for 6 min, and 100% ethanol for 2 × 5 min, followed by placing them in three different xylene (VWR, Darmstadt, Germany) baths for 5 min each. Finally, slides were cover slipped using mounting medium Roti-Histokitt (Carl Roth GmbH, Karlsruhe, Germany). The stained tissue sections were scanned using an

Olympus dotslide optical microscope with an UPLANSAPO 40x/0.90 objective (Olympus, Tokyo, Japan).

Results and Discussion

On-Tissue Identification of Taurine Conjugated Bile Acids

Because of the chemical complexity of the bile acid lipid class, high resolution/high accuracy MALDI-FTICR was employed to identify the molecules directly from mouse liver sections. In the first step, interpretation of the average as well as single pixel mass spectra from the MSI experiment was performed and annotated m/z values (mass uncertainty, ±3 ppm) within the bile duct and gall bladder regions were interrogated using the METLIN (http://metlin.scripps.edu) and LIPID MAPS (http://www.lipidmaps.org) databases. Tentative identifications were compared with an existing study of LC-MS/MS analysis of mouse bile, plasma, and liver tissue homogenates [32–34]. In the second step, CID experiments were performed directly on-tissue (bile duct and/or gall bladder regions) and MS/MS spectra manually interpreted.

A representative MALDI mass spectrum extracted from a single pixel (bile duct region) of the MSI experiment is shown in Figure 2a. The measured accurate m/z of the base peak at m/z 514.2836 (center panel) matched that of the $[M - H]^-$ ion of a compound with molecular formula $C_{26}H_{45}NO_7S$ (exact mass, m/z 514.2844), which in turn was assigned to taurocholic acid (TCA) or one of the epimers of tauromuricholic acid (α-, β-, γ-, or ω-TMCA, Figure 1). In addition, two other important signals were found. Firstly, m/z 498.2904 (top panel) was assigned a molecular formula of $C_{26}H_{45}NO_6S$ and tentatively identified as taurochenodeoxycholic acid (TCDCA); secondly, m/z 530.2789 (bottom panel) was assigned the formula $C_{26}H_{45}NO_8S$ and tentatively identified as taurotetrahydroxycholic acid (TTHBA). The molecular formulae differed by 16 u (one oxygen), thus representing the taurine conjugates of primary bile acids containing two, three, and four hydroxyl groups at the steroid cores. CID experiments of each species (Figure 2b and c) revealed characteristic fragment ions at m/z 124 ($C_2H_6NO_3S^-$) and m/z 107 ($C_2H_3O_3S^-$), resulting from cleavages from the taurine conjugated side chain. In addition, two further meaningful fragment ions were observed, originating from neutral losses of taurine and a single water molecule (m/z 355.2648) or taurine and two water molecules (m/z 353.2486), which are characteristic diagnostic ions for dihydroxy and trihydroxy BAs [31, 57]. Of note, MS/MS-based distinction between the two individual isomers of trihydroxy bile acids (TCA and TMCA) was not possible with the implemented instrument, as only low-energy CID was available, which does not provide isomer-specific ions for the two species. However, based on quantitative data for the isomers shown in previous LC-MS/MS studies of bile acids in mouse gall bladder and liver, we assume that both isomers contribute to the ion abundance at m/z 514.3 [5, 33]. Potential isomer
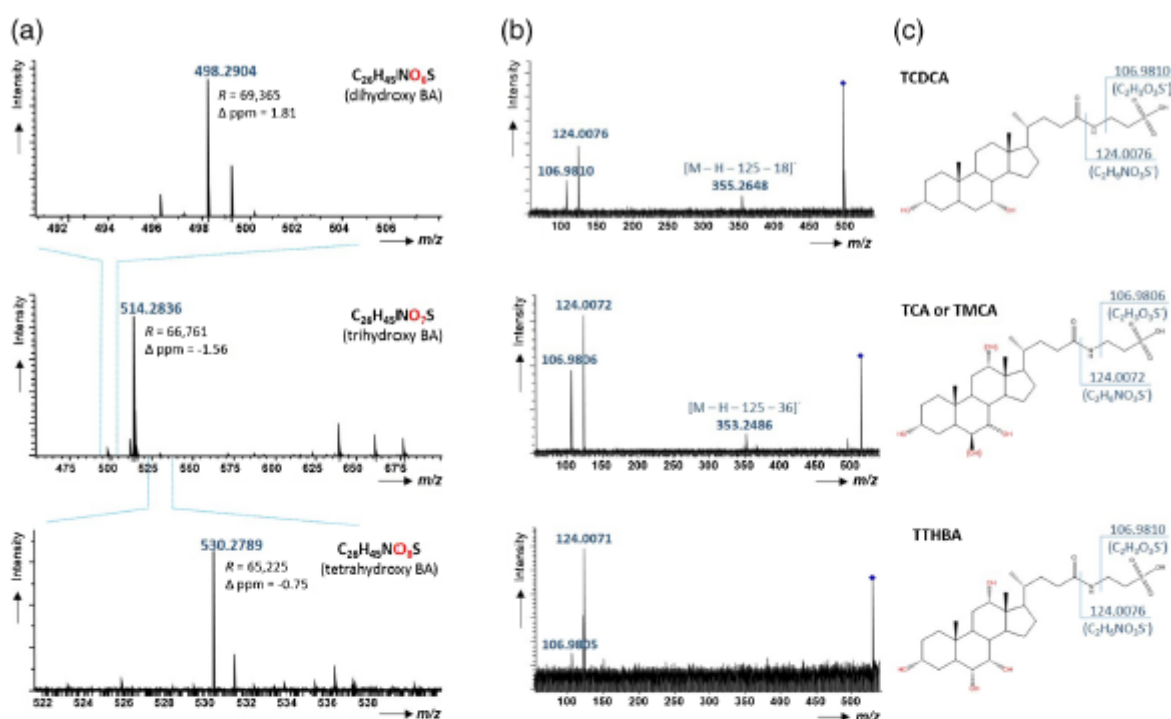
Figure 2. **(a)** MSI single pixel mass spectrum for the m/z range 450–700 (center), with two smaller expanded m/z range: m/z 492–508 (top) and m/z 522–540 (bottom), showing signals from deprotonated molecules of trihydroxy, dihydroxy, and tetrahydroxy bile acids, respectively. **(b)** CID mass spectra of three identified BAs, confirming taurine-conjugated side chains, obtained after isolation in the quadrupole and dissociation in the hexapole collision cell at energies of 50, 55, and 50 eV for dihydroxy, trihydroxy, and tetrahydroxy BAs, respectively. **(c)** Structures of the three identified BAs (TCA and TMCA isomers are both shown, as distinction was not possible with the present method)

contributions will be investigated in the future by utilizing ion mobility separation after MALDI.

High Spatial Resolution MALDI-FTICR Imaging of BAs in Mouse Liver Sections

Even though liver is often considered to be a homogenous tissue in MSI studies, it is in fact a highly vascularized organ [58]. The relatively homogenous parenchymal tissue consisting of the hepatocytes is highly permeated by branching biliary and blood vessels. Bile acids are synthesized in the hepatic lobules of liver parenchyma and, following conjugation with taurine (mice) or taurine and glycine (humans), they are secreted to the gall bladder through a branching network of bile canaliculi, canals of Hering, and different size bile ducts, which together create the characteristic biliary tree [58–60]. Here, we used MALDI-MSI to investigate molecular profiles and branching patterns of the mouse intrahepatic biliary tree at high lateral resolutions (pixel size, 25 µm). In addition to the single ion images of different bile acids, we also provide molecular differentiation between bile ducts, blood vessels and hepatic parenchymal tissue from a single tissue section, based on the

RGB ion images of three different compounds serving as the molecular surrogate markers of the three regions.

The spatial distributions of the three taurine-conjugated bile acids discussed above are shown in Figure 3. All ion images are created based on the signals from the deprotonated molecules: TCDCA at m/z 498.2904 ± 0.05, TCA/TMCA at m/z 514.2836 ± 0.05, and TTHBA at m/z 530.2789 ± 0.05. The raster width was 70 µm for whole tissue sections (Figure 3a) and 25 µm for selected smaller sub-regions of adjacent sections (Figure 3b–d). All three bile acids were clearly co-localized, correlating well with the anatomical features of bile ducts revealed by the H&E-stained images, and clearly showing the branching network of the biliary tree in the high spatial resolution images (Figure 3b). From a comparison of the relative signal intensities (normalized to 9-AA matrix signal), we determined TCA/TMCA as the most abundant investigated component of bile, and TTHBA as lowest abundant molecule. In addition, the highest intensity of all three BAs was found in the gall bladder (green arrow on the H&E image, Figure 3), which serves as storage reservoir for a concentrated bile [59, 61]. These findings are in good agreement with previously published quantitative LC-MS/MS reports [35, 36].
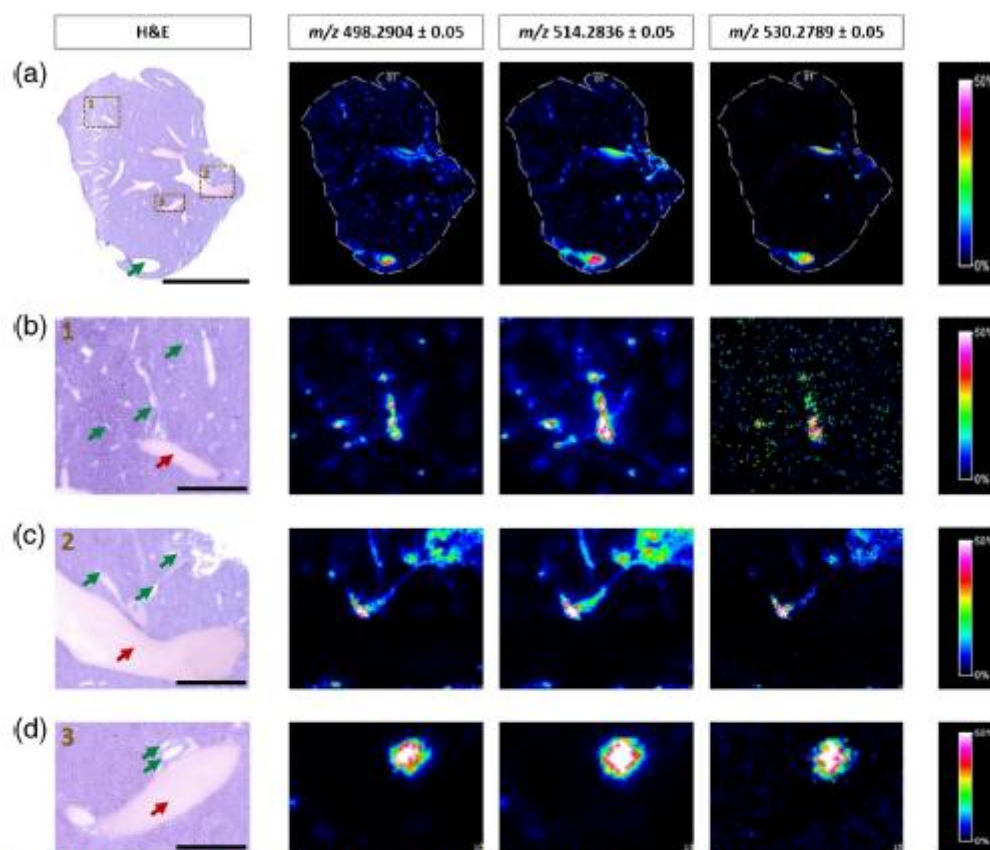
Figure 3. MS ion images representing spatial distributions of the identified taurine-conjugated bile acids at m/z 498.2904 ± 0.05 (TCDCA), m/z 514.2836 ± 0.05 (TCA/TMCA), and m/z 530.2789 ± 0.05 (TTHBA) for the whole section of mouse liver at low spatial resolution (pixel size, 70 μm) **(a)**, and in smaller sub-regions of an adjacent tissue section at high spatial resolution (pixel size, 25 μm) **(b–d)**. All ion images were normalized to the 9-AA matrix signal. The green arrows indicate gall bladder **(a)** or bile vessels **(b–d)**, whereas the red arrows show blood vessels. Scale bars: 5 mm **(a)**, 1000 μm **(b, c)**, and 500 μm **(d)**

In addition to determining spatial distribution of selected bile acids in liver sections, the MALDI-MSI method also enabled us to perform molecular fingerprinting of mouse liver microstructures. As seen in Figure 4a, three different regions can be distinguished based on the mass spectra collected from these areas: bile ducts, blood vessels, and liver parenchymal tissue. Furthermore, distinct molecular histology images can be readily obtained by selecting three different deprotonated molecules: m/z 514.2836 ± 0.05 (TCA/TMCA), 615.1703 ± 0.05 (heme B), and 885.5492 ± 0.05 (PI (18:0/20:4)), serving as surrogate molecular markers of the above-mentioned regions. Using these marker ions, Figure 4b, c illustrate RGB ion images of the whole section and the expanded regions (at spatial resolution of 70 μm) that reveal excellent correlation with the anatomical features of H&E-stained tissue images. Moreover, to emphasize the importance of imaging at higher spatial resolutions (at pixel size of 25 μm), the smaller bile ducts located in the proximity of larger blood vessels are presented in Figure 4d, e. In these experiments, the bile acids were detected even in the ducts of small diameters such as 50–

100 μm, which demonstrates the great potential of the method for studying human liver samples, including the molecular visualization of interlobular and, with further improvement of lateral resolution, the intralobular bile ducts. Of note, our experiments and results showed a minor tendency to delocalization of bile, during cryosectioning, thaw-mounting, and/or matrix spraying, even though a tightly controlled sample preparation protocol was used (see Experimental). While completely eliminating delocalization from the first two processes can be difficult (if not impossible), solvent-free matrix deposition such as dry-coating or sublimation can avoid delocalization from matrix spraying. Such an approach will be crucial in the next stage of our work, where we investigate images of smaller features of the biliary network.

Proton-Bound Dimers of Bile Acids and Taurine

Several recent LC-MS/MS studies have reported the identification of a wide range of bile acids in liver and bile samples [33, 34, 62]. We interrogated our MSI data sets for these and
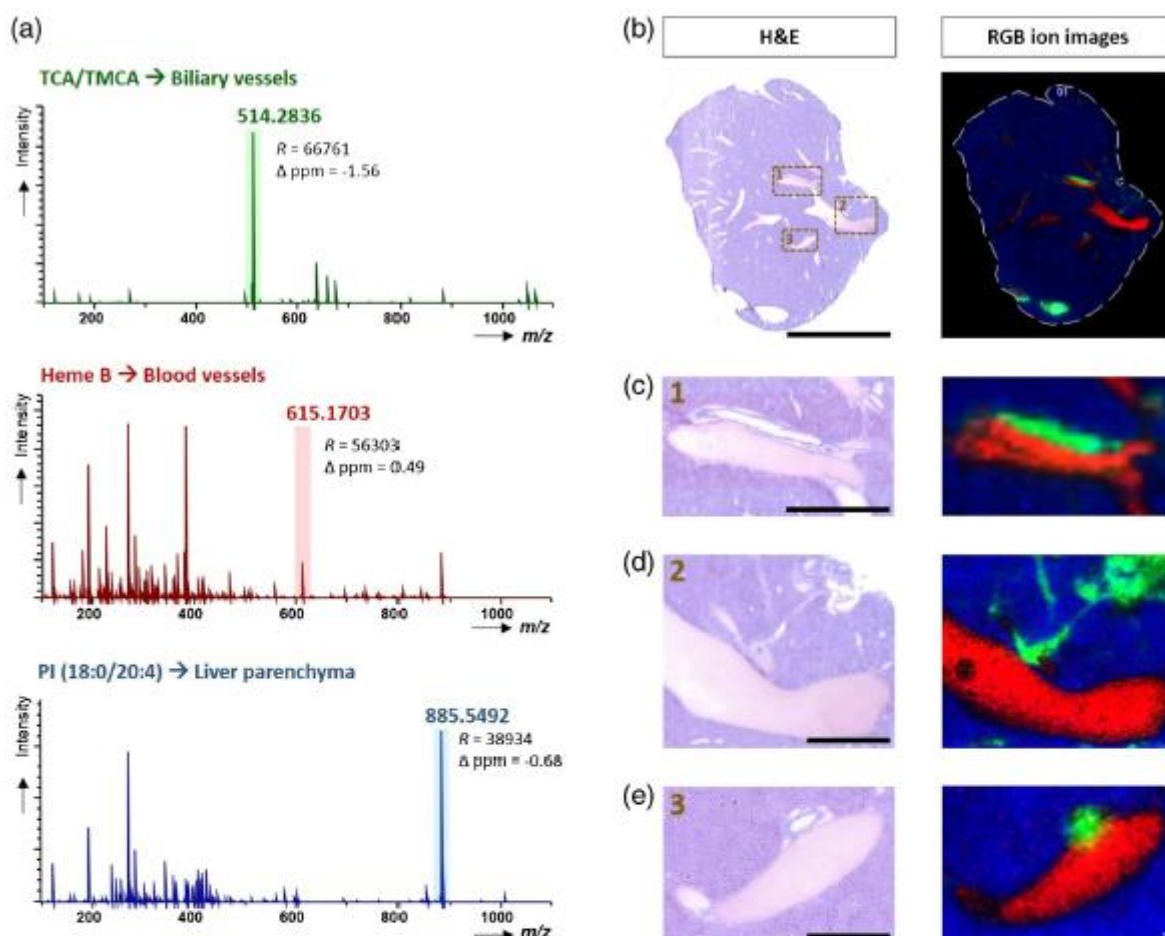
Figure 4. MALDI-MSI single pixel mass spectra from three regions of liver tissue section with different microstructures and chemical compositions: biliary tree (bile duct), blood vessel, and liver parenchyma. The *m/z* values used for RGB MS images are highlighted in the spectra **(a)**. RGB ion images representing three different compounds, showing clear distinction between anatomical features (as shown by the H&E stained images) across the whole tissue section (pixel size, 70 μm) **(b)**. Expansion of the smaller sub-region **(c)** as well as smaller sub-regions from an adjacent section (pixel size, 25 μm) **(d, e)**. Scale bars: 5 mm **(b)**, 1000 μm **(c, d)**, and 500 μm **(e)**

additional molecules, which are associated with the gall bladder and bile ducts regions. In addition to the manual investigation of selected regions of interest (ROI), we also applied mass defect filtering (MDF) based on average mass spectra from the MSI experiments, to identify further potential metabolites of bile acids. For this purpose, we chose an unconjugated monohydroxylated bile acid, litocholic acid (LCA), as core substructure and set a mass defect filter window of ±50 mDa around the exact mass of LCA (to include the most common bile acids conjugations) over a broader mass region from *m/z* 400 to 700. This combined approach of data processing revealed >20 promising monoisotopic *m/z* value candidates. Most notably, two interesting groups of signals with the highest relative signal intensities were found in the ranges between *m/z* 620 and 680 and from *m/z* 1,020 to 1080, which are shown as

single MSI pixel mass spectrum in Figure 5. Surprisingly, searching common databases (LIPID MAPS and METLIN) did not give any positive identifications. Moreover, the measured accurate mass shifts from the chosen core structure did not match any known or previously observed biotransformations. As bile acids have been reported to form proton-bound (mixed) dimers during electrospray ionization [50, 51] as well as solvent adducts in positive ion mode and carboxylic acid adducts in negative ion mode [63], we also investigated the observed mass shifts for potential formations of these cluster ions.

As a result, we were able to identify two species of proton-bound dimers formed during the MALDI-MSI experiments (Figure 5). Firstly, cluster ions of the general structure [BA-H]⁻···H⁺···[BA-H]⁻, which are dimers of TCA/TMCA (*m/z*
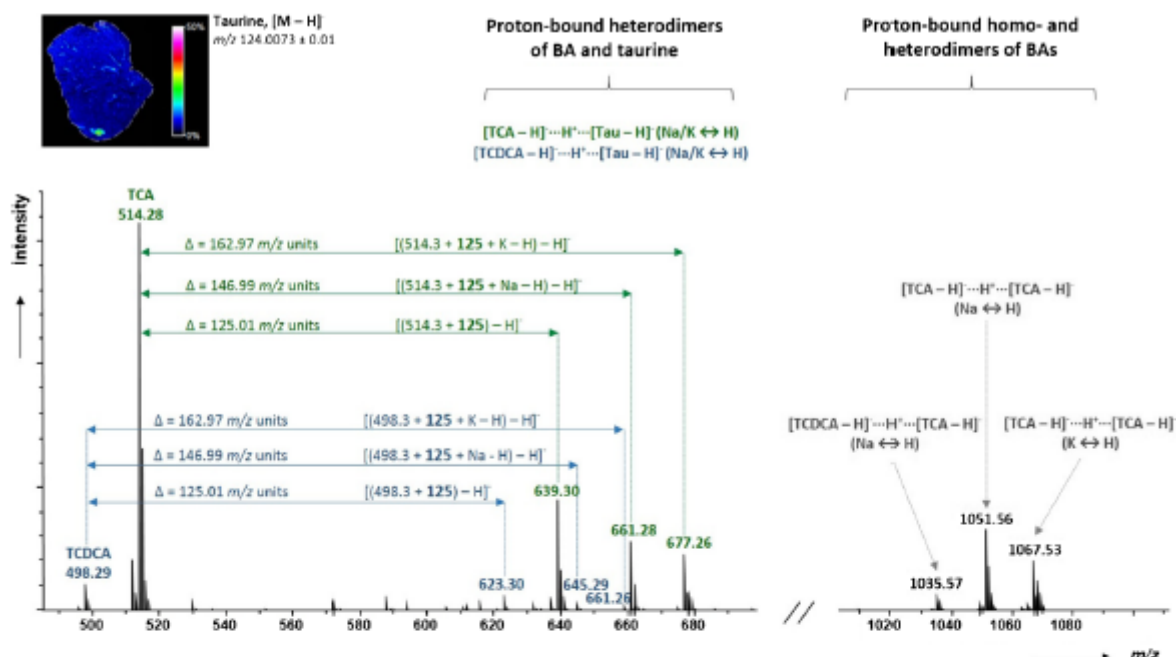
Figure 5. Single MSI pixel mass spectrum from the bile duct region in the range m/z 490–1100, showing signals from proton-bound dimers formed between bile acids (homo- and heterodimers) as well as between bile acids and taurine. The 2D ion image on the upper left illustrates the distribution of taurine in the liver section

1051.56 and 1067.53), and a mixed dimer of TCDCA and TCA/TMCA (m/z 1035.57). Secondly, [BA-H]⁻···H⁺···[Ta-H]⁻ adducts, which were, in fact, mixed dimers of TCA/TMCA and taurine (m/z 639.30, 661.28 and 677.26) or TCDCA and taurine (m/z 623.30, 645.29 and 661.26). Importantly, the high abundance of taurine across the examined liver sections is readily seen in the ion image of m/z 124.0073 ± 0.01 (from the same tissue section), which corresponds to deprotonated taurine, providing additional corroboration of our findings on the identified bile acids and the taurine dimer formation. Of note, all identified dimers showed the same localization and spatial distributions as the deprotonated BAs (Figure S3, Supplementary Information).

To unambiguously confirm the results on the PBD, we examined an equimolar mixture of standard solutions of TCA, taurine, and potassium chloride by MALDI-FTICR (via 9-AA matrix and dried-droplet sample preparation). The results (Figure S4, Supplementary Information) confirmed the previous data on the proton-bound dimers of TCA and taurine. We also performed on-tissue CID experiments of the mass selected cluster ions, by co-adding 16 individual scans of each enhance signal-to-noise ratios, and comparison with CID experiments of standard mixtures. The CID spectra illustrated in Figure S5 (Supplementary Information) showed a single product at m/z 498.3 for clusters containing TCDCA (m/z 623.3 and 645.3); or at m/z 514.3 for dimers containing TCA/TMCA (m/z 639.3, 661.3, 677.3 and 1051.6). Interestingly, MS/MS spectra of mixed dimers of bile acid and taurine did not show the product

ions related to taurine, which can readily be explained by high gas-phase acidity of taurine-conjugated bile acids [51].

Implications of PBD for MALDI-MSI: Impact on [M − H]⁻ Intensities

In addition to considerably complicating mass spectral interpretation, the formation of proton-bound dimers also diminishes signal intensities of the desired [M − H]⁻ peaks. This effect becomes even more detrimental in MALDI-MSI experiments, in particular at high lateral resolutions, where the amount of analyte in a single pixel tissue area is very limited and often requires operating at or close to the detection limits of the method. Interestingly, the intensity ratio of PBD to deprotonated BA (PBD/BA) measured in our imaging experiments varied across the regions of the tissue section (average mass spectra and PBD/BA values for four regions are shown in Table S1 and Figure S6, Supplementary Information). Of note, the heterodimers of TCA/TMCA and taurine contributed most significantly to the overall sum intensity of all PBDs, and the highest total PBD/BA ratios were observed for large and small bile ducts (0.64 and 0.78, respectively). This suggests a dependence of PBD formation on the tissue concentration of the contributing molecules and the ion density after MALDI, respectively, which will vary across the tissue.

Here, we introduce a simple technique for use on mass spectrometry platforms with a quadrupole collision cell or ability for efficient in-source CID prior to FTICR mass

analysis. Essentially, PBD are dissociated, resulting in increased signal intensities for the deprotonated molecule. We implemented two different approaches for CID in non-selective broadband mode: (1) dissociation in the transport region between skimmer and ion funnel, often referred to as "nozzle-skimmer dissociation" or "in-source CID"; (2) dissociation in the hexapole collision cell, while maintaining full transmission of the entire m/z range of interest, without any prior precursor ion isolation. To demonstrate the feasibility of the two CID methods, the standard mixture of TCA and taurine was examined using direct infusion ESI-FTICR. The ESI source was deliberately chosen here, as it allowed delivery of a constant ion current, while MALDI would have been strongly affected by crystallization irregularities. As seen in Figure 6, increasing either the absolute voltage applied to the skimmer or the collision energy for the hexapole cell resulted in an increase of signal intensities for [TCA – H]⁻ ion (m/z 514.3), while intensities for both dimer signals (m/z 639.3 and 661.3) decreased. Of the two approaches, broadband CID in the hexapole was slightly more efficient, providing an increase of

factor ~2 of the deprotonated TCA signal. Interestingly, the sodiated form of the mixed dimer of TCA and taurine (m/z 661.3) exhibited higher stability compared with the 'pure' PBD (m/z 639.3). This is, of course, often observed with sodiated species undergoing CID versus protonated species of the same molecule; for PBD, it can be explained by different gas-phase conformations of the cluster ions, where the sodium cation contributes to the bonding, creating, in fact, a sodium-bound dimer [64]. Of note, some other structural factors may also play a role in the stability of the gas-phase clusters, including formation of multiple inter- and intramolecular hydrogen bonds [50, 65], as well as different positions of the bonding hydroxyl groups at the ring [66, 67].

Furthermore, to demonstrate the utility of the developed method for MSI, a model MALDI imaging experiment was designed in which an equimolar mixture of TCA and taurine was homogenously sprayed across the liver section placed on a glass slide, followed by deposition of 9-AA matrix. Two regions (glass slide and liver tissue) were then selected for imaging experiments, with and without applying the 'in-
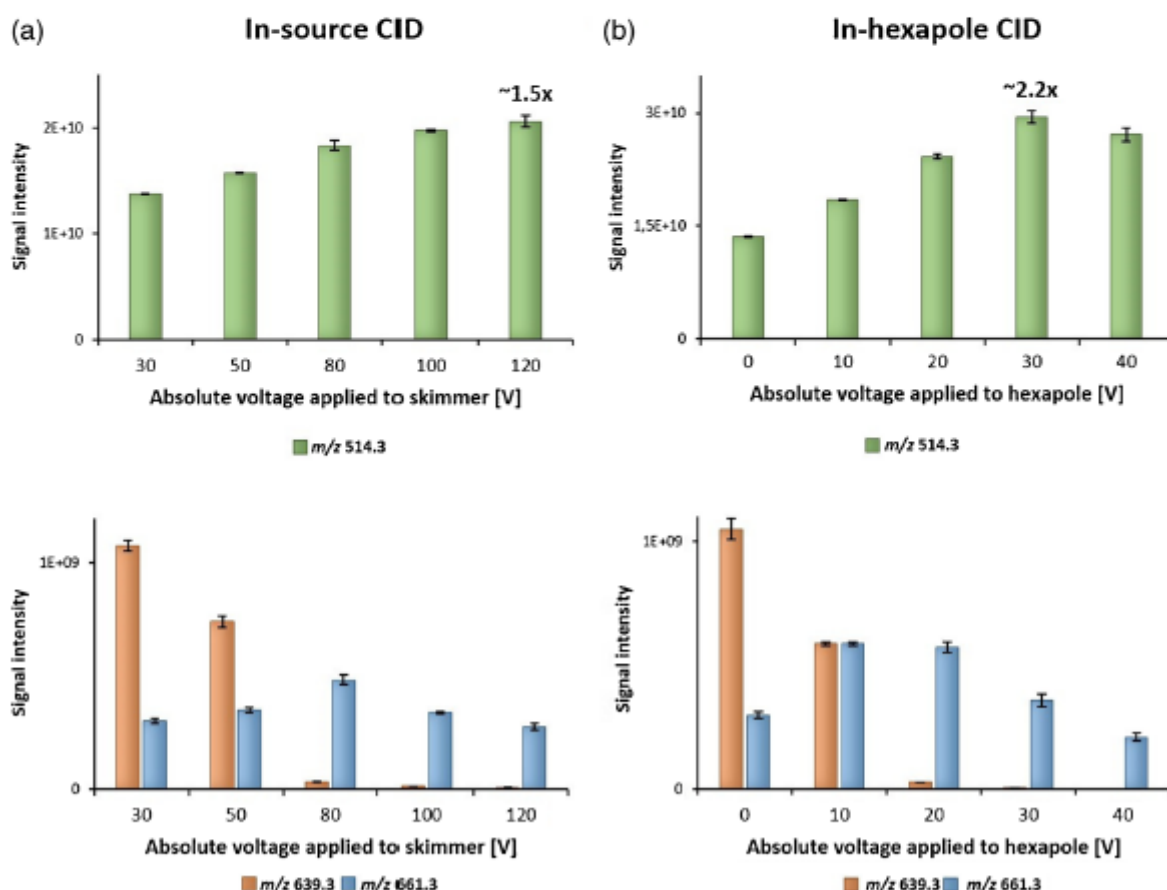

Figure 6. Bar chart showing signal intensities for three different m/z values, m/z 514.3 (deprotonated TCA), m/z 639.3 (mixed dimer of TCA and taurine), and m/z 661.3 (sodiated dimer of TCA and taurine) obtained by direct infusion ESI-FTICR and two different approaches for CID: in-source CID (increasing voltage applied to skimmer) (a) and in-hexapole CID (b)

I. Rzagalinski et al.: Mass Spectral Imaging of Bile Acids in Mouse Liver

hexapole' dissociation method (each region was composed of at least 200 single pixels at 70 μm spatial resolution, from which the average mass spectra and PBD/BA values are shown in Figures S7a, b, and 7d, e, Supplementary Material). Applying collision energy (30 V) resulted in an increase of the average signal intensity for [TCA − H]⁻ (m/z 514.3) by factors of 2.7 and 1.6 for glass and tissue regions, respectively, while the sum of averaged intensities from three heterodimer signals (m/z 639.3, 661.3 and 667.3) decreased. Increasing the laser energy might also be considered to be a potentially useful alternative for dimer dissociation. As shown by Dreisewerd and coworkers, however, optimal MALDI-MS performance (=maximum analyte signal intensity at the lowest threshold laser fluence) can be achieved by utilizing a laser energy approximately 2–3 times higher than the ion detection threshold [68], which was also used in the present study. Increasing the laser energy above this value can result in strong ablation from the tissue surface and may lead to increased thermal degradation of the analytes, leading to overall analyte signal deterioration. This was confirmed in our experiments, as shown in Figure S7c, f (Supplementary Material). Therefore, we consider the 'in-hexapole' broadband dissociation approach developed here as a superior and gentler means of increasing signal intensities from deprotonated bile acids during MALDI-MSI.

Conclusions

The primary goal of this study was the visualization of bile acid distributions across mouse livers sections on a molecular level. To our knowledge, this is the first report on the detection and identification of taurine-conjugated bile acids directly from mouse liver sections. The acquired MALDI-MSI data corresponded well with the micro-anatomical features of the mouse liver biliary tract obtained from histological examinations. Furthermore, we have demonstrated the potential of the method for high spatial resolution MALDI imaging at pixel size of 25 μm, which even allows the differentiation of small biliary ducts from blood vessels and liver parenchymal tissue. In addition to MALDI-MSI, our research revealed extensive proton-bound dimer formation between endogenous taurine and taurine-conjugated bile acids. Since formation of these dimers negatively influenced signal intensities of the desired [M − H]⁻ species, a simple method of broadband dissociation was proposed that provided increased signals of the deprotonated species. This deliberate PBD dissociation will be implemented in our future MALDI-MSI studies, in particular in applications where the sensitivity of the method will be the limiting factor; for example, when even higher spatial resolutions than presented here are required (e.g., molecular mapping of small interlobular bile ducts of diameter of ~10 μm for studying cholestasis models [69]), or for bile acid distributions in the brain at much lower concentration levels than in the liver, where they play important signaling roles in neurological disease [70–72]. Other work currently in progress includes a detailed experimental investigation of the exact structural factors stabilizing the different proton/cation-bound dimers of bile acids and amino acids.

References

1. Russell, D.W.: The enzymes, regulation, and genetics of bile acid synthesis. Annu. Rev. Biochem. **72**, 137–174 (2003)

2. Hofmann, A.F., Hagey, L.R., Krasowski, M.D.: Bile salts of vertebrates: structural variation and possible evolutionary significance. J. Lipid Res. **51**, 226–246 (2010)

3. Rudling, M.: Understanding mouse bile acid formation: Is it time to unwind why mice and rats make unique bile acids? J. Lipid Res. **57**, 2097–2098 (2016)

4. Bonde, Y., Eggertsen, G., Rudling, M.: Mice abundant in muricholic bile acids show resistance to dietary induced steatosis, weight gain, and to impaired glucose metabolism. PLoS One. **11**, (2016)

5. Qi, Y., Jiang, C., Cheng, J., Krausz, K.W., Li, T., Ferrell, J.M., Gonzalez, F.J., Chiang, J.Y.L.: Bile acid signaling in lipid metabolism: Metabolomic and lipidomic analysis of lipid and bile acid markers linked to anti-obesity and anti-diabetes in mice. Biochim. Biophys. Acta – Mol. Cell Biol. Lipids. **1851**, 19–29 (2015)

6. Hofmann, A.F.: Detoxification of lithocholic acid, a toxic bile acid: relevance to drug hepatotoxicity. Drug Metab. Rev. **36**, 703–722 (2004)

7. Heubi, J.E., Setchell, K.D.R., Bove, K.E.: Inborn errors of bile acid metabolism. Semin. Liver Dis. **27**, 282–294 (2007)

8. Milkiewicz, M., Klak, M., Kempinska-Podhorodecka, A., Wiechowska-Kozlowska, A., Urasinska, E., Blatkiewicz, M., Wunsch, E., Elias, E., Milkiewicz, P.: Impaired hepatic adaptation to chronic cholestasis induced by primary sclerosing cholangitis. Sci. Rep. **6**, 39573 (2016)

9. Li, T., Chiang, J.Y.L.: Bile acid signaling in metabolic disease and drug therapy. 948–983 (2014)

10. Hofmann, A.F.: The continuing importance of bile acids in liver and intestinal disease. Arch. Intern. Med. **159**, 2647–2658 (2015)

11. Payne, C.M., Bernstein, C., Dvorak, K., Bernstein, H.: Hydrophobic bile acids, genomic instability, Darwinian selection, and colon carcinogenesis. Clin. Exp. Gastroenterol. **1**, 19–47 (2008)

12. Hofmann, A.F., Hagey, L.R.: Bile acids: chemistry, pathochemistry, biology, pathobiology, and therapeutics. Cell. Mol. Life Sci. **65**, 2461–2483 (2008)

13. Ridlon, J.M.: Bile salt biotransformations by human intestinal bacteria. J. Lipid Res. **47**, 241–259 (2005)

14. Iida, T., Nishida, S., Yamaguchi, Y., Kodake, M.: 3-Glucosides of nonamidated and glycine- and taurine-amidated bile acids. **36**, (1995)

15. Alnouti, Y.: Bile acid sulfation: a pathway of bile acid elimination and detoxification. Toxicol. Sci. **108**, 225–246 (2009)

16. Hofmann, A.F., Sjövall, J., Kurz, G., Radominska, A., Schteingart, C.D., Tint, G.S., Vlahcevic, Z.R., Setchell, K.D.: A proposed nomenclature for bile acids. J. Lipid Res. **33**, 599–604 (1992)

17. Hylemon, P.B., Zhou, H., Pandak, W.M., Ren, S., Gil, G., Dent, P.: Bile acids as regulatory molecules. J. Lipid Res. 50, 1509–1520 (2009)

18. De Aguiar Vallim, T.Q., Tarling, E.J., Edwards, P.A.: Pleiotropic roles of bile acids in metabolism. Cell Metab. 17, 657–669 (2013)

19. Griffiths, W.J.: Tandem mass spectrometry in the study of fatty acids, bile acids, and steroids. Mass Spectrom. Rev. 22, 81–152 (2003)

20. Cheng, C., Gross, M.L.: Applications and mechanisms of charge-remote fragmentation. Mass Spectrom. Rev. 19, 398–420 (2000)

21. Griffiths, W.J., Zhang, J., Sjovall, J.: Charge-remote fragmentation of bile acids derivatized with amino-sulphonic acids. Rapid Commun. Mass Spectrom. 7, 235–240 (1993)

22. Zhang, J., Griffiths, W.J., Bergman, T., Sjovall, J.: Derivatization of bile acids with taurine for analysis by fast atom bombardment mass spectrometry with collision-induced fragmentation. J. Lipid Res. 34, 1895–1900 (1993)

23. Setchell, K.D.R., Vestal, C.H.: Thermospray ionization liquid chromatography-mass spectrometry: a new and highly specific technique for the analysis of bile acids. J. Lipid Res. 30, 1459–1469 (1989)

24. Eckers, C., East, P.B., Haskins, N.J.: The use of negative ion thermospray liquid chromatography / tandem mass spectrometry for the determination of bile acids and their glycine conjugates. J. Mass Spectrom. 20, 731–739 (1991)

25. Goto, J., Murao, N., Nakada, C., Motoyama, T., Oohashi, J., Yanagihara, T., Niwa, T., Ikegawa, S.: Separation and characterization of carboxyl-linked glucuronides of bile acids in incubation mixture of rat liver microsomes. Steroids. 63, 186–192 (1998)

26. You, J., Shi, Y., Ming, Y., Yu, Z., Yi, Y., Liu, J.: Development of a sensitive reagent, 1,2-benzo-3,4-dihydrocarbazole-9-ethyl-p-toluenesulfonate, for determination of bile acids in serum by HPLC with fluorescence detection, and identification by mass spectrometry with an APCI source. Chromatographia. 60, 527–535 (2004)

27. You, J., Fu, Y., Sun, Z., Suo, Y.: 2-(5-Benzoacridine)ethyl-p-toluenesulfonate as sensitive reagent for the determination of bile acids by HPLC with fluorescence detection and online atmospheric chemical ionization-mass spectrometric identification. Anal. Bioanal. Chem. 396, 2657–2666 (2010)

28. Goto, T., Shibata, A., Iida, T., Mano, N., Goto, J.: Sensitive mass spectrometric detection of neutral bile acid metabolites. Formation of adduct ions with an organic anion in atmospheric pressure chemical ionization [4]. Rapid Commun. Mass Spectrom. 18, 2360–2364 (2004)

29. Eneroth, P., Gordon, B., Ryhage, R., Sjövall, J.: Identification of mono- and dihydroxy bile acids in human faeces by gas-liquid chromatography and mass spectrometry. J. Lipid Res. 7, 511–523 (1966)

30. Suzuki, M., Murai, T., Yoshimura, T., Kimura, A., Kurosawa, T., Tohma, M.: Determination of 3-oxo-delta4- and 3-oxo-delta4,6-bile acids and related compounds in biological fluids of infants with cholestasis by gas chromatography-mass spectrometry. J. Chromatogr. B Biomed. Sci. Appl. 693, 11–21 (1997)

31. Griffiths, W.J., Sjovall, J.: Bile acids: analysis in biological fluids and tissues. J. Lipid Res. 51, 23–41 (2010)

32. Han, J., Liu, Y., Wang, R., Yang, J., Ling, V., Borchers, C.H.: Metabolic profiling of bile acids in human and mouse blood by LC-MS/MS in combination with phospholipid-depletion solid-phase extraction. Anal. Chem. 87, 1127–1136 (2015)

33. Jäntti, S.E., Kivilompolo, M., Ohrnberg, L., Pietiläinen, K.H., Nygren, H., Orešič, M., Hyötyläinen, T.: Quantitative profiling of bile acids in blood, adipose tissue, intestine, and gall bladder samples using ultra high performance liquid chromatography-tandem mass spectrometry. Anal. Bioanal. Chem. 406, 7799–7815 (2014)

34. Wegner, K., Just, S., Gau, L., Mueller, H., Gérard, P., Lepage, P., Clavel, T., Rohn, S.: Rapid analysis of bile acids in different biological matrices using LC-ESI-MS/MS for the investigation of bile acid transformation by mammalian gut bacteria. Anal. Bioanal. Chem. 409, 1231–1245 (2017)

35. Bobeldijk, I., Hekman, M., de Vries-van der Weij, J., Coulier, L., Ramaker, R., Kleemann, R., Kooistra, T., Rubingh, C., Freidig, A., Verheij, E.: Quantitative profiling of bile acids in biofluids and tissues based on accurate mass high resolution LC-FT-MS: Compound class targeting in a metabolomics workflow. J. Chromatogr. B Anal. Technol. Biomed. Life Sci. 871, 306–313 (2008)

36. Alnouti, Y., Csanaky, I.L., Klaassen, C.D.: Quantitative-profiling of bile acids and their conjugates in mouse liver, bile, plasma, and urine using LC-MS/MS. J. Chromatogr. B Anal. Technol. Biomed. Life Sci. 873, 209–217 (2008)

37. Mims, D., Hercules, D.: Quantification of bile acids directly from urine by MALDI-TOF-MS. Anal. Bioanal. Chem. 375, 609–616 (2003)

38. Mims, D., Hercules, D.: Quantification of bile acids directly from plasma by MALDI-TOF-MS. Anal. Bioanal. Chem. 378, 1322–1326 (2004)

39. Ruh, H., Salonikios, T., Fuchser, J., Schwartz, M., Sticht, C., Hochheim, C., Wirnitzer, B., Gretz, N., Hopf, C.: MALDI imaging MS reveals candidate lipid markers of polycystic kidney disease. J. Lipid Res. 54, 2785–2794 (2013)

40. Huang, N., Siegel, M.M., Kruppa, G.H., Laukien, F.H.: Automation of a Fourier transform ion cyclotron resonance mass spectrometer for acquisition, analysis, and e-mailing of high-resolution exact-mass electrospray ionization mass spectral data. J. Am. Soc. Mass Spectrom. 10, 1166–1173 (1999)

41. Hsu, F.F., Bohrer, A., Turk, J.: Formation of lithiated adducts of glycerophosphocholine lipids facilitates their identification by electrospray ionization tandem mass spectrometry. J. Am. Soc. Mass Spectrom. 9, 516–526 (1998)

42. Dufresne, M., Thomas, A., Breault-Turcot, J., Masson, J.-F., Chaurand, P.: Silver-assisted laser desorption ionization for high spatial resolution imaging mass spectrometry of olefins from thin tissue sections. Anal. Chem. 85, 3318–3324 (2013)

43. Cai, Y., Cole, R.B.: Stabilization of anionic adducts in negative ion electrospray mass spectrometry. Anal. Chem. 74, 985–991 (2002)

44. Zhu, J., Cole, R.B.: Formation and decompositions of chloride adduct ions, [M + Cl]-, in negative ion electrospray ionization mass spectrometry. J. Am. Soc. Mass Spectrom. 11, 932–941 (2000)

45. McLuckey, S.A., Cameron, D., Cooks, R.G.: Proton affinities from dissociations of proton-bound dimers. J. Am. Chem. Soc. 103, 1313–1317 (1981)

46. Cooks, R.G., Wong, P.S.H.: Kinetic method of making thermochemical determinations: advances and applications. Acc. Chem. Res. 31, 379–386 (1998)

47. Graham Cooks, R., Patrick, J.S., Kotiaho, T., McLuckey, S.A.: Thermochemical determinations by the kinetic method. Mass Spectrom. Rev. 13, 287–339 (1994)

48. Cheng, X.H., Wu, Z.C., Fenselau, C.: Collision energy dependence of proton-bound dimer dissociation – entropy effects, proton affinities, and intramolecular hydrogen-bonding in protonated peptides. J. Am. Chem. Soc. 115, 4844–4848 (1993)

49. Wu, Z., Fenselau, C.: Proton affinity of arginine measured by the kinetic approach. Rapid Commun. Mass Spectrom. 6, 403–405 (1992)

50. Bortolini, O., Fantin, G., Ferretti, V., Fogagnolo, M., Paolo Giovannini, P., Medici, A.: Relative acidity scale of bile acids through ESI-MS measurements. Org. Biomol. Chem. 8, 3674–3677 (2010)

51. Bortolini, O., Bernardi, T., Fantin, G., Ferretti, V., Fogagnolo, M.: Relative acidity scale of glycine- and taurine-conjugated bile acids through ESI-MS measurements. Steroids 76, 596–602 (2011)

52. Rzagalinski, I., Volmer, D.A.: Quantification of low molecular weight compounds by MALDI imaging mass spectrometry – a tutorial review. Biochim. Biophys. Acta – Proteins Proteom. 1865, 726–739 (2017)

53. Goodwin, R.J.A., Scullion, P., MacIntyre, L., Watson, D.G., Pitt, A.R.: Use of a solvent-free dry matrix coating for quantitative matrix-assisted laser desorption ionization imaging of 4-bromophenyl-1,4-diazabicyclo(3.2.2) nonane-4-carboxylate in rat brain and quantitative analysis of the drug from laser microdissected tissue. Anal. Chem. 82, 3868–3873 (2010)

54. Takai, N., Tanaka, Y., Inazawa, K., Saji, H.: Quantitative analysis of pharmaceutical drug distribution in multiple organs by imaging mass spectrometry. Rapid Commun. Mass Spectrom. 26, 1549–1556 (2012)

55. Takai, N., Tanaka, Y., Watanabe, A., Saji, H.: Quantitative imaging of a therapeutic peptide in biological tissue sections by MALDI MS. Bioanalysis. 5, 603–612 (2013)

56. Deininger, S.O., Cornett, D.S., Paape, R., Becker, M., Pineau, C., Rauser, S., Walch, A., Wolski, E.: Normalization in MALDI-TOF imaging datasets of proteins: Practical considerations. Anal. Bioanal. Chem. 401, 167–181 (2011)

57. Hager, J.W., Le Blanc, J.C.Y.: Product ion scanning using a Q-q-Q linear ion trap (Q TRAP) mass spectrometer. Rapid Commun. Mass Spectrom. 17, 1056–1064 (2003)

58. Ludwig, J., Ritman, E.L., LaRusso, N.F., Sheedy, P.F., Zumpe, G.: Anatomy of the human biliary system studied by quantitative computer-aided three-dimensional imaging techniques. Hepatology. 27, 893–899 (1998)

59. Boyer, J.L.: Bile formation and secretion. Compr. Physiol. **3**, 1035–1078 (2013)

60. Roskams, T.A., Theise, N.D., Balabaud, C., Bhagat, G., Bhathal, P.S., Bioulac-Sage, P., Brunt, E.M., Crawford, J.M., Crosby, H.A., Desmet, V., Finegold, M.J., Geller, S.A., Gouw, A.S.H., Hytiroglou, P., Knisely, A.S., Kojiro, M., Lefkowitch, J.H., Nakanuma, Y., Olynyk, J.K., Park, Y.N., Portmann, B., Saxena, R., Scheuer, P.J., Strain, A.J., Thung, S.N., Wanless, I.R., West, A.B.: Nomenclature of the finer branches of the biliary tree: Canals, ductules, and ductular reactions in human livers. Hepatology. **39**, 1739–1745

61. Chiang, J.Y.L.: Bile acids: regulation of synthesis. J. Lipid Res. **50**, 1955–1966 (2009)

62. Garcia-Canaveras, J.C., Donato, M.T., Castell, J.V., Lahoz, A.: Targeted profiling of circulating and hepatic bile acids in human, mouse, and rat using a UPLC-MRM-MS validated method. J. Lipid Res. **53**, 2231–2241 (2012)

63. Warrack, B.M., Didanatot, G.C.: Ion spray liquid chromatographic/mass spectrometric characterization of bile acids. Biol. Mass Spectrom. **22**, 101–111 (1993)

64. Marta, R.A., Wu, R., Eldridge, K.R., Martens, J.K., McMahon, T.B.: The sodium cation-bound dimer of theophylline: IRMPD spectroscopy of a highly symmetric electrostatically bound species. Int. J. Mass Spectrom. **297**, 76–84 (2010)

65. Cai, Y., Concha, M.C., Murray, J.S., Cole, R.B.: Evaluation of the role of multiple hydrogen bonding in offering stability to negative ion adducts in electrospray mass spectrometry. J. Am. Soc. Mass Spectrom. **13**, 1360–1369 (2002)

66. Mano, N., Mori, M., Ando, M., Goto, T., Goto, J.: Ionization of unconjugated, glycine- and taurine-conjugated bile acids by electrospray ionization mass spectrometry. J. Pharm. Biomed. Anal. **40**, 1231–1234 (2006)

67. Wu, R., Marta, R.A., Martens, J.K., Eldridge, K.R., McMahon, T.B.: Experimental and theoretical investigation of the proton-bound dimer of lysine. J. Am. Soc. Mass Spectrom. **22**, 1651–1659 (2011)

68. Wiegelmann, M., Soltwisch, J., Jaskolla, T.W., Dreisewerd, K.: Matching the laser wavelength to the absorption properties of matrices increases the ion yield in UV-MALDI mass spectrometry. Anal. Bioanal. Chem. **405**, 6925–6932 (2013)

69. Vartak, N., Damle-Vartak, A., Richter, B., Dirsch, O., Dahmen, U., Hammad, S., Hengstler, J.G.: Cholestasis-induced adaptive remodeling of interlobular bile ducts. Hepatology **63**. 951–964 (2016)

70. Mano, N., Goto, T., Uchida, M., Nishimura, K., Ando, M., Kobayashi, N., Goto, J.: Presence of protein-bound unconjugated bile acids in the cytoplasmic fraction of rat brain. J. Lipid Res. **45**, 295–300 (2004)

71. Dionísio, P.A., Amaral, J.D., Ribeiro, M.F., Lo, A.C., D'Hooge, R., Rodrigues, C.M.P.: Amyloid-β pathology is attenuated by tauroursodeoxycholic acid treatment in APP/PS1 mice after disease onset. Neurobiol. Aging. **36**, 228–240 (2015)

72. Keitel, V., Görg, B., Bidmon, H.J., Zemtsova, I., Spomer, L., Zilles, K., Häussinger, D.: The bile acid receptor TGR5 (Gpbar-1) acts as a neurosteroid receptor in brain. Glia **58**, 1794–1805 (2010)

Supplementary Material

MALDI Mass Spectral Imaging of Bile Acids Observed as Deprotonated and Proton-Bound Dimers from Mouse Liver Sections

Ignacy Rzagalinski[1], Nadine Hainz[2], Carola Meier[2], Thomas Tschernig[2], Dietrich A. Volmer[1]*

[1]*Institute of Bioanalytical Chemistry, Saarland University, 66123 Saarbrücken, Germany*

[2]*Institute of Anatomy and Cell Biology, Saarland University, 66421 Homburg, Germany*

*To whom correspondence should be addressed:

Prof. Dr. Dietrich A. Volmer
Institute of Bioanalytical Chemistry
Saarland University
Campus B2.2
66123 Saarbrücken, Germany
Tel: +49 681 302 3433; Fax: +49 681 302 2943
Email: dietrich.volmer@mx.uni-saarland.de
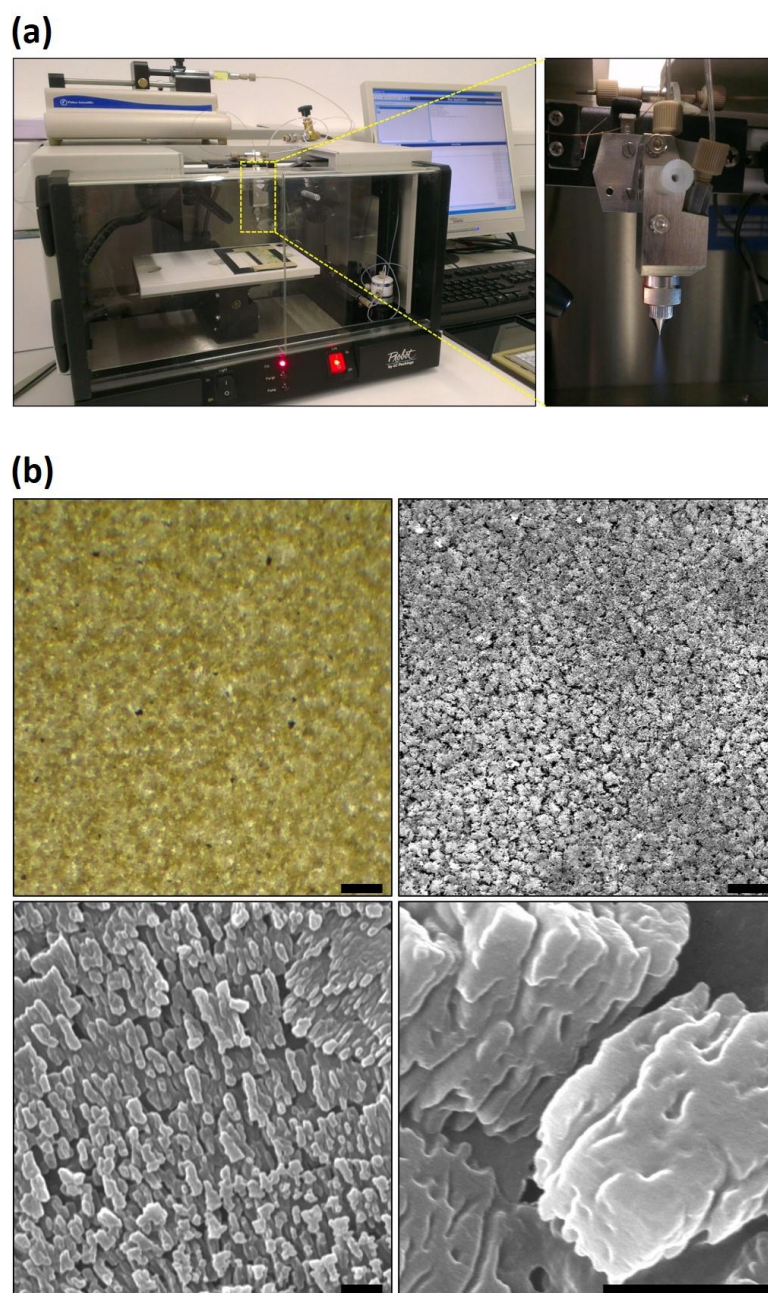
Figure S1. (a) Home-built robotic sprayer based on the Probot micro fraction collector platform, syringe pump and micro spraying nozzle, providing a fine and highly reproducible spray. **(b)** Images of 9-AA matrix sprayed onto the surface of the control liver section: light microscope image at 5× magnification (top left) and SEM images at 50× magnification (top right), 5,000× (bottom left) and 20,000× (bottom right). Scale bars: 100 µm (top left and right) and 1 µm (bottom left and right).
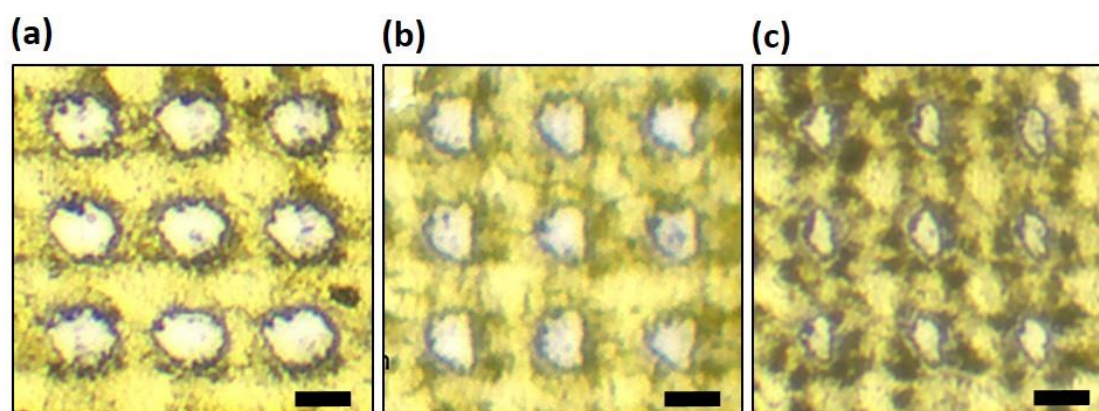
Figure S2. Light microscope images of the ablated areas of 9-AA matrix deposited onto the mouse liver section and irradiated with different number of laser shots per pixel: 1000 **(a)**, 500 **(b)** and 200 **(c)**. Other laser settings were: minimum laser beam focus setting (smallest option on commercial Bruker solariX 7T instrument); laser power, 10%; repetition rate, 1 kHz. Scale bar: 50 μm.
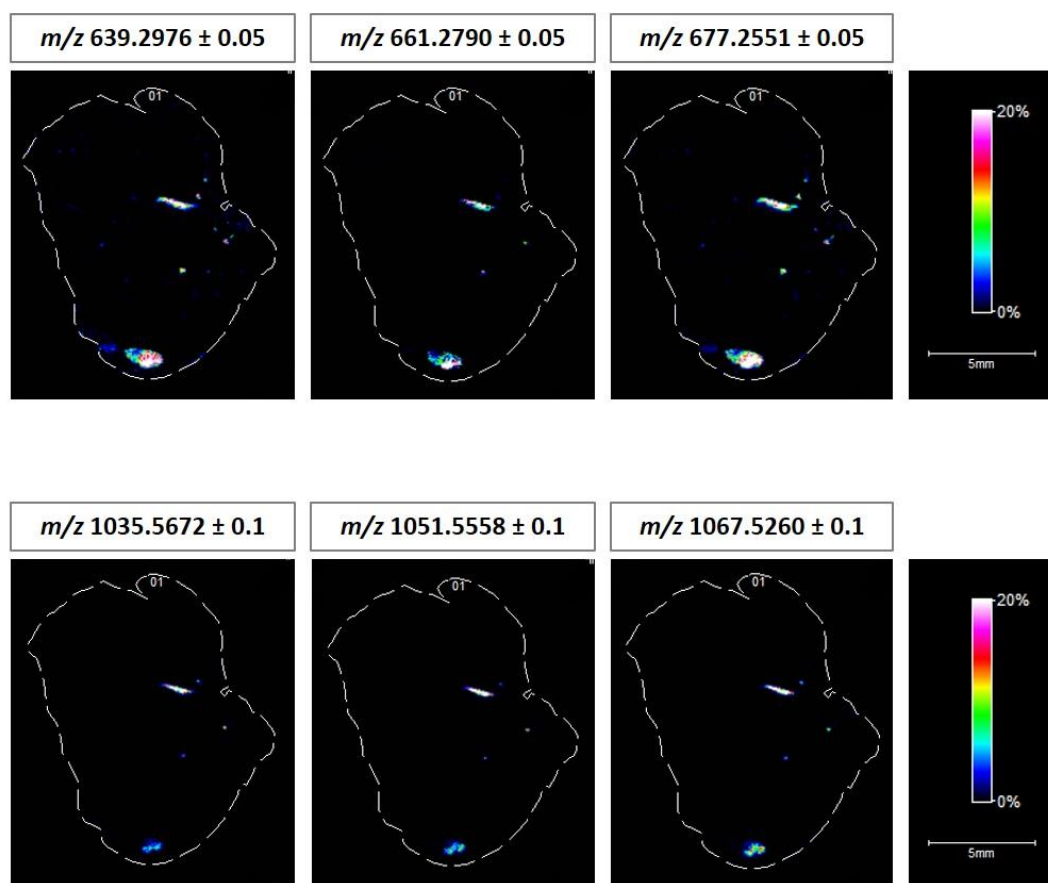
Figure S3. MS ion images representing spatial distributions of the identified TCA/TMCA-containing proton-bound dimers at *m/z* 639.2976 ± 0.05, 661.2790 ± 0.05, 677.2556 ± 0.05, 1035.5672 ± 0.05, 1051.5558 ± 0.05, 1067.5260 ± 0.05 in the whole section of mouse liver (pixel size, 70 µm). All ion images were normalized to the 9-AA matrix signal.
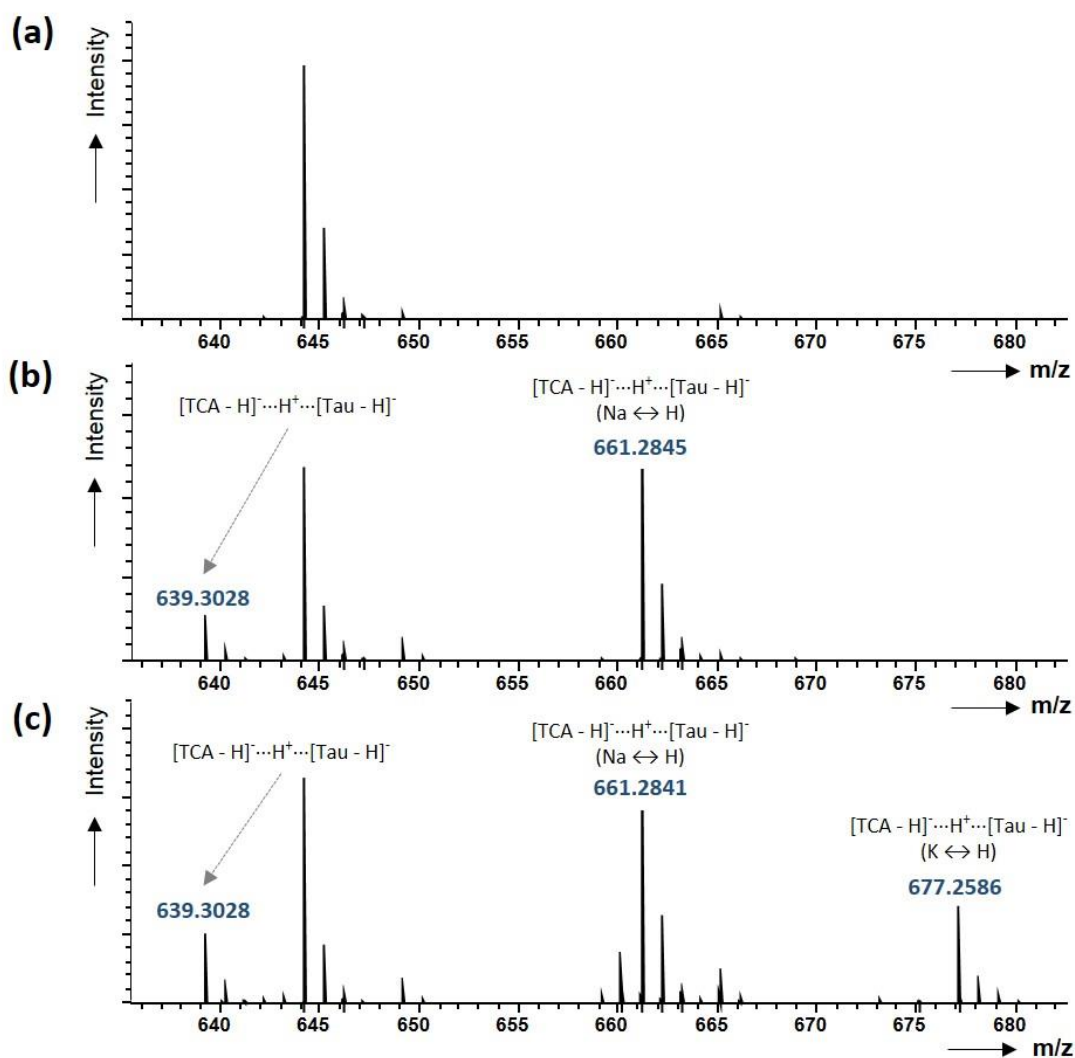
Figure S4. MALDI-FTICR mass spectra acquired after dried-droplet sample preparation using 9-AA matrix and standard mixtures of TCA **(a)**, TCA + taurine **(b)** and TCA + taurine + KCl **(c)**.
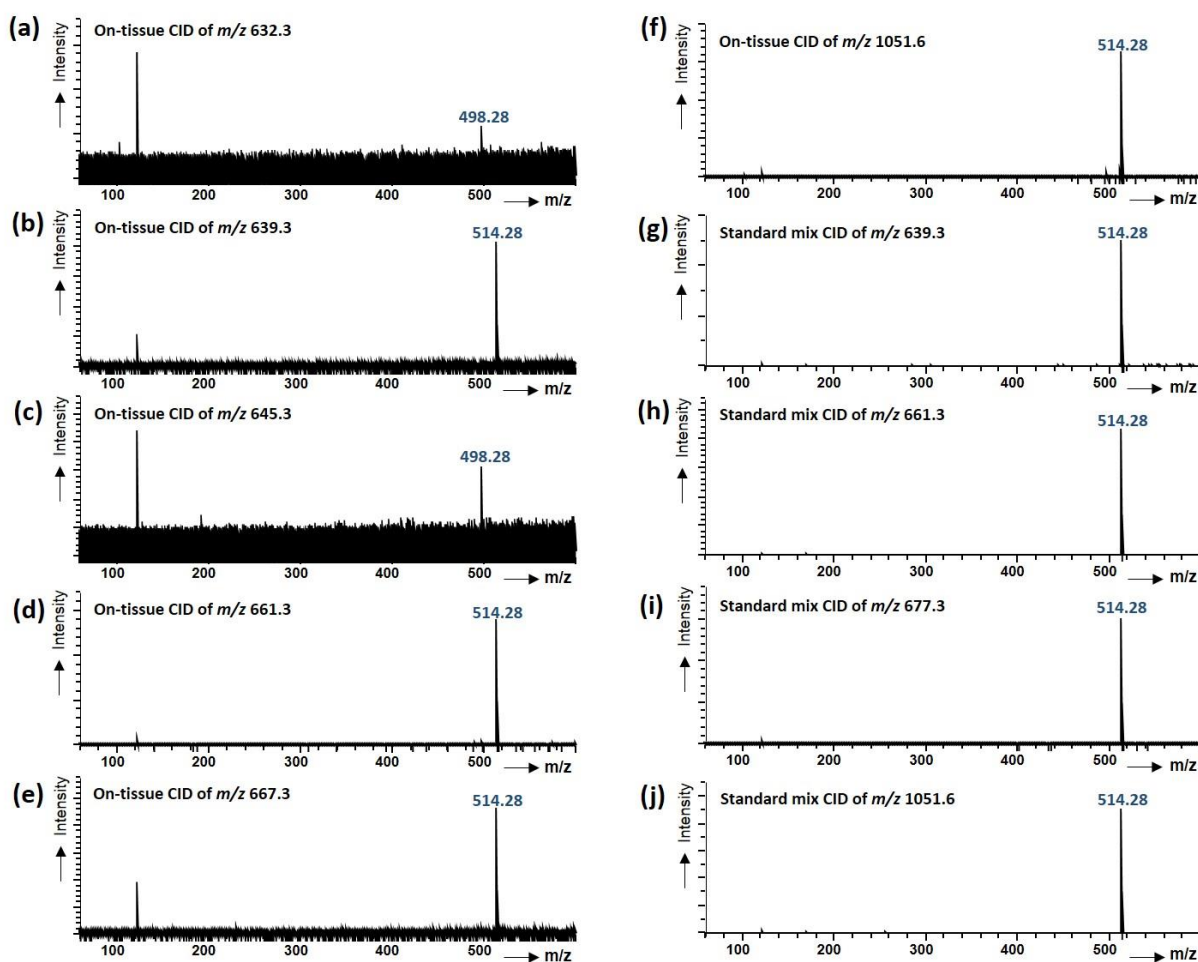
Figure S5. CID experiments of *m/z* selected dimers obtained directly from mouse liver tissue sections **(a-f)** or from standard mixture of TCA, taurine and potassium chloride **(g-j)**. (Note: *m/z* 123 is an artifact of the FTICR instrument used in the study.)
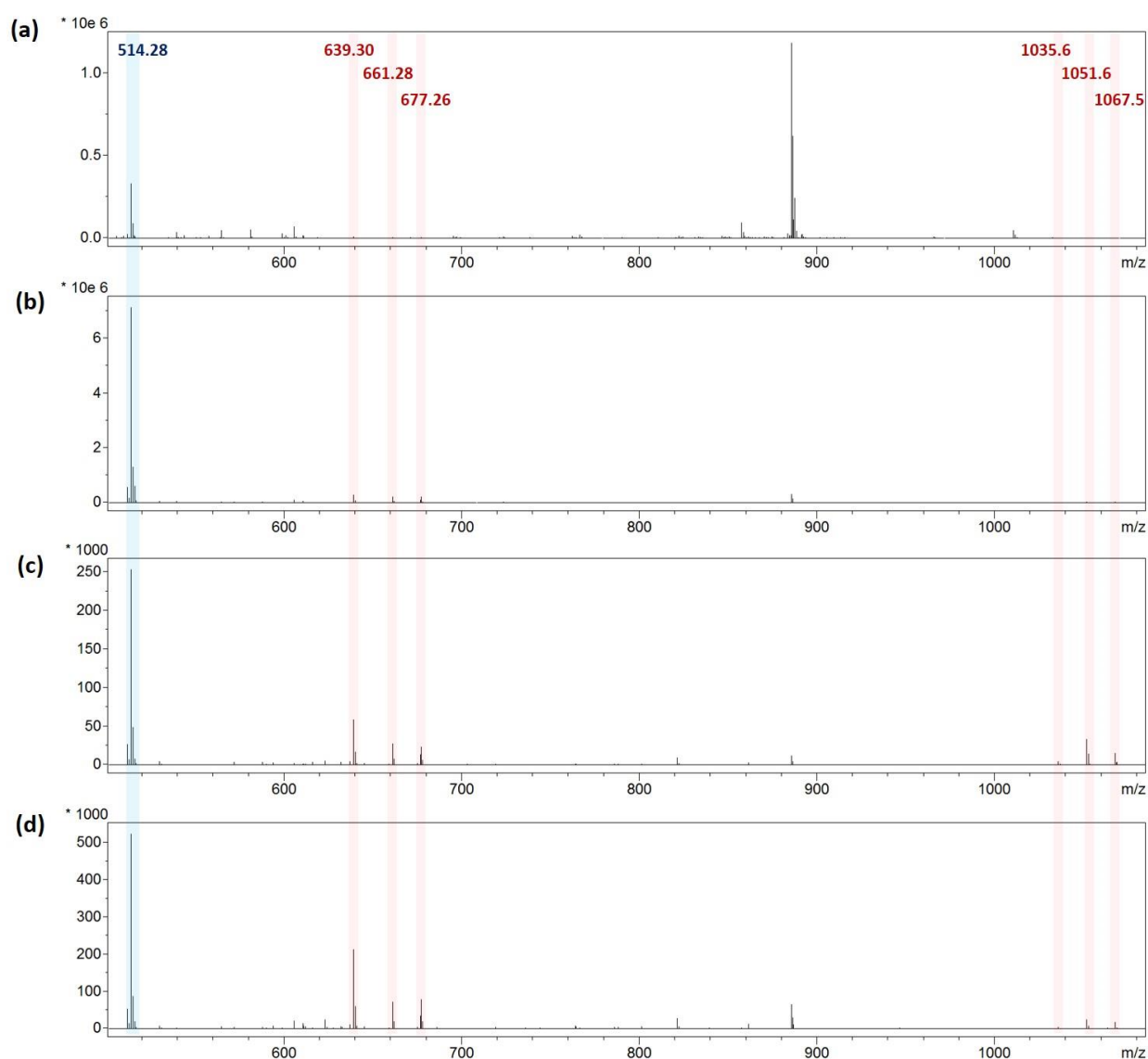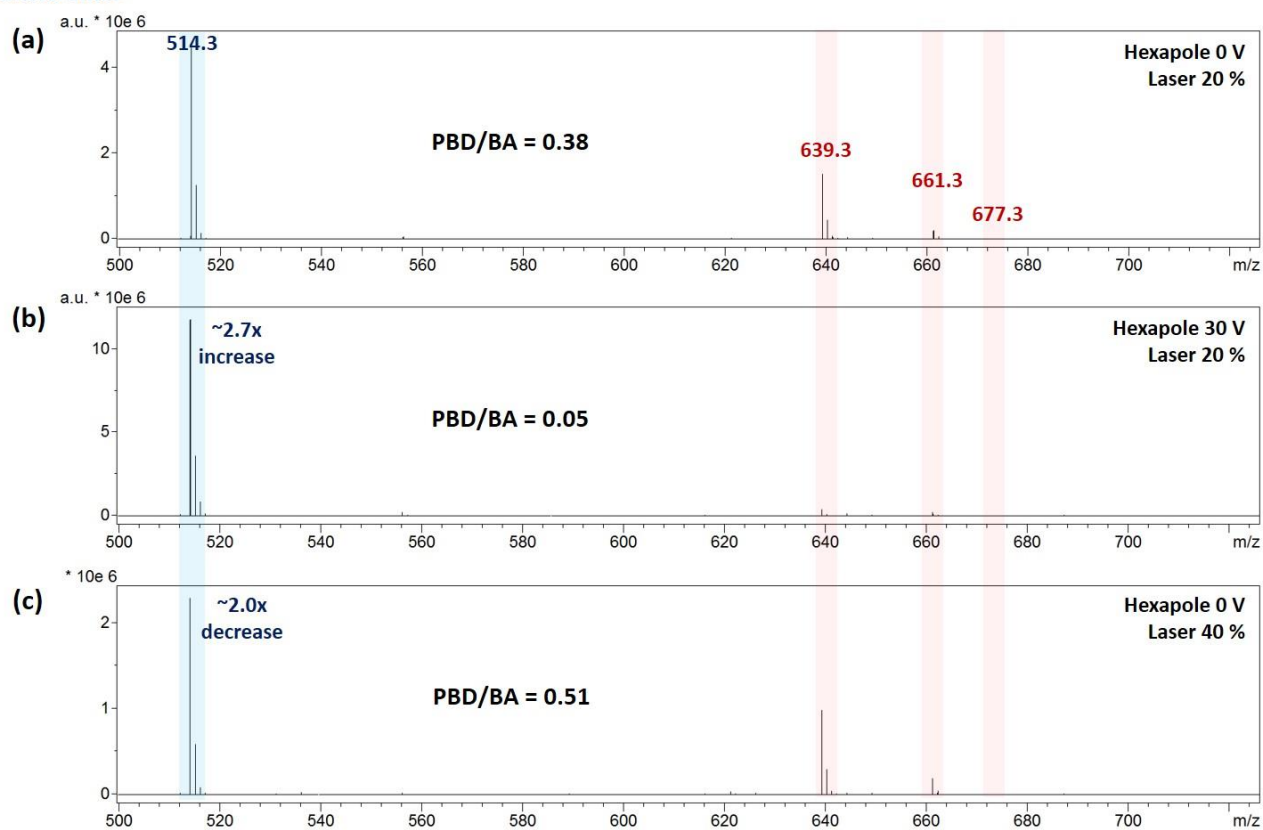
Figure S6. Average mass spectra from different selected regions of interest (ROIs): the whole liver tissue section (22,136 single mass spectra averaged) **(a)**, the gall bladder (125 single mass spectra averaged) **(b)**, the large bile duct of which MS image is shown in Figure 4c (29 single mass spectra **(c)** and the small bile duct of which MS image is shown in Figure 4e (4 single mass spectra averaged) **(d)**. All mass spectra are obtained from the MS imaging experiment performed at 70 μm spatial resolution.

ROI	PBD$_{m/z\ 639.3}$ / BA$_{m/z\ 514.3}$	PBD$_{m/z\ 661.3}$ / BA$_{m/z\ 514.3}$	PBD$_{m/z\ 677.3}$ / BA$_{m/z\ 514.3}$	PBD$_{m/z\ 1035.6}$ / BA$_{m/z\ 514.3}$	PBD$_{m/z\ 1051.6}$ / BA$_{m/z\ 514.3}$	PBD$_{m/z\ 1067.6}$ / BA$_{m/z\ 514.3}$	PBD$_{total}$ /BA$_{m/z\ 514.3}$
Whole section	0.032	0.017	0.014	0.001	0.004	0.003	**0.071**
Gall bladder	0.042	0.030	0.029	0.001	0.004	0.004	**0.109**
Large bile duct	0.232	0.110	0.093	0.017	0.132	0.059	**0.643**
Small bile duct	0.406	0.138	0.150	0.009	0.047	0.035	**0.784**

Table S1. Ratios of average signal intensities of different TCA/TMCA-containing proton-bound dimers and the average signal intensity of deprotonated TCA/TMCA. The values were obtained from four different regions of interest (ROIs) – whole liver section, gall bladder, large bile duct and small bile duct – by averaging mass spectra from 22136, 125, 29 and 4 single points, respectively (pixel size, 70 μm).

Glass slide

Liver tissue

Figure S7. Avarage mass spectra from model MALDI imaging experiments conducted on the glass slide **(a-c)** and liver tissue **(d-f)** regions sprayed homogenously with the equimolar mixture of TCA and taurine and imaged using three different instrumental settings: no collision voltage at hexapole (0 V) and laser energy set to the optimum conditions (20%) **(a, d)**; 30 V at hexapole and laser power 20% **(b, e)**; 0 V at hexapole and doubled laser power (40%) **(c, f)**. All average mass spectra were obtained from at least 200 single points (pixel size, 70 µm). The PBD/BA values were calculated based on the average sum intensity of all heterodimers (TCA/taurine) and average intensity of deprotonated TCA.

Publication 3

Toward higher sensitivity in quantitative MALDI imaging mass spectrometry of CNS drugs using a nonpolar matrix

Ignacy Rzagalinski, Borislav Kovačević, Nadine Hainz, Carola Meier, Thomas Tschernig and Dietrich A. Volmer
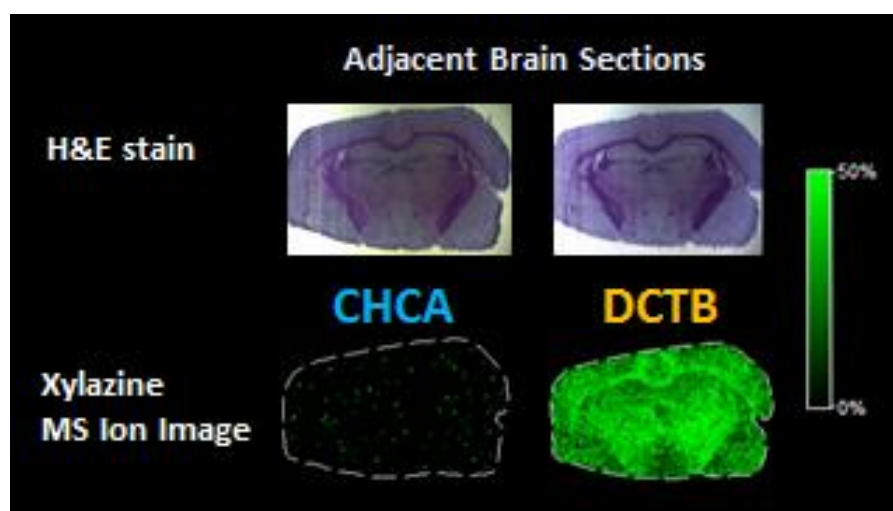
Toward Higher Sensitivity in Quantitative MALDI Imaging Mass Spectrometry of CNS Drugs Using a Nonpolar Matrix

Ignacy Rzagalinski,[†] Borislav Kovačević,[‡] Nadine Hainz,[§] Carola Meier,[§] Thomas Tschernig,[§] and Dietrich A. Volmer[*,||]

[†]Institute of Bioanalytical Chemistry, Saarland University, 66123 Saarbrücken, Germany
[‡]Group for Computational Life Sciences, Ruđer Bošković Institute, 10000 Zagreb, Croatia
[§]Institute of Anatomy and Cell Biology, Saarland University, 66421 Homburg, Germany
[||]Department of Chemistry, Humboldt University of Berlin, 12489 Berlin, Germany

Ⓢ *Supporting Information*

ABSTRACT: Tissue-specific ion suppression is an unavoidable matrix effect in MALDI mass spectrometry imaging (MALDI-MSI), the negative impact of which on precision and accuracy in quantitative MALDI-MSI can be reduced to some extent by applying isotope internal standards for normalization and matrix-matched calibration routines. The detection sensitivity still suffers, however, often resulting in significant loss of signal for the investigated analytes. An MSI application considerably affected by this phenomenon is the quantitative spatial analysis of central nervous system (CNS) drugs. Most of these drugs are low molecular weight, lipophilic compounds, which exhibit inefficient desorption and ionization during MALDI using conventional polar acidic matrices (CHCA, DHB). Here, we present the application of the (2-[(2E)-3-(4-*tert*-butylphenyl)-2-methylprop-2-enylidene]malononitrile) matrix for high sensitivity imaging of CNS drugs in mouse brain sections. Since DCTB is usually described as an electron-transfer matrix, we provide a rationale (i.e., computational calculations of gas-phase proton affinity and ionization energy) for an additional proton-transfer ionization mechanism with this matrix. Furthermore, we compare the extent of signal suppression for five different CNS drugs when employing DCTB versus CHCA matrices. The results showed that the signal suppression was not only several times lower with DCTB than with CHCA but also depended on the specific tissue investigated. Finally, we present the application of DCTB and ultrahigh resolution Fourier transform ion cyclotron resonance mass spectrometry to quantitative MALDI imaging of the anesthetic drug xylazine in mouse brain sections based on a linear matrix-matched calibration curve. DCTB afforded up to 100-fold signal intensity improvement over CHCA when comparing representative single MSI pixels and >440-fold improvement for the averaged mass spectrum of the adjacent tissue sections.
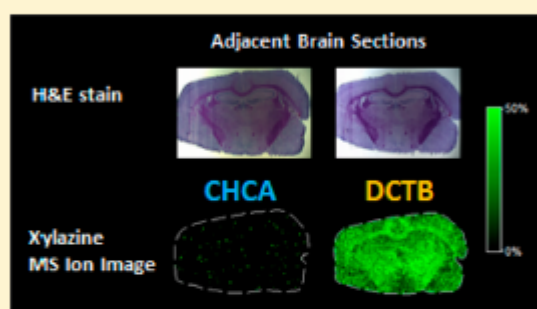
The frequency of disorders affecting the central nervous system (CNS) are growing faster than any other disease, while progress in drug development in this area continues to be slow.[1,2] This has many reasons including the high complexity of the brain, the frequent occurrence of side effects with CNS drugs, and above all, the prerequisite for drugs to cross the blood−brain barrier (BBB).[3,4] The latter requirement has limited the current CNS drug portfolio predominantly to a small group of low molecular weight lipophilic compounds that can cross the BBB via transcellular passive diffusion (according to Lipinski's rule of five),[5−7] even though new developments in carrier-mediated transport using liposomes[8] or nanoparticles[9,10] are of great interest and will potentially play a significant role in the longer perspective.

One of the most essential pieces of information at the early stages of drug discovery is the drug's and its metabolites'
distribution in the whole body, which provides insight into the drug's toxicity as well as its ability to reach the therapeutically desired organ/tissue or target receptors.[11,12] Measuring the drug's blood/plasma concentrations does not necessarily deliver adequate information about its organ/tissue distribution.[13] This is even relevant for the brain, as it is tightly isolated by the BBB; the drug distribution into the cerebrospinal fluid (CSF) is not a measure of BBB permeability into the brain parenchyma but only through the blood−CSF barrier (BSCF).[14] Consequently, analytical tools are urgently needed to quantitatively trace the drugs' spatial distributions in tissue sections, particularly brain sections for CNS drugs.

12592

Over the past decade, mass spectrometry imaging (MSI) has gained wide acceptance as a label-free molecular imaging technique in drug distribution studies, providing considerable advantages over radiolabeled methods such as (quantitative) whole-body autoradiography ((Q)WBA).[15,16] In addition, MSI allows for obtaining the information simultaneously from the parent drugs and its metabolites as well as combining it with spatiotemporal changes in the metabolomic/lipidomic profiles.[17] Another important advantage of MSI is that it can provide reliable quantitative information on the amount of drug in the examined sections.[18-20] Of all MSI ionization techniques, matrix-assisted laser desorption/ionization (MALDI) is the most popular,[21-25] particularly for imaging of pharmaceuticals.[26,27] A number of recent review articles have summarized the state-of-the-art developments of the topic.[28-32]

One of the most promising applications for MSI is the measurement of the spatial distribution of xenobiotics in CNS tissue.[33] A number of studies have described CNS spatial distribution of different drugs,[34,35,44-46,36-43] narcotics,[47-49] neurotoxins[50] and positron emission tomography (PET) ligands.[51] Two recent studies reported more sophisticated uses of MALDI-MSI, including studying drug–drug interactions and their impact on the BBB permeability[52] and amyloid-binding molecules in an experimental model of Alzheimer's disease.[53] Both examples provide an outlook to the future of MSI in the CNS pharmacology field.[54]

Although (MALDI-)MSI has proved its usefulness in pharmacology, several factors still limit its wider applicability to CNS drugs, which are predominantly linked to sensitivity issues. First, MSI is a "sample volume limited" technique, in which the effective limits of detection and quantification will strongly depend on the employed pixel size (irradiated single spot area).[55] This is further amplified by the aforementioned low permeability through the BBB that limits the amount of drug in the CNS parenchyma. Second, (MALDI-)MSI suffers significantly from the presence of tissue-specific ion suppression that cannot be entirely avoided, since no separation step is implemented prior to ionization (in contrast to GC/MS or LC/MS).[56-58] While its negative impact on precision and accuracy in quantitative MALDI-MSI can be limited to some extent by applying isotope internal standards for normalization and matrix-matched calibration routines,[19,20] the detection capabilities still suffer from this phenomenon, often resulting in a significant loss of signal for the investigated analytes.[39,59,60] As a result, MSI of tissue in its native state (in situ) has to rely on alternative strategies. Among the simple strategies are changing the polarity of ionization as well as surface chemical treatments, such as washing the tissue with different solvents, for improving signal intensities for proteins,[61] peptides,[62] lipids,[63] small metabolites[64] and drugs.[46,65] Another approach relied on using different salt additives that minimize negative ion suppression effects between different classes of lipids, as shown by Popkova and Schiller[66] or Griffiths and Bunch[67] for MALDI-MS as well as by Sugiyama et al.[68] for MALDI-MSI. Other methods used improved matrix deposition techniques such as matrix-coating assisted by an electric field (MACEF)[69] or matrix-spraying by utilizing an ultrasonic atomizing tablet and a simple mini-humidifier.[70] Furthermore, improved selectivity toward selected compound classes by increasing ionization efficiency has been demonstrated for MALDI, by using alternative ionizing agents (e.g., ionizing cholesterol in a form of silver adducts),[71] applying on-tissue derivatization

reactions[72] or even by simply utilizing different MALDI matrices such as, for example, nanoparticle-based inorganic matrices in surface-assisted laser desorption/ionization (SALDI).[73] Surprisingly, despite the intensive research on new matrices, the most common method for matrix selection is still the empirical testing of the most popular (or readily available) compounds. Consequently, despite the aforementioned physicochemical properties of CNS drugs (small lipophilic molecules with low polar surface area and limited hydrogen bonding[5-7]), virtually all MALDI-MSI studies of these pharmaceuticals use the two most common polar and acidic matrices, α-cyano-4-hydroxycinnamic acid (CHCA)[36,39,44,48,50,51,59,74] and 2,5-dihydroxybenzoic acid (DHB).[55,38,49,52,53,39-43,45-47]

In this study, we successfully applied the nonpolar DCTB (2-[(2E)-3-(4-tert-butylphenyl)-2-methylprop-2-enylidene]-malononitrile) matrix for high sensitivity imaging of CNS drugs in mouse brain sections. DCTB has been frequently used as an electron-transfer matrix. We performed computational calculations of gas-phase proton affinity and ionization energy to explain the efficient, additional proton-transfer ionization mechanism with this matrix for five selected CNS drugs. Furthermore, using tissue extinction coefficients (TEC), we compared the extent of signal suppression for CNS drugs when employing DCTB versus CHCA matrices as well as tissue-specific ionization suppression. Finally, we applied DCTB for highly sensitive, quantitative MALDI imaging of the anesthetic drug xylazine within mouse brain sections using normalization to an isotope-labeled internal standard and a tissue-matched calibration curve.

■ EXPERIMENTAL SECTION

Chemicals and Reagents. Xylazine, imipramine, and clozapine were purchased from Santa Cruz Biotechnology (Heidelberg, Germany). Ketamine, clonidine, xylazine-d_6 (internal standard), α-cyano-4-hydroxycinnamic acid (CHCA), 2,5-dihydroxybenzoic acid (DHB), trans-2-[3-(4-tert-butylphenyl)-2-methyl-2-propenylidene]malononitrile (DCTB), methanol, acetonitrile, dichloromethane and standard microscopy glass slides were from Sigma-Aldrich (Steinheim, Germany). Rabbit brain was obtained from a local butcher store. Purified water was generated by a Millipore (Bedford, MA, USA) purification system.

Animals, Tissue Preparation, and Histological Staining. C57BL/6 mice (12 weeks old) were purchased from Charles River (Sulzfeld, Germany). Xylazine/ketamine anesthesia was performed by injecting the following mixture: Rompun (0.5 mL), Ketavet (1 mL) and 0.9% NaCl (8.5 mL); the dose was calculated per body weight (0.1 mL per 10 g of body weight). Deep isoflurane anesthesia (negative control) was carried out by inhalation of 5% isoflurane in oxygen. Animals were perfused with saline to remove the blood from the organism. Permission for the mouse perfusion was obtained from the local research ethics committee. The organs were dissected immediately after the sacrifice, snap-frozen in liquid nitrogen and stored at −80 °C until sample preparation. The coronal brain-tissue sections were prepared at 14 μm thickness using a Reichert Jung 2800 Frigocut cryostat microtome (Leica Microsystems, Wetzlar, Germany), thaw-mounted onto plain microscope glass slides and dried for 30 min in a vacuum desiccator. The tissues were stored at −80 °C for no longer than 2 days prior to MSI. After MALDI-MSI, the glass slides were washed with 70% ethanol to remove the

matrix. The tissue sections were stained with regressive hematoxylin and eosin (H&E) and scanned using an Olympus slide optical microscope with an UPLANSAPO 40×/0.90 objective (Olympus, Tokyo, Japan). Rabbit brain (for "unified brain" preparation) was homogenized using a Potter-Elvehjem tissue grinder (Sartorius, Göttingen, Germany), transferred into 15 mL conical centrifuge tubes and snap-frozen in liquid nitrogen. The resulting tissue blocks were sectioned mounted, and dried at the same conditions as the native mouse brain tissues.

MALDI Matrix and Internal Standard Deposition. MALDI matrices and internal standard were homogeneously sprayed onto the tissue sections using an automated home-built sprayer as previously described.[75] Solutions of CHCA (5 mg/mL in ACN/H_2O, 70/30 [v/v]), DCTB (10 mg/mL in DCM/MeOH, 50/50 [v/v]) and xylazine-d_6 (1 μM in MeOH) were freshly prepared prior to deposition. For TEC experiments, the mixture of five CNS drugs in MeOH (at relatively high concentrations of 100 μM, to obtain a signal from all compounds with both matrices) was sprayed prior to matrix deposition with increasing flow rate in the following patterns: two layers at 20 μL/min, two layers at 40 μL/min and four layers at 60 μL/min. For the final imaging experiments, internal standard (xylazine-d_6) was sprayed prior to the matrix deposition in six layers at 20 μL/min. For both CHCA and DCTB matrices, six layers were sprayed with increasing flow rate in the following patterns: two layers at 20 μL/min and four layers at 40 μL/min. The estimated amount of matrix added to the tissue (matrix density) was calculated at 0.0167 and 0.0334 mg/mm^2 for CHCA and DCTB, respectively. In addition, in-depth visual inspection of the obtained MALDI matrix layers was performed using scanning electron microscopy (SEM) images, which revealed excellent homogeneity and reproducibility as well as crystal sizes down to 1 μm for both CHCA and DCTB matrices (Figure S-1, SI).

Limits of Detection and Limits of Quantification. Limits of detection (LOD) and quantification (LOQ) were adapted from generally accepted guidelines for LC/MS method development, to suit the quantitative MALDI-MSI data. Since a mass spectrum collected from a single MSI pixel corresponds to a single injection LC/MS run, the sampling of the entire single calibration spot provided sufficient averaging of multiple analyte measurements. Here, each calibration area provided 100−150 laser ablation spots, which far exceeded the number of technical replicates (=injections) of one calibration solution in LC/MS. The LOD was obtained from replicate analysis of multiple blank spots (n = 5, of which every spot contained at least 100 laser shots = single mass spectrum) and calculation of the standard deviation (SD). The LOD was defined as the analyte concentration giving a signal equal to the blank signal plus 3× SD of the blank. The LOQ was defined as the lowest concentration of a sample that can be quantified with acceptable precision (coefficient of variation, CV ≤ 20%) and bias (±20%). CV was measured within the single calibration spot (showing dispersion of drug signal intensity values of >100 single MSI pixels) and bias was calculated for the single spot from the calibration curve.

Mass Spectrometry and Data Analysis. MALDI experiments were performed in positive ion mode on a Bruker (Bremen, Germany) 7 T Solarix FTICR mass spectrometer, equipped with a dual ESI/MALDI ion source and Smartbeam II Nd:YAG (355 nm) laser. MALDI imaging data were collected either in a full scan mode from m/z 50 to 1000 (for TEC experiments) or in CASI (continuous accumulation of selected ions) mode with a 100 u wide isolation window, set in the quadrupole, centered on m/z 225 with a transient length of 1.0486 s and resolving power (fwhm) of ∼317 000 at m/z 220. Internal mass calibration was performed using either a series of peaks originating from the MALDI matrix (TEC experiments) or a lock mass from the internal standard signal (xylazine imaging experiments). MSI pixel size settings were 100 μm for the final imaging of xylazine from dosed animals, which assured dense pixel deposition and avoided overlap between neighboring laser spots, and 150 μm for TEC experiments (to reduce the time of the entire experiment). For all MALDI-MS and MALDI-MSI experiments, the laser was set to the "small" spot size and the repetition rate was set to 1 kHz. For experiments performed with CHCA and DHB, the laser power was set to 20% and the number of laser shots/pixel was set to 200, while for the experiments with DCTB, the laser power was set to 15% and the number of laser shots/pixel to 50. MALDI experiments with standards were carried out by using dried-droplet sample preparation onto steel MALDI target plates (Bruker) and collecting and coadding 16 individual transients for each mass spectrum from three MALDI spots, assuring correction for intra and interspot variabilities. All MS/MS experiments were performed by isolation of precursor ions in the external quadrupole (isolation window: 5−10 u) and accumulation in the hexapole for collision-induced dissociation (CID) at varying collision energies (15−25 V). Data were processed and analyzed using the Bruker Data Analysis and FlexImaging software programs for individual mass spectra and imaging data sets, respectively. For quantitative MALDI imaging of xylazine, a series of seven different calibration standard solutions was spotted onto the blank "unified brain" slices, followed by internal standard and DCTB matrix-spraying. MALDI-MSI experiments were conducted using the same experimental conditions as for the native brain tissues. Finally, calibration curves were performed by extracting the imzML[76] files from FlexImaging and processing with the open-source MSiReader software.[77]

Computational Experiments. Physicochemical properties (pK_a and clogD) of five selected CNS drugs were predicted with ACD/PhysChem Suite (version 14.0, Advanced Chemistry Development, Toronto, ON, Canada). Calculations of gas-phase deprotonation enthalpies (DPE) and gas-phase proton affinities (PA) were performed utilizing the B3LYP/6-311+G(2df,p)//B3LYP/6-31G(d) level of theory. This computational model has been confirmed as a reliable method for calculation of PA and DPE, giving values that were in good agreement with the experiment.[78] However, since the accuracy of the B3LYP method is not satisfactory for calculation of ionization energies (IE),[79] the MP2/6-31+G(2df,p)//MP2/6-31G(d) approach was applied for this purpose. All calculations were performed with the Gaussian 09 program package.[80]

■ RESULTS AND DISCUSSION

Rationale for Proton-Transfer MALDI with DCTB Matrix. DCTB is well-known for its efficient desorption/ionization capabilities at low laser fluences, which has been linked to its high molar absorption coefficient.[81] Its application range is somewhat limited, predominantly for analysis of polymers,[82] fullerenes,[83] organometallics,[84] and more recently nanoparticles and nanoclusters.[85] DCTB's mode of action in these applications is that of an aprotic, electron-transfer (ET)

secondary reaction matrix, delivering primarily radical ions in positive ion mode, or when purposely forced, cationized molecules of the investigated compounds. This mechanism of action was previously investigated in detail by Wyatt et al. for different classes of compounds.[86]

Interestingly, experiments conducted in our laboratory revealed that DCTB appears equally suited as proton-transfer (PT) matrix, which prompted us to investigate a mechanistic rationale for this additional transfer mechanism. Since both current MALDI models (gas-phase protonation and "lucky survivor" model) require an excess of protonated matrix ions for efficient MALDI analyte protonation,[87] it was important to study the MALDI mass spectrum of pure DCTB in positive ion mode (Figure 1A). The spectrum exhibited two major ions,
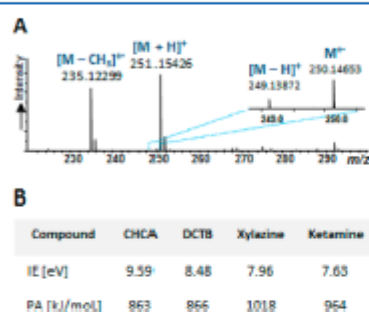

Figure 1. (A) Representative MALDI-FTICR mass spectrum of pure DCTB matrix after dried-droplet sample preparation. (B) Computationally derived proton affinities (PA) and ionization energies (IE) for CHCA and DCTB matrices as well as the two CNS drugs (xylazine and ketamine).

which were identified as the protonated molecule $[M + H]^+$ and a radical cation after methyl loss $[M - CH_3]^{+\bullet}$. In addition, low intensity signals from the radical cation $M^{+\bullet}$ and a somewhat unexpected $[M - H]^+$ ion were also observed. The relative intensities of radical versus protonated DCTB signals depended on the laser fluence, with the latter more prominent at lower energies. Furthermore, as the secondary reactions occurring in the expanding MALDI plume are believed to occur under thermodynamic rather than kinetic control,[88] we also performed computational calculations of gas-phase proton affinities (PA). PA has been shown to determine the resulting MALDI mass spectra in positive ion mode as well as the ionization efficiencies observed for the chemical matrices.[89] The low proton affinity of DCTB (see Figure 1), which is only

slightly higher than that of CHCA and significantly lower than those of the two drugs studied here (xylazine and ketamine), suggests that secondary proton-transfer reactions between protonated matrix and neutral analyte are thermodynamically possible. These findings were confirmed by analyzing an equimolar mixture of the two drugs with DCTB, where protonated ketamine and xylazine signals were readily observed, the latter of which exhibited higher intensity due to the higher PA. Interestingly, the same experiments performed with two different MALDI matrices (CHCA versus DCTB) also revealed ion species of these drugs other than protonated molecules such as radical ions as well as sodium and/or potassium adducts. Their intensities, however, were always significantly lower than those of the protonated molecules (relative abundances, ≤ 1%). Moreover, the relative intensity ratio of radical-to-protonated drug species was higher for DCTB than for CHCA. This suggests a mixed mechanism of DCTB-assisted laser desorption/ionization, with the proton transfer clearly being the dominant pathway. Of note, the additionally calculated IE confirmed the less favorable nature of potential ET reactions between the radical cation of the matrix and the neutral analyte. Moreover, calculation of DCTB gas-phase acidities (deprotonation enthalpy, DPE = 1469 kJ/mol versus 1382 kJ/mol for CHCA and 1448 kJ/mol for acetic acid) revealed the acidic character of the methyl group attached to the aliphatic chain of DCTB. This finding is in agreement with NMR data presented by Gabriel et al.,[90] who reported the highly acidic character of this methyl group, in contrast to the widely accepted aprotic description of DCTB. These data together with the above-mentioned findings support an additional proton-transfer ionization mechanism of DCTB as MALDI matrix.

MALDI Matrix-Dependent Tissue-Specific Ion Suppression. To assess the usefulness of DCTB as nonpolar MALDI matrix for low molecular weight lipophilic CNS drugs, we selected five model compounds (Figure 2), representing different fields of neuropharmacological application: xylazine (veterinary tranquilizer/anesthetic), ketamine (drugs of abuse but also promising as rapid and potent antidepressant), clonidine (anxiety disorder and withdrawal syndrome therapeutic), imipramine (tricyclic antidepressant), and clozapine (atypical antipsychotic treatment for schizophrenia). All selected compounds have molecular weights in the range of 200–400 g/mol and are predominantly in their neutral forms at physiological pH of blood and brain; consequently, the calculated distribution coefficients clogD at pH 7.4 are between 1 and 3 (Figure 2), thus confirming the liphophilic character at these conditions.
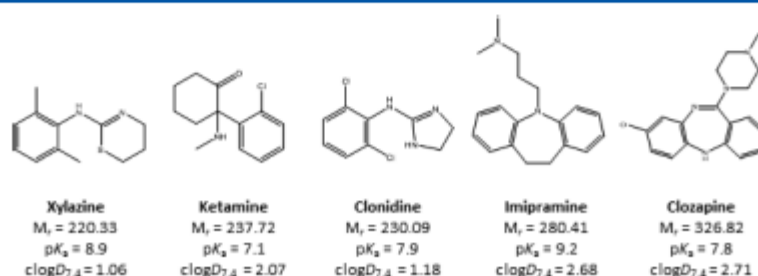

Figure 2. Chemical structures of the five CNS drugs investigated in this study, along with molecular weights and calculated pK_a and clogD values (at physiological pH of 7.4).

In the first set of experiments, we conducted MALDI-FTICR analyses. As can be seen in Figure 3A, the CHCA
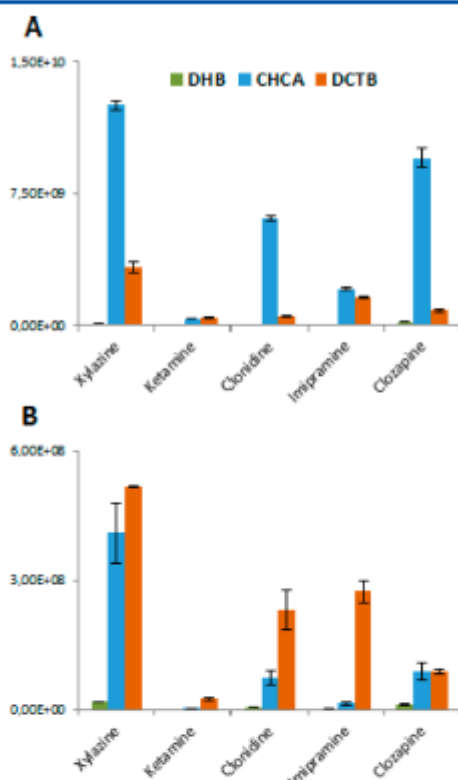

Figure 3. Bar chart showing signal intensities for (A) standard solutions of five CNS drugs obtained by MALDI-FTICR after dried-droplet sample preparation using DHB, CHCA, and DCTB matrices; (B) standard solutions spiked into mouse brain extract. (Error bars represent standard deviation, SD ($n = 3$); 16 transients from at least 3 different MALDI spots for inter and intraspot variability corrections were collected of the individual drug standards (10 μM) with dried-droplet sample preparation.).

matrix provided the highest signal intensities. The same drugs mixed with brain extract (obtained from isoflurane-anesthetized mouse according to a modified protocol[61]) to indicate the presence of potentially suppressing endogenous compounds exhibited the highest signal intensities when DCTB matrix was used (Figure 3B). This provided strong evidence for considerably lower signal suppression from endogenous brain-tissue-related compounds with a nonpolar DCTB matrix as compared to CHCA and DHB. DHB gave significantly lower signal intensities and also suffered from limitations of spatial resolving power due to the large crystals formed during spraying (see SEM images in Figure S-1, SI). In all further experiments, we therefore limited all further comparisons to CHCA versus DCTB.

To further validate these findings for MALDI-MSI, we employed the tissue extinction coefficient (TEC) technique developed by Stoeckli et al.,[59] which was later expanded by Hamm et al.[59] Recently, Taylor et al. implemented TECs for systematic comparison of DESI and MALDI (with CHCA

matrix)-related ion suppression of uniformly deposited olanzapine from heterogeneous transverse brain sections.[60] For the TEC experiments, an equimolar mixture of five CNS drugs was sprayed onto the glass slide containing the three thaw-mounted negative control (isoflurane-anesthetized) brain coronal sections, followed by MALDI-FTICR–MSI (see Experimental Section). As reference, the off-tissue glass region of interest was selected and imaged with the same experimental conditions. The final TEC values were calculated based on the relationship TEC $= I_{A,tissue}/I_{A,ref}$ where I_A are the averaged analyte ion currents on tissue and reference areas, TEC $= 1$ represents no suppression and TEC $= 0$ corresponds to total drug signal extinction. The results in Figure 4 show as much as
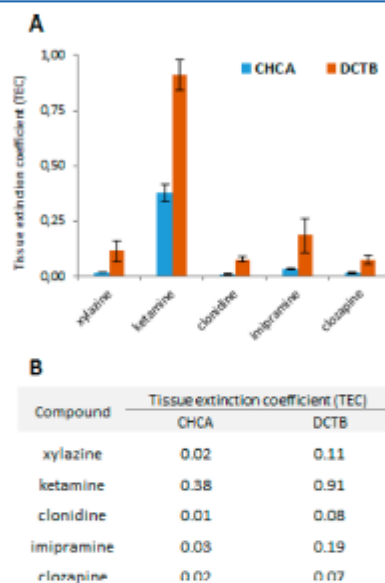

Figure 4. Bar chart (A) and numerical values (B) of tissue extinction coefficients (TEC) calculated for five CNS drugs based on the MALDI-FTICR imaging experiments performed with CHCA and DCTB matrices.

8-fold less suppression with DCTB in comparison to CHCA and thus provide strong evidence for matrix-dependent, tissue-specific ionization suppression. Furthermore, closer investigation of the ion images of the five CNS drugs (Figure S-2, SI) revealed a heterogeneous pattern of drug signal suppression (white versus gray matter), which was further underpinned by comparisons of mean mass spectra of the whole brain sections for the two matrices (see Figure S-3, SI).

In conclusion, while the current results may not provide a complete explanation of the improved performance of DCTB for MALDI imaging of the investigated CNS drugs from brain sections in comparison to CHCA, some initial positive conclusions can be drawn. DCTB clearly showed increased selectivity toward lipophilic CNS drugs as well as higher "resistance" to brain-specific ionization suppression phenomena from endogenous compounds such as salts, metabolites, lipids etc. as compared to CHCA. While the organic solvent used for dissolving DTCB may provide more efficient extraction of neutral analytes in comparison to CHCA, this does not explain the observed differences, because the lower
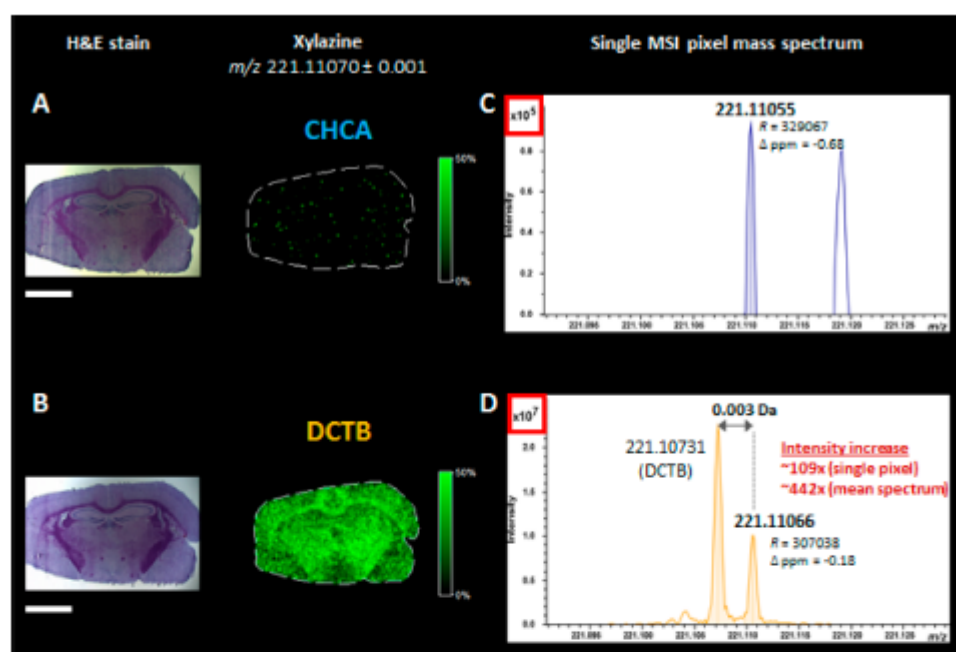
Figure 5. Spatial distribution of xylazine in mouse brain coronal sections obtained from MALDI-FTICR imaging experiments performed on two consecutive sections with two different MALDI matrices, CHCA (A) and DCTB (B), along with single MSI pixel mass spectra extracted from representative regions of the highest abundance of xylazine detected with CHCA (C) and DCTB (D). MSI pixel size: 100 μm. Scale bars: 2 mm.

signal suppression levels of DCTB were observed not only during MALDI-MSI of tissue sections but also from MALDI-MS analysis of bulk solutions containing the same interfering substances from the brain-tissue extract. Unfortunately, it was not possible to fully clarify whether the observed effects were related to favorable desorption and gas-phase protonation of the investigated analytes or whether they result from physicochemical processes such as more efficient incorporation of nonionized lipophilic drugs and/or less efficient incorporation of endogenous interfering metabolites/lipids into the nonpolar DCTB matrix crystals. Further work on this topic is ongoing in the present authors' laboratory.

Xylazine Spatial Distribution in Mouse Brain Sections Using Ultrahigh Resolution FTICR–MSI. The utility of DCTB for MALDI-MSI of lipophilic CNS drugs was demonstrated using native brain tissues of drug-dosed animals (single dose anesthesia with a mixture of xylazine/ketamine, see Experimental Section). The intense signals detected from xylazine were assigned based on accurate mass measurements and on-tissue collision-induced dissociation (CID) experiments by comparison to the drug standard and previously reported fragmentation patterns (Figure S-4, SI).[92] We then conducted two MALDI-MSI experiments on consecutive coronal brain sections at spatial resolution of 100 μm. As illustrated in Figure 5, tissue examined with CHCA matrix showed virtually no signals from xylazine, whereas tissue sprayed with DCTB matrix clearly revealed the spatial distribution of the drug (normalized to isotope-labeled internal standard). Since the examined tissue section clearly shows the anatomical regions in the H&E stain of the brain, the MS ion image of evenly sprayed xylazine-d_6 provided additional evidence for regional ion suppression, with the protonated

xylazine molecule clearly less suppressed in the region of deep cerebral white matter as compared to the cerebral cortex, hippocampus, thalamus and hypothalamus (Figure 6).

Furthermore, to quantify the differences observed for the two matrices, single MSI pixel mass spectra from representative regions of the highest xylazine abundance were compared, showing more than 100-fold higher signal intensity obtained with DCTB over CHCA. Moreover, when the average mass spectra from the whole examined tissue sections were compared, >440-fold signal improvement was achieved with DCTB versus CHCA. Importantly, the ultrahigh resolving power of the Fourier transform ion cyclotron resonance mass spectrometer used here played a significant role in this comparison, since a DCTB-derived interfering ion signal was visible only 0.003 u adjacent to protonated xylazine. This interference had practical implications on the direct on-tissue quantification of xylazine (see next section). In addition to xylazine, we also interrogated the MSI data sets for the second administered anesthetic, ketamine, as well as for potential metabolites of both drugs. As shown in the previous section, ketamine exhibited much lower ionization efficiency in comparison to xylazine and was therefore not detected in the imaging experiments. Equally, we did not observe any of the reported biotransformation products of xylazine[92] or ketamine.[93]

On-Tissue Quantification of Xylazine. Since most pharmaceutical MALDI-MSI studies require absolute quantification of the investigated compounds directly from the tissue surfaces, we also implemented the DCTB matrix for this purpose. Obtaining reliable quantitative results with MALDI-MSI requires normalization to isotopically labeled internal standard (xylazine-d_6) and matrix-matched calibration rou-
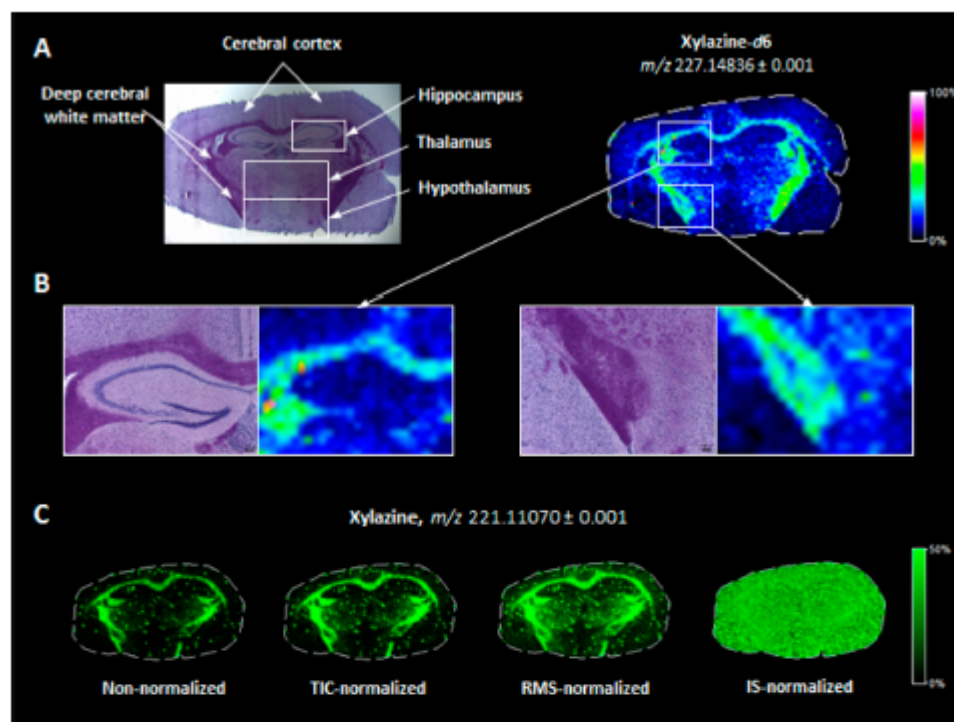
Figure 6. (A) MS ion image (not normalized) of the evenly distributed internal standard (xylazine-d_6) on brain coronal section obtained from xylazine-anesthetized mouse; (B) two expanded subregions (hippocampus and deep cerebral white matter) showing clear evidence for brain-subregion-specific ion suppression of the deuterated drug signal. MSI pixel size: 100 μm. (C) MS ion images of the evenly distributed xylazine standard on brain coronal section obtained from isoflurane-anesthetized mouse showing superior performance of normalization against an isotope-labeled internal standard (IS) in comparison with two other common strategies (TIC and RMS). MSI pixel size: 100 μm.

tines. The best results for the latter are usually obtained by using either the sophisticated "mimetic tissue" model or a simpler "on-tissue" approach.[20] Here, we combined both strategies (the workflow is presented in Figure S-5, SI). Briefly, rabbit brain was homogenized and snap-frozen in liquid nitrogen for the best possible emulation of the original intact tissue morphology, as previously reported by Jadoul et al.[94] The prepared blocks of "unified brain" tissue (containing a representation of the interfering endogenous compounds from different anatomical brain regions) were then cut with the cryomicrotome and served as large and convenient blank sections for the fast "on-tissue" spiking approach.

This approach generated linear relationships (coefficients of determination, $R^2 = 0.996$) over a wide concentration range of the calibration curve (almost 3 orders of magnitude, see Figure S-5, SI). The limits of detection (LOD, estimated from multiple blank measurements) and limits of quantification LOQ, (based on a precision of the measurements of 20% or better and calculated bias values for the lowest concentrated calibration solution within 80–120%) were 0.629 and 3.14 μg/g, respectively (assuming average brain density of 1.027 g/cm³).[95] Finally, the average absolute concentration of xylazine across the mouse brain coronal section illustrated in Figure 5B was calculated to be 21.75 ± 0.41 μg/g_{tissue}. The relatively large confidence interval of the mean was calculated based on the standard deviation of all scans (scan number, $n = 4255$),

averaged across the whole tissue section; therefore, it reflects the heterogeneity of xylazine distribution in the brain section.

■ CONCLUSIONS

The primary aim of this study was the application of the nonpolar DCTB compound as MALDI matrix for high sensitivity imaging of CNS drugs in mouse brain sections. Based on five selected neuropharmaceuticals, which all fulfilled the requirements for crossing the blood–brain barrier via transcellular passive diffusion (i.e., Lipinski's rule of five), we demonstrated that DCTB can be successfully used for highly sensitive MALDI mass spectral imaging of these compounds from murine brain sections using an ultrahigh resolution Fourier transform ion cyclotron resonance (FTICR) platform. We provided a theoretical and experimental rationale for an additional proton-transfer ionization mechanism of the DCTB matrix, even though DCTB is usually considered an electron-transfer matrix. We also investigated tissue-specific ion suppression for DCTB versus the conventional polar and acidic CHCA matrix, based on tissue extinction coefficients (TEC). These experiments showed multifold lower signal suppression for the drugs using DCTB as opposed to CHCA. Furthermore, we applied DCTB for quantitative imaging of a commonly used veterinary anesthetic drug, xylazine, from mouse coronal brain sections. Compared to CHCA, the data showed significant signal intensity improvements by as much as 100-fold for representative single MSI pixels of two serial

sections and more than 440-fold for an average mass spectrum from the whole adjacent tissue sections. Finally, the application of tissue-matched standardization allowed for excellent linearity of the calibration curve over a wide concentration range with satisfactory precision.

The use of the DCTB matrix was not without challenges, however, including difficulties linked to the low melting point (~130 versus ~249 °C for CHCA), i.e., limited stability under high vacuum conditions (which was overcome by normalization to homogeneously sprayed internal standard) and the "volcano" type ablation profiles, which can constitute a challenge for higher spatial resolutions than used here. We did not observe any formation of adducts between DCTB and drugs as previously described by Lou et al.[96]

Our future work will focus on improving the DCTB matrix solubility and stability under high vacuum conditions. Other work currently in progress includes a detailed investigation of the tissue-specific ionization suppression of different drugs when using different MALDI matrices, which will further improve the detection capabilities of MALDI-MSI for other pharmaceutical drugs.

■ ASSOCIATED CONTENT

❺ Supporting Information

The Supporting Information is available free of charge on the ACS Publications website at DOI: 10.1021/acs.analchem.8b02740.

> SEM of sprayed MALDI matrices; MS ion images and mean spectra from TEC experiments; mean mass spectra obtained from TEC experiments of mouse brain coronal sections; on-tissue identification of xylazine; on-tissue quantification workflow and calibration curves (PDF)

■ AUTHOR INFORMATION

Corresponding Author

*Mailing Address: Dr. Dietrich A. Volmer, Department of Chemistry, Humboldt University of Berlin, Brook-Taylor-Str. 2, 12489 Berlin, Germany; Tel: +49 30 2093 7588; E-mail: dietrich.volmer@hu-berlin.de.

ORCID

Dietrich A. Volmer: 0000-0003-2820-1480

Notes

The authors declare no competing financial interest.

■ ACKNOWLEDGMENTS

■ REFERENCES

(1) Pangalos, M. N.; Schechter, L. E.; Hurko, O. *Nat. Rev. Drug Discovery* **2007**, *6* (7), 521–532.

(2) Pardridge, W. M. *Drug Discovery Today* **2007**, *12* (1–2), 54–61.

(3) Pardridge, W. M. *Pharm. Res.* **2007**, *24* (9), 1733–1744.

(4) Palmer, A. M.; Alavijeh, M. S. *Drug Discovery Today* **2012**, *17* (19–20), 1068–1078.

(5) Lipinski, C. A. *J. Pharmacol. Toxicol. Methods* **2000**, *44* (1), 235–249.

(6) Mikitsh, J. L.; Chacko, A. M. *Perspect. Med. Chem.* **2014**, *6*, 11–24.

(7) Pardridge, W. M. *J. Cereb. Blood Flow Metab.* **2012**, *32* (11), 1959–1972.

(8) Lai, F.; Fadda, A. M.; Sinico, C. *Expert Opin. Drug Delivery* **2013**, *10* (7), 1003–1022.

(9) Wohlfart, S.; Gelperina, S.; Kreuter, J. *J. Controlled Release* **2012**, *161* (2), 264–273.

(10) Saraiva, C.; Praça, C.; Ferreira, R.; Santos, T.; Ferreira, L.; Bernardino, L. *J. Controlled Release* **2016**, *235*, 34–47.

(11) Rudin, M.; Weissleder, R. *Nat. Rev. Drug Discovery* **2003**, *2* (2), 123–131.

(12) Willmann, J. K.; van Bruggen, N.; Dinkelborg, L. M.; Gambhir, S. S. *Nat. Rev. Drug Discovery* **2008**, *7* (7), 591–607.

(13) Pellegatti, M.; Pagliarusco, S. *Expert Opin. Drug Metab. Toxicol.* **2011**, *7* (2), 137–146.

(14) Pardridge, W. M. *Expert Opin. Drug Delivery* **2016**, *13* (7), 963–975.

(15) Solon, E. G.; Schweitzer, A.; Stoeckli, M.; Prideaux, B. *AAPS J.* **2010**, *12* (1), 11–26.

(16) Cobice, D. F.; Goodwin, R. J. A.; Andren, P. E.; Nilsson, A.; Mackay, C. L.; Andrew, R. *Br. J. Pharmacol.* **2015**, *172* (13), 3266–3283.

(17) Sugiura, Y.; Setou, M. *J. Neuroimmune Pharmacol.* **2010**, *5* (1), 31–43.

(18) Sun, N.; Walch, A. *Histochem. Cell Biol.* **2013**, *140* (2), 93–104.

(19) Ellis, S. R.; Bruinen, A. L.; Heeren, R. M. A. *Anal. Bioanal. Chem.* **2014**, *406* (5), 1275–1289.

(20) Rzagalinski, I.; Volmer, D. A. *Biochim. Biophys. Acta, Proteins Proteomics* **2017**, *1865* (7), 726–739.

(21) Chughtai, K.; Heeren, R. M. A. *Chem. Rev.* **2010**, *110* (5), 3237–3277.

(22) Norris, J. L.; Caprioli, R. M. *Chem. Rev.* **2013**, *113* (4), 2309–2342.

(23) Spengler, B. *Anal. Chem.* **2015**, *87* (1), 64–82.

(24) Bodzon-Kulakowska, A.; Suder, P. *Mass Spectrom. Rev.* **2016**, *35* (1), 147–169.

(25) Palmer, A.; Trede, D.; Alexandrov, T. *Metabolomics* **2016**, *12* (6), 107.

(26) Karlsson, O.; Hanrieder, J. *Arch. Toxicol.* **2017**, *91* (6), 2283–2294.

(27) Swales, J. G.; Hamm, G.; Clench, M. R.; Goodwin, R. J. A. *Int. J. Mass Spectrom.* **2018**, DOI: 10.1016/j.ijms.2018.02.007.

(28) Goodwin, R. J.; Pitt, A. R. *Bioanalysis* **2010**, *2* (2), 279–293.

(29) Greer, T.; Sturm, R.; Li, L. *J. Proteomics* **2011**, *74* (12), 2617–2631.

(30) Prideaux, B.; Stoeckli, M. *J. Proteomics* **2012**, *75* (16), 4999–5013.

(31) Hochart, G.; Hamm, G.; Stauber, J. *Bioanalysis* **2014**, *6* (20), 2775–2788.

(32) Nilsson, A.; Goodwin, R. J. A.; Shariatgorji, M.; Vallianatou, T.; Webborn, P. J. H.; Andren, P. E. *Anal. Chem.* **2015**, *87* (3), 1437–1455.

(33) Shariatgorji, M.; Svenningsson, P.; Andrén, P. E. *Neuropsychopharmacology* **2014**, *39* (1), 34–39.

(34) Hsieh, Y.; Casale, R.; Fukuda, E.; Chen, J.; Knemeyer, I.; Wingate, J.; Morrison, R.; Korfmacher, W. *Rapid Commun. Mass Spectrom.* **2006**, *20* (6), 965–972.

(35) Li, F.; Hsieh, Y.; Kang, L.; Sondey, C.; Lachowicz, J.; Korfmacher, W. A. *Bioanalysis* **2009**, *1* (2), 299–307.

(36) Shin, Y. G.; Dong, T.; Chou, B.; Menghrajani, K. *Arch. Pharmacal Res.* **2011**, *34* (11), 1983–1988.

(37) Shanta, S. R.; Kim, T. Y.; Hong, J. H.; Lee, J. H.; Shin, C. Y.; Kim, K.-H.; Kim, Y. H.; Kim, S. K.; Kim, K. P. *Analyst* **2012**, *137* (24), 5757.

(38) Källback, P.; Shariatgorji, M.; Nilsson, A.; Andrén, P. E. *J. Proteomics* **2012**, *75* (16), 4941–4951.

(39) Hamm, G.; Bonnel, D.; Legouffe, R.; Pamelard, F.; Delbos, J. M.; Bouzom, F.; Stauber, J. *J. Proteomics* **2012**, *75* (16), 4952–4961.

(40) Castellino, S.; Groseclose, M. R.; Sigafoos, J.; Wagner, D.; De Serres, M.; Polli, J. W.; Romach, E.; Myer, J.; Hamilton, B. *Chem. Res. Toxicol.* **2013**, *26* (2), 241–251.

(41) Salphati, L.; Shahidi-Latham, S.; Quiason, C.; Barck, K.; Nishimura, M.; Alicke, B.; Pang, J.; Carano, R. A.; Olivero, A. G.; Phillips, H. S. *Drug Metab. Dispos.* **2014**, *42* (7), 1110–1116.

(42) Swales, J. G.; Tucker, J. W.; Strittmatter, N.; Nilsson, A.; Cobice, D.; Clench, M. R.; Mackay, C. L.; Andren, P. E.; Takáts, Z.; Webborn, P. J. H. *Anal. Chem.* **2014**, *86* (16), 8473–8480.

(43) Liu, X.; Ide, J. L.; Norton, I.; Marchionni, M. A.; Ebling, M. C.; Wang, L. Y.; Davis, E.; Sauvageot, C. M.; Kesari, S.; Kellersberger, K. A. *Sci. Rep.* **2013**, *3*, 2859.

(44) Aikawa, H.; Hayashi, M.; Ryu, S.; Yamashita, M.; Ohtsuka, N.; Nishidate, M.; Fujiwara, Y.; Hamada, A. *Sci. Rep.* **2016**, *6*, 23749.

(45) Tanaka, Y.; Hirata, M.; Shinonome, S.; Torii, M.; Nezasa, K. I.; Tanaka, H. *Sci. Rep.* **2018**, *8*, 343.

(46) Shariatgorji, M.; Källback, P.; Gustavsson, L.; Schintu, N.; Svenningsson, P.; Goodwin, R. J. A.; Andren, P. E. *Anal. Chem.* **2012**, *84* (10), 4603–4607.

(47) Reich, R. F.; Cudzilo, K.; Levisky, J. A.; Yost, R. A. *J. Am. Soc. Mass Spectrom.* **2010**, *21* (4), 564–571.

(48) Kuwayama, K.; Tsujikawa, K.; Miyaguchi, H.; Kanamori, T.; Iwata, Y. T.; Inoue, H. *Anal. Bioanal. Chem.* **2012**, *404* (6–7), 1823–1830.

(49) Pirman, D. A.; Reich, R. F.; Kiss, A.; Heeren, R. M. A.; Yost, R. A. *Anal. Chem.* **2013**, *85* (2), 1081–1089.

(50) Kadar, H.; Le Douaron, G.; Amar, M.; Ferrié, L.; Figadère, B.; Touboul, D.; Brunelle, A.; Raisman-Vozari, R. *Neurotoxic. Res.* **2014**, *25* (1), 135–145.

(51) Goodwin, R. J. A.; MacKay, C. L.; Nilsson, A.; Harrison, D. J.; Farde, L.; Andren, P. E.; Iverson, S. L. *Anal. Chem.* **2011**, *83* (24), 9694–9701.

(52) Vallianatou, T.; Strittmatter, N.; Nilsson, A.; Shariatgorji, M.; Hamm, G.; Pereira, M.; Källback, P.; Svenningsson, P.; Karlgren, M.; Goodwin, R. J. A.; et al. *NeuroImage* **2018**, *172*, 808–816.

(53) McClure, R. A.; Chumbley, C. W.; Reyzer, M. L.; Wilson, K.; Caprioli, R. M.; Gore, J. C.; Pham, W. *NeuroImage Clin.* **2013**, *2* (1), 620–629.

(54) Goodwin, R. J.; Webborn, P. J. *Bioanalysis* **2015**, *7* (20), 2667–2673.

(55) Castellino, S.; Groseclose, M. R.; Wagner, D. *Bioanalysis* **2011**, *3* (21), 2427–2441.

(56) Annesley, T. M. *Clin. Chem.* **2003**, *49* (7), 1041–1044.

(57) Volmer, D. A.; Jessome, L. L. *LCGC North Am.* **2006**, *24* (5), 498–510.

(58) Furey, A.; Moriarty, M.; Bane, V.; Kinsella, B.; Lehane, M. *Talanta* **2013**, *115*, 104–122.

(59) Stoeckli, M.; Staab, D.; Schweitzer, A. *Int. J. Mass Spectrom.* **2007**, *260* (2–3), 195–202.

(60) Taylor, A.; Dexter, A.; Bunch, J. *Anal. Chem.* **2018**, *90*, 5637–5645.

(61) Seeley, E. H.; Oppenheimer, S. R.; Mi, D.; Chaurand, P.; Caprioli, R. M. *J. Am. Soc. Mass Spectrom.* **2008**, *19* (8), 1069–1077.

(62) Andersson, M.; Groseclose, M. R.; Deutch, A. Y.; Caprioli, R. M. *Nat. Methods* **2008**, *5* (1), 101–108.

(63) Wang, H. Y. J.; Wu, H. W.; Tsai, P. J.; Liu, C. *Anal. Bioanal. Chem.* **2012**, *404* (1), 113–124.

(64) Yang, H.; Ji, W.; Guan, M.; Li, S.; Zhang, Y.; Zhao, Z.; Mao, L. *Metabolomics* **2018**, *14* (4), 50.

(65) Song, X.; Luo, Z.; Li, X.; Li, T.; Wang, Z.; Sun, C.; Huang, L.; Xie, P.; Liu, X.; He, J.; et al. *Anal. Chem.* **2017**, *89* (12), 6318–6323.

(66) Popkova, Y.; Schiller, J. *Rapid Commun. Mass Spectrom.* **2017**, *31* (5), 411–418.

(67) Griffiths, R. L.; Bunch, J. *Rapid Commun. Mass Spectrom.* **2012**, *26* (13), 1557–1566.

(68) Sugiyama, E.; Masaki, N.; Matsushita, S.; Setou, M. *Anal. Chem.* **2015**, *87* (22), 11176–11181.

(69) Wang, X.; Han, J.; Yang, J.; Pan, J.; Borchers, C. H. *Chem. Sci.* **2015**, *6* (1), 729–738.

(70) Huang, X.; Zhan, L.; Sun, J.; Xue, J.; Liu, H.; Xiong, C.; Nie, Z. *Anal. Chem.* **2018**, *90* (14), 8309–8313.

(71) Dufresne, M.; Thomas, A.; Breault-Turcot, J.; Masson, J.-F.; Chaurand, P. *Anal. Chem.* **2013**, *85* (6), 3318–3324.

(72) Esteve, C.; Tolner, E. A.; Shyti, R.; van den Maagdenberg, A. M. J. M.; McDonnell, L. A. *Metabolomics* **2016**, *12* (2), 30.

(73) Lin, Z.; Cai, Z. *Mass Spectrom. Rev.* **2018**, *37* (5), 681–696.

(74) Wang, H. Y. J.; Jackson, S. N.; McEuen, J.; Woods, A. S. *Anal. Chem.* **2005**, *77* (20), 6682–6686.

(75) Rzagalinski, I.; Hainz, N.; Meier, C.; Tschernig, T.; Volmer, D. A. *J. Am. Soc. Mass Spectrom.* **2018**, *29* (4), 711–722.

(76) Schramm, T.; Hester, A.; Klinkert, I.; Both, J. P.; Heeren, R. M. A.; Brunelle, A.; Laprévote, O.; Desbenoit, N.; Robbe, M. F.; Stoeckli, M.; et al. *J. Proteomics* **2012**, *75* (16), 5106–5110.

(77) Bokhart, M. T.; Nazari, M.; Garrard, K. P.; Muddiman, D. C. *J. Am. Soc. Mass Spectrom.* **2018**, *29* (1), 8–16.

(78) Toomsalu, E.; Koppel, I. A.; Burk, P. *J. Chem. Theory Comput.* **2013**, *9* (9), 3947–3958.

(79) Rayne, S.; Forest, K. *Can. J. Chem.* **2016**, *94* (3), 251–258.

(80) Frisch, M. J.; Trucks, G. W.; Schlegel, H. B.; Scuseria, G. E.; Robb, M. A.; Cheeseman, J. R.; Scalmani, G.; Barone, V.; Mennucci, B.; Petersson, G. A.; Nakatsuji, H.; Caricato, M.; Li, X.; Hratchian, H. P.; Izmaylov, A. F.; Bloino, J.; Zheng, G.; Sonnenberg, J. L.; Hada, M.; Ehara, M.; Toyota, K.; Fukuda, R.; Hasegawa, J.; Ishida, M.; Nakajima, T.; Honda, Y.; Kitao, O.; Nakai, H.; Vreven, T.; Montgomery, J. A., Jr.; Peralta, J. E.; Ogliaro, F.; Bearpark, M.; Heyd, J. J.; Brothers, E.; Kudin, K. N.; Staroverov, V. N.; Kobayashi, R.; Normand, J.; Raghavachari, K.; Rendell, A.; Burant, J. C.; Iyengar, S. S.; Tomasi, J.; Cossi, M.; Rega, N.; Millam, J. M.; Klene, M.; Knox, J. E.; Cross, J. B.; Bakken, V.; Adamo, C.; Jaramillo, J.; Gomperts, R.; Stratmann, R. E.; Yazyev, O.; Austin, A. J.; Cammi, R.; Pomelli, C.; Ochterski, J. W.; Martin, R. L.; Morokuma, K.; Zakrzewski, V. G.; Voth, G. A.; Salvador, P.; Dannenberg, J. J.; Dapprich, S.; Daniels, A. D.; Farkas, O.; Foresman, J. B.; Ortiz, J. V.; Cioslowski, J.; Fox, D. J. *Gaussian 09*, revision A.02; Gaussian, Inc.: Wallingford, CT, 2009.

(81) Ulmer, L.; Mattay, J.; Torres-Garcia, H.; Luftmann, H. *Eur. J. Mass Spectrom.* **2000**, *6* (1), 49.

(82) Mizukado, J.; Sato, H.; Chen, L.; Suzuki, Y.; Yamane, S.; Aoyama, Y.; Yoshida, Y.; Suda, H. *J. Mass Spectrom.* **2015**, *50* (8), 1006–1012.

(83) Markov, V. Y.; Borschevsky, A. Y.; Sidorov, L. N. *Int. J. Mass Spectrom.* **2012**, *325–327*, 100–112.

(84) Bergman, N.; Thapper, A.; Styring, S.; Bergquist, J.; Shevchenko, D. *Anal. Methods* **2014**, *6* (21), 8513–8518.

(85) Kumara, C.; Dass, A. *Anal. Chem.* **2014**, *86* (9), 4227–4232.

(86) Wyatt, M. F.; Stein, B. K.; Brenton, A. G. *Anal. Chem.* **2006**, *78* (1), 199–206.

(87) Jaskolla, T. W.; Karas, M. *J. Am. Soc. Mass Spectrom.* **2011**, *22* (6), 976–988.

(88) Knochenmuss, R. *Analyst* **2006**, *131* (9), 966.

(89) Soltwisch, J.; Jaskolla, T. W.; Hillenkamp, F.; Karas, M.; Dreisewerd, K. *Anal. Chem.* **2012**, *84* (15), 6567–6576.

(90) Gabriel, S. J.; Pfeifer, D.; Schwarzinger, C.; Panne, U.; Weidner, S. M. *Rapid Commun. Mass Spectrom.* **2014**, *28* (5), 489–498.

(91) Want, E. J.; Masson, P.; Michopoulos, F.; Wilson, I. D.; Theodoridis, G.; Plumb, R. S.; Shockcor, J.; Loftus, N.; Holmes, E.; Nicholson, J. K. *Nat. Protoc.* **2013**, *8* (1), 17–32.

(92) Meyer, G. M. J.; Maurer, H. H. *Anal. Bioanal. Chem.* **2013**, *405* (30), 9779–9789.

(93) Porpiglia, N.; Musile, G.; Bortolotti, F.; De Palo, E. F.; Tagliaro, F. *Forensic Sci. Int.* **2016**, *266*, 304–310.

(94) Jadoul, L.; Longuespée, R.; Noël, A.; De Pauw, E. *Anal. Bioanal. Chem.* **2015**, *407* (8), 2095–2106.

(95) Barber, T. W.; Brockway, J. A.; Higgins, L. S. *Acta Neurol. Scand.* **1970**, *46* (1), 85–92.

(96) Lou, X.; De Waal, B. F. M.; Van Dongen, J. L. J.; Vekemans, J. A. J. M.; Meijer, E. W. *J. Mass Spectrom.* **2010**, *45* (10), 1195–1202.

Supporting Information

Toward Higher Sensitivity in Quantitative MALDI Imaging Mass Spectrometry of CNS Drugs Using a Nonpolar Matrix

Ignacy Rzagalinski[1], Borislav Kovačević[2], Nadine Hainz[3], Carola Meier[3], Thomas Tschernig[3], Dietrich A. Volmer[4]*

[1]*Institute of Bioanalytical Chemistry, Saarland University, 66123 Saarbrücken, Germany*
[2]*Group for Computational Life Sciences, Ruđer Bošković Institute, 10000 Zagreb, Croatia*
[3]*Institute of Anatomy and Cell Biology, Saarland University, 66421 Homburg, Germany*
[4]*Department of Chemistry, Humboldt University of Berlin, 12489 Berlin, Germany*

*To whom correspondence should be addressed:

Prof. Dr. Dietrich A. Volmer
Department of Chemistry
Humboldt University of Berlin
Brook-Taylor-Str. 2
12489 Berlin, Germany
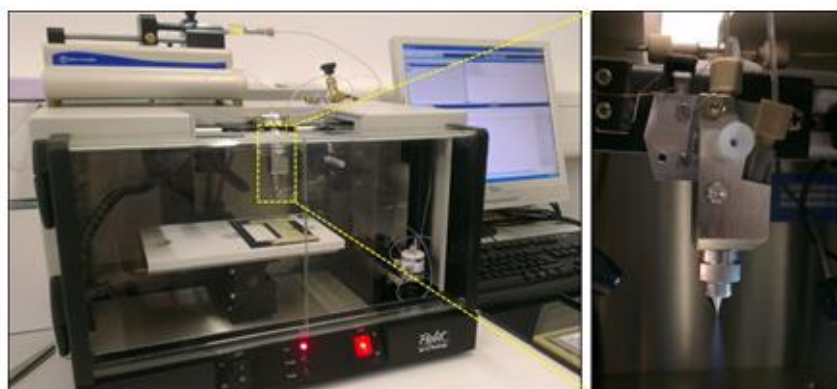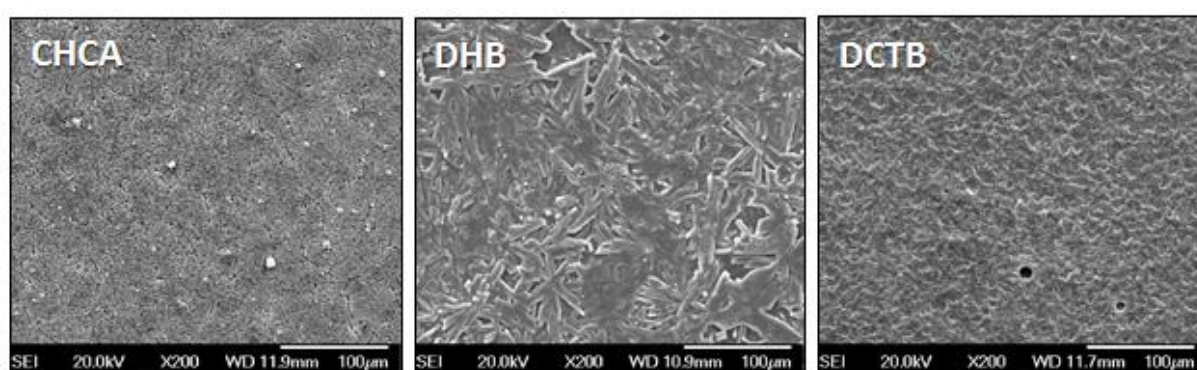Tel: +49 30 2093 7575
Email: dietrich.volmer@hu-berlin.de

Figure S-1. (A) Home-built robotic sprayer based on the Probot micro fraction collector platform, syringe pump and micro spraying nozzle, providing a fine and highly reproducible spray. **(B)** SEM images of different MALDI matrices: CHCA (left), DHB (middle) and DCTB (right) sprayed onto the surface of the control brain section. Magnification: 200×; scale bars: 100 μm.
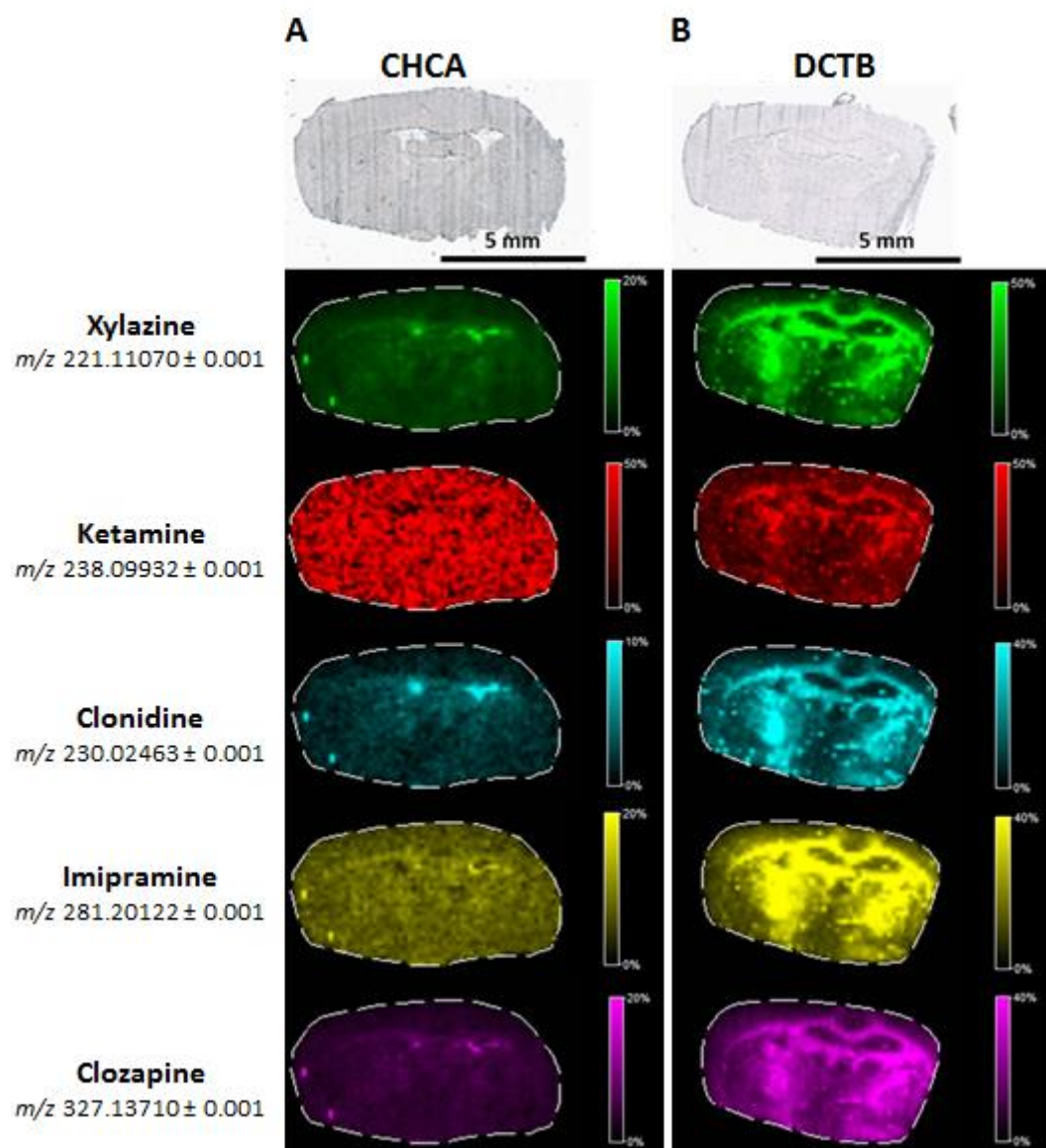
Figure S-2. MS ion images (non-normalized) of five investigated CNS drugs (xylazine, ketamine, clonidine, imipramine and clozapine) acquired from MALDI-FTICR imaging TEC experiments of mouse brain coronal sections (optical images above) performed with two different MALDI matrices: CHCA **(A)** and DCTB **(B)**. Pixel size: 150 µm; scale bars: 5 mm. (Note: different scales of the color schemes were used here in to expose the heterogeneity of tissue-specific ion suppression. For quantitative comparison of the averaged intensities obtained from CNS drugs with two different matrices, see the graphs presented in Figures 3 and 4 in the main text.)
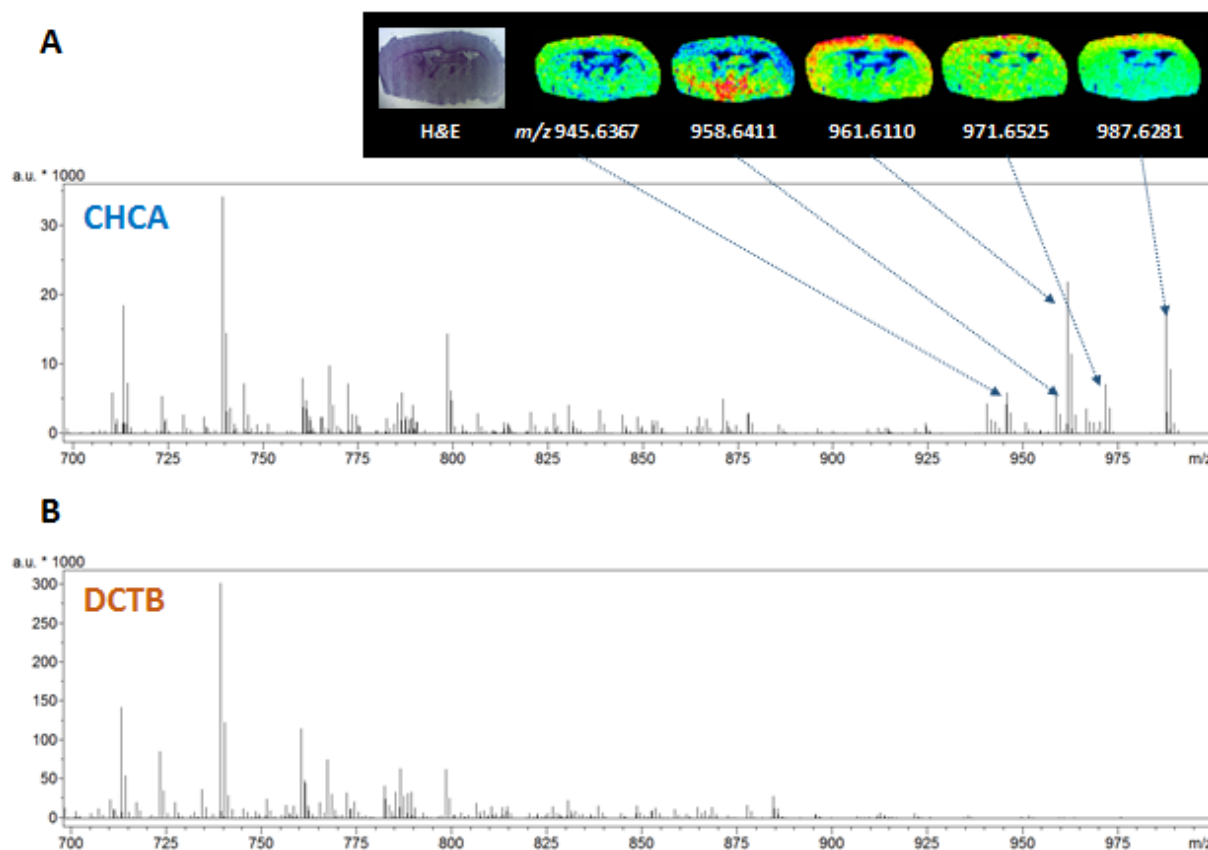
Figure S-3. Mean mass spectra obtained from MALDI-FTICR imaging TEC experiments of mouse brain coronal sections performed with two different MALDI matrices: CHCA **(A)** and DCTB **(B)** within the range from *m/z* 700 to 1000. As can be seen, several prominent signals were detected exclusively with CHCA matrix in the region between m/z 900 and 1000 and they were tentatively assigned to the sodiated or potassiated phosphatidylinositols based on accurate mass measurement and matching to the METLIN database (http://metlin.scripps.edu).
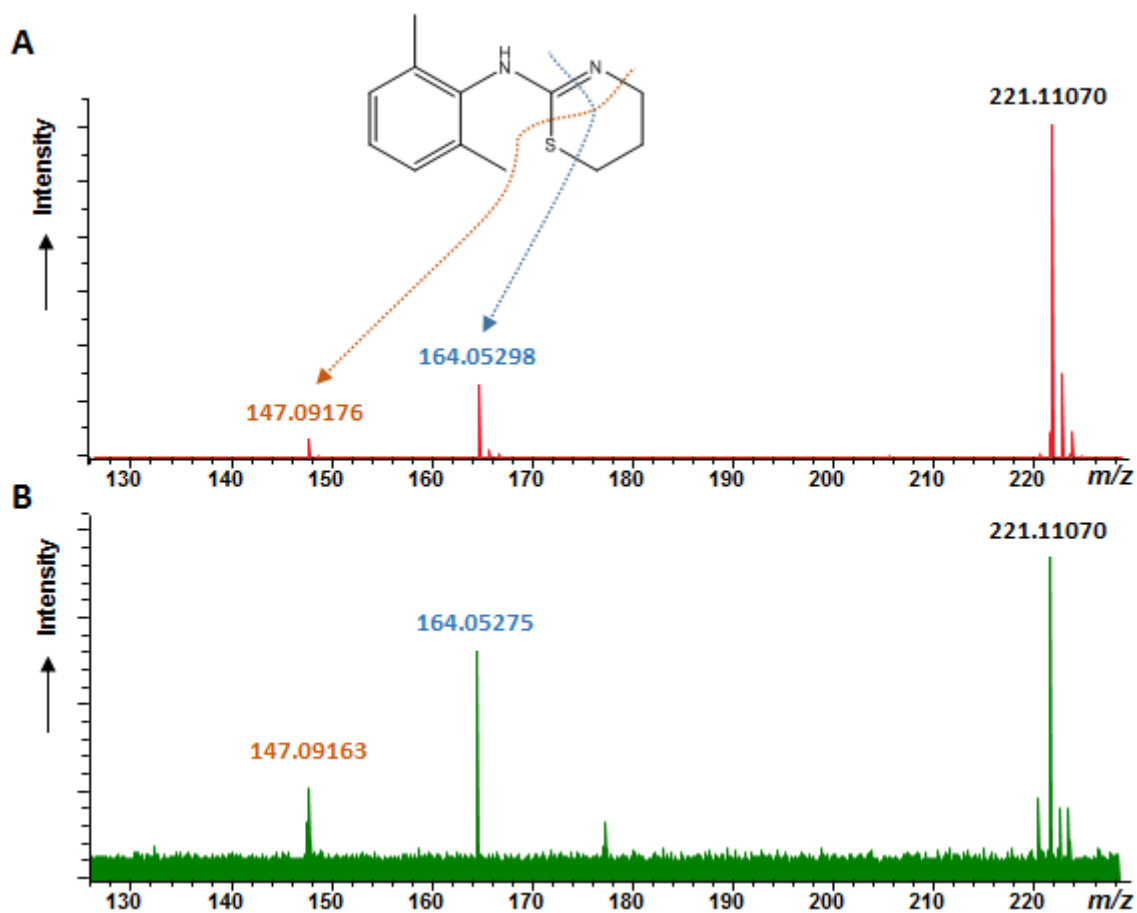
Figure S-4. Collision-induced dissociation mass spectra of protonated xylazine obtained with MALDI-FTICR from drug standard after dried-droplet sample preparation **(A)** and from on-tissue (mouse brain) MALDI-FTICR **(B)**. The proposed fragmentation pattern is shown in the upper spectrum. Quadrupole isolation window: 10 u; hexapole collision energy: 20 V.
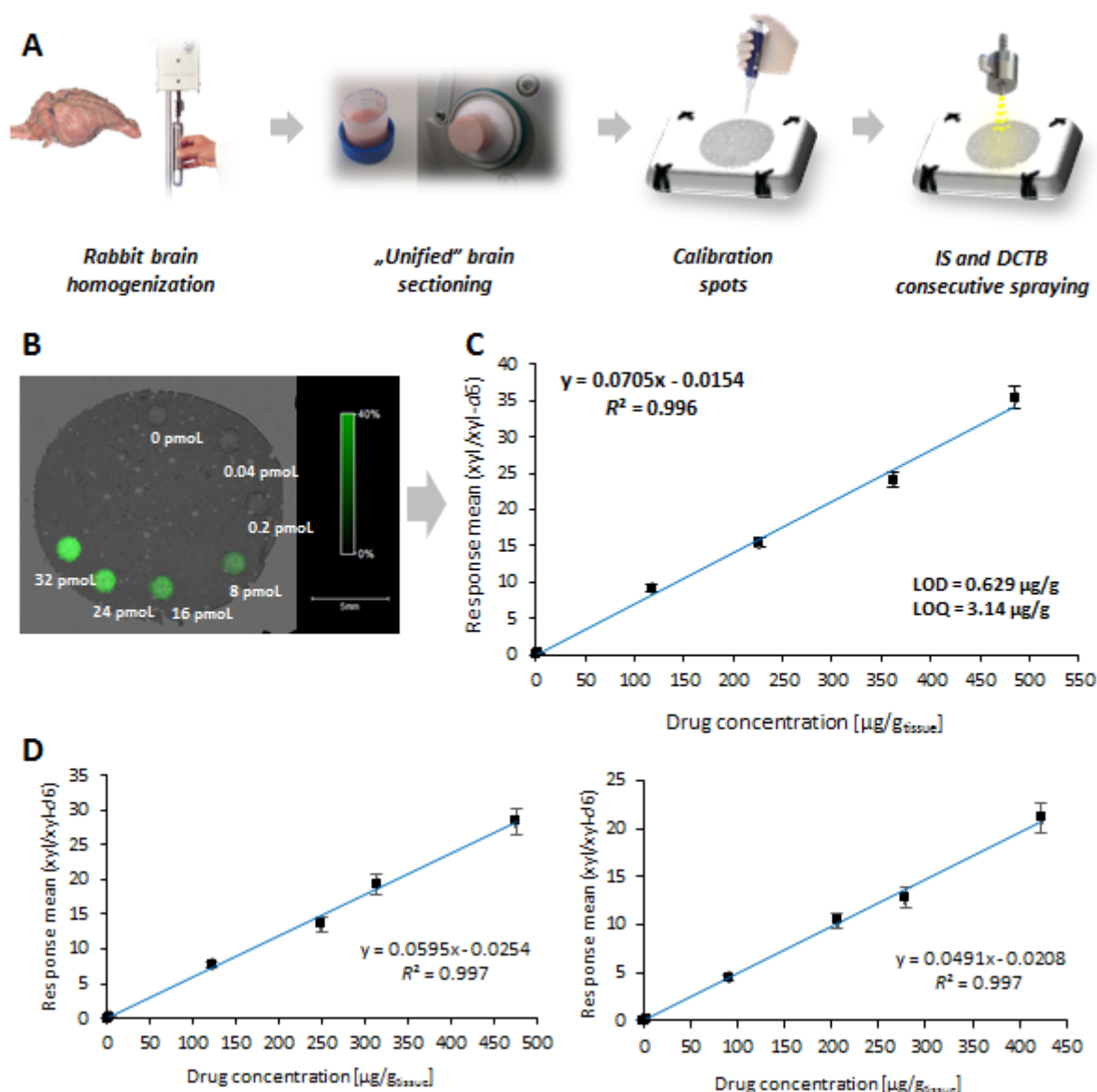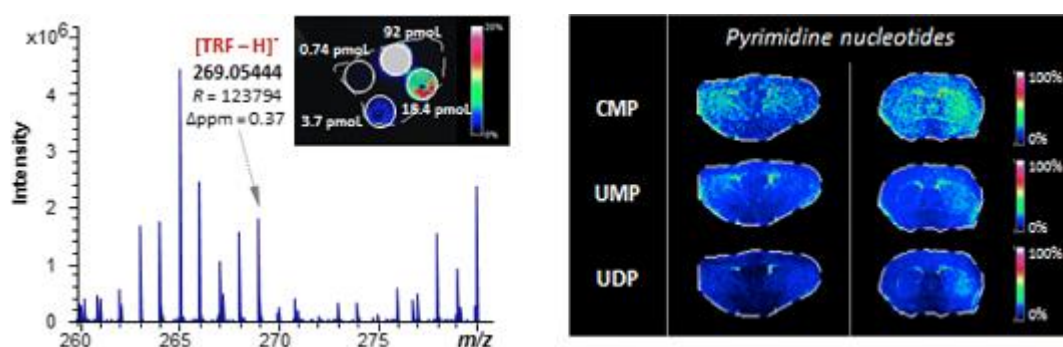
Figure S-5. (A) Workflow of "unified" mimetic brain/on-tissue mixed approach. **(B)** MS ion image of xylazine (*m/z* 221.11070 ± 0.001) calibration spots (0.2 or 0.4 µL), deposited manually on top of the "unified" brain tissue section. **(C)** On-tissue calibration curve (the error bars indicate the 95% confidence limits of the mean.) used to calculate average xylazine concentration across the brain tissue section illustrated in Figure 5-B. Coefficient of determination ($R^2 = 0.996$) illustrates linear relationship between tissue drug concentration and signal response (xylazine/xylazine-d_6(IS)). Limit of detection (LOD) was estimated here from multiple blank spot measurements, as the analyte concentration giving a signal equal to the blank signal plus 3 standard deviations of the blank. Limit of quantification (LOQ) was here considered being the lowest calibration standard (spot) fulfilling acceptance criteria of precision better than 20% of coefficient of variation (intra-calibration spot precision) and back-calculated bias within ±20% (80-120%). **(D)** Two additional example calibration curves (created from separate spiked "unified" brain section).

Publication 4

Spatial and molecular changes of mouse brain metabolism in response to immunomodulatory treatment with teriflunomide as visualized by MALDI-MSI

Ignacy Rzagalinski, Nadine Hainz, Carola Meier, Thomas Tschernig and Dietrich A. Volmer

RESEARCH PAPER

CrossMark

Spatial and molecular changes of mouse brain metabolism in response to immunomodulatory treatment with teriflunomide as visualized by MALDI-MSI

Ignacy Rzagalinski[1] · Nadine Hainz[2] · Carola Meier[2] · Thomas Tschernig[2] · Dietrich A. Volmer[3]

Abstract

Multiple sclerosis (MS) is an immune-mediated neurodegenerative disease of the central nervous system (CNS). One of the most promising recent medications for MS is teriflunomide. Its primary mechanism of action is linked to effects on the peripheral immune system by inhibiting dihydroorotate dehydrogenase (DHODH)-catalyzed de novo pyrimidine synthesis and reducing the expansion of lymphocytes in the peripheral immune system. Some in vitro studies suggested, however, that it can also have a direct effect on the CNS compartment. This potential alternative mode of action depends on the drug's capacity to traverse the blood-brain barrier (BBB) and to exert an effect on the complex network of brain biochemical pathways. In this paper, we demonstrate the application of high-resolution/high-accuracy matrix-assisted laser desorption/ionization Fourier-transform ion cyclotron resonance mass spectrometry for molecular imaging of the mouse brain coronal sections from animals treated with teriflunomide. Specifically, in order to assess the effect of teriflunomide on the mouse CNS compartment, we investigated the feasibility of teriflunomide to traverse the BBB. Secondly, we systematically evaluated the spatial and semi-quantitative brain metabolic profiles of 24 different endogenous compounds after 4-day teriflunomide administration. Even though the drug was not detected in the examined cerebral sections (despite the high detection sensitivity of the developed method), in-depth study of the endogenous metabolic compartment revealed noticeable alterations as a result of teriflunomide administration compared to the control animals. The observed differences, particularly for purine and pyrimidine nucleotides as well as for glutathione and carbohydrate metabolism intermediates, shed some light on the potential impact of teriflunomide on the mouse brain metabolic networks.

Keywords Mass spectrometry imaging · MALDI · FTICR · Teriflunomide · Multiple sclerosis · Metabolomic imaging

Introduction

Multiple sclerosis (MS) is a multifactorial, immune-mediated demyelinating and neurodegenerative disease of the central

✉ Dietrich A. Volmer
dietrich.volmer@hu-berlin.de

[1] Institute of Bioanalytical Chemistry, Saarland University, 66123 Saarbrücken, Germany

[2] Institute of Anatomy and Cell Biology, Saarland University, 66421 Homburg, Germany

[3] Department of Chemistry, Humboldt University of Berlin, 12489 Berlin, Germany

nervous system (CNS). It is characterized by blood-brain barrier (BBB) disruption, followed by the infiltration of immune cells into the CNS and nerve fibers demyelination and axonal loss of the brain and spinal cord [1, 2]. In most cases, multiple sclerosis has a relapsing-remitting course (RRMS), which is considered to mainly reflect inflammatory processes. It can, however, successively develop into a secondary progressive form of disease (SPMS), thought to represent a degenerative process that leads to lasting neurological impairment [3, 4]. The multiple sclerosis disease process consists of loss of myelin, disappearance of oligodendrocyte, and eventually formation of lesions scattered throughout the whole CNS including both white and gray matter regions [5]. Although the molecular mechanism underlying the pathology remains unclear, several promising oral disease modifying therapies (DMT) have been approved in recent years by regulatory agencies [6]. Three immunomodulatory low molecular weight

🖄 Springer

drugs—dimethyl fumarate, fingolimod, and teriflunomide (TRF)—have generated significant interest as they have shown benefit in clinical trials and offer the convenience of oral administration over the first-line injectable medications (e.g., interferon) [7, 8].

Teriflunomide is an active metabolite of leflunomide, an immunosuppressive drug previously approved for treatment of rheumatoid arthritis [9]. Although TRF has been shown to ameliorate the disease course in experimental autoimmune encephalomyelitis (EAE)—an animal model of multiple sclerosis—as well as in human clinical trials, the molecular mechanism underlying its therapeutic effect have not been fully elucidated yet [10, 11]. The primary mode of action of TRF is linked to the peripheral immune system. By selective and reversible inhibition of mitochondrial enzyme dihydroorotate dehydrogenase (DHODH), teriflunomide hinders the de novo pyrimidine synthesis and reduces the number of highly proliferative lymphocytes (activated T and B cells) in the peripheral immune system, thus lowering their expansion and infiltration into the CNS [12, 13]. Several in vitro and in vivo studies, however, have shown DHODH-independent functions of teriflunomide, including its potential for inhibiting Janus tyrosine kinases (Jak1 and Jak3) [14] as well as cyclooxygenase-2 (COX-2)-catalyzed formation of prostaglandin E2 (PGE2), a well-known lipid (neuro)inflammatory mediator [15]. Furthermore, TRF was shown to block tumor necrosis factor-α (TNF-α)-induced nuclear factor-kappa B (NF-κB) activation, a proinflammatory signaling pathway, which is also observed in the pathogenesis of multiple sclerosis [16]. Since the MS disease course is demonstrated by not only the peripheral but also the neuroimmune system (i.e., glial cells including microglia and astrocytes) activation [17], all the alternative TRF actions directly within the central nervous system are currently of great interest. The potential teriflunomide effect directly on the CNS compartment (e.g., reducing neuroinflammation or inducing neuroprotection), however, will depend on the drug's capability to traverse the BBB and/or to interfere with the complex biochemical network of brain metabolic pathways. Surprisingly, despite the numerous studies dedicated to teriflunomide action, its direct effect on the CNS metabolomic profile has not been to date investigated, which prompted us to investigate this as the main objective of the present study.

Metabolomics, in particular mass spectrometric-based metabolomics, has gained significant popularity in recent years and has been applied to studying various central nervous system diseases [18–20]. Multiple sclerosis and the EAE animal model were subject to experimental analytical studies conducted predominantly by gas chromatography-mass spectrometry (GC-MS), liquid chromatography-mass spectrometry (LC-MS), and nuclear magnetic resonance (NMR) techniques [21, 22]. The vast majority of these studies were aimed at identifying biomarkers of the onset or progression of the disease and were mainly applied to cerebrospinal fluid (CSF) samples [23–25]. Metabolomics approaches, however, can also be utilized to monitoring endogenous metabolism alterations as a result of drug administration. This strategy (termed pharmacometabolomics) provides a snapshot of the response of a certain (personalized) phenotype to the treatment and can be applied to study both the diseased and healthy species [26, 27]. While the first approach can be used for monitoring drug efficacy, the latter, when translated into a larger scale and proper biochemical interpretation, delivers additional insight into understanding the action of the drug at the molecular level.

In recent years, mass spectrometry imaging (MSI), in particular in a combination with matrix-assisted laser desorption/ionization (MALDI), has gained acceptance in tissue-based metabolomics research [28–30]. Firstly, it permits to link qualitative molecular information of compounds to their spatial localization and distribution within the investigated section (2D MSI) or even the whole organ (3D MSI) [31, 32], since MSI relies on in situ analysis of chemical compounds directly from the surface of biological tissue slices. Secondly, (MALDI-)MSI can provide reliable (semi-)quantitative information on the investigated compounds, if proper normalization and calibration routines are applied [33, 34]. Furthermore, MSI allows for simultaneous monitoring the spatial distributions of drug and endogenous metabolites from a single tissue section as well as for spatial correlation with pathologically changed areas revealed by histological staining (e.g., brain lesions in Alzheimer's or multiple sclerosis diseases). As a consequence, mass spectrometry imaging has recently become an important analytical tool for neuroscience research [35, 36] and has been successfully applied to study different neuropathological conditions, including Alzheimer's disease [37, 38], traumatic brain injury [39, 40], amyotrophic lateral sclerosis [41, 42], and, more recently, multiple sclerosis [43]. Furthermore, MSI was also employed to investigate tissue metabolomic changes in response to administration of xenobiotics. For example, metabolic response was studied by Jones et al. in a mouse tumor xenograft model after treatment with the sphingosie-1-phosphate/ceramide pathway targeting drugs, as well as by Sun et al. in lung sections after pirfenidone administration [44]. Furthermore, different research groups have discovered considerable changes of brain lipid spatial profiles as a result of narcotics administration [45–47] or chronic ethanol consumption [48]. Finally, Hanrieder et al. described substantial metabolism changes in rat hippocampus resulting from the exposure to an environmental neurotoxin revealed by molecular imaging at high spatial resolutions using time-of-flight secondary ion mass spectrometry (TOF-SIMS) [49].

In the present study, we employed MALDI mass spectral imaging using a high-resolution/high-accuracy Fourier-transform ion cyclotron resonance (FTICR) platform for

assessment of the molecular effects of the peripheral immuno-modulatory drug teriflunomide on the mouse brain compartment. Firstly, we examined the potential penetration of the drug into the central nervous system. Secondly, we investigated spatial and molecular changes of mouse brain metabolomic profile after 4-day drug administration.

Materials and methods

Chemicals and reagents

Teriflunomide (TRF), 9-aminoacridine (9-AA), α-cyano-4-hydroxycinnamic acid (CHCA), 1,5-diaminonaphthalene (1,5-DAN), 2-mercaptobenzothiazole (MBT) 6-aza-2-thiothymine (ATT), 3-aminoquinoline (3-QA), 1,8-bis(dimethylamino)naphthalene (DMAN), ethanol, methanol, acetonitrile, and standard microscopic glass slides were purchased from Sigma-Aldrich (Steinheim, Germany). Teriflunomide-d_4 (internal standard, IS) was obtained from Biozol GmbH (Eching, Germany). Purified water was generated by a Millipore (Bedford, MA, USA) purification system.

Animals and tissue preparation

All animal experiments were performed in accordance with international regulations and permission from the local research ethics committee (Landesamt für Verbraucherschutz Saarland, TVV 23/2015). C57BL/6 mice were purchased from Charles River (Sulzfeld, Germany). Teriflunomide (TRF) was suspended in 0.9% sodium chloride (NaCl) and administered to mice by oral gavage at a dose of 10 mg/kg body weight daily during a 4-day treatment. Control (vehicle) animals received only NaCl. The dose of 10 mg/kg body weight was chosen based on the EAE animal model in the original work by Ringheim et al. [10], which is far lower than the lethal doses (200 mg/kg for mice) described in the assessment report on Aubagio (trade name of teriflunomide) by the European Medicines Agency [50]. The mice were euthanized after 24 h following the final drug administration. The organs were dissected immediately after the sacrifice, snap-frozen in liquid nitrogen and stored at − 80 °C until sample preparation. The 12-μm-thick coronal brain sections from both vehicle and TRF mice were cut at comparable stereotactic coordinates (∼ Bregma + 0.2/0.3 mm) [51] using a Reichert Jung 2800 Frigocut cryostat microtome (Leica Microsystems, Wetzlar, Germany). Sections from vehicle and TRF animals were thaw-mounted onto the same plain microscope glass slides (to minimize signal variations resulting from sample preparation process) and dried for 30 min in a vacuum desiccator. Tissues on glass slides were stored at − 80 °C for no longer than 2 days prior to mass spectrometry imaging experiments.

MALDI matrix selection and automated spraying

Electrospray (ESI)-FTICR experiments of teriflunomide standards revealed primary formation of deprotonated molecules for TRF; therefore, different matrices for efficient negative ion formation were tested for the MALDI-FTICR experiments after dried-droplet sample preparation. CHCA and ATT matrices were prepared at 10 mg/mL in acetonitrile/water (70/30 [v/v]); 9-AA and DMAN were prepared at 10 mg/mL; MBT was prepared at 25 mg/mL in ethanol/water (70/30 [v/v]); and 1,5-DAN and 3-QA were dissolved in methanol/water (70/30 [v/v]) at 15 and 10 mg/mL, respectively. For MSI experiments of endogenous molecules, 9-aminoacridine (9-AA) was chosen as MALDI matrix because of its ability to efficiently ionize low molecular weight metabolites from the tissue surfaces [29, 52, 53]. For imaging experiments, a freshly prepared solution of 9-AA (5 mg/mL in ethanol/water, 70/30 [v/v]) was homogenously sprayed onto the tissue sections using an automated home-built sprayer as previously described [54], which provided homogenous, reproducible matrix deposition as well as small crystal sizes (see Electronic Supplementary Material (ESM) Fig. S1). Seven layers of 9-AA were deposited with increasing flow rate in the following patterns: two layers at 20 μL/min and five layers at 40 μL/min. From these experiments, the estimated amount of matrix added to the tissue (= matrix density) was calculated at 0.0201 mg/mm^2. Prior to matrix deposition, IS solution (1 μM teriflunomide-d_4 in ethanol/water, 70/30 [v/v]) was sprayed with increasing flow rate in the following pattern: 1 layer at 10 μL/min, 1 layer at 20 μL/min, and 2 layers at 30 μL/min.

Mass spectrometry and data analysis

ESI, MALDI, and MALDI imaging experiments were performed in negative ion mode on a Bruker (Bremen, Germany) 7 Tesla Solarix FTICR mass spectrometer, equipped with a dual ESI/MALDI ion source and Smartbeam II Nd:YAG (355 nm) laser. MALDI imaging data were collected either in full scan mode from m/z 50 to 1100 (for imaging of endogenous metabolites) or in CASI (continuous accumulation of selected ions) mode with a quadrupole isolation window from 20 to 200 u (for enhanced sensitivity in targeted drug imaging experiments), with a transient length of ∼0.5 s and resolving power (FWHM) of ∼114,000 at m/z 300. Internal mass calibration was performed using either a series of peaks originating from the MALDI matrix and endogenous compounds (for metabolomic imaging) or a lock-mass approach with peaks from the internal standard (for drug imaging experiments). For all MALDI imaging measurements, the laser focus was set to the "small" setting, laser power to 20%, number of laser shots/pixel to 200, and repetition rate to 1 kHz. MSI pixel size was set to

70 μm, assuring a dense array of laser ablation spots while avoiding overlap (see ESM Fig. S2). MALDI experiments with standards were carried out by using dried-droplet sample preparation and spotting onto steel MALDI target plates (Bruker). ESI was performed using direct infusion with the instrument's syringe pump at 2 μL/min. All MS/MS experiments were performed by isolation of precursor ions in the external quadrupole (isolation window, 5–10 u) and accumulation in the hexapole for collision-induced dissociation (CID) at varying collision energies (collision offset voltages, 10–30 V). Data were processed and analyzed using the Bruker Data Analysis and FlexImaging software for single mass spectra and imaging data sets, respectively. To obtain the average tissue intensities of endogenous brain metabolites, the imzML [55] files were extracted from FlexImaging and analyzed with the open-source MSiReader software [56]. Mass spectral interpretations were conducted using the METLIN (http://metlin.scripps.edu) [57] and HMDB (http://http://www.hmdb.ca) [58] databases to match the accurate masses of the precursor ions. Furthermore, the identified metabolites were assessed with existing biochemical pathways described in the KEGG atlas of metabolic pathways (https://www.genome.jp/kegg/pathway.html#metabolism) [59]. MS ion images of the endogenous metabolites were normalized to the deprotonated 9-AA signal, which was shown to be an efficient normalization routine when isotope-labeled internal standards are not feasible [34]. This strategy was chosen here over the more common RMS and TIC approaches since both RMS and TIC can induce unrealistic enhancements of ion signal values when applied to highly heterogeneous tissues (e.g., brain). The procedure complies well with histological structures as previously described by Deininger et al. [60].

Histological staining and optical microscopy

Glass slides were rinsed with ethanol (70% v/v) for removal of the matrix after MSI. Staining was performed with hematoxylin and eosin (H&E) by dipping the slides into ethanol (100% v/v, − 20 °C; 5 min), then deionized water (2 min), immersion in Ehrlich's hematoxylin (Carl Roth, Karlsruhe, Germany) for 5 min, washing with deionized water, and bluing (tap water, 10 min). Eosin (Carl Roth) staining (10 s) of slides was followed by washing with deionized water and dipping into ethanol (80% v/v, 3 min), ethanol (90% v/v, 6 min), and ethanol (100%, 2 × 5 min) and then exposing them to three different xylene (VWR, Darmstadt, Germany) soaks (5 min each). Coverslips were placed onto the slides using mounting medium Roti-Histokitt (Carl Roth GmbH, Karlsruhe, Germany). Stained tissue sections were digitized with a Zeiss Axio

Scan.Z1 slide scanner (Carl Zeiss Microscopy GmbH, Jena, Germany).

Results and discussion

Capacity to traverse BBB

Method development for on-tissue teriflunomide detection Teriflunomide (Fig. 1a) was the subject of several LC-MS quantification studies, indicating strong signals under electrospray ionization in negative ion mode [61, 62]. Our preliminary direct infusion ESI-FTICR experiments confirmed this preferred mode and we therefore conducted a systematic investigation of a series of negative ion mode MALDI matrices. Seven different compounds (CHCA, 9-AA, 1,5-DAN, ATT, 3-QA, MBT, and DMAN) were investigated with MALDI-FTICR after dried-droplet sample preparation, where equal volumes of the drug standard solution (7.4 μM) and MALDI matrix solutions (for concentrations and solvents, see the "Materials and methods" section) were mixed and manually deposited onto the steel target plates. Collection of 16 individual transients from three MALDI spots allowed for intra- and inter-spot variability correction and revealed deprotonated TRF (theoretical m/z at 269.054336) for six of the seven matrices (with the exception of DMAN, where no signal was obtained). The intensities obtained with 9-AA were superior to the other five matrices, as seen in Fig. 1b. Therefore, 9-AA was further utilized for method development for on-tissue teriflunomide detection (based on the drug standard spiked on top of the control mouse brain section and then sprayed with the matrix) with different FTICR settings (i.e., full scan versus CASI modes). Of note, different settings of the quadrupole isolation window (between 20 and 200 u) were tested, of which the highest intensity from deprotonated teriflunomide was obtained with a window size of 100 u. Finally, to fully illustrate detection capabilities of the developed method, we performed imaging experiment of a control mouse brain section with a manually spotted (0.5 μL) series of teriflunomide solutions (184, 36.8, 7.40, and 1.48 μM). Figure 1c shows MS ion images resulting from these experiments (all spots are indicated with the exact amount of deposited drug) and a representative single MSI pixel mass spectrum obtained from one of the spots at 7.40 μM. Further quantitative analyses of the obtained data using MSiReader (based on imzML files extracted from the instrument vendor imaging software) generated a linear relationship between the calculated tissue drug concentration and the normalized drug signal intensities from the spots (coefficient of determination, R^2 = 0.999) over a concentration range exceeding two orders of magnitude (see ESM Fig. S3). Manual inspection of several representative single pixels mass spectra from the lowest concentration spot (which corresponded to the tissue drug
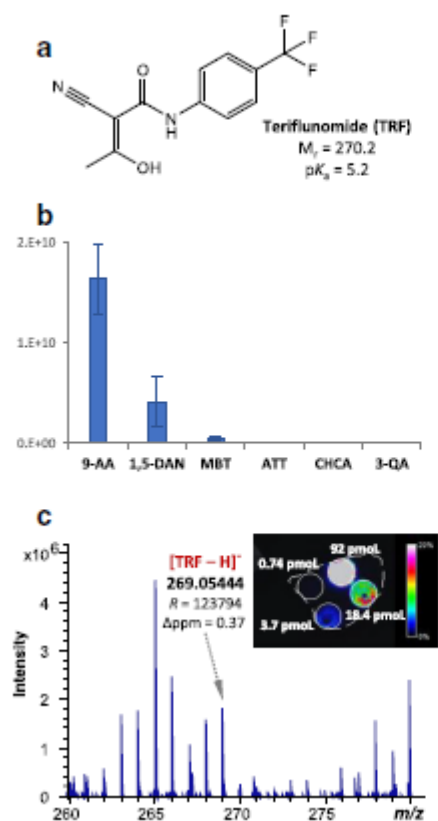
Fig. 1 a Chemical structure, molecular weight, and pK_a of teriflunomide (TRF). b Bar graph showing average signal intensities from deprotonated teriflunomide (7.4 μM) obtained with MALDI-FTICR after dried-droplet sample preparation with six different negative ion MALDI matrices. Error bars represent standard deviation, SD ($n = 3$). c Single MSI pixel mass spectrum (m/z 260–280) obtained from MALDI-FTICR imaging experiment conducted in CASI mode (quadrupole isolation window, 100 u) of the control mouse brain section after manually spotted (0.5 μL) drug standard solutions of four different concentrations: 184 μM, 36.8 μM, 7.40 μM, and 1.48 μM (2D ion image is on upper right). The shown mass spectrum was exported from the representative single pixel of a 7.4-μM spot

concentration of 11.05 μg/g as calculated from MSiReader based on a measured spot area of 1.46 mm², tissue thickness of 12 μm, and assumed average brain density of 1.027 g/cm³ [63]) revealed the drug signal-to-noise ratio (S/N) within the range of 10 to 20. These analytical figures of merit demonstrate that teriflunomide, when present in the mouse brain at or above the mentioned concentration level, can be successfully detected and quantified with the present method directly from the tissue sections.

MSI of brain sections from drug-treated animals The above-described highly sensitive MSI method was applied to in situ imaging of brain coronal sections from mouse that had undergone a 4-day teriflunomide treatment. Unfortunately, no drug

signal was detected in any of the tested native tissues. In addition to the parent drug, we did not detect any of the previously described metabolites (despite most of them having acidic character for deprotonation). This includes the only known plasma metabolite, 4-trifluoro-methylaniline (4-TFMA), as well as the major urine metabolite, 4-TFMA oxanilic acid [64]. These negative findings might result from the previously reported strong protein binding of teriflunomide (>90%) in plasma and, consequently, its limited volume of distribution [62, 65]. In addition, teriflunomide and its parent drug leflunomide have been shown to express high affinity to the breast cancer resistance protein (BCRP), which is a membrane efflux transporter abundantly expressed on the endothelial cells layer of the BBB [66]. It is also worth pointing out that even disruption of the BBB (evident in both multiple sclerosis and EAE) does not necessarily increase the penetration of small molecule drugs into the CNS as shown by Cheng et al. [67]. Indeed, additional MALDI-MSI experiments of brain sections obtained from EAE mice treated with TRF did not reveal signals from the drug, thus confirming the above-mentioned findings.

The effect of teriflunomide on the mouse brain metabolism

Even though teriflunomide signal was not detected from the native tissues, we investigated the drug's indirect effect on the metabolism in the brain. To do that, we performed MALDI-FTICR imaging experiments on brain coronal sections from the mice treated with the drug for 4 days and compared the results with vehicle treated species. High-resolution/high mass accuracy MS experiments were performed for putative identification of m/z values from several representative single MSI pixels (of different anatomical regions of brain), followed by a search of two metabolomics databases (METLIN and HMDB) with the mass uncertainty set to ± 2 ppm. From these experiments, we annotated and tentatively identified 24 compounds (Fig. 2). Of note, all putatively annotated mouse brain metabolites exhibited relative mass errors of $< \pm 1$ ppm at calculated resolving powers (FWHM) between 60,000 and 300,000, depending on m/z range.

Purine and pyrimidine nucleotide metabolism The first investigated biochemical route was nucleotide metabolism, including both purine and pyrimidine nucleotides. This pathway is of importance in MS disease pathology because teriflunomide's major mode of action is linked to the inhibition of the de novo pyrimidine synthesis, specifically its blocking of the dihydroorotate to orotate enzymatic (DHODH-catalyzed) conversion. In addition, it is widely accepted that both purinergic and pyrimidinergic signaling pathways play a key role in both neurotransmission and neuromodulation mechanisms [68, 69]. Moreover, several

Fig. 2 MALDI-FTICR single MSI pixel mass spectra (from imaging experiment of the vehicle mouse brain section) showing tentatively identified metabolites in different selected mass-to-charge ratio regions: m/z 120–180 (a), m/z 210–260 (b), m/z 300–370 (c), m/z 400–620 (d). Mass resolving power was calculated based on full-width-at-half-maximum (FWHM) of each signal, while relative mass errors are given in ppm. Mass spectra were obtained from the representative single MSI pixels of two different spatial coordinates: $x = 308/y = 146$ (a) and $x = 297/y = 130$ (b–d)
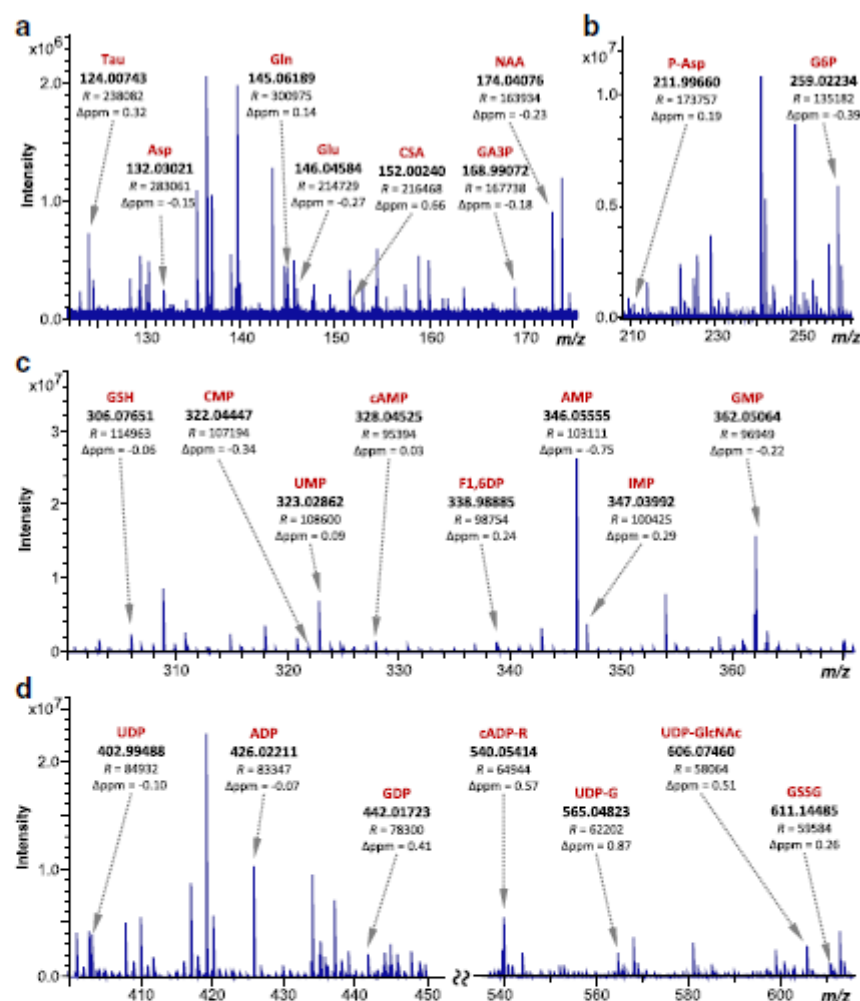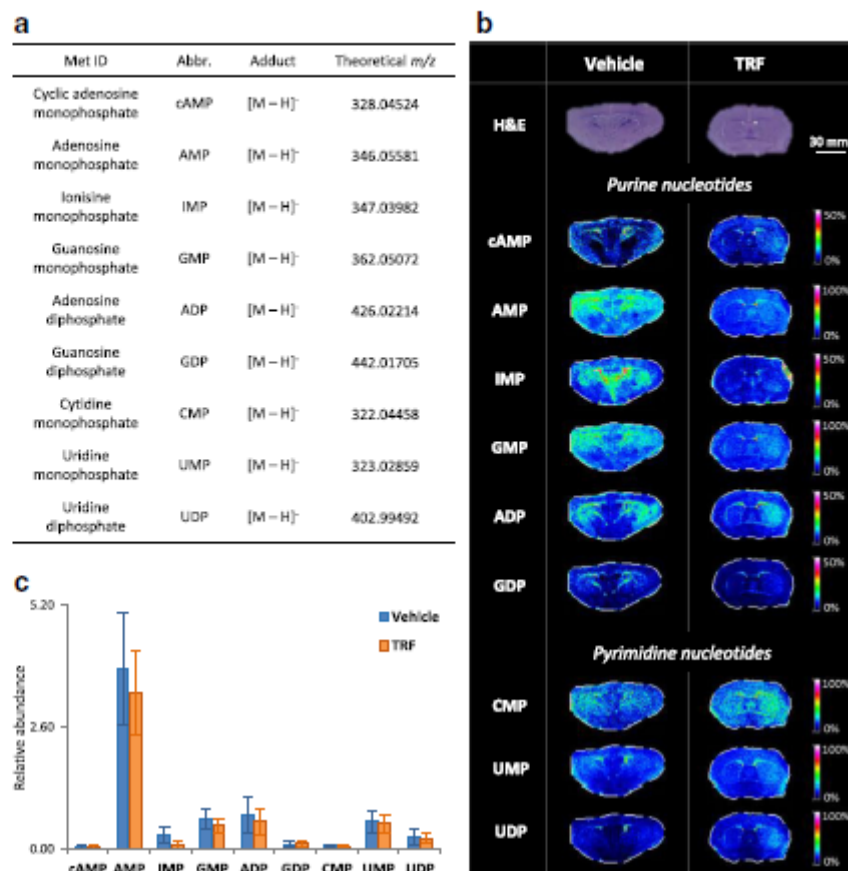

studies suggest that alterations in purine and pyrimidine metabolism can be involved in developing different CNS dysfunctions, including neuroinflammation and neurodegeneration conditions, both occurring in multiple sclerosis course [70, 71].

In our MALDI-MSI experiments, we detected both purine (AMP, cAMP, ADP, IMP, GMP, and GDP) and pyrimidine nucleotides (CMP, UMP, and UDP); the full names and observed adducts of which along with their theoretical m/z values are summarized in Fig. 3a. Figure 3b shows MS ion images of spatial distributions of all nucleotide derivatives detected during MALDI-MSI. We did not observe any significant differences of their spatial distributions between TRF and vehicle sections. The bar graph in Fig. 3c compares average intensities obtained for brain coronal sections from vehicle versus drug-treated mice. The mean abundances for all metabolites were obtained using the MSiReader software by

setting the mass error threshold to ± 2 ppm; the standard deviation bars shown in the graph represent the heterogeneity of the respective compound's spatial distribution across the entire examined section. From nine detected nucleotides, cAMP and GDP were elevated in TRF versus vehicle mice, while the remaining compounds showed lower abundance. Essentially, the average abundances of almost all compounds were altered by >10%, while some (IMP, GMP, and ADP) decreased by more than 20%. Interpretation of these data is particularly interesting for adenine and uracil derivatives, since their potential role in neuroinflammation and neurodegeneration processes has been broadly discussed in recent years. While the main function of cyclic AMP (cAMP, increased in our experiments after TRF treatment) is widely accepted to suppress neuroinflammation [72], the other nucleotides' function in multiple sclerosis pathology remains elusive due to the multifaceted role of these molecules in immune responses [73].

Spatial and molecular changes of mouse brain metabolism in response to immunomodulatory treatment with...

Fig. 3 MALDI-FTICR imaging of mouse brain nucleotide (purines and pyrimidines) metabolism from the vehicle versus teriflunomide (TRF)-treated animals: a list of detected and identified nucleotide metabolites; b spatial distributions across mouse brain coronal sections; c bar chart showing average intensities (error bars represent standard deviation of the single pixel intensities across the whole tissue section and thus reflect heterogeneity of the certain metabolite distribution). Pixel size, 70 μm; scale bar, 30 mm

a

Met ID	Abbr.	Adduct	Theoretical m/z
Cyclic adenosine monophosphate	cAMP	[M − H]⁻	328.04524
Adenosine monophosphate	AMP	[M − H]⁻	346.05581
Ionisine monophosphate	IMP	[M − H]⁻	347.03982
Guanosine monophosphate	GMP	[M − H]⁻	362.05072
Adenosine diphosphate	ADP	[M − H]⁻	426.02214
Guanosine diphosphate	GDP	[M − H]⁻	442.01705
Cytidine monophosphate	CMP	[M − H]⁻	322.04458
Uridine monophosphate	UMP	[M − H]⁻	323.02859
Uridine diphosphate	UDP	[M − H]⁻	402.99492

b

c

Nonetheless, some evidence has been provided that while adenine nucleoside (adenosine) have mainly anti-inflammatory functions [74], the extracellularly released adenine and uracil nucleotides (ADP, ATP, UDP, and UTP) serve rather as damage-associated molecular patterns (DAMP), activating proinflammatory mechanisms (e.g., microglial activation) [75–77]. In light of these findings, the noticeably decreased brain levels of uracil (UDP, UMP) and adenine (ADP, AMP) nucleotides in response to teriflunomide administration might suggest an additional anti-inflammatory and immunosuppressive CNS effect of the drug along with its beneficial action in the peripheral immune system.

Amino acid metabolism We also investigated the effect of teriflunomide on the metabolism of amino acids in the brain, for two reasons. Firstly, most amino acid neurotransmitters are thought to play key roles in neuroinflammation and neurodegeneration [78]. Secondly, several amino acids were investigated in metabolomics studies as potential biomarkers of multiple sclerosis disease onset or progression [21, 22]. For example, a metabolomics study of CSF samples from an EAE rat

model revealed elevated levels of taurine, which is a well-known anti-inflammatory and antioxidant agent [23], as well as glutamic acid, which is known for its excitotoxicity in brain neurons [24]. Furthermore, a nuclear magnetic resonance (NMR) study by Lutz et al. revealed increased amounts of glutamine in CSF samples of multiple sclerosis patients with active inflammatory brain plaques [79]. Glutamine is a precursor of glutamic acid in brain. Moreover, an in vivo human brain study conducted with magnetic resonance spectroscopy (MRS) by Vingara et al. revealed decreased levels of N-acetylaspartic acid (NAA) in the brain correlated well with neurological impairment of multiple sclerosis patients. The authors suggested NAA as a potential biomarker of neuroaxonal damage progression [80]. Finally, glutathione (both in reduced, GSH, and oxidized, GSSG, states) is one the most important endogenous antioxidant agents. It was previously described to be significantly impaired during the multiple sclerosis course [81].

In our experiments, we detected and tentatively identified seven amino acids and two peptide metabolites. All species were observed as deprotonated molecules (Fig. 4).

Fig. 4 MALDI-FTICR imaging of mouse brain amino acid metabolism from vehicle versus teriflunomide (TRF)-treated animals: **a** list of detected and identified metabolites; **b** spatial distributions across mouse brain coronal sections; **c** bar chart showing average intensities (error bars represent standard deviation of the single pixel intensities across the whole tissue section and thus reflect heterogeneity of the particular metabolite distribution). Pixel size, 70 μm; scale bar, 30 mm
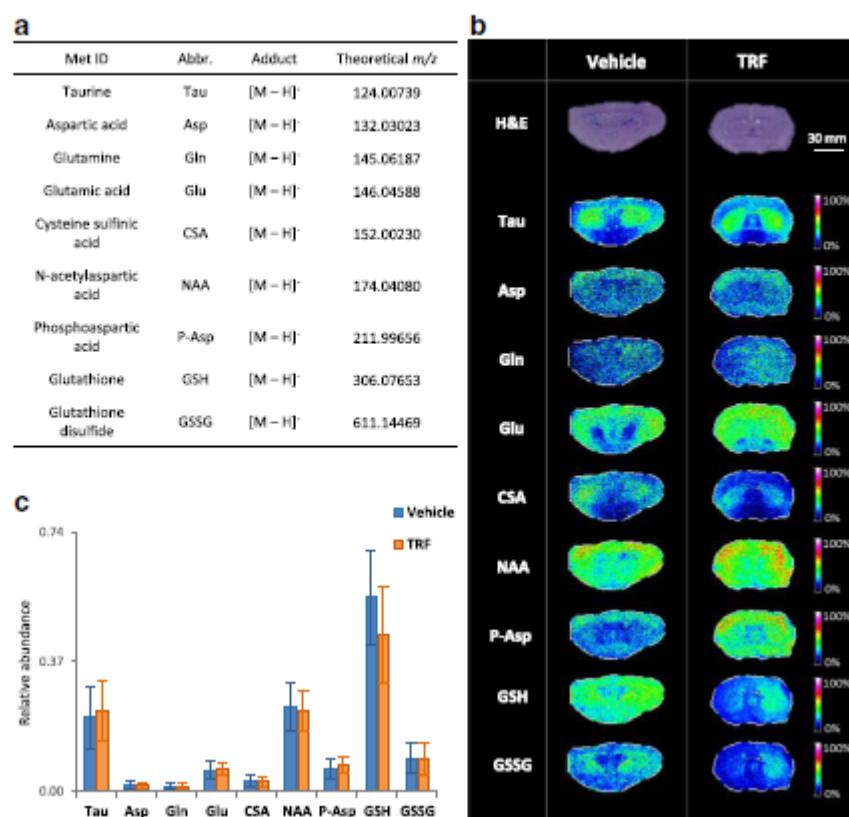
The visual inspection of most of the molecular images did not provide any indication for significant changes in amino acids' spatial distribution across the examined mouse brain coronal sections from TRF versus vehicle animals. Two glutathione compounds, however, showed clearly asymmetrical distribution in the TRF section as compared to the non-treated mouse. Furthermore, the comparison of average intensities (Fig. 4c) revealed some alterations in response to drug treatment, yet most of the compounds (seven of nine detected compounds) were altered by less than 10%. Larger changes were observed only for phosphoaspartic acid (increase by 15%) and, in particular, for glutathione in its reduced form (GSH), which decreased by almost 20% in TRF sections. In conclusion, despite the small overall changes of teriflunomide-induced changes in the amino acid brain metabolism (except for glutathione) as compared to nucleotides shown above, the experiments clearly illustrated drug effects, such as the increased levels of taurine (involved in neuroprotection) with simultaneous elevated levels of glutamic acid (involved in excitotoxicity) at the same time and decreased amount of the internal antioxidant glutathione.

Carbohydrate metabolism Finally, the last group of compounds investigated in our MSI experiments were metabolites involved in carbohydrate biochemical routes. Alterations in glucose and energy metabolism pathways were previously observed in multiple sclerosis patients [82, 83]. We detected three compounds involved in the glycolysis/gluconeogenesis cycle as well as three nucleotide sugars, all of which were detected as deprotonated molecules (Fig. 5a). Their MS ion images (Fig. 5b) did not reveal significant changes of spatial distributions across the examined brain coronal sections from TRF versus control animals. The bar graph (Fig. 5c) illustrating average intensities, however, shows considerable downregulation (> 30%) for glucose-6-phosphate (G6P) and UDP-glucose. As the latter molecule is a sugar conjugate of the uracil nucleotide, its decreased abundance might be linked to the lower UDP levels detected in drug-treated animals (see above). UDP-glucose along with UDP-N-acetylglucosamine (for which almost no change was observed here) has been reported to be involved in multiple biochemical pathways [77]. This includes brain glycogen synthesis, which requires enzymatically catalyzed formation of UDP-glucose from UTP and glucose-6-phosphate

Fig. 5 MALDI-FTICR imaging of mouse brain carbohydrate metabolism (including nucleotide sugars) from vehicle versus teriflunomide (TRF)-treated animals: **a** list of detected and identified metabolites; **b** spatial distributions across mouse brain coronal sections; **c** bar chart showing average intensities (error bars represent standard deviation of the single pixel intensities across the whole tissue section and thus reflect heterogeneity of the particular metabolite distribution). Pixel size, 70 μm; scale bar, 30 mm
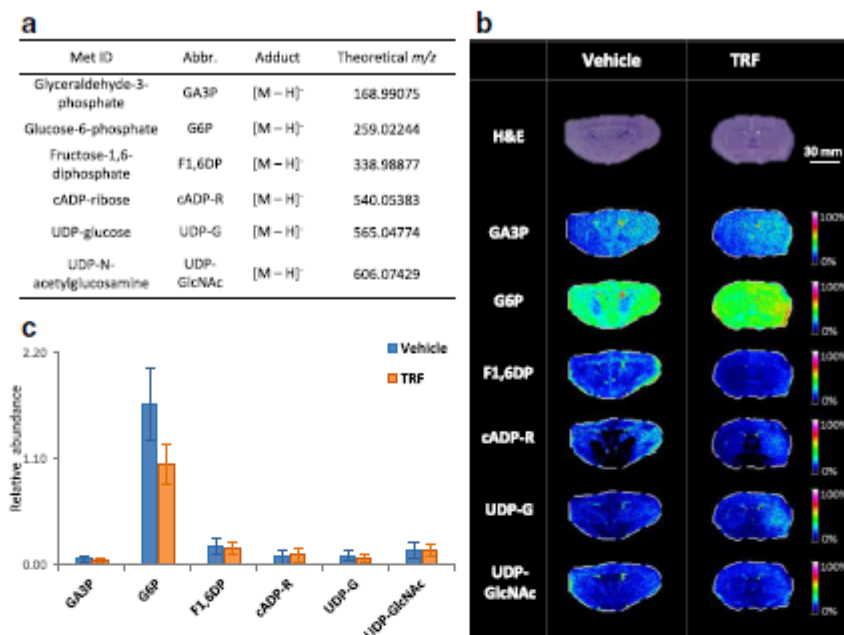
(G6P) [84]. Interestingly, G6P was also downregulated in the brain sections of the drug-treated animals in our experiments. In addition to participating in brain energy metabolism, UDP-glucose was postulated to play a role as extracellular signaling molecule in the central nervous system (similar to adenine and uracil nucleotides, see above) since G protein-coupled receptors for UDP-glucose were identified to be expressed in a wide variety of different brain regions [85, 86]. In particular, UDP-glucose was recently described to induce inflammatory effects in microglia, which might suggest an important role in neuroinflammation [87]. While a part of the UDP-glucose pool might be epimerized to UDP-galactose, separation of the two isomers was not possible with the current instrumentation. Since this enzymatically catalyzed epimerization takes place under very specific physiological circumstances (e.g., for lactose synthesis during breast-feeding) [77], we assumed UDP-glucose as the major nucleotide sugar contributing to the signal at the theoretical m/z of 565.04774. In contrast to the downregulated metabolites, another sugar nucleotide, cyclic ADP-ribose (cADP-R), significantly increased (> 20%) in TRF-treated animals versus control. cADP-ribose is an important intracellular calcium-releasing second messenger, which is particularly known for its crucial role in regulating inflammation and innate immune responses [88, 89]. The elevated levels of this sugar nucleotide in response to TRF administration might suggest a role in CNS inflammation.

Conclusions

The aim of this paper was the investigation of the impact of immunomodulatory treatment with teriflunomide on the central nervous system's metabolic profile of mice. Specifically, FTICR imaging mass spectrometry was utilized to assess teriflunomide's capacity to cross the blood-brain barrier as well as to visualize potential alterations of spatial and quantitative profiles of brain metabolites in response to drug administration. Firstly, in accordance with previously reported results, our experiments confirmed the limited access of teriflunomide into the CNS. This was seen from the lack of drug signal in coronal brain tissue sections from animals after 4-day treatment at relatively high doses, even though the developed method exhibited excellent signal response in spiked tissue experiments. Despite the drug's absence in the brain, however, further in-depth investigation of the spatial profiles of 24 endogenous metabolites from three different classes (nucleotides, amino acids, and carbohydrates) was performed based on tentative identifications by high resolving power/accurate mass measurements (uncertainty < 1 ppm) via FTICR. Interestingly, some of metabolites exhibited noticeable downregulation (> 20%) in brain sections from teriflunomide-treated mice when compared to vehicle animals. The most significant changes were seen for adenine and uracil nucleotides as well as glutathione (GSH) and two carbohydrate intermediates, glucose-6-phosphate (G6P) and UDP-glucose. Even though the mechanism by which teriflunomide exerts its action in the CNS is not fully

understood, our findings might support a mechanism that involves an indirect pathway, as the drug seemed incapable to cross the BBB. Such a potential mechanism, which involves circulating drug-induced modulation of some peripheral molecules, which could then interact with the cells lining the BBB and finally activate CNS cells, was recently proposed by Moore et al. for mouse brain changes induced by stimulation with bacterial endotoxin lipopolysaccharide (LPS) [90]. In summary, we believe that the results of our experiments demonstrated the potential of our method for future MALDI-MSI investigations of a larger number of healthy or EAE animals, post-mortem human brain samples, or human CSF samples from teriflunomide-treated MS patients.

Compliance with ethical standards

All animal experiments were performed in accordance with international regulations and permission from the local research ethics committee (Landesamt für Verbraucherschutz Saarland, TVV 23/2015).

Conflict of interest The authors declare that they have no competing interests.

References

1. Dendrou CA, Fugger L, Friese MA. Immunopathology of multiple sclerosis. Nat Rev Immunol. 2015;15:545–58. https://doi.org/10.1038/nri3871.
2. Grigoriadis N, van Pesch V. A basic overview of multiple sclerosis immunopathology. Eur J Neurol. 2015;22:3–13. https://doi.org/10.1111/ene.12798.
3. Trapp BD, Nave K-A. Multiple sclerosis: an immune or neurodegenerative disorder? Annu Rev Neurosci. 2008;31:247–69. https://doi.org/10.1146/annurev.neuro.30.051606.094313.
4. Stys PK, Zamponi GW, Van MJ, Geurts JJG. Will the real multiple sclerosis please stand up? Nat Rev Neurosci. 2012;13:507–14.
5. Kipp M, van der Valk P, Amor S. Pathology of multiple sclerosis. CNS Neurol Disord - Drug Targets. 2012;11:506–17. https://doi.org/10.2174/187152712801661248.
6. English C, Aloi JJ. New FDA-approved disease-modifying therapies for multiple sclerosis. Clin Ther. 2015;37:691–715. https://doi.org/10.1016/j.clinthera.2015.03.001.
7. Killestein J, Rudick RA, Polman CH. Oral treatment for multiple sclerosis. Lancet Neurol. 2011;10:1026–34. https://doi.org/10.1016/S1474-4422(11)70228-9.
8. Freedman MS, Montalban X, Miller AE, Dive-Pouletty C, Hass S, Thangavelu K, et al. Comparing outcomes from clinical studies of oral disease-modifying therapies (dimethyl fumarate, fingolimod, and teriflunomide) in relapsing MS: assessing absolute differences using a number needed to treat analysis. Mult Scler Relat Disord. 2016;10:204–12. https://doi.org/10.1016/j.msard.2016.10.010.
9. Mladenovic V, Domljan Z, Rozman B, Jajic I, Mihajlovic D, Dordevic J, et al. Safety and effectiveness of leflunomide in the treatment of patients with active rheumatoid arthritis. Arthritis Rheum. 1995;38:1595–603. https://doi.org/10.1002/art.1780381111.
10. Ringheim GE, Lee L, Laws-Ricker L, Delohery T, Liu L, Zhang D, et al. Teriflunomide attenuates immunopathological changes in the Dark Agouti rat model of experimental autoimmune encephalomyelitis. Front Neurol. 2013;4:1–12. https://doi.org/10.3389/fneur.2013.00169.
11. Wiese MD, Rowland A, Polasek TM, Sorich MJ, O'Doherty C. Pharmacokinetic evaluation of teriflunomide for the treatment of multiple sclerosis. Expert Opin Drug Metab Toxicol. 2013;9:1025–35. https://doi.org/10.1517/17425255.2013.800483.
12. Claussen MC, Korn T. Immune mechanisms of new therapeutic strategies in MS—teriflunomide. Clin Immunol. 2012;142:49–56. https://doi.org/10.1016/j.clim.2011.02.011.
13. Bar-Or A, Pachner A, Menguy-Vacheron F, Kaplan J, Wiendl H. Teriflunomide and its mechanism of action in multiple sclerosis. Drugs. 2014;74:659–74. https://doi.org/10.1007/s40265-014-0212-x.
14. González-Alvaro I, Ortiz AM, Domínguez-Jiménez C, Aragón-Bodi A, Díaz Sánchez B, Sánchez-Madrid F. Inhibition of tumour necrosis factor and IL-17 production by leflunomide involves the JAK/STAT pathway. Ann Rheum Dis. 2009;68:1644–50. https://doi.org/10.1136/ard.2008.096743.
15. Hamilton LC, Vojnovic I, Warner TD. A771726, the active metabolite of leflunomide, directly inhibits the activity of cyclo-oxygenase-2 in vitro and in vivo in a substrate-sensitive manner. Br J Pharmacol. 1999;127:1589–96. https://doi.org/10.1038/sj.bjp.0702708.
16. Manna SK, Aggarwal BB. Immunosuppressive leflunomide metabolite (A77 1726) blocks TNF-dependent nuclear factor-kappa B activation and gene expression. J Immunol. 1999;162:2095–102. https://doi.org/10.4049/jimmunol.164.10.5156.
17. Healy LM, Michell-Robinson MA, Antel JP. Regulation of human glia by multiple sclerosis disease modifying therapies. Semin Immunopathol. 2015;37:639–49. https://doi.org/10.1007/s00281-015-0514-4.
18. Kaddurah-Daouk R, Krishnan KRR. Metabolomics: a global biochemical approach to the study of central nervous system diseases. Neuropsychopharmacology. 2009;34:173–86. https://doi.org/10.1038/npp.2008.174.
19. Wood PL. Mass spectrometry strategies for clinical metabolomics and lipidomics in psychiatry, neurology, and neuro-oncology. Neuropsychopharmacology. 2014;39:24–33. https://doi.org/10.1038/npp.2013.167.
20. Ivanisevic J, Siuzdak G. The role of metabolomics in brain metabolism research. J NeuroImmune Pharmacol. 2015;10:391–5. https://doi.org/10.1007/s11481-015-9621-1.
21. Tumani H, Hartung HP, Hemmer B, Teunissen C, Deisenhammer F, Giovannoni G, et al. Cerebrospinal fluid biomarkers in multiple sclerosis. Neurobiol Dis. 2009;35:117–27. https://doi.org/10.1016/j.nbd.2009.04.010.
22. Kang J, Zhu L, Lu J, Zhang X. Application of metabolomics in autoimmune diseases: insight into biomarkers and pathology. J Neuroimmunol. 2015;279:25–32. https://doi.org/10.1016/j.jneuroim.2015.01.001.
23. Noga MJ, Dane A, Shi S, Attali A, van Aken H, Suidgeest E, et al. Metabolomics of cerebrospinal fluid reveals changes in the central nervous system metabolism in a rat model of multiple sclerosis. Metabolomics. 2012;8:253–63. https://doi.org/10.1007/s11306-011-0306-3.
24. Coulier L, Muilwijk B, Bijlsma S, Noga M, Tienstra M, Attali A, et al. Metabolite profiling of small cerebrospinal fluid sample volumes with gas chromatography-mass spectrometry: application to a rat model of multiple sclerosis. Metabolomics. 2013;9:78–87. https://doi.org/10.1007/s11306-012-0428-2.

Spatial and molecular changes of mouse brain metabolism in response to immunomodulatory treatment with...

25. Pieragostino D, D'Alessandro M, di Ioia M, Rossi C, Zucchelli M, Urbani A, et al. An integrated metabolomics approach for the research of new cerebrospinal fluid biomarkers of multiple sclerosis. Mol BioSyst. 2015;11:1563–72. https://doi.org/10.1039/C4MB00700J.

26. Kantae V, Krekels EHJ, Esdonk MJV, Lindenburg P, Harms AC, Knibbe CAJ, et al. Integration of pharmacometabolomics with pharmacokinetics and pharmacodynamics: towards personalized drug therapy. Metabolomics. 2017;13:1–11. https://doi.org/10.1007/s11306-016-1143-1.

27. Wishart DS. Emerging applications of metabolomics in drug discovery and precision medicine. Nat Rev Drug Discov. 2016;15:473–84. https://doi.org/10.1038/nrd.2016.32.

28. Miura D, Fujimura Y, Warishi H. In situ metabolomic mass spectrometry imaging: recent advances and difficulties. J Proteome. 2012;75:5052–60. https://doi.org/10.1016/j.jprot.2012.02.011.

29. Dekker TJA, Jones EA, Corver WE, van Zeijl RJM, Deelder AM, Tollenaar RAEM, et al. Towards imaging metabolic pathways in tissues. Anal Bioanal Chem. 2015;407:2167–76. https://doi.org/10.1007/s00216-014-8305-7.

30. Palmer A, Trede D, Alexandrov T. Where imaging mass spectrometry stands: here are the numbers. Metabolomics. 2016;12:107. https://doi.org/10.1007/s11306-016-1047-0.

31. Norris JL, Caprioli RM. Analysis of tissue specimens by matrix-assisted laser desorption/ionization imaging mass spectrometry in biological and clinical research. Chem Rev. 2013;113:2309–42. https://doi.org/10.1021/cr3004295.

32. Spengler B. Mass spectrometry imaging of biomolecular information. Anal Chem. 2015;87:64–82. https://doi.org/10.1021/ac504543v.

33. Ellis SR, Bruinen AL, Heeren RMA. A critical evaluation of the current state-of-the-art in quantitative imaging mass spectrometry. Anal Bioanal Chem. 2014;406:1275–89. https://doi.org/10.1007/s00216-013-7478-9.

34. Rzagalinski I, Volmer DA. Quantification of low molecular weight compounds by MALDI imaging mass spectrometry—a tutorial review. Biochim Biophys Acta - Proteins Proteomics. 2017;1865:726–39. https://doi.org/10.1016/j.bbapap.2016.12.011.

35. Shariatgorji M, Svenningsson P, Andrén PE. Mass spectrometry imaging, an emerging technology in neuropsychopharmacology. Neuropsychopharmacology. 2014;39:34–9. https://doi.org/10.1038/npp.2013.215.

36. Hanrieder J, Phan NTN, Kurczy ME, Ewing AG. Imaging mass spectrometry in neuroscience. ACS Chem Neurosci. 2013;4:666–79. https://doi.org/10.1021/cn400053c.

37. Kaya I, Brinet D, Michno W, Syvänen S, Sehlin D, Zetterberg H, et al. Delineating amyloid plaque associated neuronal sphingolipids in transgenic Alzheimer's disease mice (tgArcSwe) using MALDI imaging mass spectrometry. ACS Chem Neurosci. 2017;8:347–55. https://doi.org/10.1021/acschemneuro.6b00391.

38. Kaya I, Brinet D, Michno W, Başkurt M, Zetterberg H, Blenow K, et al. Novel trimodal MALDI imaging mass spectrometry (IMS3) at 10 μm reveals spatial lipid and peptide correlates implicated in Aβ plaque pathology in Alzheimer's disease. ACS Chem Neurosci. 2017;8:2778–90. https://doi.org/10.1021/acschemneuro.7b00314.

39. Sparvero LJ, Amoscato AA, Kochanek PM, Pitt BR, Kagan VE, Bayär H. Mass-spectrometry based oxidative lipidomics and lipid imaging: applications in traumatic brain injury. J Neurochem. 2010;115:1322–36. https://doi.org/10.1111/j.1471-4159.2010.07055.x.

40. Barbacci DC, Roux A, Muller L, Jackson SN, Post J, Baldwin K, et al. Mass spectrometric imaging of ceramide biomarkers tracks therapeutic response in traumatic brain injury. ACS Chem Neurosci. 2017;8:2266–74. https://doi.org/10.1021/acschemneuro.7b00189.

41. Hanrieder J, Ekegren T, Andersson M, Bergquist J. MALDI imaging of post-mortem human spinal cord in amyotrophic lateral sclerosis. J Neurochem. 2013;124:695–707. https://doi.org/10.1111/jnc.12019.

42. Hanrieder J, Ewing AG. Spatial elucidation of spinal cord lipid- and metabolite- regulations in amyotrophic lateral sclerosis. Sci Rep. 2014;4:1–7. https://doi.org/10.1038/srep05266.

43. Bergholt MS, Serio A, McKenzie JS, Boyd A, Soares RF, Tillner J, et al. Correlated heterospectral lipidomics for biomolecular profiling of remyelination in multiple sclerosis. ACS Cent Sci. 2018;4:39–51. https://doi.org/10.1021/acscentsci.7b00367.

44. Sun N, Fernandez IE, Wei M, Wu Y, Aichler M, Eickelberg O, et al. Pharmacokinetic and pharmacometabolomic study of pirfenidone in normal mouse tissues using high mass resolution MALDI-FTICR-mass spectrometry imaging. Histochem Cell Biol. 2016;145:201–11. https://doi.org/10.1007/s00418-015-1382-7.

45. Bodzon-Kulakowska A, Antolak A, Drabik A, Marszalek-Grabska M, Kotlińska J, Suder P. Brain lipidomic changes after morphine, cocaine and amphetamine administration—DESI—MS imaging study. Biochim Biophys Acta - Mol Cell Biol Lipids. 2017;1862:686–91. https://doi.org/10.1016/j.bbalip.2017.04.003.

46. Joye T, Bararpour N, Augsburger M, Boutrel B, Thomas A. In situ metabolomic changes in rat hippocampus after acute cocaine administration. Int J Mass Spectrom. 2017:1–5. https://doi.org/10.1016/j.ijms.2017.12.001.

47. Philipsen MH, Phan NNT, Fletcher JS, Malmberg P, Ewing AG (2018) Mass spectrometry imaging shows cocaine and methylphenidate have opposite effects on major lipids in Drosophila brain. ACS Chem Neurosci acschemneuro.8b00046. doi: https://doi.org/10.1021/acschemneuro.8b00046.

48. Roux A, Muller L, Jackson SN, Baldwin K, Womack V, Pagiazitis JG, et al. Chronic ethanol consumption profoundly alters regional brain ceramide and sphingomyelin content in rodents. ACS Chem Neurosci. 2015;6:247–59. https://doi.org/10.1021/cn500174c.

49. Hanrieder J, Gerber L, Persson Sandelius Å, Brittebo EB, Ewing AG, Karlsson O. High resolution metabolite imaging in the hippocampus following neonatal exposure to the environmental toxin BMAA using ToF-SIMS. ACS Chem Neurosci. 2014;5:568–75. https://doi.org/10.1021/cn500039b.

50. European Medicines Agency (2013) AUBAGIO—Assessment Report No. EMEA/H/C/002514/0000. 44:150.

51. Franklin KBJ, Paxinos G. The mouse brain in stereotaxic coordinates, compact. In: The coronal plates and diagrams. Amsterdam: Elsevier Academic Press; 2008.

52. Miura D, Fujimura Y, Yamato M, Hyodo F, Utsumi H, Tachibana H, et al. Ultrahighly sensitive in situ metabolomic imaging for visualizing spatiotemporal metabolic behaviors. Anal Chem. 2010;82:9789–96. https://doi.org/10.1021/ac101998z.

53. Irie M, Fujimura Y, Yamato M, Miura D, Warishi H. Integrated MALDI-MS imaging and LC-MS techniques for visualizing spatiotemporal metabolomic dynamics in a rat stroke model. Metabolomics. 2014;10:473–83. https://doi.org/10.1007/s11306-013-0588-8.

54. Rzagalinski I, Hainz N, Meier C, Tschernig T, Volmer DA. MALDI mass spectral imaging of bile acids observed as deprotonated molecules and proton-bound dimers from mouse liver sections. J Am Soc Mass Spectrom. 2018. https://doi.org/10.1007/s13361-017-1886-6.

55. Schramm T, Hester A, Klinkert I, Both JP, Heeren RMA, Brunelle A, et al. ImzML—a common data format for the flexible exchange and processing of mass spectrometry imaging data. J Proteome. 2012;75:5106–10. https://doi.org/10.1016/j.jprot.2012.07.026.

56. Bokhart MT, Nazari M, Garrard KP, Muddiman DC. MSiReader v1.0: evolving open-source mass spectrometry imaging software for targeted and untargeted analyses. J Am Soc Mass Spectrom. 2018;29:8–16. https://doi.org/10.1007/s13361-017-1809-6.

57. Smith CA, O'Maille G, Want EJ, Qin C, Trauger SA, Brandon TR, et al. METLIN: a metabolite mass spectral database. Ther Drug Monit. 2005;27:747–51. https://doi.org/10.1097/01.ftd. 0000179845.53213.39.

58. Wishart DS, Feunang YD, Marcu A, Guo AC, Liang K, Vázquez-Fresno R, et al. HMDB 4.0: the human metabolome database for 2018. Nucleic Acids Res. 2018;46:D608–17. https://doi.org/10. 1093/nar/gkx1089.

59. Okuda S, Yamada T, Hamajima M, Itoh M, Katayama T, Bork P, et al. KEGG Atlas mapping for global analysis of metabolic pathways. Nucleic Acids Res. 2008;36:423–6. https://doi.org/10.1093/nar/gkn282.

60. Deininger SO, Cornett DS, Paape R, Becker M, Pineau C, Rauser S, et al. Normalization in MALDI-TOF imaging datasets of proteins: practical considerations. Anal Bioanal Chem. 2011;401:167–81. https://doi.org/10.1007/s00216-011-4929-z.

61. Parekh JM, Vaghela RN, Sutariya DK, Sanyal M, Yadav M, Shrivastav PS. Chromatographic separation and sensitive determination of teriflunomide, an active metabolite of leflunomide in human plasma by liquid chromatography-tandem mass spectrometry. J Chromatogr B Anal Technol Biomed Life Sci. 2010;878:2217–25. https://doi.org/10.1016/j.jchromb.2010.06.028.

62. Rakhila H, Rozek T, Hopkins A, Proudman S, Cleland L, James M, et al. Quantitation of total and free teriflunomide (A77 1726) in human plasma by LC-MS/MS. J Pharm Biomed Anal. 2011;55: 325–31. https://doi.org/10.1016/j.jpba.2011.01.034.

63. Barber TW, Brockway JA, Higgins LS. The density of tissues in and about the head. Acta Neurol Scand. 1970;46:85–92.

64. (2013) Australian public assessment report for teriflunomide. Aust Gov Dep Heal Ageing Ther Good Adm.

65. Rozman B. Clinical pharmacokinetics of leflunomide. Clin Pharmacokinet. 2002;41:421–30. https://doi.org/10.2165/00003088-200241060-00003.

66. Kis E, Nagy T, Jani M, Molnár É, Jánossy J, Ujhellyi O, et al. Leflunomide and its metabolite A771726 are high affinity substrates of BCRP: implications for drug resistance. Ann Rheum Dis. 2009;68:1201–7. https://doi.org/10.1136/ard.2007.086264.

67. Cheng Z, Zhang J, Liu H, Li Y, Zhao Y, Yang E. Central nervous system penetration for small molecule therapeutic agents does not increase in multiple sclerosis- and Alzheimer's disease-related animal models despite reported blood-brain barrier disruption. Drug Metab Dispos. 2010;38:1355–61. https://doi.org/10.1124/dmd.110. 033324.Animal.

68. Burnstock G. Purine and pyrimidine receptors. Cell Mol Life Sci. 2007;64:1471–83. https://doi.org/10.1007/s00018-007-6497-0.

69. Abbracchio MP, Burnstock G, Verkhratsky A, Zimmermann H. Purinergic signalling in the nervous system: an overview. Trends Neurosci. 2009;32:19–29. https://doi.org/10.1016/j.tins.2008.10.001.

70. Burnstock G. Purinergic signalling and disorders of the central nervous system. Nat Rev Drug Discov. 2008;7:575–90. https://doi.org/10.1038/nrd2605.

71. Micheli V, Camici M, Tozzi MG, Ipata PL, Sestini S, Bertelli M, et al. Neurological disorders of purine and pyrimidine metabolism. Curr Top Med Chem. 2011;1:923–47. https://doi.org/10.2174/156802611795347645.

72. Veremeyko T, Yung AWY, Dukhinova M, Kuznetsova IS, Pomytkin I, Lyundup A, et al. Cyclic AMP pathway suppress autoimmune neuroinflammation by inhibiting functions of encephalitogenic CD4 T cells and enhancing M2 macrophage polarization at the site of inflammation. Front Immunol. 2018. https://doi.org/10.3389/fimmu.2018.00050.

73. Cieślak M, Kukulski F, Komoszyński M. Emerging role of extracellular nucleotides and adenosine in multiple sclerosis. Purinergic Signal. 2011;7:393–402. https://doi.org/10.1007/s11302-011-9250-y.

74. Safarzadeh E, Jadidi-Niaragh F, Motallebnezhad M, Yousefi M. The role of adenosine and adenosine receptors in the immunopathogenesis of multiple sclerosis. Inflamm Res. 2016;65: 511–20. https://doi.org/10.1007/s00011-016-0936-z.

75. Hidetoshi TS, Makoto T, Inoue K. P2Y receptors in microglia and neuroinflammation. Wiley Interdiscip Rev Membr Transp Signal. 2012;1:493–501. https://doi.org/10.1002/wmts.46.

76. Burnstock G. An introduction to the roles of purinergic signalling in neurodegeneration, neuroprotection and neuroregeneration. Neuropharmacology. 2016;104:4–17. https://doi.org/10.1016/j.neuropharm.2015.05.031.

77. Lecca D, Ceruti S. Uracil nucleotides: from metabolic intermediates to neuroprotection and neuroinflammation. Biochem Pharmacol. 2008;75:1869–81. https://doi.org/10.1016/j.bcp.2007.12.009.

78. Mandolesi G, Gentile A, Musella A, Fresegna D, De Vito F, Bullitta S, et al. Synaptopathy connects inflammation and neurodegeneration in multiple sclerosis. Nat Rev Neurol. 2015;11:711–24. https://doi.org/10.1038/nrneurol.2015.222.

79. Lutz NW, Viola A, Malikova I, Confort-Gouny S, Audoin B, Ranjeva JP, et al. Inflammatory multiple-sclerosis plaques generate characteristic metabolic profiles in cerebrospinal fluid. PLoS One. 2007;2:1–9. https://doi.org/10.1371/journal.pone.0000595.

80. Vingara LK, Yu HJ, Wagshul ME, Serafin D, Christodoulou C, Pelczer I, et al. Metabolomic approach to human brain spectroscopy identifies associations between clinical features and the frontal lobe metabolome in multiple sclerosis. Neuroimage. 2013;82:586–94. https://doi.org/10.1016/j.neuroimage.2013.05.125.

81. Carvalho AN, Lim JL, Nijland PG, Witte ME, Van Horssen J. Glutathione in multiple sclerosis: more than just an antioxidant? Mult Scler J. 2014;20:1425–31. https://doi.org/10.1177/1352458514533400.

82. Regenold WT, Phatak P, Makley MJ, Stone RD, M a K. Cerebrospinal fluid evidence of increased extra-mitochondrial glucose metabolism implicates mitochondrial dysfunction in multiple sclerosis disease progression. J Neurol Sci. 2008;275:106–12. https://doi.org/10.1016/j.jns.2008.07.032.

83. Shkil'nyuk GG, Il'ves AG, Kataeva GV, Prakhova LN, Reznikova TN, Seliverstova NA, et al. The role of changes in glucose metabolism in the brain in the formation of cognitive impairments in patients with remitting and secondary-progressive multiple sclerosis. Neurosci Behav Physiol. 2013;43:565–70.

84. Obel LF, Müller MS, Walls AB, Sickmann HM, Bak LK, Waagepetersen HS, et al. Brain glycogen—new perspectives on its metabolic function and regulation at the subcellular level. Front Neuroenerg. 2012;4:1–15. https://doi.org/10.3389/fnene.2012.00003.

85. Chambers JK, Macdonald LE, Sarau HM, Ames RS, Freeman K, Foley JJ, et al. A G protein-coupled receptor for UDP-glucose. J Biol Chem. 2000;275:10767–71.

86. Harden TK, Sesma JI, Fricks IP, Lazarowski ER. Signalling and pharmacological properties of the P2Y14 receptor. Acta Physiol. 2010;199:149–60. https://doi.org/10.1111/j.1748-1716.2010. 02116.x.

87. Brautigam VM, Dubyak GR, Crain JM, Watters JJ. The inflammatory effects of UDP-glucose in N9 microglia are not mediated by P2Y14 receptor activation. Purinergic Signal. 2008;4:73–8. https://doi.org/10.1007/s11302-008-9095-1.

88. Partida-Sánchez S, Cockayne DA, Monard S, Jacobson EL, Oppenheimer N, Garvy B, et al. Cyclic ADP-ribose production by CD38 regulates intracellular calcium release, extracellular calcium influx and chemotaxis in neutrophils and is required for bacterial clearance in vivo. Nat Med. 2001;7:1209–16. https://doi.org/10.1038/nm1101-1209.

Spatial and molecular changes of mouse brain metabolism in response to immunomodulatory treatment with...

89. Higashida H, Hashii M, Yokoyama S, Hoshi N, Asai K, Kato T. Cyclic ADP-ribose as a potential second messenger. J Neurochem. 2001;76:321–31.
90. Moore DJ, Murdock PR, Watson JM, Faull RLM, Waldvogel HJ, Szekeres PG, et al. GPR105, a novel Gi/o-coupled UDP-glucose receptor expressed on brain glia and peripheral immune cells, is regulated by immunologic challenge: possible role in neuroimmune function. Mol Brain Res. 2003;118:10–23. https://doi.org/10.1016/S0169-328X(03)00330-9.

Electronic Supplementary Material

Spatial and molecular changes of mouse brain metabolism in response to immunomodulatory treatment with teriflunomide as visualized by MALDI-MSI

Ignacy Rzagalinski[1], Nadine Hainz[2], Carola Meier[2], Thomas Tschernig[2], Dietrich A. Volmer[3]*

[1]Institute of Bioanalytical Chemistry, Saarland University, 66123 Saarbrücken, Germany
[2]Institute of Anatomy and Cell Biology, Saarland University, 66421 Homburg, Germany
[3]Department of Chemistry, Humboldt University of Berlin, 12489 Berlin, Germany

*To whom correspondence should be addressed:

Prof. Dr. Dietrich A. Volmer
Department of Chemistry
Humboldt University of Berlin
Brook-Taylor-Str. 2
12489 Berlin, Germany
Tel: +49 30 2093 7588
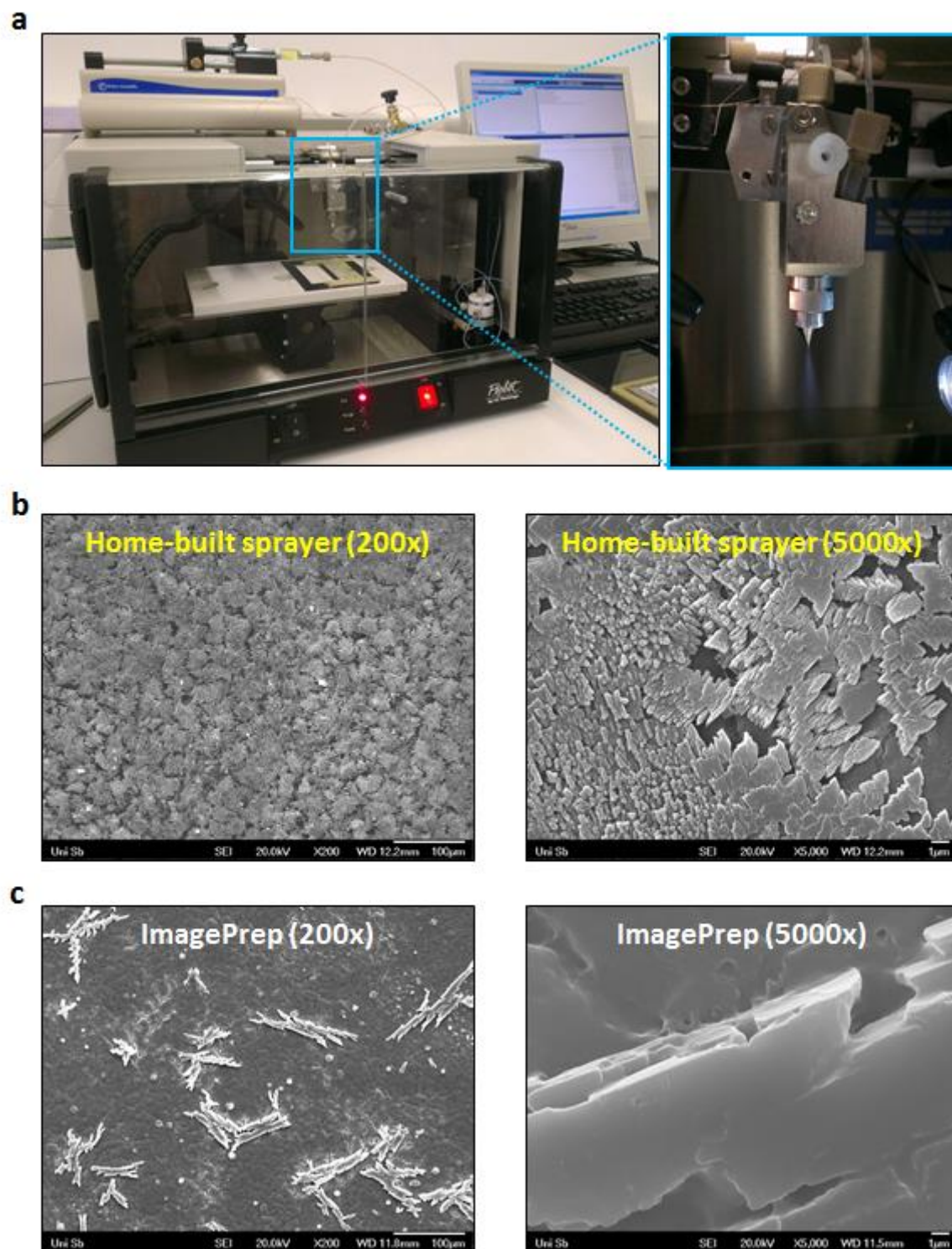Email: dietrich.volmer@hu-berlin.de

Fig. S1. (a) Home-built robotic MALDI matrix sprayer based on the Probot fraction collector platform, micro spraying nozzle and syringe pump (left panel). The constructed device provided a fine and highly reproducible spray (zoomed micro nozzle in the right panel). **(b, c)** SEM images of 9-AA matrix sprayed onto the surface of the control brain section using two different instruments: home-built sprayer **(b)** and commercially available ImagePrep **(c)**. Magnification: 200× (left panels); 5000x (right panels). Scale bars: 100 μm (left panels); 1 μm (right panels).
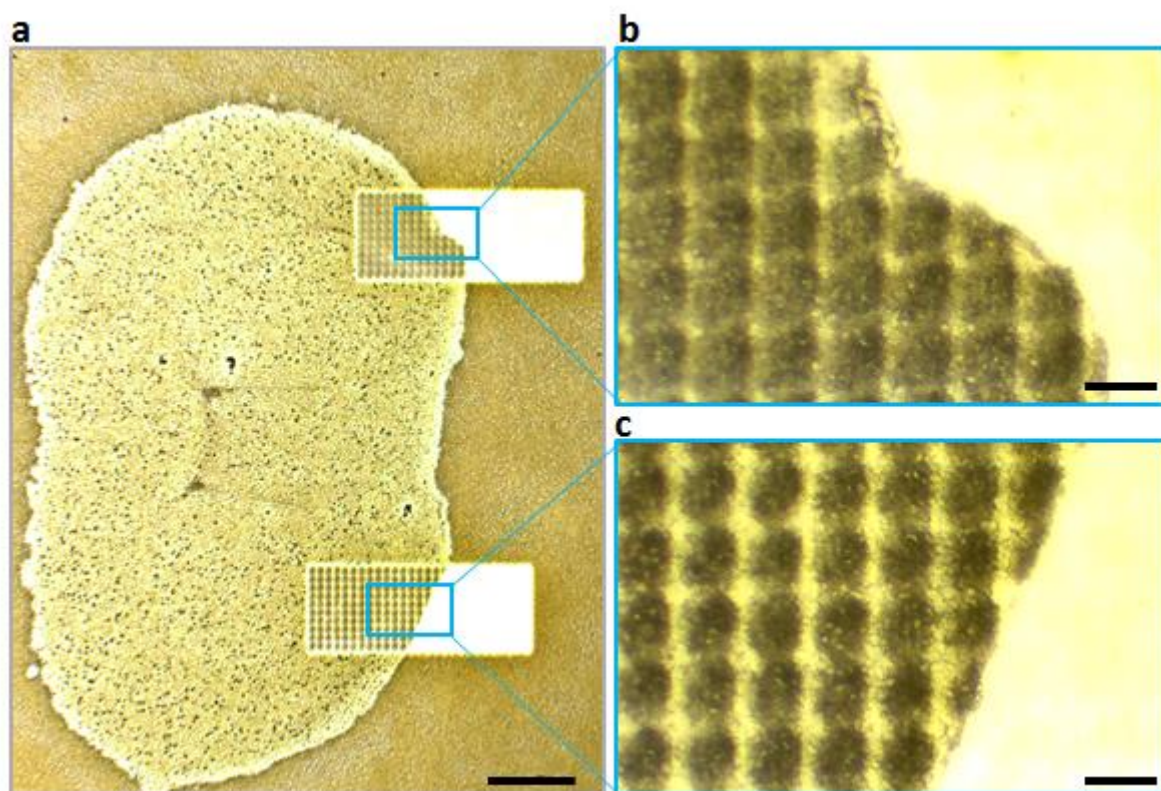
Fig. S2. Microscopic images of mouse brain coronal section sprayed with 9-AA matrix **(a)** with two smaller regions processed at the typical MALDI imaging settings at the raster width of 100 µm. Laser focus: "small", laser power: 20%, repetition rate: 1 kHz and two different settings of laser shots number/pixel: 500 **(b)** or 200 **(c)**. The latter setting (200 laser shots/pixel at 70 µm pixel size) were selected to provide optimal conditions for all imaging experiments in the current study. Scale bars: 1000 µm (a); 100 µm (b, c).
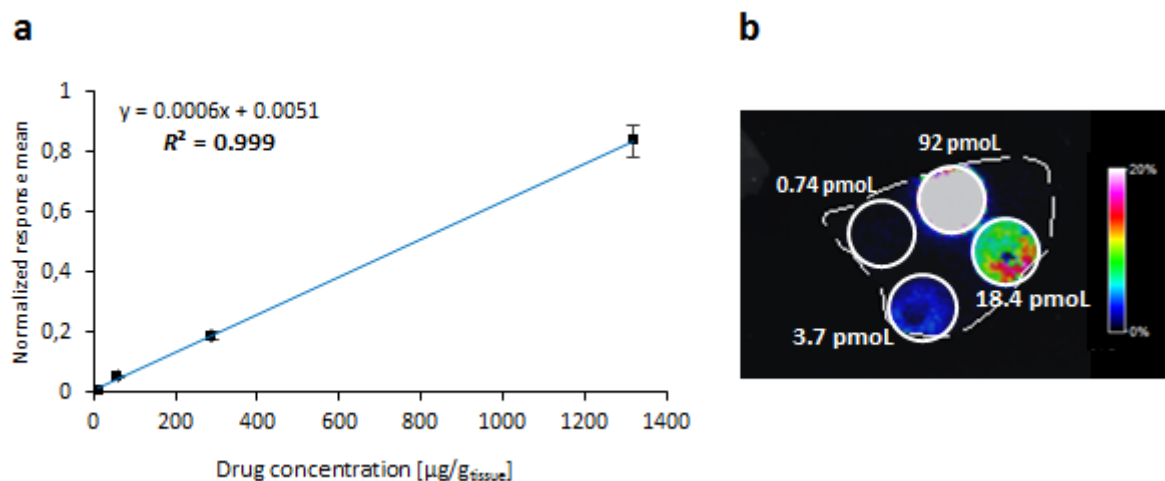
Fig. S3. (a) Linear relationship (coefficient of determination, $R^2 = 0.999$) between calculated tissue concentration of teriflunomide spiked on the top of control mouse brain section and normalized mean abundance. Error bars indicate 95% confidence intervals of the mean. **(b)** Corresponding MS ion image obtained from the control mouse brain section after manually spotted (0.5 µL) drug standard solutions of four different concentrations: 184 µM, 36.8 µM, 7.40 µM and 1.48 µM. (Note: this is enlarged version of the 2D ion image showed in Fig. 1c).

VIII. Curriculum vitae

// EDUCATION

01.2015 – 12.2018   **Ph.D. in Analytical Chemistry**
Saarland University, Institute of Bioanalytical Chemistry, Germany
Thesis: Novel approaches for molecular tissue imaging of drugs and metabolites using high-resolution mass spectrometry

01.2013 – 01.2014   **Postgraduate Diploma in Marketing and Marketing Strategies**
Warsaw School of Economics, Poland
Thesis: Marketing communication strategies for liquid chromatography instrumentation market

10.2002 – 10.2007   **M.Sc. in Chemistry**
Univeristy of Warsaw, Laboratory for Flow Analysis and Chromatography, Poland
Thesis: Enzymatic derivatization in capillary electrophoresis

// PROFFESIONAL POSITIONS

01.2015 - 07.2018   **Research Associate**
Saarland University, Institute of Bioanalytical Chemistry, Germany
Planning and conducting research; teaching and supervising students

11.2007 – 11.2014   **Scientific Representative (Liquid Chromatography and Sample Preparation Division)**
A.G.A. Analytical – Thermo Scientific Authorized Partner, Poland
Application and sales support for customers with high performance liquid chromatography (HPLC, IC) and automated extraction (SPE, ASE)

// ADITIONAL COURSES AND TRAININGS

2016   **Future Directions in Disease Profiling and Molecular Pathology**, Heidelberg University, Germany

2015   **Matlab course**, Saarland University, Saarbrücken, Germany

2013   **Automated solid phase-extraction (SPE)**, Gilson BV, Hague, Netherlands

2011   **High performance capillary ion chromatography**, Dionex Thermo Fisher Scientific, Munich, Germany

2010   **High performance ion chromatography (HPIC) and accelerated solvent extraction (ASE)**, Dionex Thermo Fisher Scientific, Olten, Switzerland

2007   **Chemical metrology – statistics and uncertainty of measurement results**
Scientific presentation and communication, University of Warsaw, Poland

IX. Scientific contributions

// PUBLICATIONS

- <u>Rzagalinski I</u>, Hainz N, Meier C, Tschernig T, Volmer DA (**2018**). Spatial and molecular changes of mouse brain metabolism in response to immunomodulatory treatment with teriflunomide as visualized by MALDI-MSI. *Analytical and Bioanalytical Chemistry*, 411:353–365, DOI: 10.1007/s00216-018-1444-5

- <u>Rzagalinski I</u>, Kovacevic B, Hainz N, Meier C, Tschernig T, Volmer DA (**2018**). Toward higher sensitivity in quantitative MALDI imaging mass spectrometry of CNS drugs using a nonpolar matrix. *Analytical Chemistry*, 90, 12592−12600, DOI: 10.1021/acs.analchem.8b02740

- <u>Rzagalinski I</u>, Hainz N, Meier C, Tschernig T, Volmer DA (**2018**). MALDI mass spectral imaging of bile acids observed as deprotonated molecules and proton-bound dimers from mouse liver sections. *Journal of the American Society for Mass Spectrometry*, 29:711-722, DOI: 10.1007/s13361-017-1886-6

- <u>Rzagalinski I</u>, Volmer DA (**2017**). Quantification of low molecular weight compounds by MALDI imaging mass spectrometry – a tutorial review. *Biochimica et Biophysica Acta–Proteins and Proteomics*, 1865(7): 726-739. DOI: 10.1016/j.bbapap.2016.12.011

- Fukuyama T, Ganchingco JR, Mishra SK, Olivry T, <u>Rzagalinski I</u>, Volmer DA, Bäumer W (**2017**). Janus-kinase inhibitors display broad anti-itch properties – a possible link via TRPV1-receptor. *Journal of Allergy and Clinical Immunology*, 140(1): 306-309.e3. DOI: 10.1016/j.jaci.2016.12.960

- <u>Rzygalinski I</u>, Pobozy E, Drewnowska R, Trojanowicz M (**2008**). Enzymatic in-capillary derivatization for glucose determination by electrophoresis with spectrophotometric detection. *Electrophoresis*, 29: 1741-1748. DOI: 10.1002/elps.200700726

// ORAL PRESENTATIONS

2018	<u>Rzagalinski I</u>, **Molecular tissue imaging of drugs and metabolites by MALDI mass spectrometry** Public seminar at the Max Planck Institute of Molecular Cell Biology and Gentics (MPI-CBG) in Dresden, Germany
2018	<u>Rzagalinski I</u>, Volmer D. **MALDI mass spectral imaging of bile acids – increasing signal intensities for deprotonated molecules by broadband dissociation of proton-bound dimers** Mass Spectrometry Imaging Workshop during the European Mass Spectrometry Conference (EMSC 2018), Saarbrücken, Germany
2018	<u>Rzagalinski I</u>, Volmer D. **Towards higher sensitivity in MALDI-FTICR imaging of CNS drugs using a matrix matching unique analyte properties** European Mass Spectrometry Conference (EMSC 2018), Saarbrücken, Germany

2017	<u>Rzagalinski I</u>, Volmer D. **MALDI imaging of bile acids in mouse liver sections: impact of proton-bound dimer formation between endogenous tissue metabolites** 5th Imaging Mass Spectrometry Conference (OurCon V), Doorn, Netherlands
2016	<u>Rzagalinski I</u>, Volmer D. **MALDI-FTICR imaging for studying the penetration of teriflunomide through the blood-brain barrier** 49th Annual Conference of the German Society for Mass Spectrometry (DGMS), Hamburg, Germany
2012	<u>Rzagalinski I</u>. **Modern extraction techniques in pharmaceutical and clinical analysis** 3rd Scientific Symposium on modern analytical techniques for quality assessment of medicinal products, Lublin, Poland
2011	<u>Rzagalinski I</u>. **Capillary ion chromatography - new frontiers in analysis of ionic substances** 2nd Scientific Conference on chromatographic methods for the determination of ionic substances, Torun, Poland

// POSTER PRESENTATIONS

2016	<u>Rzagalinski I</u>, Volmer D. **MALDI-FTICR imaging of the distribution of teriflunomide in CNS tissues in an experimental model of multiple sclerosis** 64th Conference of the American Society for Mass Spectrometry (ASMS), San Antonio, USA
2015	<u>Rzagalinski I</u>, Volmer D. **Mass spectrometry imaging of drugs and metabolites for studying multiple sclerosis** PhD Students Day of UdS 2015, Saarbrücken, Germany
2007	<u>Rzagalinski I</u>, Poboży E, Trojanowicz M. **Determination of glucose by capillary electrophoresis with spectrophotometric detection using enzymatic systems** 7th International Symposium and Summer School on Bioanalysis, Pecs, Hungary